Dynamics of an interacting hadron gas and Measurements of Υ(nS) production and polarization in proton-proton collisions at $\sqrt{s} = 13.6$ TeV with ALICE

A THESIS

Submitted in partial fulfilment of the requirements

for the award of the degree

of

DOCTOR OF PHILOSOPHY

by

Kshitish Kumar Pradhan

DEPARTMENT OF PHYSICS

INDIAN INSTITUTE OF TECHNOLOGY INDORE

December 2025

INDIAN INSTITUTE OF TECHNOLOGY INDORE

I hereby certify that the work which is being presented in the thesis entitled **Dynamics of an interacting hadron gas, and measurements of Υ(nS) production and polarization in proton-proton collisions at $\sqrt{s} = 13.6$ TeV with ALICE** in the partial fulfilment of the requirements for the award of the degree of **DOCTOR OF PHILOSOPHY** and submitted in the **DEPARTMENT OF PHYSICS, Indian Institute of Technology Indore**, is an authentic record of my own work carried out during the time period from December 2020 to December 2025 under the supervision of Raghunath Sahoo, Professor, Department of Physics, Indian Institute of Technology Indore.

The matter presented in this thesis has not been submitted by me for the award of any other degree of this or any other institute.

Kshitish Kumar Pradhan
07/04/2026

Signature of the student with date

(Kshitish Kumar Pradhan)

This is to certify that the above statement made by the candidate is correct to the best of my knowledge.

Rahoo 07.04.26

Signature of Thesis Supervisor with date

(Prof. Raghunath Sahoo)

Mr. Kshitish Kumar Pradhan has successfully given his Ph.D. Oral Examination held on the 7th April 2026.

Rahoo 07-04-26

Signature of Thesis Supervisor with date

(Prof. Raghunath Sahoo)

Dedicated to my father

ACKNOWLEDGEMENTS

With the grace of the Almighty, the completion of this thesis has been a long and fulfilling journey, made possible through the constant guidance, support, and encouragement of many individuals. I would like to take this opportunity to express my heartfelt gratitude to all those who have contributed, directly or indirectly, to the successful completion of this work.

First and foremost, I would like to express my deepest gratitude to my thesis supervisor for his constant guidance, valuable discussions, and constructive feedback throughout my doctoral research. His dedication to physics and enthusiasm for research have created a motivating and supportive environment to work in. His punctuality and strong work ethic have always inspired me. I greatly respect his leadership and his encouragement to think independently, explore new ideas, and push beyond our perceived limits. I am thankful not only for his academic guidance but also for his understanding and thoughtful approach to professional and personal interactions.

I feel privileged to have been part of one of the largest collider experiments, ALICE, at the Large Hadron Collider, the most powerful accelerator in operation. I sincerely acknowledge the support of the DST, DAE, Government of India, and IIT Indore, as well as my supervisor, for providing me with the opportunity and platform to contribute to experimental analysis and data-taking activities at CERN. I gratefully acknowledge the members of the Physics Working Group on Dileptons and Quarkonia (PWG-DQ), in particular the PWG-DQ conveners, Dr. Luca Micheletti, Dr. Cristiane Jahnke, Dr. Maurice Coquet, and Dr. Batoul Diab, for their thoughtful feedback and important contributions, which significantly strengthened the results presented in this thesis.

I would like to express my sincere thanks to my PSPC members, Dr. Manaven-

dra Mahato and Dr. Sumanta Samal, for their guidance and valuable suggestions throughout the course of my research. I also extend my appreciation to Mr. Vedprakash, Mr. Prashant, and Mr. Rahul for their assistance with administrative matters at IIT Indore, which greatly helped in easing several tasks during my doctoral studies. I gratefully acknowledge the financial support provided by the University Grants Commission (UGC), Government of India, for this doctoral research.

I am thankful to my fellow lab mates in the Experimental High Energy Physics Laboratory at IIT Indore for the collaborative and supportive environment in the lab. The numerous discussions, shared ideas, and mutual encouragement within the group played a crucial role in shaping my work and broadening my understanding throughout this journey. A special thanks to Dr. Dushmanta Sahu for always being ready to get involved in discussions and for helping whenever I need it. I will always be grateful for his guidance and the collaboration to work on various problems. I will always be grateful to Dr. Ronald Scaria for providing a friendly attitude and helping with many physics discussions throughout my research. I enjoyed our discussions as collaborators and as colleagues working alongside one another at neighboring desks, which made the research experience both productive and enjoyable. I thank Mr. Kamlajeet Singh for being a close friend and for the constant support and kindness. I thank my collaborators, Dr. Dushmanta Sahoo, Dr. Ronald Scaria, Dr. Jayanta Dey, Bhagyarathi Sahoo, Kangkan Goswami, and Kamaljeet Singh, for fruitful discussions on various physics problems. I am thankful to my lab mate, Aswathy Menon, for a great friendship and for our discussions on physics from fundamental to advanced theories. Long walks with discussions ranging from physics to philosophy and spirituality had a significant impact on my thoughts and actions. I am grateful to all my lab mates for creating and maintaining a positive, constructive, and friendly research environment in the lab.

I am deeply grateful to my parents for their unconditional love and constant

encouragement. Their support, values, and faith in me have been a source of strength and motivation at every stage of my journey. I also extend my heartfelt thanks to my elder brother, Pritish, who is one of the reasons I was able to reach this point in pursuing my interests. I am deeply grateful to have a sister like mine, Priliva, whose love, care, and encouragement have meant a great deal to me. I also thank my uncle Ashwini for his constant encouragement throughout my academic life. Finally, I would like to express my sincere gratitude to everyone whose collective support, encouragement, and guidance have been instrumental in this endeavor.

(Kshitish Kumar Pradhan)

ABSTRACT

Ultra-relativistic heavy-ion collision programs at the Large Hadron Collider (LHC) at CERN and the Relativistic Heavy Ion Collider (RHIC) at BNL are designed to explore strongly interacting matter under extreme conditions of temperature and energy density. In these experiments, the so-called little Bang created in ultra-relativistic nuclear collisions leads to the formation of a novel state of matter known as the quark–gluon plasma (QGP), in which quarks and gluons are no longer confined within hadrons. This state of matter is believed to have existed during the first few microseconds after the Big Bang. Consequently, studying the properties of QGP not only deepens our understanding of the strong interaction at the microscopic level but also provides valuable insight into the early evolution of the universe. The short lifetime of the QGP matter does not leave any direct signature. Its properties are inferred through indirect signatures and through a detailed understanding of the system's evolution across different stages of the space-time evolution of the created fireball.

The transport properties can play a major role in characterizing the dynamical evolution of the produced medium. Since the transport coefficients can, in principle, be derived from fundamental theory, their variation with thermodynamic parameters such as temperature and chemical potential can be useful in identifying the phase structure of QCD. Furthermore, non-central heavy-ion collisions generate intense but transient magnetic fields and huge vorticity in the medium. The combined effect of these fields can significantly influence the bulk properties of QCD matter and modify the conditions governing the transitions between different phases. This thesis investigates the transport properties of the hadronic phase using an interacting hadron resonance gas (HRG) model. The van der Waals HRG (VDWHRG) model, which incorporates attractive and repulsive interactions among hadrons, is found to provide an improved description of thermodynamic observables when compared with lattice QCD calculations

and experimental data. Within this framework, we investigate key transport coefficients, including thermal and electrical conductivities, and study the role of interactions by comparing with those from the ideal HRG model. In addition, we explore the possible formation of a Bose–Einstein condensate in a high-density pion gas and analyze its influence on thermodynamic quantities and transport coefficients.

The effects of global rotation on interacting hadronic matter are examined using a rotating system described by a grand canonical ensemble. We investigate whether rotation can influence the phase transition and, consequently, the corresponding liquid-gas critical point associated with VDW interactions. Moreover, we study the effect of rotation in achieving the condition for the onset of Bose-Einstein condensation. By studying a rotating vector meson gas in the presence of condensation, we demonstrate an interesting interplay between different physical phenomena of condensation, rotation, and polarization. In addition, we revisit the applicability of the VDWHRG model and present a modification that incorporates temperature and chemical potential-dependent VDW parameters. We calculate the proton number cumulants in the modified VDWHRG model and compare the results with those of existing ideal HRG and VDWHRG models, as well as with experimental measurements.

The experimental analysis of the polarization measurements of Υ(1S) is conducted in proton-proton collisions at $\sqrt{s} = 13.6$ TeV using the ALICE detector. The polarization measurement can further help in understanding their production. Moreover, the polarization measurements in proton-proton collisions can serve as a baseline for similar studies in heavy-ion collisions. The dimuon decay channel is used to reconstruct the Υ(1S) using the muon spectrometer in the forward rapidity region. The polarization parameters are obtained as a function of transverse momentum by fitting the angular distribution with the corresponding function. Finally, we compare our results with those obtained in ALICE Run 2 measurements at $\sqrt{s} = 13$ TeV.

PUBLICATIONS

Included in the Thesis

Research Papers

1. K. K. Pradhan, S. Sahu, R. Scaria, and R. Sahoo, "Conductivity, diffusivity, and violation of the Wiedemann-Franz Law in a hadron resonance gas with van der Waals interactions", Phys. Rev. C 107, 014910 (2023).

2. K. K. Pradhan, D. Sahu, C. R. Singh, and R. Sahoo, "Bose-Einstein condensation and dissipative dynamics in a relativistic pion gas", Phys. Rev. D 112, 074031 (2025).

3. K. K. Pradhan, B. Sahoo, D. Sahu, and R. Sahoo, "Thermodynamics of a rotating hadron resonance gas with van der Waals interaction", Eur. Phys. J. C 84, 936 (2024).

4. K. K. Pradhan, D. Sahu, and R. Sahoo, "Emergent spin polarization from ρ meson condensation in rotating hadronic matter", Phys. Lett. B 872, 140090 (2026).

5. K. K. Pradhan, R. Scaria, D. Sahu, and R. Sahoo, "Proton number cumulants in a modified van der Waals hadron resonance gas", [arXiv:2308.09337].

6. K. K. Pradhan and R. Sahoo, "Relative Upsilon production and measurement of Υ (1S) polarization in pp collisions in forward rapidity at $\sqrt{s}$ = 13.6 TeV", Analysis note ID number: ANA-1645, `https://alice-notes.web.cern.ch/node/1645` (ALICE Internal).

Conference Proceedings

1. K. K. Pradhan, D. Sahu, R. Scaria, and R. Sahoo, "Electrical and thermal conductivities in a hadron resonance gas with van der Waals interactions," DAE Symp. Nucl. Phys. 66, 853 (2023).

2. K. K. Pradhan, R. Scaria, D. Sahu, and R. Sahoo, "Higher order proton number fluctuations in a modified van der Waals hadron resonance gas model," DAE Symp. Nucl. Phys. 67, 887 (2024).

3. K. K. Pradhan, D. Sahu, R. Scaria, and R. Sahoo, "The Effect of van der Waals Interactions on Transport Properties in a Hadron Gas," Springer Proc. Phys. 304, 928 (2024).

4. K. K. Pradhan, B. Sahoo, D. Sahu, and R. Sahoo, "Effect of rotation on the liquid-gas phase transition in a hadron resonance gas," DAE Symp. Nucl. Phys. 68, 943 (2025).

5. K. K. Pradhan, D. Sahu, R. Scaria, and R. Sahoo, "Estimating the thermal and electrical conductivities in a Hadron resonance gas with van der Waals interaction," J. Subatomic Part. Cosmol. 4, 100204 (2025).

6. K. K. Pradhan, B. Sahoo, D. Sahu, and R. Sahoo, "Studying liquid-gas phase transition under the effect of rotation in a hadron resonance gas," J. Subatomic Part. Cosmol. 4, 100134 (2025).

7. K. K. Pradhan, B. Sahoo, D. Sahu, and R. Sahoo, "The Liquid-Gas Phase Transition in a Rotating Hadron Resonance Gas," Springer Proc. Phys. 432, 1084. (2026).

8. K. K. Pradhan, R. Scaria, D. Sahu, and R. Sahoo, "Studying Net-Proton Number Cumulants in a Modified van der Waals Hadron Resonance Gas," Springer Proc. Phys. 432, 1120 (2026).

Other Publications

Research Papers

1. B. Sahoo, K. K. Pradhan, D. Sahu, and R. Sahoo, "Effect of a magnetic field on the thermodynamic properties of a high-temperature hadron resonance gas with van der Waals interactions", Phys. Rev. D 108, 074028 (2023).

2. K. Goswami, K. K. Pradhan, D. Sahu, and R. Sahoo, "Diffusion and fluctuations of open charmed hadrons in an interacting hadronic medium", Phys. Rev. D 108, 074011 (2023).

3. K. Goswami, K. K. Pradhan, D. Sahu, J. Dey, and R. Sahoo, "Can charm fluctuation be a better probe to study the QCD critical point?", Phys. Rev. D 111, 014029 (2025).

4. K. Singh, K. K. Pradhan, D. Sahu, and R. Sahoo, "Thermoelectric effects of an interacting hadron gas in the presence of an external magnetic field", Phys. Rev. D 111, 074033 (2025).

5. K. Goswami, K. K. Pradhan, D. Sahu, and R. Sahoo, "Partial pressure and susceptibilities of charmed sector in the van der Waals hadron resonance gas model", Phys. Rev. D 113, 014042 (2026).

6. K. Singh, K. K. Pradhan, and R. Sahoo, "Magneto-Thomson and transverse Thomson effects in an interacting hadron gas in the presence of an external magnetic field", Phys. Rev. D 113, 034021 (2026).

7. B. Sahoo, K. K. Pradhan, D. Sahu, and R. Sahoo, "Rotational susceptibility of a hot and dense hadronic matter: A possible probe of QCD phase transition", [arXiv:2507.03708].

8. N. Padhan, K. K. Pradhan, A. Chatterjee and R. Sahoo, "Vorticity-induced modifications of chemical freeze-out in heavy-ion collisions," [arXiv:2603.27267].

Conference Proceedings

1. B. Sahoo, K. K. Pradhan, D. Sahu, and R. Sahoo, "Refractive index of the hadronic medium in the presence of a magnetic field, "DAE Symp. Nucl. Phys. 67, 885 (2024).

2. K. Goswami, K. K. Pradhan, D. Sahu, and R. Sahoo, "Dynamics of charmed hadron in an interacting hadron gas," DAE Symp. Nucl. Phys. 67 883 (2024).

3. B. Sahoo, K. K. Pradhan, D. Sahu, and R. Sahoo, "Exploring the effect of magnetic field on the liquid-gas phase transition in a hadron resonance gas approach with van der Waals interactions," DAE Symp. Nucl. Phys. 68, 863 (2025).

4. K. Goswami, K. K. Pradhan, D. Sahu, and R. Sahoo, "Exploring the melting of heavy-flavor hadrons and diffusion of charm quarks," PoS QNP2024, 115 (2025).

5. K. Goswami, K. K. Pradhan, D. Sahu, J. Dey, and R. Sahoo, "Possibility of charm diffusion in an interacting hadronic matter," J. Subatomic Part. Cosmol. 4, 100151 (2025).

6. K. Goswami, K. K. Pradhan, D. Sahu, and R. Sahoo, "Partial pressure of charmed hadrons in an interacting hadronic medium," DAE Symp. Nucl. Phys. 69, 1119 (2026).

7. K. Goswami, K. Kumar Pradhan, D. Sahu, J. Dey, and R. Sahoo, "Diffusion Matrix Related to Charmed State and a New Probe for QCD Critical Point," Springer Proc. Phys. 432, 831 (2026).

Contents

Figures

Tables

Chapter 1

Introduction

Human curiosity to understand the origin of the universe at its largest, as well as how it behaves at the smallest scale, has led to some of the most remarkable scientific discoveries. Through the discovery of electrons in cathode ray experiments in 1897, J. J. Thomson opened the door to understanding the atom's composition. Following Ernest Rutherford's famous 1911 gold-foil experiment, which revealed the nuclear structure of the atom, he subsequently identified the proton in 1919 through α-particle scattering experiments on nitrogen. In 1932, James Chadwick completed the picture of the atomic nucleus by discovering the neutron. From then on, with the advancement of quantum mechanics and quantum field theory, a lot of fundamental particles and anti-particles were proposed and discovered, stretching the horizon of our knowledge of the subatomic field and its interactions. In 1964, Murray Gell-Mann and George Zweig independently introduced the Quark model, proposing that hadrons, such as protons and neutrons, consist of even more fundamental constituents known as quarks. These quarks are bound together by strong interaction mediated by a color-charged boson called a gluon. This led to the formation of Quantum Chromodynamics (QCD), a non-Abelian Gauge theory that describes the dynamics of the strong interaction among quarks and gluons. Understanding QCD not only helps describe the hadronic structure but also provides a framework for studying matter at extreme thermodynamic

conditions, similar to those created at the early stages of the universe's beginning, which remains an extraordinary ongoing journey of our understanding.

American astronomer Edwin Hubble's discovery in 1929 provided the first compelling evidence that the universe is expanding [1]. This discovery implied that in the distant past, all the matter must have been close together, offering the first observational support for the Big Bang hypothesis of the universe, started in 1927 by a Belgian cosmologist and Catholic priest, Georges Lemaître [2, 3]. Lemaître further postulated in 1931 that the universe must have originated at a definite point in time from an extremely dense state. He argued that the universe began as a single compact entity, so-called "primeval atom", whose disintegration initiated the expansion of space and time of the present universe. Detailed measurements of the universe's expansion rate indicate that the Big Bang event occurred roughly 13.8 billion years ago [4], and is therefore considered the age of the observable universe. Just after the Big Bang, an exotic state of a hot and dense phase of matter is believed to have prevailed. This phase is known as the quark-gluon plasma state of matter, consisting of relatively free quarks and gluons from the hadronic boundary. It has therefore become essential to understand the mechanism of fundamental particles and their interaction to understand matter at extreme conditions, which in principle allows us to understand the early phase of the universe.

1.1 Quantum Chromodynamics (QCD)

Quantum Chromodynamics (QCD) constitutes the fundamental theory of the strong interaction that binds quarks and gluons together inside hadrons. It is a non-Abelian gauge field theory with the SU (3) symmetry group. Analogous to the electric charge in Quantum Electrodynamics (QED), quarks in QCD carry a new kind of charge known as color charge. Like photons in QED, here, the strong interaction is mediated by the gluons. Another interesting difference between

the QED and QCD is that, in QED, the photon does not carry any electric charge. However, the gluon has color degrees of freedom and is therefore they are self-interacting. One can find more exciting features of QCD from the QCD Lagrangian itself, which is given by [5]

$$\mathcal{L}_{\mathrm{QCD}} = \sum_{q} \psi_{q,a} \left(i\gamma^{\mu}\partial_{\mu}\delta_{ab} - g_s\gamma^{\mu}t^{C}_{ab}A^{C}_{\mu} - m_q\delta_{ab} \right) \psi_{q,b} - \frac{1}{4}F^{A}_{\mu\nu}F^{A\,\mu\nu}. \tag{1.1}$$

Here, the summation runs over the index q from 1 to 6, corresponding to six quark flavours with mass m_q. The $\psi_{q,a}$ are the quark-field spinors, where, a index is for three color flavors, and the γ^{μ} are the Dirac-γ matrices. The gluon field A^{C}_{μ} carries the color index C from 1 to 8 corresponding to 8 gluons, while g_s here is the QCD coupling constant. The t^{C}_{ab} are the eight generators of the SU (3) group. The associated field-strength tensor $F^{A}_{\mu\nu}$ is given as

$$F^{A}_{\mu\nu} = \partial_{\mu}A^{A}_{\nu} - \partial_{\nu}A^{A}_{\mu} + g f_{ABC}A^{B}_{\mu}A^{C}_{\nu}, \tag{1.2}$$

where the f_{ABC} represents the structure constant of the SU(3) group. In the above expression, the non-Abelian nature of QCD is represented by the third term, the self-interaction term in QCD, which allows gluon-gluon interactions. Hence, the four terms in Eq. (1.1) correspond to the quark kinetic term representing free propagation of quarks; the quark-gluon interaction term; then comes the quark mass term; and finally the gluon field term. The self-interacting property of gluons in QCD gives rise to striking features of QCD, including color confinement and asymptotic freedom.

1.1.1 Color confinement and asymptotic freedom

One of the fundamental properties of quantum chromodynamics is the different nature of strong interactions at different distance scales. At large distances (or low momentum scales), i.e., at ordinary conditions, a single quark can not be isolated from a hadron. Therefore, the quarks are always bound within a color-neutral

hadron. This is known as color confinement [6]. The effective QCD potential between partons (quarks and gluons) is given as [7]

$$V_{\mathrm{QCD}}(r) = -\frac{4}{3}\frac{\alpha_s}{r} + kr. \tag{1.3}$$

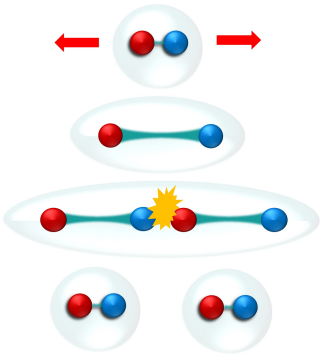

Figure 1.1: Illustration of quark confinement mechanism in QCD. The color flux tube broke at a large enough separation, giving rise to a pair of quark and anti-quark [8].

Here α_s denotes the strong coupling constant (related to g_s through the relation, $\alpha_s = g_s/4\pi$). The distance between two interacting partons is given by r, whereas k is the color string tension constant. The first term represents Coulomb-like behavior at short distances, and the second term corresponds to the linear confining potential dominant at large separations. Therefore, unlike the electric field in QED, which diminishes with increasing distance among charged particles, the color field in Quantum Chromodynamics (QCD) becomes increasingly strong as one attempts to separate two color charges. Beyond a certain separation, the energy stored in the color flux tube between them becomes sufficient enough for a quark–antiquark pair creation rather than allowing the existence of an isolated color charge, as illustrated in Fig. 1.1. Consequently, when one attempts to pull a quark out of a meson, the system does not yield a free quark. Instead, the energy supplied to separate the quark is converted into the production of a new

quark–antiquark pair, ultimately resulting in the formation of two color-neutral mesons.

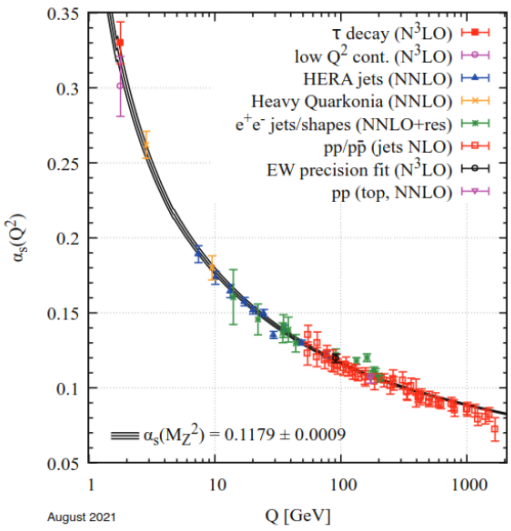

Figure 1.2: Running coupling constant shown as functions of momentum transfer between the partons [5].

Another distinct property of QCD is asymptotic freedom, which refers to the gradual weakening of the strong interaction as the separation between quarks and gluons becomes smaller. The effective coupling strength, denoted by α_s, which is not exactly constant, but depends on the momentum transfer involved in the interaction among the partons, i.e., $\alpha_s \equiv \alpha_s(Q^2)$. It is therefore called as running coupling constant and is given as [5]

$$\alpha_s(Q^2) = \frac{12\pi}{(11 - 2n_f)\ln(Q^2/\Lambda^2_{\text{QCD}})}, \tag{1.4}$$

where, Λ^2_{QCD} represents the non-perturbative QCD scale parameter. The n_f and Q^2 are the number of quark flavors and momentum transfer between the partons, respectively. Therefore, with an increase in momentum transfer among the partons, the coupling constant decreases asymptotically (as shown in Fig. 1.2), and hence the partons at short distances (with high momentum transfer) behave as almost free.

1.1.2 Lattice QCD

At a very high energy regime, or equivalently, a short distance scale, the coupling constant is small enough to allow the use of the perturbation theory approximation technique for QCD calculations. This is known as perturbative QCD, which explains the hard scattering phenomena observed in high-energy collision experiments successfully. As the interaction energy of the parton decreases, the coupling constant increases, leading towards color confinement. Here, one can not adopt a perturbative method. One way to study this non-perturbative physics of QCD is to use Wilson's lattice gauge theory [9], where the four-dimensional space-time is discretized into a lattice (similar to that in crystals).

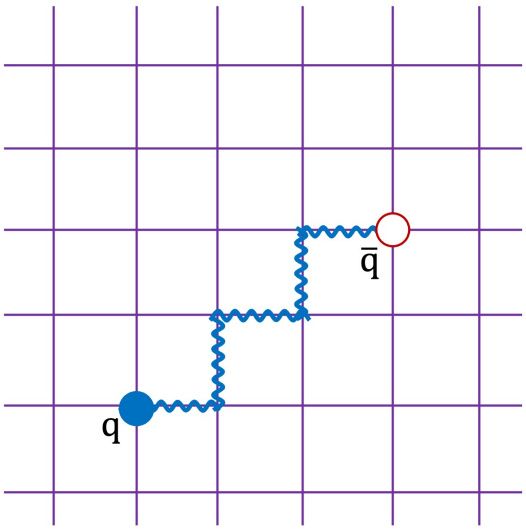

Figure 1.3: Representation of quarks and gluons in a space-time lattice QCD [9].

The quarks occupy the lattice points, while the gluon fields are described using the links connecting the quarks (lattice points). And in the limit of an infinitely large lattice, the lattice sites are infinitesimally close together, and the continuum QCD is recovered. Lattice QCD is a first-principle theory with minimal assumptions. For a detailed review, one can refer to Ref. [5].

One of the remarkable achievements made using lattice QCD calculations

was the prediction of the QCD crossover temperature for the transition from hadronic matter to a quark–gluon plasma at vanishing baryochemical potential at around $T \approx 155$ MeV [10, 11]. Along with the thermodynamic observables, lattice calculations of fluctuations and correlations of conserved charges have become essential tools for constraining the QCD phase diagram. In subsequent sections, we will discuss more on the QCD phase diagram, the phase transitions, as well as the lattice QCD results that allow us to understand the properties of the phases of QCD matter at low baryon density.

1.1.3 The QCD phase diagram

The color confinement property of QCD does not allow a free parton to exist outside the hadronic boundary. They are bound within the hadrons. However, extreme conditions can be achieved, which can help break these barriers and allow quarks and gluons to become relatively free from a single hadron. This can be done either by increasing the temperature of a system of hadrons or by increasing their density.

Let us assume a QCD vacuum in a box. As shown in Fig. 1.4, with an increase in temperature, T, the lighter hadrons, such as pions, kaons, protons, etc., are thermally produced from the QCD vacuum [9], which at a certain critical temperature T_c start to overlap. At temperature, $T > T_c$, the hadrons melt and the box is filled with quarks and gluons (the quark-gluon plasma (QGP)) without any identity of hadron. Another way to achieve the deconfined state is by increasing the baryon density. Let us put a large number of baryons in a cylinder and compress it adiabatically using a piston. At some critical density n_c, the hadrons start to overlap, and above which they dissolve to a state of deconfined quarks and gluons. This suggests that one expects to find QGP in extreme conditions which may occur at the early universe phase, where the temperature is so high, or at the center of compact stars like neutron stars, where the baryon

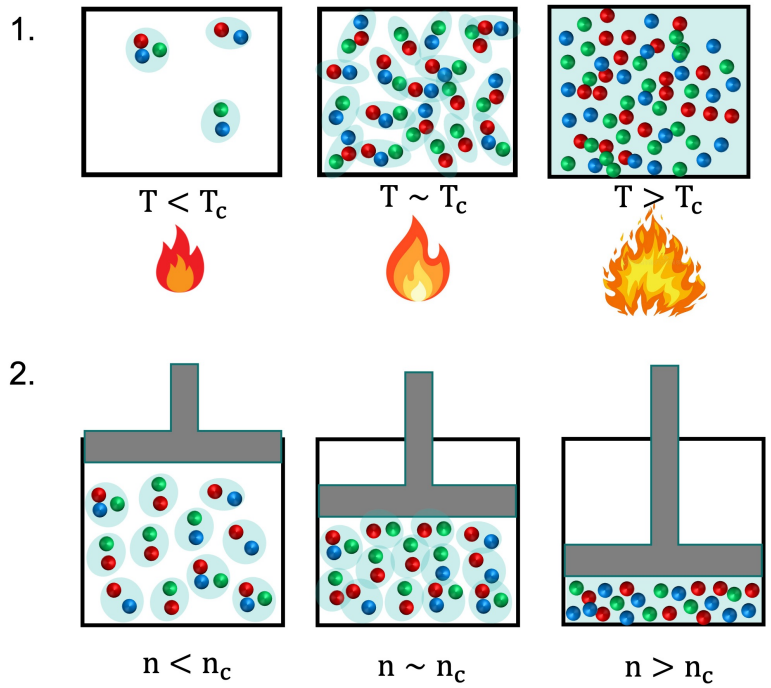

Figure 1.4: The condition for the formation of quark-gluon plasma is achieved at (1) high temperature, and (2) high baryon density [9].

density is too high, or by colliding two heavy nuclei, where, depending on the collision energy and collision system, the condition for the formation of QGP can be achieved.

This also led to one of the conclusions that the phases of QCD matter and their transitions can be studied by using two parameters, namely, temperature and the quark density (or baryon density) of the system. More fundamentally, the baryon chemical potential is used instead of the net baryon density. As we already know, the chemical potential represents the energy required to add a particle to the system. The baryon chemical potential can be understood in a similar way, i.e., the amount of energy released or absorbed to a change in the baryon number of the system through the imbalance of the baryon (quark) and anti-baryon (anti-quark). A high chemical potential implies that the system has more baryons than anti-

baryons (more quarks than anti-quarks). The conjectured QCD phase diagram characterized by temperature, T, and baryon chemical potential, μ_B, in the y-axis and x-axis, respectively, is shown in Fig. 1.5. At low temperatures and chemical

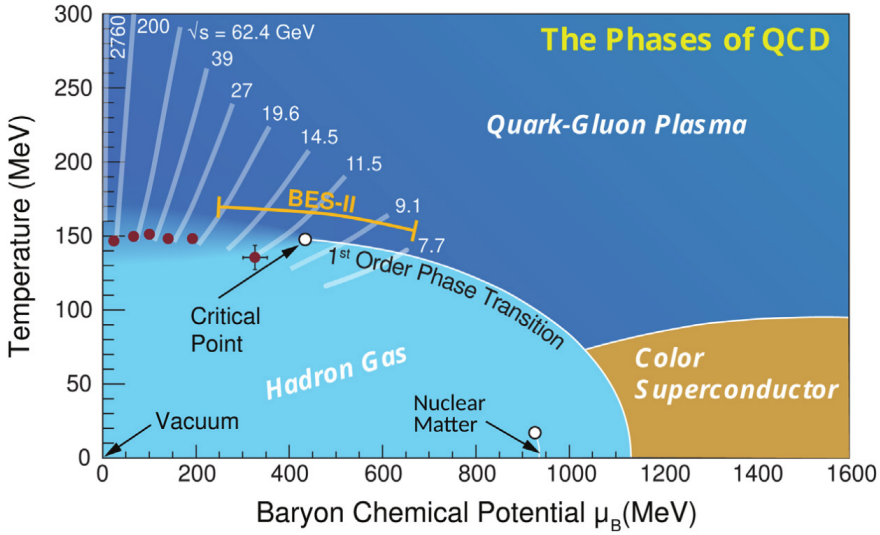

Figure 1.5: Schematic representation of the QCD Phase diagram in $T - \mu_B$ plane [12]

potentials, the QCD matter resides in the hadronic phase, where the quarks are confined within a colorless stable hadron. At vanishing μ_B and very high T, the phase diagram corresponds to the early universe case, where the quarks and gluons are deconfined and the state is known as the QGP phase. Such conditions are achieved in experiments by colliding heavy nuclei at relativistic speeds at a very large center-of-mass energy, for example, at the Large Hadron Collider (LHC) and the Relativistic Heavy Ion Collider (RHIC). The lQCD calculations predict a smooth crossover transition from the hadronic phase to the QGP phase at $\mu_B = 0$ MeV and at a temperature around $T \sim 155$ MeV [10, 11]. It shows a continuous change, rather than a discontinuity, in different thermodynamic observables. Though at high μ_B, lQCD could not be used because of the fermion sign problem [13, 14], but a lot of theoretical calculations predict a first-order phase transition at low T and very high μ_B (such as the core of the neutron

star). Now, this phase transition line must terminate at a possible critical point that joins the crossover and first-order transition line. The QCD critical point is one of the most active areas of research from both theoretical and experimental perspectives. The Beam Energy Scan (BES) program at RHIC [15, 16] is currently undertaking its search to locate this critical point in the QCD phase diagram.

1.2 Heavy-Ion Collisions

Experimentally, the extreme thermodynamic conditions required for the formation of hot and dense QCD matter—analogous to those that existed microseconds following the Big Bang can be reproduced through ultrarelativistic heavy-ion collisions. In such experiments, also known as the Little Bangs, massive ions, including gold (Au) and lead (Pb), are accelerated to ultra-relativistic speeds at experimental facilities, including RHIC and the LHC. When these ions collide at center-of-mass energies per nucleon pair reaching several tera-electron volts, an enormous energy density is deposited in a small space-time volume. This extreme environment results in temperatures exceeding the QCD critical temperature ($T_c \sim 155$ MeV), leading to the creation of a deconfined state of strongly interacting matter known as the QGP.

1.2.1 Space-time evolution of heavy-ion collision

Figure 1.6 presents a schematic illustration of the space–time evolution of ultra-relativistic hadronic as well as nuclear collisions. Due to their high speed, approaching the velocity of light, the two incident nuclei become Lorentz contracted along the beam (longitudinal) direction. At time $t = 0$ and $z = 0$, the collision occurs. Immediately after the first impact, the system undergoes a pre-equilibrium stage, during which a dense medium of quarks and gluons is produced from the enormous amount of energy deposited, but it has not yet been thermalized. Due

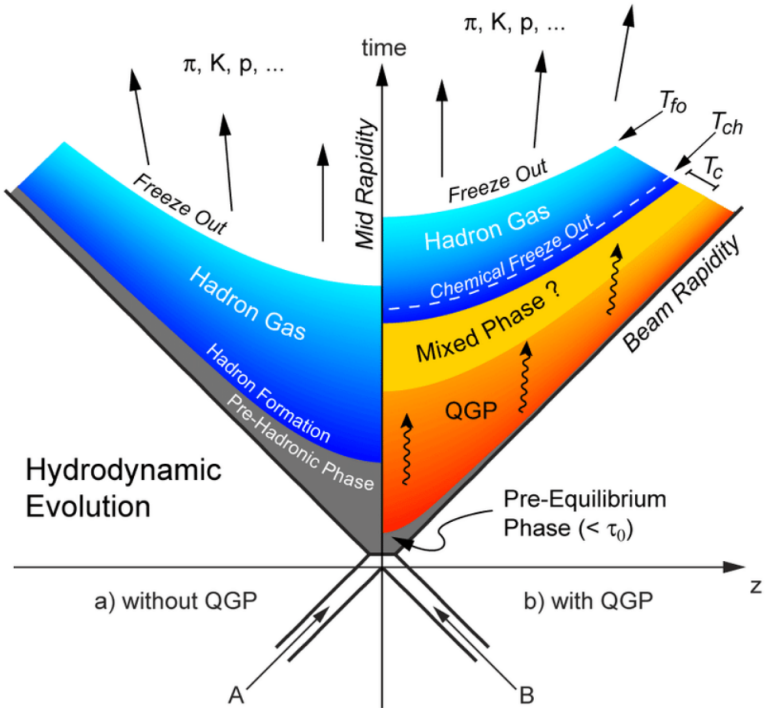

Figure 1.6: Schematic diagram showing space-time evolution of an ultra-relativistic high-energy collision [17].

to the multiple hard (high transverse momentum) partonic interactions, heavier quarks, such as charm and beauty, are produced at this stage. The time period for this stage is typically < 1 fm/c. As time evolves, further multiple scattering of partons leads to local thermalization of the system. At this point, the formation of QGP, a local thermalized deconfined state of quarks and gluons, is said to have formed. During this phase, the system exhibits collective behavior characterized by strong pressure gradients and anisotropic expansion, which is propagated to further stages of the evolution and can be well described using relativistic hydrodynamics.

As the system expands and cools down, the energy density begins to be lower than that of individual hadrons. The coupling constant α_s becomes large enough, and this leads partons to start confining inside the hadron. This phase, where the hadronization process (the conversion of partons to hadrons) begins, is known as

the mixed phase, where both partons and hadrons coexist. The hadrons produced can still undergo inelastic collisions and maintain chemical equilibrium. The hadronization process continues until all the partons are converted into hadrons. At this temperature, denoted by T_{ch}, when all inelastic collisions stop and the particle abundance gets fixed, the chemical freezeout is said to occur. Further evolution through elastic collisions of the produced hadrons goes on for some time, allowing momentum distributions to evolve. Heavier resonances decay to lighter hadrons. Once the mean free path of the hadrons exceeds the system size, kinetic freezeout occurs (at T_{kin}), and the final stable particle stream is directed towards the sophisticated detectors designed for their detection.

1.2.2 Probing QCD matter with heavy quarkonia

In collider experiments, the detector detects the final-state particles produced from the collision, thereby lacking any direct signature of the different phases of the collision. The formation of QGP, if it exists, and the whole evolution of the collision last only for a few femtoseconds. This makes it impossible to have any direct probe to study the properties of QGP. Therefore, one needs to rely on a variety of indirect experimental signatures that reflect the collective behavior and deconfined nature of strongly interacting matter. Observables such as particle spectra, collective flow, and correlations measured in experiments thus encode valuable information about the properties and evolution of the strongly interacting QCD matter created in these collisions. One of the earliest proposed signals is the jet quenching. Energetic partons produced in the early hard scatterings traverse the hot medium and lose energy through multiple scatterings (collisional loss) and induced gluon radiation (radiative loss). Consequently, the number of high p_{T} hadrons observed in nucleus–nucleus collisions is significantly reduced compared to that in proton–proton interactions. Experimental observation of jet quenching is already seen in heavy ion collisions [18, 19]. The QGP also exhibits

collective flow phenomena, such as elliptic flow (v_2), indicating the development of strong pressure gradients [20, 21]. Additionally, strangeness enhancement, characterized by the large production of strange hadrons because of the abundance of strange quarks in the thermalized partonic environment [22, 23], serves as another key signature of QGP formation.

Another key observable for studying the dynamics and evolution of the strongly interacting medium created in high-energy nuclear collisions is the heavy quarkonia. The quarkonia consist of a heavy quark bound to its corresponding antiquark, forming states such as a charmonium ($c\bar{c}$) and bottomonium ($b\bar{b}$). The production mechanisms of these quarkonia in proton-proton (pp) collisions, as well as their subsequent modification in proton-nucleus (pA) and nucleus-nucleus (AA) collisions, make it a powerful probe to study QCD dynamics in both vacuum and medium [24]. Firstly, owing to their relatively large masses ($m_{\mathrm{c}} \sim 1.3$ GeV/c^2, $m_{\mathrm{b}} \sim 4.2$ GeV/c^2), they are predominantly produced during the early stages of collision through hard scattering [25, 26]. Consequently, the resulting bound states traverse the entire space–time evolution of the medium and retain valuable information about its properties. Secondly, the production mechanism of these particles involves both perturbative and non-perturbative aspects of QCD. The initial creation of heavy quarks, such as charm and bottom, and their anti-quark pairs, occurs via high-momentum-transfer processes that can be treated within perturbative QCD. On the other hand, the subsequent binding of the pair into a quarkonium is governed by non-perturbative dynamics [27]. It's therefore important to understand the production mechanism of these heavy quarkonia in order to understand the properties of QCD matter.

Furthermore, in heavy ion collisions, when a thermalized deconfined medium of color charge is formed, the heavy quarkonium states (like J/ψ) produced at the initial stages of collision now have the probability to dissociate. For example, the charm and anticharm of the charmonia become separated due to the color screening effect [24]. In this process, the potential binding the heavy quark and

anti-quark, such as the charm and anti-charm constituents of charmonium, is effectively weakened by the surrounding medium, analogous to Debye screening in electromagnetic plasmas. The color field screens the effective interaction among the heavy quark pairs, thereby reducing the survival probability of the bound states. Instead, these heavy quarks gain the tendency to combine with other light quarks to produce open charm hadrons like D^0 ($c\bar{u}$). The consequent reduction in the yield of quarkonium states relative to that in pp collisions is known as the quarkonium suppression, and it serves as a key indicator of deconfinement and the presence of a strongly interacting partonic medium in heavy-ion collisions. The suppression is generally quantified by calculating a quantity called nuclear modification factor, $R_{\rm AA}$, defined as the normalized single particle yield ratio in AA to pp collisions, and is given by

$$R_{\rm AA} = \frac{d^2N_{\rm AA}/(dy\,dp_{\rm T})}{\langle N_{\rm coll}\rangle\, d^2N_{\rm pp}/(dy\,dp_{\rm T})}, \tag{1.5}$$

where the yield ratio is normalized by the average number of binary nucleon-nucleon collisions ($N_{\rm coll}$) happening in a single nucleus-nucleus (AA) collision.

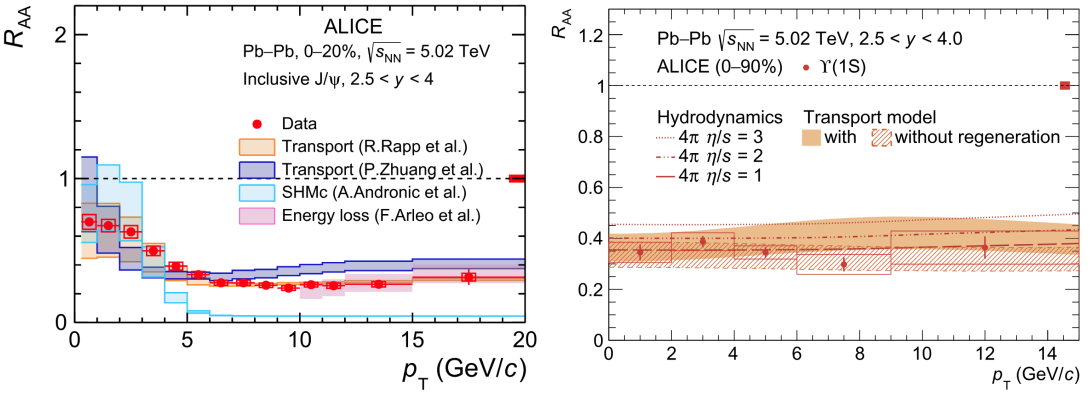

Figure 1.7: Transverse momentum dependence of (left) J/ψ R_{AA} in the 0-20% centrality class [28], and (right) Υ $(1S)$ R_{AA} in 0-90% centrality [29] in Pb-Pb collisions in ALICE experiment at $\sqrt{s_{NN}} = 5.02$ TeV at forward rapidity.

If there is no medium in AA collision and it can be regarded as the superpo-

sition of a number of pp collisions, then one expects $R_{\mathrm{AA}} \sim 1$. Any suppression in the yield will result in $R_{\mathrm{AA}} < 1$. Fig. 1.7 presents the experimentally measured for J/ψ and $\Upsilon\ (1S)$ at forward rapidity in Pb-Pb collisions at $\sqrt{s_{NN}} = 5.02$ TeV, showing a clear suppression throughout the p_{T} range considered. Moreover, the melting temperature of each quarkonium state depends on its binding energy, which leads to an interesting concept of sequential suppression [30]. Tightly bound states like J/ψ or $\Upsilon\ (1S)$ can survive up to high temperatures in comparison to their excited states like $\psi\ (2S)$ or $\Upsilon\ (2S)$ and $\Upsilon\ (3S)$, which melt earlier in the medium. One must also consider the fact that when the colliding energy is so high, there is a possibility of an abundant production of heavy quark pairs. This leads to an additional mechanism of regeneration or a recombination process, where two uncorrelated heavy quarks and antiquarks coalesce into a quarkonium state during the later stages of the system's evolution. This mechanism enhances the Quarkonium yield, especially at low transverse momentum, as evident for the case of J/ψ from Fig. 1.7 [28]. For bottomonium, on the other hand, the regeneration effects are expected to be smaller due to the lower number of $b - \bar{b}$ pairs produced (for being more massive) [29], making bottomonium suppression a comparatively clean probe of color screening in the high-temperature deconfined medium. The interplay between dissociation and regeneration needs to be considered when interpreting quarkonium yields.

Apart from their production, the polarization measurements of the heavy quarkonia provide important insights into their production mechanism and hence into the dynamics of QCD [31]. The polarization, i.e., the angular momentum state in which it was created, is a result of the production mechanism, which itself is sensitive to the specific experimental conditions, such as the colliding particles, the collision energy, and the kinematic phase space [31, 32]. Measurements of polarization, therefore, provide an opportunity to discriminate between different theoretical models, thereby helping to understand the fundamental interactions governing particle production.

The experimental and theoretical studies of heavy quarkonia thus provide profound insights into the microscopic behavior of the quark–gluon plasma and the underlying dynamics of Quantum Chromodynamics under extreme conditions. Nevertheless, to achieve a complete and quantitative description of this novel state of matter, in addition to the deconfinement signatures, a quantitative description of its bulk properties, such as the equation of state, pressure, entropy density, and transport coefficients like viscosity and conductivity, is also necessary. These quantities characterize the thermodynamic and collective behavior of the medium and are essential for connecting QCD theory with experimental observables.

1.3 Understanding the Properties of Hot QCD Matter

A quantitative understanding of the QGP and its transition to hadronic matter requires detailed knowledge of its thermodynamic and transport properties. Observables measured in experiments, such as the transverse momentum distributions and the elliptic flow coefficients of charged hadrons, provide crucial constraints on the transport parameters that govern the medium's hydrodynamic evolution.

1.3.1 Thermodynamic and transport properties

Various thermodynamic and transport quantities serve as essential probes for understanding the dynamical evolution of the strongly interacting matter created in ultra-relativistic heavy-ion collisions. The variation of these quantities with temperature, T, and baryon chemical potential, μ_B, provides valuable insights into the overall structure of the QCD phase diagram, particularly in identifying the boundary that separates the hadronic phase from the deconfined QGP phase. A

thermodynamic system can be described primarily by its state variables, including the pressure (P), energy density (ε), number density (n), and entropy density (s). These quantities are connected through Euler's thermodynamic relation, given as

$$\varepsilon + P = Ts + \mu n, \tag{1.6}$$

where μ is the total chemical potential. By using this, one can obtain other key thermodynamic quantities like specific heat (c_v), speed of sound (c_s^2).

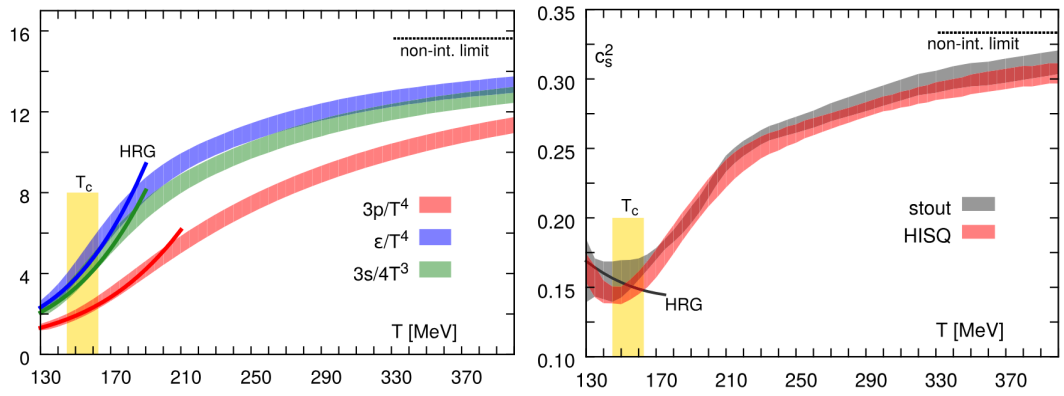

Figure 1.8: Left panel shows the scaled pressure, energy density, and entropy density from lattice QCD (colored band) compared with those obtained in the hadron resonance gas (HRG) model (solid lines). The speed of sound squared from lattice QCD compared with HRG is shown in the right panel [13].

As in Fig. 1.8, results from lQCD calculations at $\mu_B = 0$ show a continuous increase in thermodynamic quantities such as scaled pressure, energy density, and entropy density (in the left panel) along with the squared speed of sound (in the right panel) [13], while going from low to high temperature. The lQCD calculations at zero baryon chemical potential ($\mu_B = 0$) have revealed a smooth but rapid variation in thermodynamic quantities such as energy density, entropy density as the system transitions from the hadronic to the partonic regime, indicating a crossover transition rather than a first-order phase change[10, 13]. However, direct lattice simulations become infeasible at high μ_B due to the fermion sign

problem [13, 14]. This limitation necessitates the use of various phenomenological models to study the QCD matter at finite baryon densities. At low temperatures and moderate μ_B, the hadron resonance gas model [33] has proven remarkably effective in reproducing the equilibrium thermodynamic observables by assuming a system of a non-interacting ensemble of all established hadrons and resonances. On the other hand, perturbative QCD and quasi-particle approaches become relevant at asymptotically high temperatures, where partonic degrees of freedom dominate [34]. The possibility of the existence of a first-order phase transition at high μ_B and of a critical end point (CEP) in the QCD phase diagram can be investigated by analyzing the nature of T and μ_B dependence of free energy and its first-order derivative. The higher-order thermodynamic susceptibilities serve as a sensitive probe of the fluctuations and correlations of conserved charges, and hence are useful in mapping the phase boundary [35].

Moreover, the transport coefficients of the QGP play a crucial role in determining how a non-equilibrium system evolves toward local thermodynamic equilibrium. These coefficients quantify the medium's response to spatial and temporal gradients of quantities, such as energy, momentum, and conserved charges. Experimental observations at RHIC have revealed a strong degree of collectivity in the matter created in ultra-relativistic heavy-ion collisions [36–39]. The collective behaviour is significant not only in the transverse-momentum spectra of individual particles but also in the azimuthal anisotropy of the emitted hadrons. In collisions with a nonzero impact parameter, the overlap zone of the colliding nuclei possesses an initial spatial asymmetry, which is subsequently converted to momentum-space anisotropy, resulting in an azimuthally asymmetric distribution of emitted particles. This anisotropy, quantified by the second-order Fourier coefficient of the azimuthal distribution, referred to as the elliptic flow (v_2), and serves as one of the key signatures of the QGP formation. While the equilibration of this momentum anisotropy is governed by the shear viscosity coefficient, the bulk viscosity, in general, quantifies the fluid's resistance to uniform expansion

or compression during the evolution [40].

The anti-de Sitter/conformal field theory (AdS/CFT) correspondence suggests a lower bound to the shear viscosity to entropy ratio (η/s) given by $1/4\pi$ [41]. Remarkably, experimental analyses of elliptic flow data obtained at RHIC (and later at LHC) have indicated that the QGP exhibits an η/s value approaching this theoretical bound [42], as illustrated in Fig. 1.9. This observation led to the characterization of the QGP as an almost "perfect fluid" exhibiting the lowest viscosity ever observed in a physical system. Note that the ratio of shear viscos-

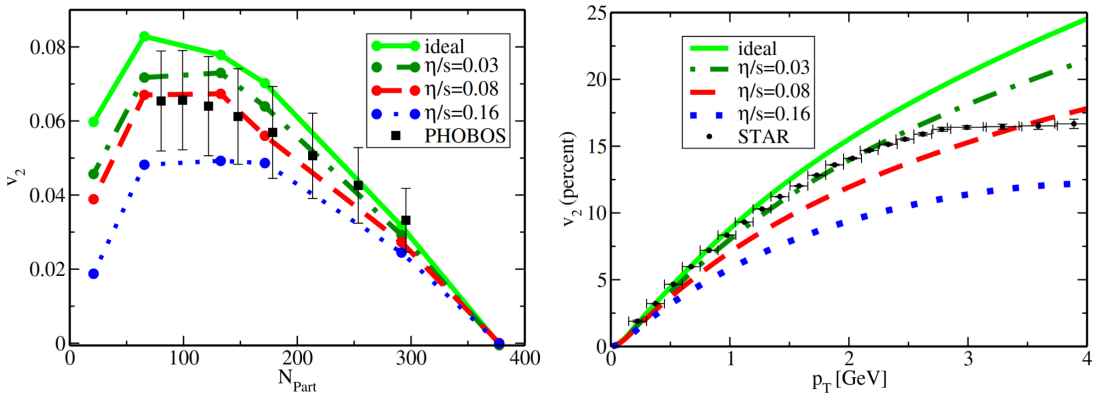

Figure 1.9: v_2 for charged particles in Au + Au collisions at $\sqrt{s_{NN}}$ = 200 GeV for p_{T} integrated (left) and minimum bias data (right) is compared with results from hydrodynamic models for different values of η/s [42].

ity to entropy density is the relativistic analog of the kinematic viscosity, which is defined as the ratio between the shear viscosity (dynamic viscosity) and the mass density of the fluid (ρ) as η/ρ. In Fig. 1.10, the η/s of various fluids (basically for molecular, atomic, as well as for nuclear matter) is compared as a function of the scaled temperature variable $(T - T_c)/T$, where T_c denotes the critical temperature of the respective fluid. The open hexagons are the estimates of η/s for nuclear matter extracted from momentum transport data obtained at intermediate energy (IE) heavy-ion collisions [43, 44]. The data for QGP are obtained from the lQCD results [45], whereas the results marked with RHIC were obtained

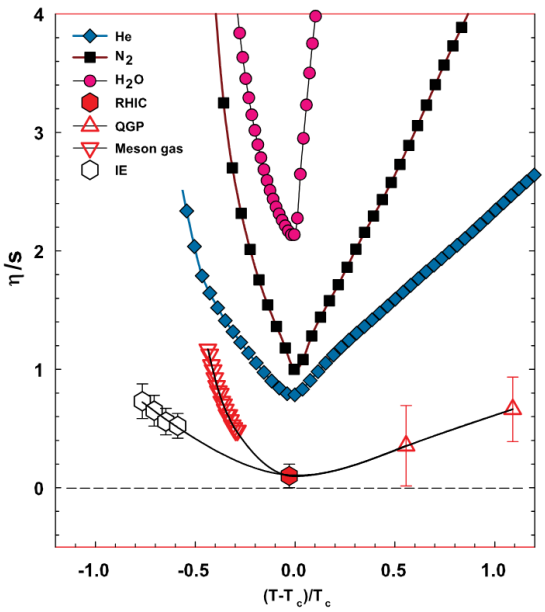

Figure 1.10: Comparison of shear viscosity to entropy density ratio for different kinds of fluids [46].

by adjusting viscous hydrodynamic simulations to reproduce the experimentally measured elliptic flow results, as already discussed. This led to one of the most famous claims that RHIC produces the most perfect fluid ever observed.

With this, the high-energy physics community drew intense attention towards the investigation of transport properties of QCD matter. Along with the shear and bulk viscosities, transport coefficients such as electrical conductivity and thermal conductivity also help to understand the dissipative properties of a medium. In a peripheral heavy-ion collision, the motion of charged spectator nucleons at nearly the speed of light generates a very strong but transient magnetic field. The rapid decay of this field, however, is moderated by the induced electric field within the medium, a phenomenon governed by its electrical conductivity. On the other hand, the transport of heat conduction in baryon-rich (high μ_B) regimes can be studied using thermal conductivity. Therefore, studying transport coefficients and relating them to experimentally observable quantities has the potential to significantly enhance our understanding of QCD matter and its evolution in

heavy-ion collisions.

1.3.2 Effects of Magnetic Fields and Rotation

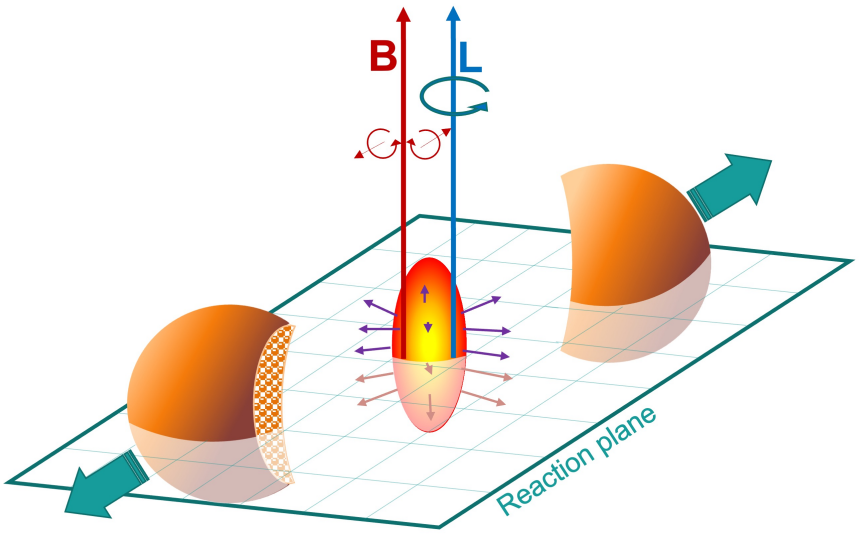

Figure 1.11: Illustration of a non-central heavy-ion collision of two nuclei. The direction of the magnetic field produced and the angular momentum deposited are indicated by solid red and blue arrows, respectively.

We know from our classical electrodynamics that a moving charge gives rise to electric currents, while time-dependent electric fields in turn generate magnetic fields [47]. In the context of ultra-relativistic heavy-ion collisions, a large magnetic field is expected to form because of fast-moving protons. For two heavy nuclei of each radius R and mass m_N, moving towards each other at relativistic speed with an impact parameter b, the magnitude of the resulting magnetic field can be estimated using the Biot–Savart law as [48]

$$B \sim \gamma Z e \frac{b}{R^3}, \tag{1.7}$$

where the Lorentz factor $\gamma = \sqrt{s_{NN}}/2m_N$. At RHIC, for a Au + Au collision with $\sqrt{s_{NN}} = 200$ GeV, $Z = 79$ and $R \sim b = 7$ fm, one can estimate $eB \simeq m_\pi^2 \sim 10^{18}$

Gauss [49, 50]. At the LHC energies, similar calculations show $eB \sim 10\ m_\pi^2$. Recent findings on the finite global polarization of the Λ hyperon have revealed that the medium created in heavy-ion collisions exhibits a strong vortical nature [51]. The spin-orbit coupling of the hyperon with that of local vorticity or the rotation leads to the observed polarization. In non-central heavy-ion collisions, the fast-moving nuclei deposit a large amount of angular momentum at the collision point. For example, considering an Au + Au collision at $\sqrt{s_{NN}} = 39$ GeV, with impact parameter, $b = 5$ fm, the initial angular momentum can be estimated to be $L \sim bA\sqrt{s_{NN}}/2 \approx 2 \times 10^5 \hbar$ [52].

The indirect estimation of the magnetic field and vorticity that is expected to be produced in a heavy-ion collision is the highest that could be observed in nature till now, and therefore, the matter produced in the collision is known to be the most magnetized as well as the most vortical fluid ever observed. Both of these quantities create an anisotropy in the medium and, therefore, can significantly affect its thermodynamic and transport properties. In the presence of a magnetic field and rotation, Euler's thermodynamic relation in Eq. (1.6) is modified as

$$\varepsilon + P = Ts + \mu n + B\mathcal{M} + \omega\mathcal{J}, \tag{1.8}$$

where $\mathcal{M}$ and $\mathcal{J}$ represent the magnetization and angular momentum associated with the magnetic field B and rotation ω, respectively. The single-particle energy spectrum is quantized, and the density of states is modified, which in turn affects thermodynamic observables such as pressure, entropy density, energy density, etc. A strong magnetic field gives rise to several interesting phenomena, including the chiral magnetic effect (CME) [53–55] — the separation of electric charges along the direction of the magnetic field due to an imbalance between left and right-handed quarks (chiral imbalance). The magnetic field can also influence the chiral phase transition. An enhancement of the transition temperature in the presence of a magnetic field is termed as magnetic catalysis, whereas in some scenarios, an opposite trend known as inverse magnetic catalysis is observed [56–

58]. Similarly, vorticity can polarize particles with non-zero spin, as evidenced by the global polarization of Λ hyperons [51]. Beyond these novel effects, such as the chiral vortical effect (CVE) [59, 60], rotation can also influence chiral and deconfinement phase transitions [61]. Studying these effects is therefore crucial for understanding the dynamics of hot and dense QCD matter, as they directly impact both its thermodynamic and transport properties.

1.4 Thesis Structure

In this thesis, an attempt is made to study the final state dynamics of hadrons, as well as to understand the production mechanism of heavy Quarkonium, which acts as a probe of the evolution of the QCD matter produced in the collision. The thesis consists of two parts: the phenomenological and the experimental.

1.4.1 Phenomenological motivation

The first-principles lattice field theoretical simulation is well-defined and provides the QCD equation of state at $\mu_B = 0$ [13]. It predicts a crossover transition from hadron to quark degrees of freedom. It does not specify a fixed transition temperature, which can strictly differentiate the dominant degrees of freedom on each side of that temperature. Due to its limited applications at high μ_B, a phenomenological input is highly recommended to study the dynamics of the QCD matter at high μ_B and intermediate temperatures. One of the notable alternatives is the use of a statistical model for hadrons, known as the hadron resonance gas model. In chapter 2, we describe the main features of an ideal hadron resonance gas (HRG) model and its applicability. There have been modifications to the ideal HRG by introducing interactions among the hadrons. The excluded volume (EV) HRG is followed by the van der Waals HRG model, which consists of both attractive and repulsive interactions. We discuss their construction and sig-

nificance in detail. We then demonstrate the significance of interactions among hadrons by examining the transport properties, such as thermal and electrical conductivities, of the hadronic medium. One interesting phenomenon, known as Bose-Einstein condensation (BEC) in a highly dense pion gas, and the effect of such condensation on the transport properties of the gas is also studied.

Chapter 3 explores how rotation affects the thermodynamic characteristics of an interacting hadron resonance gas. When inter-hadronic interactions are modeled through a van der Waals–type equation of state, the system is expected to undergo a first-order liquid–gas phase transition at large baryon chemical potential (μ_B) and relatively low temperature (T) [62]. Here, we investigate whether rotation can influence the conditions necessary for the phase transition and whether it can impact the critical point.

The van der Waals hadron resonance gas (VDWHRG) model was the most successful interacting hadronic model that agrees with lQCD calculations at $\mu_B = 0$, even at high temperature, where ideal HRG fails. A key feature of the VDWHRG approach is the emergence of a first-order phase transition accompanied by a critical point, which is entirely absent in the ideal, non-interacting scenario. This serves as a valuable tool for the ongoing efforts to locate the QCD critical point experimentally. The behavior of higher-order fluctuations near the critical region thereby offers a deeper understanding of the expected patterns close to the QCD critical point. In that way, it is extremely useful. However, the conventional VDWHRG model still shows room for modification. The constant VDW parameters are considered to be crude approximations. In chapter 4, we show the limitations of the use of such a VDWHRG model and suggest an improvement to it by considering T and μ_B dependence of the VDW parameters. In the same chapter, we estimate the proton number cumulants, which are used to probe the QCD critical point in experiments, to demonstrate the reliability of the modified VDWHRG (MVDWHRG) model by comparing its results with the latest available experimental data.

1.4.2 Experimental motivation

The production mechanism of heavy Quarkonia such as J/ψ and Υ involves both perturbative and non-perturbative regimes of QCD [27]. The initial creation of heavy quark–antiquark pairs demands large transverse momentum transfers, and is therefore accessible to perturbative QCD. Whereas, the evolution of the formation of a heavy quarkonium out of those produced heavy quarks and anti-quarks is non-perturbative. Therefore, studying their production in proton-proton (pp) collisions provides an opportunity to constrain different QCD-based models and broaden our understanding of the collision dynamics at the early stage. Apart from this, the polarization measurements can help us better understand their production mechanism. Moreover, the production and polarization measurements of Υ resonances in pp collisions can be used as a benchmark or baseline for the search for medium effects in heavy-ion collisions.

In Chapter 5, we study the measurements of Upsilon (Υ) resonances in pp collisions at $\sqrt{s}$ = 13.6 TeV with ALICE. The chapter is introduced with a motivation for studying Υ states in pp collisions. Then, a brief discussion of the ALICE detector used for this analysis is made. In particular, we use the muon decay channel to reconstruct Υ in experiments. The muons in the experiments are detected using the muon spectrometer of the ALICE experiment. The details of the analysis, along with the various experimental cuts employed, are discussed. The measurement of the Upsilon resonances ratio at the forward rapidity region ($2.0 < \eta < 4.2$) is analysed as a function of transverse momentum. Following this, the results for Υ ($1S$) polarization are also presented.

Finally, in Chapter 6, the thesis is summarized with a brief outlook.

Chapter 2

Transport properties of the hadron resonance gas with van der Waals interactions

Transport coefficients, such as viscosities and conductivities, serve as essential probes for understanding the dynamic properties of the exotic hot and dense matter produced in high-energy collisions. In this chapter, we estimate various transport properties in the hadronic phase, i.e., below the QCD transition temperature, where hadrons constitute the fundamental degrees of freedom. This hadronic medium can be effectively described by the Hadron Resonance Gas (HRG) model, an equilibrium thermodynamic ensemble comprising all known hadrons and resonances. The ideal HRG (IHRG) model assumes that all hadrons are point particles without any interaction among them. It provides a simple yet remarkably successful framework for describing the bulk thermodynamics of strongly interacting matter in this regime. However, at higher temperatures and baryon chemical potentials (μ_B), the effects of hadronic interactions become increasingly important. To extend the applicability of the HRG approach, various corrections have been proposed to incorporate both repulsive and attractive interactions among hadrons.

In the following sections, we provide a detailed discussion of the formulation of the ideal HRG model and its improved versions, followed by the estimation of

different transport coefficients within each framework. This comparative analysis highlights the role and significance of hadronic interactions in determining the transport and thermodynamic behavior of QCD matter in the confined phase.

2.1 Variants of the hadron resonance gas (HRG) models

2.1.1 Ideal HRG (IHRG) model

In the ideal HRG framework, the hadronic phase of the QCD matter is described by a gas of non-interacting hadrons and resonances consisting of experimentally identified states listed in the Particle Data Group (PDG) [5]. Within the Grand Canonical Ensemble (GCE), the single-particle partition function for each hadron species of having mass m is given by [33]

$$\ln Z_i^{id} = \pm \frac{V g_i}{2\pi^2} \int_0^\infty p^2 dp \; ln\{1 \pm \exp[-(E_i - \mu_i)/T]\}, \tag{2.1}$$

where V is the system volume, g_i is the spin degeneracy, p denotes the momentum, and $E_i = \sqrt{p^2 + m^2}$ gives the energy of the ith hadron. The $\pm$ sign corresponds to fermions and bosons, respectively. The corresponding chemical potential, μ_i for each hadronic species is

$$\mu_i = B_i \mu_B + S_i \mu_S + Q_i \mu_Q, \tag{2.2}$$

where μ_B, μ_S, and μ_Q represent the baryon, strangeness, and electric charge chemical potential, respectively. Similarly, the B_i, S_i, and Q_i denote the baryon number, strangeness, and electric charge of the ith hadron.

The pressure of the hadron gas is given by

$$P^{id} = \sum_i P_i^{id}(T, \mu_i) = T \sum_i \frac{\partial \ln Z_i^{id}}{\partial V} \tag{2.3}$$

where the sum goes over all the hadrons and resonances considered here. The P_i^{id} is the pressure of the ideal gas due to ith species, and is given by

$$P_i^{id}(T,\mu_i) = \pm\frac{Tg_i}{2\pi^2}\int_0^\infty p^2dp\ ln\{1\pm\exp[-(E_i-\mu_i)/T]\}. \tag{2.4}$$

Other thermodynamic quantities such as number density (n), energy density (ε), and entropy density (s) due to the ith hadronic species can be obtained as

$$n_i^{id}(T,\mu_i) = \frac{g_i}{2\pi^2}\int_0^\infty \frac{p^2dp}{\exp[(E_i-\mu_i)/T]\pm 1} \tag{2.5}$$

$$\varepsilon_i^{id}(T,\mu_i) = \frac{g_i}{2\pi^2}\int_0^\infty \frac{E_i\ p^2dp}{\exp[(E_i-\mu_i)/T]\pm 1} \tag{2.6}$$

$$s_i^{id}(T,\mu_i) = \pm\frac{g_i}{2\pi^2}\int_0^\infty p^2dp\Big[\ln\{1\pm\exp[-(E_i-\mu_i)/T]\} \pm\frac{(E_i-\mu_i)/T}{\exp[(E_i-\mu_i)/T]\pm 1}\Big] \tag{2.7}$$

With this formalism, the ideal Hadron Resonance Gas (IHRG) model has become one of the most widely used thermal approaches to describe the hadronic phase of strongly interacting matter. It has been successfully employed to extract the thermodynamic parameters, namely the temperature (T) and baryon chemical potential (μ_B), by fitting hadron yield data from low-energy experiments at the SchwerIonen-Synchrotron (SIS) up to the highest collision energies available at the Large Hadron Collider (LHC) [63–69]. Furthermore, the IHRG model successfully reproduces various thermodynamic observables obtained from lattice QCD (lQCD) calculations at vanishing baryon chemical potential and low temperatures ($T \approx$ 100–150 MeV) [13, 14].

Despite its success in describing bulk particle yields, the ideal HRG model exhibits certain limitations. It fails to reproduce higher-order cumulants of conserved charge fluctuations measured experimentally, which are particularly sensitive to the critical behavior of QCD matter. In addition, the model shows deviations from lattice QCD results at higher temperatures, approaching the transition

region [13, 70]. These discrepancies highlight the limitations of treating hadrons as non-interacting, point-like particles. To achieve a more realistic description of the hadronic medium, interaction effects must be taken into account. The inclusion of a finite hadron volume introduces short-range repulsive interactions, while the presence of hadronic resonances effectively accounts for attractive interactions among the constituents [71, 72]. These improvements have led to the development of several extended versions of the HRG model that extend the applicability of the HRG model to high μ_B and T region.

2.1.2 Excluded volume HRG (EVHRG) model

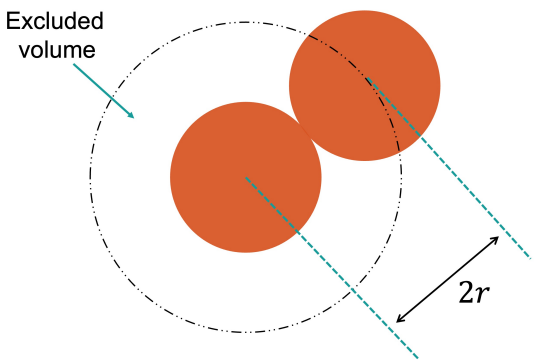

Figure 2.1: Illustration of excluded volume due to finite hardcore radius of two hadrons, each with radius r.

The ideal HRG model assumes all hadrons to be point-like particles, implying that the entire system volume is accessible to each hadron without spatial restriction. However, in a more realistic physical scenario, hadrons possess a finite size, and the short-range repulsive interactions between them become significant at high temperatures and densities. To account for these effects, a van der Waals-type volume correction is introduced [33]. The hadrons are considered as hard spheres having radius r, such that the minimum separation between two hadrons is $2r$, as schematically illustrated in Fig. 2.1. The finite size of hadrons effectively reduces

the available volume of the system, resulting in an excluded-volume correction that mimics repulsive interactions, and therefore, the model is known as the excluded volume HRG (EVHRG). For the corresponding excluded volume between two particles, $2b = (4/3)\pi(2r)^3$, the volume correction factor b for each hadron is given by $b = (16/3)\pi r^3$.

The available system volume V is then reduced and is given by V_{av} as

$$V \to V_{av} = V - \sum_i b_i N_i, \tag{2.8}$$

where, the N_i and $b_i(= \frac{16}{3}\pi r_i^3)$ are the particle number and excluded volume parameter due to ith hadronic species. The hardcore radii of hadrons are denoted by r_i. In the GCE, the introduction of a finite hardcore volume for hadrons leads to a transcendental relation for the system pressure as [33, 73]

$$P^{EV} = \sum_i P_i^{id}(T, \tilde{\mu}_i), \tag{2.9}$$

where the effective chemical potential $\tilde{\mu}_i$ for the ith hadron species is modified due to the repulsive interaction, and is defined by

$$\tilde{\mu}_i = \mu - b_i P(T, \mu_i). \tag{2.10}$$

From these relations, the remaining thermodynamic quantities, such as the number density, energy density, and entropy density, can be derived in a consistent manner with the excluded-volume formalism, as

$$n^{EV}(T, \mu) = \frac{\sum_i n_i^{id}(T, \tilde{\mu}_i)}{1 + \sum_i b_i n_i^{id}(T, \tilde{\mu}_i)}, \tag{2.11}$$

$$\varepsilon^{EV}(T, \mu) = \frac{\sum_i \varepsilon_i^{id}(T, \tilde{\mu}_i)}{1 + \sum_i b_i n_i^{id}(T, \tilde{\mu}_i)}, \tag{2.12}$$

$$s^{EV}(T, \mu) = \frac{\sum_i s_i^{id}(T, \tilde{\mu}_i)}{1 + \sum_i b_i n_i^{id}(T, \tilde{\mu}_i)}. \tag{2.13}$$

It can be easily observed that every thermodynamic observable calculated here for the EVHRG model is reduced by a factor $[1 + \sum_i b_i n_i^{id}(T, \tilde{\mu}_i)]$ in comparison

to what is formulated in ideal HRG. This behavior is physically consistent and aligns with expectations. For example, let us look at the number density. Due to the finite size of the hadrons, the effective volume available is now reduced for each hadron. As a result, the particle number density in a given volume is now less in comparison to that of the ideal HRG consisting of point-like hadrons. Consequently, the reduction in the number density also leads to corresponding decreases in other thermodynamic observables, such as the energy density and entropy density, reflecting the repulsive nature of the short-range interactions among hadrons.

In principle, this model extends the applicability of the HRG framework to higher temperatures, where the repulsive interactions among hadrons become increasingly important. The inclusion of excluded-volume corrections also leads to a better agreement with lattice QCD (lQCD) calculations for various thermodynamic observables and their higher-order fluctuations, compared to the estimations from the ideal HRG model [73]. However, the model's predictions are highly sensitive to the assumed hadronic radii, and therefore on the choice of the excluded-volume parameter b_i [33]. Moreover, since the EVHRG model accounts only for repulsive interactions, the attractive forces among hadrons are not yet explicitly quantified within this framework, leaving room for further improvement. These limitations motivate the development of more advanced formulations, such as the van der Waals Hadron Resonance Gas (VDWHRG) model, which incorporates both repulsive and attractive interactions in a thermodynamically consistent manner.

2.1.3 van der Waals HRG (VDWGRG) model

If we consider a system consisting solely of nucleons (protons and neutrons), the interaction among them inside a nucleus resembles that of a van der Waals (VDW) fluid, characterized by a short-range repulsive core and a long-range at-

tractive tail [74]. Due to this van der Waals–type interaction, nuclear matter is expected to exhibit a liquid–gas phase transition [75–77]. At sufficiently high temperatures and/or densities, the normal nuclear matter dissolves into quark degrees of freedom, whereas at lower temperatures, within the hadronic regime, one anticipates a liquid–gas transition driven by the interplay of attractive and repulsive nuclear forces [75]. The ideal HRG model does not capture this feature, as it completely neglects inter-hadronic interactions. Similarly, the EVHRG model incorporates only repulsive interactions through the finite size of hadrons but omits the attractive part. Consequently, the VDWHRG model provides a more comprehensive and realistic framework for describing the hadronic phase. By including both repulsive and attractive interactions among hadrons, it naturally leads to a liquid–gas–like phase transition featuring a critical point. Since a similar structure is theoretically anticipated in the QCD phase diagram, studying the VDWHRG model becomes particularly important for understanding and predicting potential signatures of the QCD critical point.

In the canonical ensemble (CE) framework, where the particle number is treated as a conserved and independent quantity, the repulsive interaction is introduced by assigning a finite size to the hadrons, similar to the EVHRG model, and the equation of state becomes

$$P^{id}(T,V,N) = \frac{NT}{V} \quad \rightarrow \quad P^{EV}(T,V,N) = \frac{NT}{V-bN}, \tag{2.14}$$

where, the volume V of the system get replaced by the effective available volume $V_{av} = V - bN$, b being the excluded volume parameter as discussed in Sec. 2.1.2. Now introducing the attractive interaction, the equation of state in CE becomes [78, 79]

$$P(T,V,N) = \frac{NT}{V-bN} - a\frac{N^2}{V^2}, \tag{2.15}$$

where a is the attractive VDW parameter. The effect of repulsive forces is incorporated in the first term of Eq. (2.15) by substituting the total volume of the system V with the available volume that can be occupied by the hadrons. The

second term represents the mean field attraction between particles. We derive the equation of state for the VDW equation of state in detail below, with a transition from CE to GCE, so as to make it applicable to study the hadronic system produced after heavy-ion collisions. To ensure that the van der Waals equation of state in GCE is thermodynamically consistent, it must reduce to EVHRG form when $a \to 0$, and to the ideal HRG limit when both a and b are set to zero.

2.1.3.1 van der Waals equation of state for a hadron gas

To begin the derivation, we consider a single-particle ideal partition function in CE, expressed as

$$Z_1 = \frac{gV}{2\pi^2} \int p^2 dp \ \exp[-(\sqrt{p^2+m^2})/T], \tag{2.16}$$

where the degeneracy of each particle is denoted by g, while V represents the total system's volume. The total partition function for N particles is then given by

$$\begin{aligned} Z(T,V,N) &= \frac{Z_1^N}{N!} \\ &= \frac{1}{N!}\Big[\frac{gV}{2\pi^2} \int p^2 dp \ \exp[-(\sqrt{p^2+m^2})/T]\Big]^N \end{aligned} \tag{2.17}$$

The Helmholtz free energy $F(T,V,N)$ in CE is given by

$$\begin{aligned} F = -T\ln Z \ &= \ -T\ln\left(\frac{Z_1^N}{N!}\right) \\ &= -T\big[N\ln Z_1 - \ln N!\big] \\ &= -T[N\ln Z_1 - N\ln N + N] \\ &= -NT\Big[\ln\frac{Z_1}{N} + 1\Big] \\ &= -NT\Big[1 + \ln\left(\frac{V}{N}\frac{g}{2\pi^2}\int p^2 dp \exp[-(\sqrt{p^2+m^2})/T]\right)\Big] \\ \Rightarrow F &= -NT\Big[1 + \ln\frac{V\phi(T;m,g)}{N}\Big], \end{aligned} \tag{2.18}$$

where,

$$\phi(T;m,g) = \frac{g}{2\pi^2}\int p^2 dp \exp[-(\sqrt{p^2+m^2})/T]. \tag{2.19}$$

For a complete thermodynamic picture, so as to be able to obtain other thermodynamic observables, we can obtain the Free energy $F(T,V,N)$ explicitly using the relation below

$$\left(\frac{\partial F}{\partial V}\right) = -P \tag{2.20}$$

$$F(T,V,N) = F(T,V_0,N) - \int_{V_0}^{V} dV'\ P(T,V',N) \tag{2.21}$$

We assume that at very small density, $N/V \to 0$, the interaction can be neglected. Then in the limit $V \to \infty$, we can approximate $F(T,V_0,N) \approx F^{id}(T,V_0,N)$. Then we can use Eq. (2.18) and the VDW equation of state Eq. (2.15) in Eq. (2.20), we get

$$\begin{aligned} F(T,V,N) &= -NT\Big[1+\ln\frac{V_0\phi}{N}\Big] - \int_{V_0}^{V} dV'\Big(\frac{NT}{V'-bN} - a\frac{N^2}{V^2}\Big) \\ &= -NT\Big[1+\ln\frac{V_0\phi}{N}\Big] - NT\ln\Big(\frac{V-bN}{V_0-bN}\Big) - aN^2\Big(\frac{1}{V}-\frac{1}{V_0}\Big) \\ &= -NT\Big[1+\ln\Big(\frac{V_0\phi}{N}\times\frac{V-bN}{V_0-bN}\Big)\Big] - aN^2\Big(\frac{1}{V}-\frac{1}{V_0}\Big) \\ &= -NT\Big[1+\ln\Big(\frac{\phi(V-bN)}{N}\times\frac{1}{1-b\frac{N}{V_0}}\Big)\Big] - aN^2\Big(\frac{1}{V}-\frac{1}{V_0}\Big), \end{aligned} \tag{2.22}$$

taking $1-b\frac{N}{V_0} \to 1$ as $V_0 \to \infty$, we have

$$\begin{aligned} F(T,V,N) &= -NT\Big[1+\ln\Big(\frac{(V-bN)\phi(T;g,m)}{N}\Big)\Big] - a\Big(\frac{N^2}{V}\Big) \\ &= F^{id}(T,V-bN,N) - a\frac{N^2}{V}. \end{aligned} \tag{2.23}$$

For the free energy given in the above Eq. (2.23), the chemical potential is eval-

uated using

$$\begin{aligned}\mu &= \left(\frac{\partial F}{\partial N}\right)_{V,T} \\ &= -T\left(1+\ln\frac{(V-bN)\phi}{N}\right) - NT\left[\frac{N}{(V-bN)\phi}\times\frac{-bN\phi-(V-bN)\phi}{N^2}\right] - 2a\frac{N}{V} \\ &= -T\left[1+\ln\frac{(V-bN)\phi}{N}\right] - T\left[\frac{-bN}{(V-bN)}-1\right] - 2a\frac{N}{V} \\ &= -T\ln\frac{(V-bN)\phi}{N} + \frac{bNT}{V-bN} - 2a\frac{N}{V}. \end{aligned} \tag{2.24}$$

Note that for an ideal gas, when there is no interaction ($a = b = 0$), we denote the number density as $n^{id} = N/V$. Therefore, we can write for an ideal gas

$$\begin{aligned}&\Rightarrow \mu = -T\ln\frac{V\ \phi(T;g,m)}{N} = T\ln\frac{N}{V\phi(T;g,m)} \\ &\Rightarrow \frac{N}{V} = n^{id}(T,\mu) = e^{\mu}\phi(T;g,m). \end{aligned} \tag{2.25}$$

This allows us to obtain μ/T from Eq. (2.24) in presence of interaction (for $a > 0$ and $b > 0$) as

$$\begin{aligned}\frac{\mu}{T} &= -\ln\frac{(V-bN)\phi}{N} + \frac{bN}{V-bN} - 2a\frac{N}{TV} \\ &= -\ln\frac{(1-bn)\phi}{n} + \frac{bn}{1-bn} - \frac{2an}{T} \\ \Rightarrow &\frac{n}{1-bn} = \phi\exp\left(\frac{\mu}{T} - \frac{bn}{1-bn} + \frac{2an}{T}\right) \\ \Rightarrow &n = \phi\exp\left(\frac{\mu}{T} - \frac{bn}{1-bn} + \frac{2an}{T}\right) - b\ n\ \phi\exp\left(\frac{\mu}{T} - \frac{bn}{1-bn} + \frac{2an}{T}\right) \\ \Rightarrow &n\left[1+b\ \phi\exp\left(\frac{\mu}{T} - \frac{bn}{1-bn} + \frac{2an}{T}\right)\right] = \phi\exp\left(\frac{\mu}{T} - \frac{bn}{1-bn} + \frac{2an}{T}\right) \end{aligned} \tag{2.26}$$

Let us now define a quantity, called the effective chemical potential, or the modified chemical potential, as

$$\begin{aligned}&\frac{\mu^*}{T} = \frac{\mu}{T} - \frac{bn}{1-bn} + \frac{2an}{T} \\ &\Rightarrow \boxed{\mu^* = \mu - \frac{bnT}{1-bn} + 2an}. \end{aligned} \tag{2.27}$$

Hence, the chemical potential, μ, is modified to μ^* because of interaction. In the ideal case, when $a = b = 0$, it again reduces to μ. Using this in Eq. (2.26) and then taking the analogy from Eq. (2.25) we can have

$$\begin{aligned} & n\Big[1 + b\ \phi e^{\mu^*/T}\Big] = \phi\ e^{\mu^*/T} \\ \Rightarrow & n\Big[1 + b\ n^{id}(T,\mu^*)\Big] = n^{id}(T,\mu^*) \\ \Rightarrow & \boxed{n = \frac{n^{id}(T,\mu^*)}{1 + b\ n^{id}(T,\mu^*)}} \end{aligned} \tag{2.28}$$

We then proceed to obtain pressure in the VDWHRG model, knowing the ideal pressure given by $P^{id} = n^{id}T$. We have from Eq. (2.15) as

$$\begin{aligned} P(T,\mu) &= \frac{n(T,\mu)T}{1 - bn(T,\mu)} - an^2(T,\mu) \\ &= \frac{\frac{n^{id}(T,\mu^*)}{1+bn^{id}(T,\mu^*)}T}{1 - b\frac{n^{id}(T,\mu^*)}{1+bn^{id}(T,\mu^*)}} - an^2(T,\mu) \\ &= n^{id}(T,\mu^*)T - an^2(T,\mu) \\ \boxed{P(T,\mu) = P^{id}(T,\mu^*) - an^2(T,\mu)} & \end{aligned} \tag{2.29}$$

The VDW equation of state in GCE can therefore be expressed as shown in Eq. (2.29), where n represents the VDW number density, defined in Eq. (2.28).

2.1.3.2 Thermodynamic quantities in VDWHRG model

Thermodynamic consistency of the VDW equation of state in Eq. (2.29) requires that it obeys all fundamental relations of equilibrium thermodynamics. In GCE, the following relations should hold with the equation of state in (2.29)

$$n = \left(\frac{\partial P}{\partial \mu}\right)_T, \quad s = \left(\frac{\partial P}{\partial T}\right)_\mu, \tag{2.30}$$

and

$$\varepsilon = Ts + \mu n - P. \tag{2.31}$$

We start with the derivation of the number density from the pressure. The VDW pressure is

$$P(T,\mu) = P^{\rm id}(T,\mu^*) - an^2(T,\mu). \tag{2.32}$$

The number density can then be obtained using

$$\begin{aligned} n &= \left(\frac{\partial P(T,\mu)}{\partial \mu}\right)_T, \\ &= \left(\frac{\partial P^{\rm id}(T,\mu^*)}{\partial \mu^*}\right)_T \frac{\partial \mu^*}{\partial \mu} - 2an\frac{\partial n(T,\mu)}{\partial \mu}. \end{aligned} \tag{2.33}$$

Now, since

$$\mu^* = \mu - bP - abn^2 + 2an, \tag{2.34}$$

we have

$$\frac{\partial \mu^*}{\partial \mu} = 1 - bn - 2abn\frac{\partial n}{\partial \mu} + 2a\frac{\partial n}{\partial \mu}, \tag{2.35}$$

Using Eq. (2.35) in Eq. (2.33), we get

$$\begin{aligned} n &= n^{\rm id}\left[1 - bn - 2abn\frac{\partial n}{\partial \mu} + 2a\frac{\partial n}{\partial \mu}\right] - 2an\frac{\partial n}{\partial \mu} \\ &= n^{\rm id}(1-bn) - n^{\rm id}2abn\frac{\partial n}{\partial \mu} + n^{\rm id}2a\frac{\partial n}{\partial \mu} - 2an\frac{\partial n}{\partial \mu} \\ \Rightarrow & n^{\rm id}(1-bn) + n^{\rm id}2a\frac{\partial n}{\partial \mu}(1-bn) - n\left[1 + 2a\frac{\partial n}{\partial \mu}\right] = 0 \\ \Rightarrow & \left[n^{\rm id}(1-bn) - n\right]\left[1 + 2a\frac{\partial n}{\partial \mu}\right] = 0. \end{aligned} \tag{2.36}$$

For a physically acceptable solution, we have

$$n^{\rm id}(1-bn) - n = 0. \tag{2.37}$$

Therefore,

$$n = \frac{n^{\rm id}}{1+bn^{\rm id}}, \quad \text{or equivalently} \quad n(T,\mu) = \frac{n^{\rm id}(T,\mu^*)}{1 + b\, n^{\rm id}(T,\mu^*)}, \tag{2.38}$$

which is the same as in Eq. (2.28).

For entropy density, let us obtain the derivative of VDW pressure, $P(T,\mu)$ with T as

$$s = \left(\frac{\partial P(T,\mu)}{\partial T}\right)_{\mu}. \tag{2.39}$$

For the VDWHRG model,

$$\begin{aligned} s &= \frac{\partial}{\partial T}\left[P^{\rm id}(T,\mu^*) - an^2(T,\mu)\right], \\ &= \frac{\partial P^{\rm id}(T,\mu^*)}{\partial T} + \frac{\partial P^{\rm id}(T,\mu^*)}{\partial \mu^*}\frac{\partial \mu^*}{\partial T} - 2an\frac{\partial n(T,\mu)}{\partial T}. \end{aligned} \tag{2.40}$$

Using from Eq. (2.34)

$$\frac{\partial \mu^*}{\partial T} = -b\frac{\partial P}{\partial T} - 2abn\frac{\partial n}{\partial T} + 2a\frac{\partial n}{\partial T}, \tag{2.41}$$

we have

$$\begin{aligned} s &= s^{\rm id} + n^{\rm id}\left[-bs - 2abn\frac{\partial n}{\partial T} + 2a\frac{\partial n}{\partial T}\right] - 2an\frac{\partial n}{\partial T} \\ &= s^{\rm id} - bn^{\rm id}s - 2abnn^{\rm id}\frac{\partial n}{\partial T} + 2an^{\rm id}\frac{\partial n}{\partial T} - 2an\frac{\partial n}{\partial T} \\ \Rightarrow s(1+bn^{\rm id}) &= s^{\rm id} + 2a\frac{\partial n}{\partial T}\left(n^{\rm id} - n - bnn^{\rm id}\right) \\ \Rightarrow s(1+bn^{\rm id}) &= s^{\rm id} + 2a\frac{\partial n}{\partial T}\left[n^{\rm id}(1-bn) - n\right]. \end{aligned} \tag{2.42}$$

Using the relation $n = n^{\rm id}(1-bn)$ from Eq. (2.28), we get

$$s(1+bn^{\rm id}) = s^{\rm id}. \tag{2.43}$$

Therefore, the entropy density becomes

$$\boxed{s(T,\mu) = \frac{s^{\rm id}(T,\mu^*)}{1+b\,n^{\rm id}(T,\mu^*)}.} \tag{2.44}$$

To determine the energy density in the VDWHRG model, we employ Euler's thermodynamic equation, which serves as a fundamental consistency condition of the model. We have

$$\varepsilon + P = Ts + \mu n. \tag{2.45}$$

where s, n, and P denote entropy density, number density, and pressure, respectively. For the VDWHRG model, let us substitute s, n, and P from the previous relations for VDWHRG. We have

$$\varepsilon = Ts + \mu n - P \tag{2.46}$$

$$= \frac{Ts^{\rm id}(T,\mu^*)}{1+b\,n^{\rm id}(T,\mu^*)} + \frac{\mu n^{\rm id}(T,\mu^*)}{1+b\,n^{\rm id}(T,\mu^*)} - P^{id} + an^2 \tag{2.47}$$

$$= \frac{s^{\rm id}T + (\mu^* + bP + abn^2 - 2an)\,n^{\rm id}}{1+bn^{\rm id}} - P^{\rm id} + an^2,$$

$$= \frac{s^{\rm id}T + \mu^* n^{\rm id}}{1+bn^{\rm id}} + \frac{(bP + abn^2 - 2an)\,n^{\rm id}}{1+bn^{\rm id}} - P^{\rm id} + an^2,$$

$$= \frac{s^{\rm id}T + \mu^* n^{\rm id} - P^{\rm id}(1+bn^{\rm id})}{1+bn^{\rm id}} + [bP + abn^2 - 2an]\frac{n^{id}}{1+bn^{id}} + an^2,$$

$$= \frac{s^{\rm id}T + \mu^* n^{\rm id} - P^{\rm id}}{1+bn^{\rm id}} + bPn + abn^3 - 2an^2 - bP^{id}n + an^2,$$

Now, considering that

$$\varepsilon^{\rm id}(T,\mu^*) = s^{\rm id}(T,\mu^*)T + \mu^* n^{\rm id}(T,\mu^*) - P^{\rm id}(T,\mu^*), \tag{2.48}$$

we obtain

$$\varepsilon = \frac{\varepsilon^{\rm id}(T,\mu^*)}{1+bn^{\rm id}(T,\mu^*)} + bPn + abn^3 - bP^{id}n - an^2$$

$$= \frac{\varepsilon^{\rm id}(T,\mu^*)}{1+bn^{\rm id}(T,\mu^*)} + bn(P - P^{id} + an^2) - an^2. \tag{2.49}$$

Using the relation

$$P(T,\mu) = P^{\rm id}(T,\mu^*) - an^2(T,\mu),$$

We finally have

$$\boxed{\varepsilon(T,\mu) = \frac{\varepsilon^{\rm id}(T,\mu^*)}{1+bn^{\rm id}(T,\mu^*)} - an^2(T,\mu).} \tag{2.50}$$

Following the van der Waals formalism, one can derive several thermodynamic quantities such as the specific heat ($c_V = \frac{\partial\varepsilon}{\partial T}$) and the squared speed of sound

($c_s^2 = \frac{\partial P}{\partial \varepsilon}$). These quantities play an essential role in characterizing the equation of state of strongly interacting matter at high temperatures and baryon densities.

In the initial implementation of the VDWHRG model, inter-particle interactions were included only among pairs of baryons and pairs of antibaryons independently [62, 80–82]. The interactions between baryons and antibaryons were excluded, since the short-range dynamics in such pairs are primarily governed by annihilation processes rather than by typical hadronic interactions [33, 80]. Likewise, the meson-related interactions (meson–meson and meson–(anti)baryon) were also ignored in this version, as their inclusion tends to suppress thermodynamic observables in the crossover region at $\mu_B = 0$ relative to the lQCD results [80]. Nevertheless, a generalized version of the model that includes meson–meson interactions has been developed, where the van der Waals parameters are chosen to best reproduce the lattice QCD data [83], by introducing a finite hard-core radius r_M for mesons. Accordingly, in the VDWHRG framework, one can express the total pressure as [62, 80–83]

$$P(T,\mu) = P_M(T,\mu) + P_B(T,\mu) + P_{\bar{B}}(T,\mu), \tag{2.51}$$

where the separate contributions from mesons and (anti)baryons, denoted as $P_M(T,\mu), P_{B(\bar{B})}(T,\mu)$, respectively, are expressed by

$$P_M(T,\mu) = \sum_{i\in M} P_i^{id}(T,\mu^{*M}), \tag{2.52}$$

$$P_B(T,\mu) = \sum_{i\in B} P_i^{id}(T,\mu^{*B}) - an_B^2(T,\mu), \tag{2.53}$$

$$P_{\bar{B}}(T,\mu) = \sum_{i\in \bar{B}} P_i^{id}(T,\mu^{*\bar{B}}) - an_{\bar{B}}^2(T,\mu). \tag{2.54}$$

Here, M, B, and $\bar{B}$ correspond to mesons, baryons, and anti-baryons, respectively. The quantities μ^{*M}, $\mu^{*B(\bar{B})}$ are the modified chemical potentials of mesons and (anti)baryons due to the excluded volume correction and VDW interactions, respectively [83]. For simplicity, when the electric charge and strangeness chemical potentials are neglected [84], $\mu_Q = \mu_S = 0$, the effective chemical potentials

for mesons and (anti)baryons can be derived from Eq. (2.27) as follows

$$\mu^{*M} = -bP_M(T,\mu), \tag{2.55}$$

$$\mu^{*B(\bar{B})} = \mu_{B(\bar{B})} - bP_{B(\bar{B})}(T,\mu) - abn^2_{B(\bar{B})} + 2an_{B(\bar{B})}, \tag{2.56}$$

where n_M, n_B, and $n_{\bar{B}}$ denote the corresponding modified number densities of mesons, baryons, and antibaryons, respectively, and are explicitly defined as

$$n_M(T,\mu) = \frac{\sum_{i\in M} n_i^{id}(T,\mu^{*M})}{1+b\sum_{i\in M} n_i^{id}(T,\mu^{*M})}, \tag{2.57}$$

$$n_{B(\bar{B})}(T,\mu) = \frac{\sum_{i\in B(\bar{B})} n_i^{id}(T,\mu^{*B(\bar{B})})}{1+b\sum_{i\in B(\bar{B})} n_i^{id}(T,\mu^{*B(\bar{B})})}. \tag{2.58}$$

The van der Waals parameters (a and b) can either be determined by reproducing the properties of nuclear matter at the saturation density [62] or by fitting lattice QCD results for different thermodynamic observables as done in Ref. [81, 83]. The latter approach interprets these parameters as effective representations of the residual nuclear force, which mimics both short-range repulsion and long-range attraction. In this study, the parameters used are estimated in Ref. [83] by fitting lQCD data of pressure and energy density with the corresponding calculations from the VDWHRG model. The parameters obtained are as $a = 0.926$ GeV fm^3 and $b = (16/3)\pi r^3$, with hard-core radii $r_M = 0.2$ fm and $r_{B,(\bar{B})} = 0.62$ fm for mesons and (anti)baryons, respectively [83]. In a number of studies, like in Ref. [80], the use of the VDWHRG model is found to be more successful in describing the thermodynamic properties of the hadronic phase and reproduces lQCD results over a wider range of temperature than that of the ideal HRG was able to.

In Fig. 2.2, a comparison of different hadron gas models is presented, using calculations that show the behavior of the scaled energy density and scaled pressure in the left panel, while the right panel is for the squared speed of sound. The lQCD results are presented to study the overall agreement of each model with the first-principles theory. The ideal HRG model (black dashed line) shows

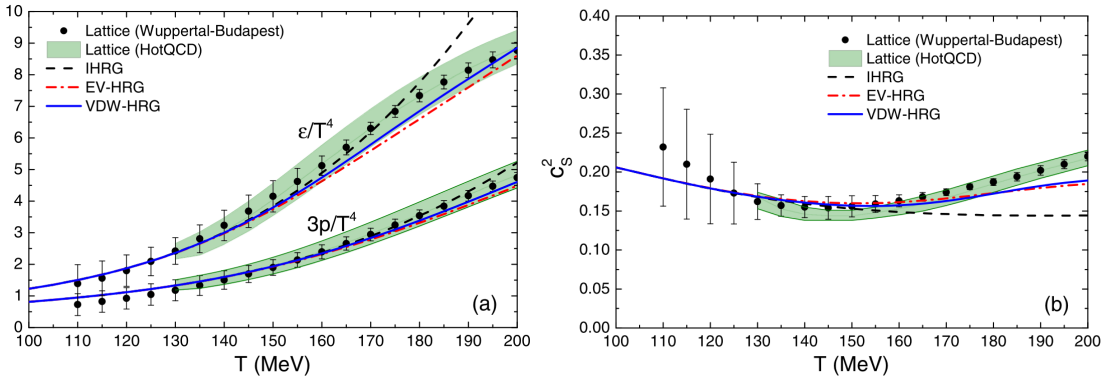

Figure 2.2: Thermodynamic quantities obtained in ideal HRG, EVHRG, and VDWHRG are compared with those from lQCD calculations. The VDWHRG model shows better agreement to lQCD even at high temperature. Figure is taken from Ref. [80].

good agreement with lQCD results only up to a temperature of approximately $T \sim 155$ MeV, beyond which it significantly deviates due to the absence of inter-hadronic interactions. The Excluded Volume HRG (EVHRG) model, shown by the red dot–dashed line, provides an improvement over the ideal case; however, since it incorporates only repulsive interactions, it tends to suppress thermodynamic quantities more strongly at higher temperatures. In contrast, the van der Waals HRG (VDWHRG) model, which incorporates both repulsive and attractive interactions, yields results that lie intermediate between the ideal and EVHRG predictions.

2.2 Transport properties in VDWHRG

For a thermodynamically equilibrated system, a small perturbation can lead to an anisotropy in the density of the medium. The system then tends to restore the equilibrium through induced currents or fluxes. Within the linear response framework, the flux is linearly proportional to the corresponding thermodynamic force, which is typically the negative gradient of a conserved quantity [85]. For

instance, the Ohm's law, $\mathbf{J_{el}} = \sigma_{el}\mathbf{E} = -\sigma_{el}\nabla\phi$, and Fourier's law of heat conduction, $\mathbf{Q} = -\kappa_{th}\nabla T$, describe the transport of charge and heat, respectively, with σ_{el} and κ_{th} denoting the electrical and thermal conductivities. The high magnetic field generated in heavy-ion collisions decays rapidly in the absence of a thermalized medium. On the other hand, if there is a thermalized system, the electrical conductivity of the medium slows down the decay by inducing a magnetic field in the direction of the decaying field. Although a direct experimental determination of the electrical conductivity, $\sigma_{\rm el}$, is not feasible, numerous theoretical and phenomenological investigations have been carried out to estimate its value. In particular, $\sigma_{\rm el}$ has been evaluated using first-principle calculations based on lQCD simulations [86]. Thermal conductivity, which involves the flow of energy, is of significant importance in the high baryon-rich environments like the matter produced at low-energy collisions in FAIR and NICA. In this section, we investigate the electrical and thermal conductivities of the hadron gas with van der Waals interactions among the hadrons. We employ the Boltzmann transport equation within the relaxation time approach to determine the conductivities and investigate them in the VDWHRG model as functions of temperature and baryon chemical potential.

2.2.1 Electrical and thermal conductivities

2.2.1.1 Electrical conductivity

The single-particle distribution for the ith hadron at equilibrium is given by

$$f_i^0 = \frac{1}{\exp\left[\left(\sqrt{p_i^2 + m_i^2} - \mu\right)/T\right] \pm 1} \tag{2.59}$$

where p_i, m_i are the momentum and mass of the hadronic species, respectively. The T denotes temperature, whereas the chemical potential of the system is given by μ. The $\pm$ is for fermion and boson, respectively. Under relaxation

time approximation (RTA), the Boltzmann equation can be expanded linearly in terms of the single-particle distribution function, f_i, around its equilibrium value, f_i^0. In this approach, the total distribution function for the ith particle species is expressed as $f_i = f_i^0 + \delta f_i$, where δf_i represents a small deviation from equilibrium. The relativistic Boltzmann transport equation (BTE) under RTA for an ith species is given by

$$p^\mu \partial_\mu f_i(x,p) + q_i F^{\nu\rho} p_\rho \frac{\partial}{\partial p^\nu} f_i(x,p) = \mathcal{C}_i[f_i]. \tag{2.60}$$

Here, the $F^{\nu\rho}$ represents the electromagnetic field strength tensor, and q_i denotes the electric charge of the ith hadronic species. The term $\mathcal{C}_i[f_i]$ corresponds to the collision integral, which governs how the non-equilibrium distribution function f_i evolves due to the interactions among particles. Although the system may initially be slightly away from equilibrium, with successive collisions among the hadrons, it gradually approaches a state of local thermodynamic equilibrium over a characteristic relaxation time.

Within the framework of the relaxation time approximation (RTA), the collision integral can be expressed as

$$\mathcal{C}i[fi] \simeq -\frac{p^\mu v_\mu}{\tau_i}(f_i - f_i^0) = -\frac{p^\mu v_\mu}{\tau_i}\delta f_i, \tag{2.61}$$

where τ_i denotes the relaxation time of the ith species, which is typically of the order of the mean collision time. Here, v_μ denotes the four-velocity of the fluid element.

When the deviation from the equilibrium is small and assumed to be space-time translationally invariant, the first term in Eq. (2.60) vanishes. Considering a four-velocity with only a time-like component, i.e., in the local rest frame of the fluid, the four-velocity takes the form $v_\mu = (1, \mathbf{0})$, such that $p^\mu v_\mu = p^0$. Assuming the presence of a constant external electric field, Eq. (2.60) can then be written as

$$q_i \left(p_0 \mathbf{E} \cdot \frac{\partial f_i^0}{\partial \mathbf{p}} + \mathbf{E} \cdot \mathbf{p} \frac{\partial f_i^0}{\partial p^0} \right) = -\frac{p^0}{\tau_i}\delta f_i. \tag{2.62}$$

We have $\frac{\partial f_i^0}{\partial \mathbf{p}} = \mathbf{v_i}\frac{\partial \mathbf{f_i^0}}{\partial \mathbf{p^0}}$, where $\mathbf{v_i} = \mathbf{p}/p^0$ is the velocity of ith hadron. Under the Boltzmann approximation, for a very small change from equilibrium, the above equation can be solved to obtain

$$\delta f_i = \frac{q_i \tau_i}{T}\frac{\mathbf{E}\cdot\mathbf{p}}{p^0} f_i^0. \tag{2.63}$$

The electric four current j^μ_{el} is defined as

$$j^\mu_{el} = \sum_i q_i g_i \int \frac{d^3p}{(2\pi)^3 E_i} p^\mu f_i(x,p), \tag{2.64}$$

where q_i denotes the charge of the ith hadron with $f_i(x,p)$ as its phase-space distribution function. For a system that is only slightly perturbed from equilibrium, the four-current can be expressed as the sum of its equilibrium value and a perturbation, as

$$j^\mu_{el} = (j^\mu_0)_{el} + \Delta j^\mu_{el}, \tag{2.65}$$

where the perturbation term is given by

$$\Delta j^\mu_{el} = \sum_i q_i g_i \int \frac{d^3p}{(2\pi)^3 E_i} p^\mu \delta f_i(x,p), \tag{2.66}$$

Substituting the expression for δf_i from Eq. (2.63) into the above equation and then employing the standard definition of electrical conductivity, we obtain [87]

$$\boxed{\sigma_{el} = \frac{1}{3T}\sum_i g_i \tau_i q_i^2 \int \frac{d^3p}{(2\pi)^3}\frac{\mathbf{p^2}}{E_i^2} \times f_i^0}, \tag{2.67}$$

where q_i and τ_i denote the electric charge and the mean relaxation time of the ith hadronic species, respectively, while f_i^0 represents the equilibrium distribution function given in Eq. (2.59).

The relaxation time introduced above is averaged over all particle species and can be expressed as

$$\tilde{\tau}_i^{-1} = \sum_j n_j \langle \sigma_{ij} v_{ij} \rangle, \tag{2.68}$$

where n_j denotes the number density of the j^{th} hadronic species. The thermal average of the total cross-section multiplied by the relative velocity, $\langle\sigma_{ij}v_{ij}\rangle$, is evaluated as [88–90]

$$\langle\sigma_{ij}v_{ij}\rangle = \frac{\sigma_{ij}\int d^3p_i\ d^3p_j\ v_{ij}\ f_i^0\ f_j^0}{\int d^3p_i\ d^3p_j\ f_i^0\ f_j^0}, \tag{2.69}$$

where the total cross-section is approximated as $\sigma_{ij} = \pi(r_i + r_j)^2$, with r representing the hard-core radius corresponding to mesonic or baryonic (anti-baryonic) species. For identical hadronic species, this reduces to $\sigma = 4\pi r^2$.

The general expression for the thermal-averaged cross-section involving scattering between two distinct particle species, $[i(p_i)+j(p_j) \to i(p_k)+j(p_l)]$, is given by [90]

$$\begin{aligned}\langle\sigma_{ij}v_{ij}\rangle =& \frac{\sigma_{ij}}{8Tm_i^2m_j^2K_2(\frac{m_i}{T})K_2(\frac{m_j}{T})}\int_{(m_i+m_j)^2}^{\infty} ds \\ &\times \frac{s-(m_i-m_j)^2}{\sqrt{s}}[s-(m_i+m_j)^2]K_1\Big(\frac{\sqrt{s}}{T}\Big),\end{aligned} \tag{2.70}$$

where $s = (p_i + p_j)^2$ denotes the Mandelstam variable, m_i and m_j are the respective particle masses, and K_n represents the modified Bessel function of the second kind of order n. Once the thermally averaged cross-section is obtained, the corresponding relaxation time can be determined using Eq. (2.68).

In the present analysis, we employ the VDWHRG framework, which incorporates the excluded-volume correction for mesons, along with van der Waals–type attractive and repulsive interactions among (anti)baryon pairs. The hadronic spectrum for the calculation includes all established hadrons and resonances up to a mass cutoff of 2.25 GeV, following the Particle Data Group listings [91]. We estimate the electrical conductivity utilizing the Boltzmann transport equation framework, and its dependence on temperature and net baryon density is subsequently explored. For the analysis, five representative values of the baryon chemical potential μ_B are considered: $\mu_B = 0.0$ GeV corresponding to LHC

energies; $\mu_B = 0.025$ GeV and 0.2 GeV corresponding to RHIC energies at $\sqrt{s_{NN}} = 200$ GeV and 19.6 GeV, respectively; $\mu_B = 0.436$ GeV corresponding to RHIC/FAIR at $\sqrt{s_{NN}} = 7.7$ GeV; and $\mu_B = 0.630$ GeV corresponding to NICA energies at $\sqrt{s_{NN}} = 3$ GeV [92–95].

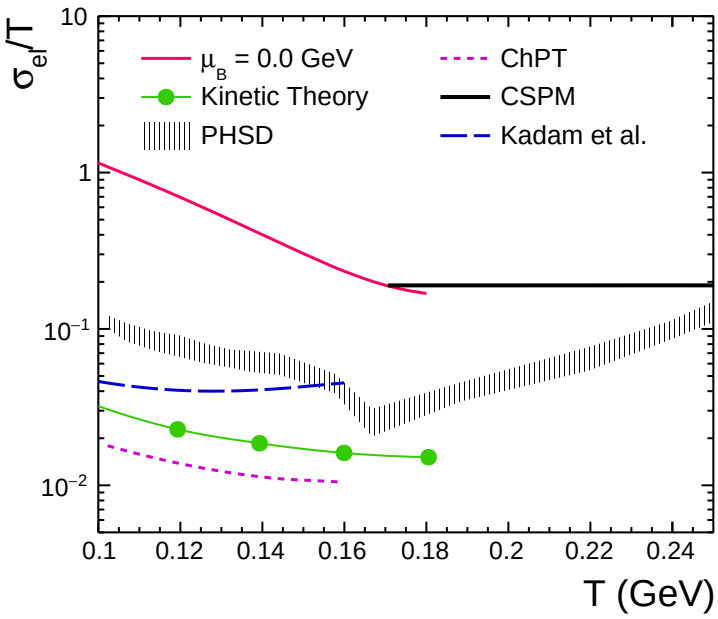

Figure 2.3: Temperature dependence of scaled electrical conductivity is shown using the solid red curve [96]. For comparison, we have shown results from CSPM calculations [100], represented by the black line, whereas the grey band represents the result obtained from PHSD [97]. The solid green markers represent the kinetic theory calculations [98]. The dotted magenta and the dashed blue line show results from chiral perturbation theory [99] and from the excluded volume HRG model [87], respectively.

The temperature dependence of the scaled electrical conductivity, σ_{el}/T, within the VDWHRG framework (solid red line) is illustrated in Fig. 2.3 [96]. It is observed that σ_{el}/T decreases with increasing temperature. As the temperature rises, the particle number density increases, which consequently reduces the re-

laxation time due to more frequent collisions among particles. This enhanced collision rate leads to greater randomness in the system at higher temperatures, restricting the net charge flow in a particular direction and thereby suppressing σ_{el}. Such a decreasing trend of σ_{el}/T with temperature is also consistent with the behavior observed in other hadronic models. Our results are compared with those obtained from the parton-hadron-string dynamics (PHSD) transport framework [97], the excluded volume HRG (EVHRG) model [87], kinetic theory estimates [98], chiral perturbation theory (ChPT) [99], and the color string percolation model (CSPM) [100]. Within the PHSD approach, the σ_{el} decreases throughout the temperature ranges considered in the hadronic phase, reaching a minimum near the critical temperature T_c, and subsequently increases in the partonic phase. A smooth transition is also observed between our VDWHRG results and the QCD-inspired CSPM results around the critical temperature region, indicating consistency with expectations from QCD phenomenology.

Moreover, we also examined the μ_B dependence of the electrical conductivity. The variation of σ_{el}/T with temperature for several distinct values of the baryon chemical potential μ_B is shown in Fig. 2.4 [96]. The results are presented for both the ideal and VDWHRG models to examine the effect of interaction, if any. For low μ_B values, we observe a smooth decrease of σ_{el}/T with temperature in both models, with the VDWHRG predictions lying slightly above those of the ideal HRG towards the high temperature region. The density of mesons and baryons at $\mu_B = 0.0$ GeV is small in low temperatures, leading to nearly identical behavior in both models. As temperature increases, the particle density rises rapidly, and the repulsive component of the Van der Waals interaction becomes dominant. This reduces the effective particle densities and increases the relaxation time relative to the ideal gas scenario. Consequently, the magnitude of σ_{el}/T is enhanced in the presence of VDW-type interactions. As there is an increase in the magnitude of μ_B, the baryon density also rises, and a significant deviation from the ideal HRG behavior emerges at comparatively lower temperatures. In the region of low

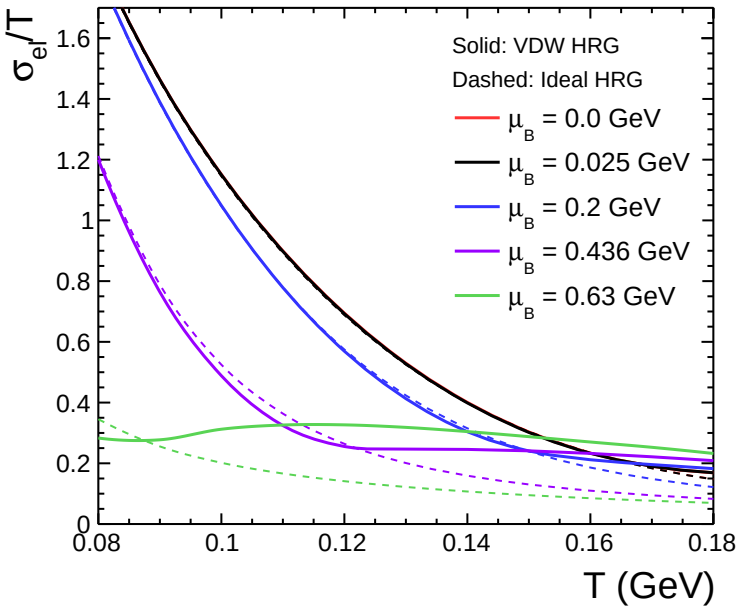

Figure 2.4: Dependence of scaled electrical conductivity on temperature and baryon chemical potentials in both ideal HRG and VDWHRG scenario [96].

T and high-μ_B, the attractive part of the VDW interaction dominates, leading to a higher particle density than that in the ideal HRG case. With increasing temperature, this trend reverses, resulting in a larger σ_{el}/T. At sufficiently high temperatures, when the particle density saturates and thermal motion becomes significant, σ_{el}/T increases gradually with further rises in temperature.

2.2.1.2 Thermal conductivity

Another key transport coefficient that helps understand the dissipative dynamics of hadronic matter is the thermal conductivity (κ), which quantifies the ability of an interacting system to conduct heat. For a relativistic system, the thermal current originates from the flow of energy relative to the baryonic enthalpy. The Boltzmann transport equation, in the absence of any external field, can be

expressed as [87, 101]

$$p^{\mu}\partial_{\mu}f_i(x,p) = -\frac{p^{\mu}v_{\mu}}{\tau_i}\delta f_i. \tag{2.71}$$

The macroscopic properties of a relativistic fluid can be characterized through the energy–momentum tensor $T^{\mu\nu}$, and the particle (baryon) four-current j^{μ}_{B}, both of which satisfy their respective conservation laws. Within the framework of kinetic theory, transport coefficients can be formulated in terms of microscopic properties of the particles, such as their single-particle energy, momentum, and the phase-space distribution function. Accordingly, the energy–momentum tensor and the net-baryon four-current are defined as

$$T^{\mu\nu} = \sum_i g_i \int \frac{d^3p}{(2\pi)^3}\frac{p^{\mu}p^{\nu}}{E_i} f_i(x,p), \tag{2.72}$$

$$j^{\mu}_{B} = \sum_i g_i t_i \int \frac{d^3p}{(2\pi)^3}\frac{p^{\mu}}{E_i} f_i(x,p), \tag{2.73}$$

where g_i denotes the degeneracy factor and t_i represents the baryonic charge of the ith hadronic species.

For small perturbations, when the system slightly deviates from its equilibrium distribution function, the energy–momentum tensor can be written as

$$\Delta T^{\mu\nu} = \sum_i g_i \int \frac{d^3p}{(2\pi)^3}\frac{p^{\mu}p^{\nu}}{E_i} \delta f_i(x,p), \tag{2.74}$$

and within the RTA, the quantity δf_i can be evaluated from the collision term of the Boltzmann transport equation using Eq. (2.71).

Hence, the expression for $\Delta T^{\mu\nu}$ becomes

$$\Delta T^{\mu\nu} = -\sum_i g_i \int \frac{d^3p}{(2\pi)^3}\frac{p^{\mu}p^{\nu}}{E_i}\frac{\tau_i}{p.v} p^{\rho}\partial_{\rho} f_i(x,p). \tag{2.75}$$

Similarly, the change in the baryon four-current, Δj^{μ}_{B}, can be written as

$$\Delta j^{\mu}_{B} = -\sum_i g_i t_i \int \frac{d^3p}{(2\pi)^3}\frac{p^{\mu}}{E_i}\frac{\tau_i}{p.v} p^{\rho}\partial_{\rho} f_i(x,p). \tag{2.76}$$

So that the $T^{\mu\nu}$ and j^{μ}_{B} can be expressed as the sum of their ideal and dissipative parts, respectively, as

$$T^{\mu\nu} = T^{\mu\nu}_{\text{ideal}} + \Delta T^{\mu\nu}$$
$$j^{\mu}_{B} = j^{\mu}_{B_{\text{ideal}}} + \Delta j^{\mu}_{B} \tag{2.77}$$

Now if one decompose the derivative ∂_μ into components parallel and orthogonal to the four-velocity v^μ as [101]

$$\partial_\mu = v_\mu D + \nabla_\mu, \tag{2.78}$$

where the local four-velocity is again taken as $v^\mu = (1, \mathbf{0})$. The corresponding operators are then defined as

$$D = v^\mu \partial_\mu = (\partial_t, \mathbf{0})$$
$$\nabla_\mu = \partial_\mu - v_\mu D = (0, \partial_i). \tag{2.79}$$

For a perfect fluid, the energy-momentum tensor is given by $T^{\mu\nu} = (\varepsilon + P)v^\mu v^\nu - P g^{\mu\nu}$, whereas the baryon four-current is given by $j^\mu_B = n_{\text{net}} v^\mu$. Here, ε is the energy density, P is the pressure, n_{net} the net baryon density, and v^μ the fluid four-velocity (with $u^\mu u_\nu = 1$). Then from the conservation equations $\partial_\mu T^{\mu\nu} = 0$ and $\partial_\mu j^\mu_B = 0$, using Eq. (2.79) one obtains the following relations

$$(\epsilon + P) D v^\mu - \nabla^\mu P = 0, \tag{2.80}$$

$$D\ n_{net} + n_{net} \nabla_\mu v^\mu = 0. \tag{2.81}$$

Using the above relations, the non-equilibrium corrections to the energy–momentum tensor and the baryon current can be expressed as [87, 96, 101]

$$\begin{aligned}\Delta T^{\mu\nu} = \sum_i g_i \int \frac{d^3p}{(2\pi)^3 E_i} \frac{p^\mu p^\nu}{p.v} \frac{1}{T} \tau_i f^0 i \\ \times \Big[p.v \Big(\frac{\partial P}{\partial \epsilon}\Big) n_{net} \nabla_\alpha v^\alpha + p^\alpha X_\alpha + \frac{p^\alpha p^\beta}{p.v} \nabla_\alpha v_\beta \\ + \Big(\frac{\partial P}{\partial n_{net}}\Big) \epsilon \nabla_\alpha v^\alpha - \frac{\epsilon + P}{n_{net}} \frac{p^\alpha}{p.v} X_\alpha \Big],\end{aligned} \tag{2.82}$$

and

$$\Delta j_B^\mu = \sum_i g_i \int \frac{d^3p}{(2\pi)^3 E_i} \frac{p^\mu}{p.v} \frac{1}{T} \tau_i f^0 i \times \Big[p.v \Big(\frac{\partial P}{\partial \epsilon}\Big) n_{net} \nabla_\alpha v^\alpha + p^\alpha X_\alpha + \frac{p^\alpha p^\beta}{p.v} \nabla_\alpha v_\beta + \Big(\frac{\partial P}{\partial n_{net}}\Big) \epsilon \nabla_\alpha v^\alpha - \frac{\epsilon + P}{n_{net}} \frac{p^\alpha}{p.v} X_\alpha \Big], \tag{2.83}$$

where

$$X_\alpha = \frac{\nabla_\alpha P}{\epsilon + P} - \frac{\nabla_\alpha T}{T}, \tag{2.84}$$

and ϵ and n_{net} represent the energy density and net baryon number density, respectively. In relativistic hydrodynamics, when dealing with systems that are slightly out of equilibrium, it becomes crucial to specify the hydrodynamic four-velocity. In the literature, two choices are considered. Eckart's definition relates the hydrodynamic velocity to particle four-flow (along the baryon-flow), whereas Landau and Lifshitz's definition relates the fluid velocity to the flow of energy (or the momentum density) [102]. Considering Eckart's frame, where one can define v^i as [101]

$$j_B^i = n_{net} v^i + \Delta j_B^i = 0.$$

so that the energy flux component T^{0i} becomes

$$\begin{aligned} T^{0i} &= (\epsilon + P) v^i + \Delta T^{0i} \\ &= -\frac{\epsilon + P}{n_{net}} \Delta j_B^i + \Delta T^{0i} \equiv I^i, \end{aligned} \tag{2.85}$$

the I^i being the heat current, the ΔT^{0i} and the Δj_B^i is given by

$$\Delta T^{0i} = \sum_i g_i \int \frac{d^3p}{(2\pi)^3} \frac{\mathbf{p^2}}{3T} \tau_i f_i^0 \Big(1 - \frac{\epsilon + P}{n_{net} E_i}\Big) X_i, \tag{2.86}$$

and

$$\Delta j_B^i = \sum_i t_i g_i \int \frac{d^3p}{(2\pi)^3} \frac{\mathbf{p^2}}{3T E_i} \tau_i f_i^0 \Big((1 - \frac{\epsilon + P}{n_{net} E_i}\Big) X_i. \tag{2.87}$$

The heat conductivity is then defined as [101]

$$I^i = -\kappa\big[\partial_i T - T\partial_i P/(\epsilon + P)\big]. \tag{2.88}$$

We calculate I^i using Eq. (2.82) and Eq. (2.83) in above Eq. (2.85), and then the expression for the thermal conductivity, κ can be found as

$$\boxed{\kappa = \frac{1}{3T^2}\sum_i g_i\tau_i \int \frac{d^3p}{(2\pi)^3}\frac{\mathbf{p^2}}{E_i^2}\Big(E_i - \frac{t_i\omega}{n_{net}}\Big)^2 \times f_i^0}, \tag{2.89}$$

where τ_i denotes the relaxation time defined in Eq. (2.69). Here, t_i represents the baryonic charge of the ith hadronic species, $\omega = \epsilon_i + P_i$ corresponds to the enthalpy per particle, and n_{net} is the net baryon density of the system.

The temperature evolution of the scaled thermal conductivity, κ/T^2, obtained within the VDWHRG framework at a finite value $\mu_B = 0.025$ GeV (solid red line) is presented in Fig. 2.5 [96]. The variation of κ/T^2 exhibits a temperature dependence similar to that of the electrical conductivity shown in Fig. 2.3. As the temperature increases, the particle number density in the system rises, leading to a higher collision rate among the constituent hadrons. These frequent and random scatterings disrupt the coherent transport of heat energy, thereby reducing the medium's thermal conductivity. Our results are compared with those obtained from the three-flavor (u, d, s) Nambu–Jona-Lasinio (NJL) model [103], the excluded volume HRG (EVHRG) model [87], the chiral perturbation theory (ChPT) approach [99], the color string percolation model (CSPM) [100], and the pion gas model in the relaxation time approximation (RTA) [104]. Across all models, the κ/T^2 shows a uniformly decreasing behavior with increasing temperature. The quantitative differences among various approaches arise from the underlying physical assumptions: in the NJL model, the relevant degrees of freedom are partonic, while in the EVHRG model, the difference mainly stems from the choice of hadronic radii. In our model, we have considered different hadronic radii for mesons and baryons, $r_M = 0.2$ fm and $r_{B,\bar{B}} = 0.62$ fm, respectively. On the other hand, the authors in Ref. [87] have considered a common hadronic radius, $r_h =$

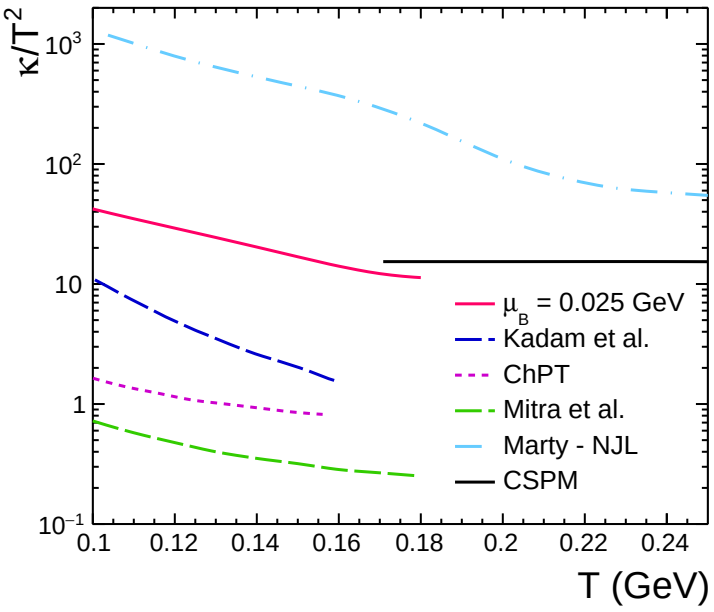

Figure 2.5: Temperature dependence of scaled thermal conductivity using VDW HRG model at $\mu_B = 0.025$ GeV is shown in solid red curve [96]. The results are then compared to the estimations obtained from different models, including those from CSPM [100], the NJL calculations [103], and from chiral perturbation theory [99]. The calculations made using the excluded volume HRG model [87] as well as those for pion gas [104] are also shown.

0.3 fm for all hadrons. For a detailed study of the impact of hadronic size, one may refer to Ref. [33]. The relatively low values obtained by Mitra *et al.* [104] for a pion gas highlight the significance of including heavier hadronic species in the estimation of thermal conductivity. Furthermore, a good agreement is observed between our VDWHRG results and the QCD-inspired CSPM model near the critical temperature, indicating consistency across theoretical frameworks in this regime.

The μ_B dependence of κ/T^2 is shown in Fig. 2.6 [96]. As the baryon chemical potential increases, the particle number density also increases, leading to a

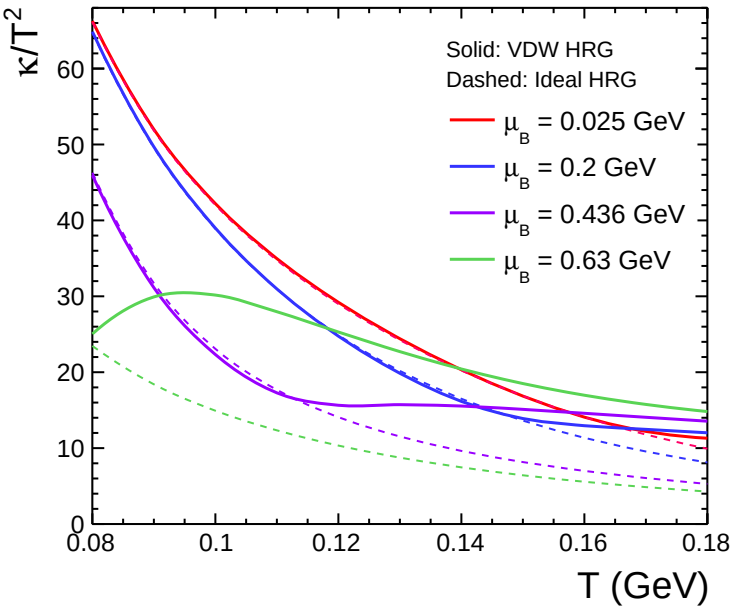

Figure 2.6: Temperature dependence of scaled thermal conductivity for distinct values of baryon chemical potentials under both ideal HRG and VDWHRG scenarios [96].

decrease in relaxation time τ, which in turn suppresses the transport of thermal energy through the system. Similar to the behavior observed for electrical conductivity, the results from VDWHRG also show deviation from the ideal HRG case at higher temperatures, due to the suppression of particle density arising from the repulsive van der Waals interactions. Although there is an overall decrease in the thermal conductivity with temperature, a non-monotonic behavior is observed at high μ_B. This arises because the effect of van der Waals interaction moderates the growth of enthalpy and net baryon density as a function of temperature. However, the reduction in net baryon density is comparatively stronger than the suppression in enthalpy, resulting in a localized enhancement of thermal conductivity, and consequently the appearance of a minimum. As μ_B increases further, this minimum shifts toward lower temperatures, reflecting the

growing influence of baryonic interactions in the medium.

2.2.1.3 Wiedemann-Franz law

The electrical conductivity reflects how an interacting system of charged particles responds to an externally applied electric field, whereas the thermal conductivity characterizes the transport of heat resulting from a temperature gradient. The Wiedemann–Franz law relates these two quantities, stating that their ratio is proportional to temperature, with the proportionality constant known as the Lorenz number. This empirical law is well satisfied in metals, where the Lorenz number depends on the material properties.

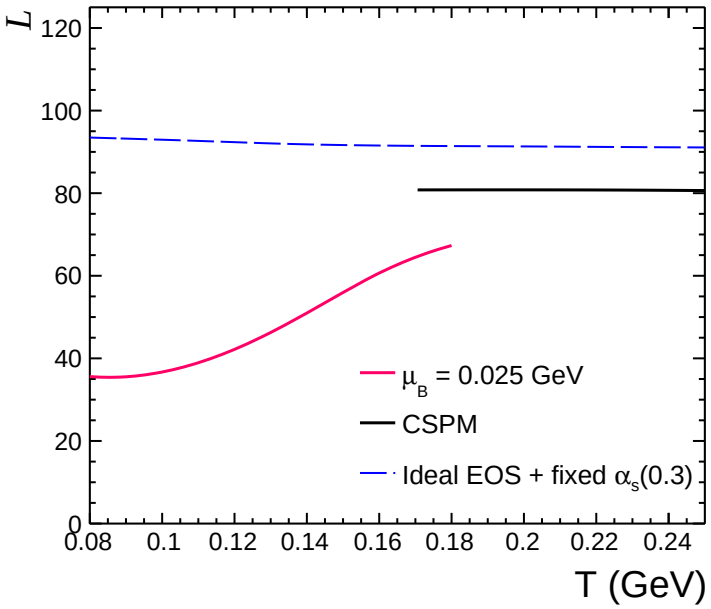

Figure 2.7: Temperature dependence of the Lorenz number, $L = \kappa/(\sigma_{el}T)$, within the VDWHRG model [96] compared with results from the CSPM framework [100] (black solid line) and the ideal equation of state with a fixed coupling constant $\alpha_s = 0.3$ (blue dashed line) [105].

The temperature variation of the Lorenz number at $\mu_B = 0.025$ GeV is shown

in Fig. 2.7 [96] and compared with the results from the CSPM model [100] and from an ideal equation of state framework with a fixed coupling constant, $\alpha_s = 0.3$ [105]. Both these approaches show little to no dependence of L on temperature. In contrast, our analysis indicates that at low temperatures, the Lorenz number remains nearly constant but begins to rise almost linearly beyond $T \sim 110$ MeV. This behavior suggests that the Wiedemann–Franz law no longer holds for a hadron gas at higher temperatures. The near constancy of L at lower temperatures implies proportionality between electrical and thermal conductivities, while its subsequent rise reflects that thermal conductivity becomes comparatively more dominant as temperature increases.

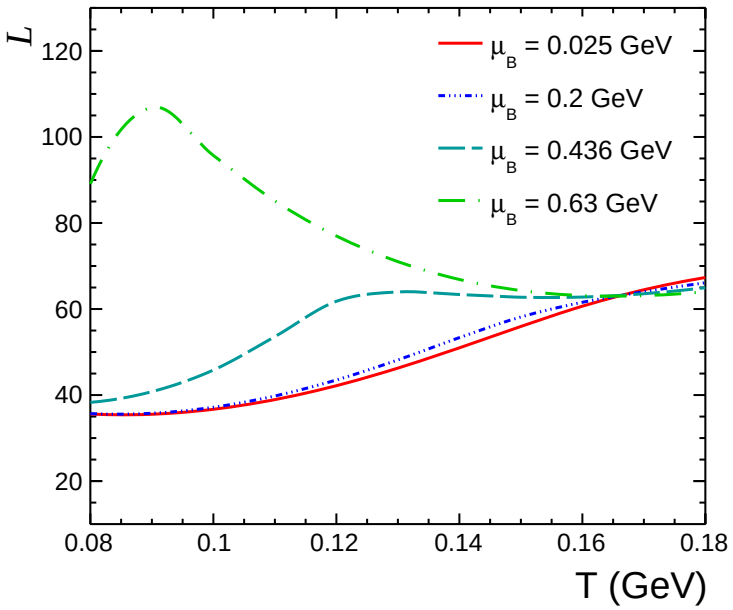

Figure 2.8: Temperature dependence of the Lorenz number for several distinct values of baryon chemical potential, μ_B [96]. The observed increase of L with μ_B highlights the effect of baryon density on transport properties in the interacting hadronic medium.

A noticeable change in the trend of the Lorenz number appears around $T \sim$

170 MeV when the VDWHRG results are compared with the QCD-inspired CSPM results. Since the VDWHRG model considers hadronic degrees of freedom, while CSPM involves color degrees of freedom, this crossover-like behavior could signify the onset of a quark–hadron phase transition near $T \sim 170$ MeV, consistent with the lattice QCD prediction of the deconfinement temperature [106].

Figure 2.8 displays the dependence of the Lorenz number on μ_B [96]. An overall increase of L with baryon chemical potential is observed. This is because both electrical and thermal conductivities decrease with increasing μ_B, but the reduction in electrical conductivity is more significant, resulting in an enhanced Lorenz number. At large μ_B and higher temperatures, the increased thermal conductivity is reflected in the behavior of L. A clear maximum appears in its temperature dependence, which shifts toward lower temperatures as μ_B increases. Such a trend could be a possible indication of a phase transition, likely of liquid–gas type, given that the underlying framework involves van der Waals interactions among hadrons.

2.2.2 Diffusivity

In simple terms, diffusion refers to the process by which matter or energy undergoes a net transport due to a concentration gradient, typically flowing from regions of higher concentration to regions of lower concentration. The diffusivity quantifies the rate at which this diffusion occurs.

In the context of charge transport, the charge diffusion coefficient quantifies the rate at which electric charge diffuses along the direction of the concentration gradient and is linked to the electrical conductivity using the following relation [107]:

$$D_{el} = \frac{\sigma_{el}}{\chi_Q}, \tag{2.90}$$

where χ_Q denotes the electric charge susceptibility, which measures the response of the system to fluctuations in the electric charge. In general, suscep-

tibilities associated with conserved charges can be evaluated as the second (or higher) order derivative of the free energy, or equivalently, of the pressure, with respect to the chemical potential corresponding to the conserved charge under consideration [81]. The electric charge susceptibility is thus expressed as

$$\chi_Q = \frac{\partial^2(P(T,\mu)/T^4)}{\partial(\mu_Q/T)^2}. \tag{2.91}$$

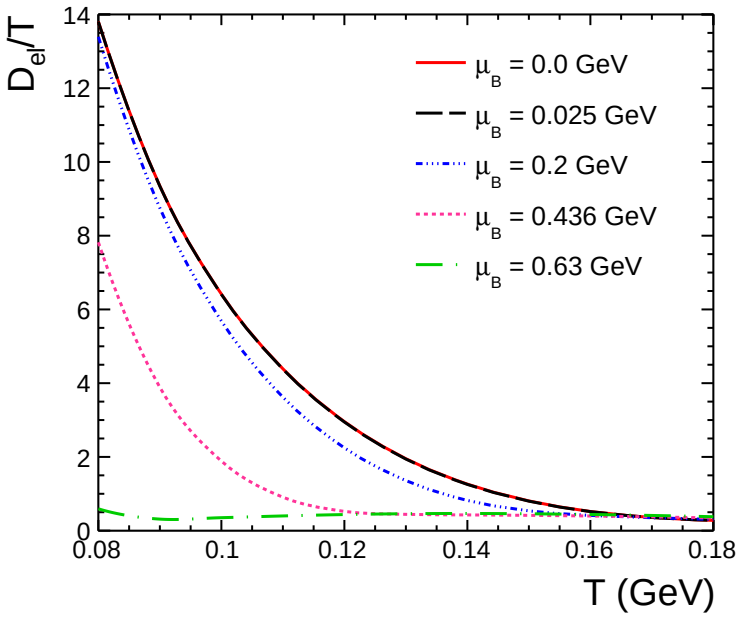

Figure 2.9: (Color Online) Scaled electrical diffusivity, D_{el}/T, as a function of temperature for several distinct values of baryochemical potential, μ_B [96].

Figure 2.9 illustrates the temperature dependence of the scaled electrical diffusivity, D_{el}/T, for various values of the baryon chemical potential, μ_B [96]. It is evident that D_{el}/T decreases monotonically with increasing temperature. Since diffusivity characterizes the rate at which a conserved quantity spreads along a concentration gradient, a smaller diffusivity at higher temperatures implies that the medium becomes denser and less capable of transporting charge through diffusion compared to the low-temperature regime. This behavior is consistent with

the trend observed in electrical conductivity, where higher temperature conditions correspond to reduced transport strength. Furthermore, lattice QCD (lQCD) calculations indicate the presence of a minimum in the electrical diffusivity near the critical temperature, followed by an increase as the system transitions to the quark–gluon plasma (QGP) phase [107]. The observed minimum can thus be associated with the crossover or phase transition from the hadronic to the deconfined QGP phase.

The thermal diffusivity, on the other hand, characterizes the rate of heat propagation through the medium and is defined as the ratio of the thermal conductivity to the product of specific heat capacity and density. Since the specific heat capacity can be expressed as the temperature derivative of the entropy, the thermal diffusivity can equivalently be written as [108]

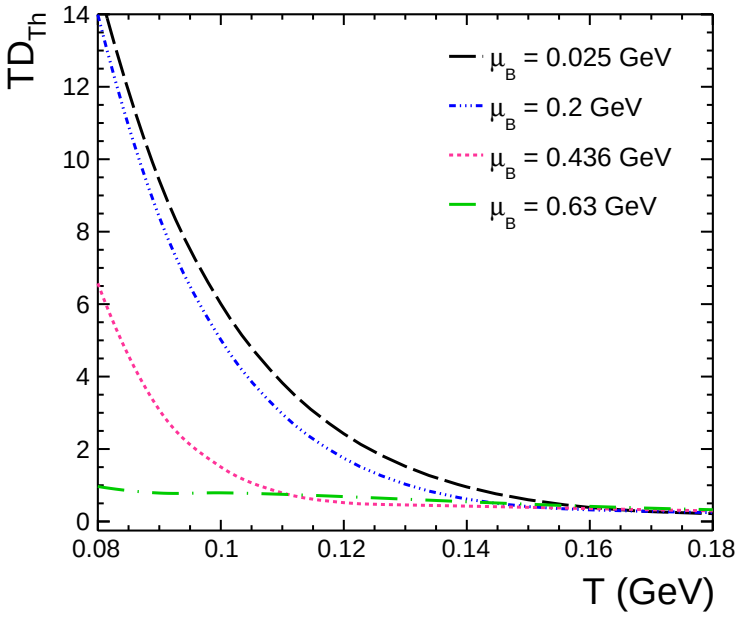

Figure 2.10: (Color Online) Scaled electrical diffusivity, D_{el}/T, as a function of temperature for several distinct values of baryochemical potential, μ_B.

$$D_{Th} = \kappa \Big/ \Big(\frac{T}{V}\frac{\partial S}{\partial T}\Big), \tag{2.92}$$

where κ is the thermal conductivity, S is the total entropy, T is the temperature, and V denotes the system volume.

As in electrical diffusivity, a similar behavior is observed for the thermal diffusivity, as shown in Fig. 2.10. The dimensionless quantity TD_{Th} is found to decrease with increasing temperature. At higher temperatures, the rise in particle number density and the frequency of collisions make the medium less efficient in transferring thermal energy, thereby slowing down the overall diffusion process. Consequently, more heat tends to be retained within the system rather than being transported. Both electrical and thermal diffusivities exhibit minima near the critical temperature, making them potential indicators for identifying the onset of a phase transition.

2.3 Transport properties in a high temperature Bose-Einstein condensate

One of the most remarkable macroscopic consequences of quantum statistics is the emergence of the phenomenon of Bose-Einstein Condensation (BEC). In 1924, by treating light as a gas of identical particles, Satyendra Nath Bose derived Planck's quantum radiation law [109]. Building upon this, Einstein extended the idea to systems of massive particles, thereby formulating the quantum theory of an ideal gas in two seminal papers published in 1924 [110] and 1925 [111]. Einstein demonstrated that a system of bosons exhibits a remarkable property, at sufficiently low temperatures ($T \sim 0$ K) and nearly vanishing momenta, a macroscopic fraction of the particles can occupy the lowest quantum state [109, 110], forming a single quantum entity, now known as the Bose–Einstein (BE) condensate. Owing to the symmetric nature of bosonic wave functions, a large number of particles can

coherently occupy the same state, leading to macroscopic quantum phenomena arising from the interference of their wave functions. However, this theory remained unverified for decades, as the extreme physical conditions necessary to realize the condensation were experimentally challenging. It was only in 1995, when two experimental groups, using a combination of magnetic trapping and evaporative cooling, successfully achieved BEC in a dilute gas of rubidium-87 atoms at a temperature of some nano Kelvin [112].

The phenomenon of BEC has been understood as a low-temperature phenomenon to a great extent. However, in recent decades, theoretical studies have suggested that BEC-like properties may also emerge in highly dense systems, such as those created in relativistic heavy-ion collisions. This leads to an intriguing question: How can such a rapidly evolving and violently expanding system sustain a BEC-like state? As proposed by Fowler, Stelte, and Weiner [113], the presence of a condensate may be interpreted as a manifestation of coherence among bosons, observable through characteristic Bose–Einstein correlations in their momentum spectra. In ultra-relativistic collisions, the large particle multiplicities and high energy densities lead to a situation where bosons, such as pions or vector mesons, occupy overlapping regions in phase space with small relative momenta. Consequently, despite the high temperature, the combination of high density, strong interactions, and limited spatial volume can give rise to transient domains exhibiting partial coherence. These domains may be viewed as remnants or signatures of a Bose–Einstein–like condensate within the hot hadronic environment.

Pions, the lightest hadron, dominate the final-state particle spectrum in relativistic nuclear collisions. As spin-zero mesons, pions obey Bose–Einstein (BE) statistics, and the high pion multiplicity in the hadronic medium provides favorable conditions for the possible onset of Bose–Einstein condensation (BEC). Such a possibility has been explored within chemically non-equilibrated frameworks, where pion abundances are governed by a finite chemical potential [114]. This

could indicate a potential emergence of BEC at LHC energies. The formation of a high-temperature condensate in an ultra-relativistic collision has been a subject of considerable theoretical interest and has been extensively studied in several works [115–118]. Furthermore, the effects of interactions among pions, modeled through excluded-volume and mean-field approximations, have also been investigated to understand their influence on the onset of condensation [119].

Despite these theoretical indications, an unambiguous experimental confirmation of pion BEC in heavy-ion collisions remains challenging. One of the proposed signatures is an enhancement of the pion yield at low transverse momentum (p_{T}), where condensate effects are expected to dominate. However, no distinct signal has yet been observed, primarily due to the contamination from resonance decays and the experimental difficulty of measuring pion spectra at very low p_{T}. The possibility of realizing a coherent pion production has also been explored through multi-pion correlation studies. Recent measurements by the ALICE Collaboration, based on two- and three-pion correlation analyses, indicate that almost 23 % coherence in the charged pion emission [120]. Since pion radiation from a condensate is expected to be coherent, this coherence would lead to a suppression of Bose–Einstein correlations [113]. An effective suppression of three-pion correlations relative to two-pion correlations at low triplet momenta has been observed, which is consistent with partial coherence and possibly the formation of a Bose–Einstein–like condensate [120]. Moreover, measurements of event-by-event particle number fluctuations have also been proposed as an additional observable signature of BEC formation [115]. The emergence of such coherent behavior in pion production could therefore have significant implications for understanding the microscopic dynamics and collective evolution of the hadronic medium formed in high-energy nuclear collisions.

Given these considerations, it would be interesting to investigate the properties of hot and dense matter when condensation is expected to happen at such extreme conditions. The study of transport coefficients, particularly shear and

bulk viscosities, can help quantify the medium's dissipative response and hence understand the collectivity of the medium. Here, we focus on the influence of Bose–Einstein condensation on transport phenomena by studying a pion gas that undergoes partial or full condensation. Before computing transport coefficients, we first analyse the thermodynamic properties of the pion gas in the presence of BEC. These equilibrium quantities provide the essential inputs and intuition required to understand how condensation modifies the viscosities in a condensed phase.

2.3.1 Thermodynamic properties of a pion gas undergoing BEC

Let us start from the basics. The Bose-Einstein distribution function is given by

$$f = \left[\exp\left(\frac{E-\mu}{T}\right) - 1\right]^{-1} \tag{2.93}$$

where $E = \sqrt{p^2 + m^2}$ is the single-particle energy with p as the momentum and m being the particle mass. Using μ and T as the chemical potential and temperature, respectively, the total particle multiplicity in natural units ($c = \hbar = 1$) is given as [116],

$$\begin{aligned} N &= g \int \frac{d^3x d^3p}{(2\pi)^3} \left[\exp\left(\frac{\sqrt{p^2+m^2}-\mu}{T}\right) - 1\right]^{-1} \\ &\simeq \frac{gV}{(2\pi)^3} \int d^3p \left[\exp\left(\frac{\sqrt{p^2+m^2}-\mu}{T}\right) - 1\right]^{-1} \end{aligned} \tag{2.94}$$

where g denotes the degeneracy of the particle. Volume of the system is given by V. The total number density ($n_{\rm tot}$) then becomes

$$\begin{aligned} n_{\rm tot} &= \frac{g}{(2\pi)^3} \int \frac{d^3p}{\exp\left(\frac{\sqrt{p^2+m^2}-\mu}{T}\right) - 1} \\ &\approx \frac{gTm^2}{2\pi^2} \sum_{r=1}^{\infty} \frac{1}{r} K_2(rm/T) \exp(r\mu/T), \end{aligned} \tag{2.95}$$

where the modified Bessel function is given by K_2, and r represent a positive integer. Here, the sum over discrete momentum states transitions to an integral over momentum space as one approaches the thermodynamic limit (for $V \to \infty$). This formulation holds well when $\mu < m$. However, as $\mu \to m$, an interesting situation arises. The integrand in the first line of Eq. (2.95) remains finite for $p \to 0$ because the apparent singularity in the denominator is compensated by the integration measure d^3p. Consequently, the momentum integral stays convergent. In contrast, when one considers the discrete sum over quantum states, the occupation number of the lowest energy level ($p = 0$) diverges for $\mu = m$. This can be expressed as

$$n_{\rm cond} \simeq \frac{g}{V[\exp(\frac{m-\mu}{T}) - 1]} \to \infty \quad \text{for} \quad \mu \to m. \tag{2.96}$$

Physically, this divergence indicates that as μ approaches m, a macroscopic number of particles begin to occupy the ground state, leading to the onset of Bose–Einstein condensation. This necessitates separating the total number density into contributions from the condensed and non-condensed parts. Accordingly, Eq. (2.94) can be rewritten by isolating the contribution from the zero-momentum mode ($p = 0$) and the terms with non-zero momentum ($p > 0$,), as

$$\begin{aligned} n_{\rm tot} &\simeq \frac{g}{V[\exp(\frac{m-\mu}{T}) - 1]} + \int \frac{d^3p}{(2\pi)^3} \frac{g}{\exp\left(\frac{\sqrt{p^2+m^2}-\mu}{T}\right) - 1} \\ &\Rightarrow n_{\rm tot} = n_{\rm cond} + n_{\rm ex}. \end{aligned} \tag{2.97}$$

Here, $n_{\rm cond}$ and $n_{\rm ex}$ denote the particle number densities associated with the condensate and the excited states, respectively. In this work, the statistical description of the pion medium is carried out within the Grand Canonical Ensemble, assuming the total pion yield after chemical freeze-out.

Since the condensate density is expressed as $n_{\rm cond} = (g/V)[\exp{(m-\mu)/T} - 1]^{-1}$, it follows that for $\mu \to m$, a finite number of particles occupy the condensed

state, i.e., $n_{\rm cond} > 0$. In this limit, the difference between the ground-state energy and the chemical potential is given by [121]

$$m - \mu = T \ln\left(1 + \frac{g}{n_{\rm cond} V}\right). \tag{2.98}$$

However, this condition ceases to hold when $n_{\rm cond} = 0$, in which case $n_{\rm ex} = n_{\rm tot}$. Therefore, the onset of Bose–Einstein condensation corresponds to the transition from a non-condensed phase ($n_{\rm cond} = 0$) to one where $n_{\rm cond} > 0$. The critical temperature T_c for condensation can thus be defined as the lowest temperature where the population of the excited states reaches its maximum possible value [121–123], i.e.,

$$n_{\rm critical} = n_{\rm ex}(T = T_c, \mu = m) = n_{\rm tot}. \tag{2.99}$$

For temperatures below the critical point ($T < T_c$), the number density of particles occupying the excited states decreases compared to its value at T_c. The surplus particles are therefore forced to occupy the ground state, resulting in the formation of the condensate. We can define the condensate fraction as the ratio of the number density in the condensed state to the total number density, which is given as

$$\frac{n_{\rm cond}}{n_{\rm tot}} = 1 - \frac{n_{\rm ex}}{n_{\rm tot}} = 1 - \frac{n_{\rm ex}(T, \mu = m)}{n_{\rm ex}(T_c, \mu = m)}. \tag{2.100}$$

This expression describes how the condensate fraction evolves with temperature. As $T \to 0$, the condensate fraction ($n_{\rm cond}/n_{\rm tot}$) approaches unity, indicating that nearly all particles occupy the ground state. Let us study the asymptotic behaviour of $n(T, \mu)$ given in Eq. (2.95) in the thermodynamic limit as $\mu \to m - 0$. Following Ref. [115], we have

$$n(T, m) - n(T, \mu) = \frac{g}{2\pi^2} \int p^2 dp \left[\frac{1}{e^{(\sqrt{p^2+m^2}-m)/T} - 1} - \frac{1}{e^{(\sqrt{p^2+m^2}-\mu)/T} - 1} \right]. \tag{2.101}$$

As in the case of the non-relativistic one, here, substituting [115]

$$p = \sqrt{2m(m-\mu)}\, x,$$

we obtain

$$n(T,m)-n(T,\mu)=\frac{g}{2\pi^2}(2m)^{3/2}(m-\mu)^{3/2}\int x^2dx \times\left[\frac{1}{e^{(\sqrt{2m(m-\mu)x^2+m^2}-m)/T}-1}-\frac{1}{e^{(\sqrt{2m(m-\mu)x^2+m^2}-\mu)/T}-1}\right]. \tag{2.102}$$

Now, since we can write

$$\coth\left(\frac{y}{2}\right)=\frac{e^{y/2}+e^{-y/2}}{e^{y/2}-e^{-y/2}}=\frac{e^y+1}{e^y-1}=\frac{e^y-1+2}{e^y-1}=1+\frac{2}{e^y-1},$$

therefore,

$$\frac{1}{e^y-1}=\frac{1}{2}\left[\coth\left(\frac{y}{2}\right)-1\right].$$

Substituting this in the above equation, where $y=(\sqrt{2m(m-\mu)x^2+m^2}-m)/T$, one can write

$$n(T,m)-n(T,\mu)=\frac{g}{2\pi^2T^2}(2m)^{3/2}(m-\mu)^{3/2}\int x^2dx \times\frac{1}{2}\left[\coth\left(\frac{\sqrt{2m(m-\mu)x^2+m^2}-m}{2T}\right)-\coth\left(\frac{\sqrt{2m(m-\mu)x^2+m^2}-\mu}{2T}\right)\right]. \tag{2.103}$$

We can expand to the lowest order in $(m-\mu)/m$ as

$$\sqrt{2m(m-\mu)x^2+m^2}-m=m\sqrt{1+\frac{2(m-\mu)}{m}x^2}-m$$
$$=m+(m-\mu)x^2+...-m \tag{2.104}$$
$$\simeq(m-\mu)x^2. \tag{2.105}$$

Therefore, the above equation becomes

$$n(T,m)-n(T,\mu)=\frac{g}{\sqrt{2}\pi^2}(m)^{3/2}(m-\mu)^{3/2}\int x^2dx \times\left[\coth\left(\frac{(m-\mu)x^2}{2T}\right)-\coth\left(\frac{(m-\mu)(x^2+1)}{2T}\right)\right]. \tag{2.106}$$

Taking up to the first term in the expansion of $\coth(y/2)$, we can write

$$\begin{aligned} n(T,m) - n(T,\mu) &= \frac{g}{\sqrt{2}\pi^2} T m^{3/2} (m-\mu)^{3/2} \int x^2 dx \\ &\quad \times \left[\frac{2T}{(m-\mu)x^2} - \frac{2T}{(m-\mu)(x^2+1)} \right] \\ &= \frac{6Tm^{3/2}}{\sqrt{2}\pi^2} \sqrt{m-\mu} \int x^2 dx \left[\frac{1}{x^2} - \frac{1}{x^2+1} \right]. \end{aligned} \tag{2.107}$$

Simplifying,

$$\begin{aligned} n(T,m) - n(T,\mu) &= \frac{2gTm^{3/2}}{\sqrt{2}\pi^2} \sqrt{m-\mu} \int \frac{dx}{1+x^2} = \frac{2gTm^{3/2}}{\sqrt{2}\pi^{3/2}\sqrt{m-\mu}} \tan^{-1}(x)\Big|_0^\infty \\ &= \frac{2gTm^{3/2}}{\sqrt{2}\pi^2} \sqrt{m-\mu} \left(\frac{\pi}{2}\right) \\ &= \frac{gTm^{3/2}}{\sqrt{2}\pi} \sqrt{m-\mu}. \end{aligned} \tag{2.108}$$

To find the behavior of the chemical potential μ at constant density, note that for $T > T_c$, the μ decreases with T so as to maintain the condition of fixed density. To see this behavior at $T \to T_c + 0$, We have [115]

$$n(T = T_c, \mu = m) \tag{2.109}$$

$$\begin{aligned} &= n(T,\mu) \simeq n(T,\mu=m) - \frac{gTm^{3/2}}{\sqrt{2\pi}\sqrt{m-\mu}} \\ &\simeq n(T=T_c,\mu=m) + (T-T_c) \frac{\partial n(T,\mu=m)}{\partial T}\bigg|_{T=T_c} - \frac{gT_c m^{3/2}}{\sqrt{2}\pi} \sqrt{m-\mu}. \end{aligned} \tag{2.110}$$

This gives, for $T \to T_c + 0$,

$$\boxed{m - \mu(T) = \frac{2\pi^2}{g^2 T_c^2 m^3} \left(\frac{\partial n(T,\mu=m)}{\partial T}\bigg|_{T=T_c} \right)^2 (T-T_c)^2}. \tag{2.111}$$

In the present analysis, we consider a pion gas, neglecting the small mass difference between neutral and charged pions and taking an average pion mass of $m \simeq 0.14$ GeV, with a degeneracy of $g = 3$ for simplicity. The focus of this work is extended to exploring finite-size effects on the Bose–Einstein condensate, as such studies may provide insights into possible experimental signatures of pion

condensation, for instance, fluctuations associated with a pion BEC as discussed in Ref. [115]. To see the finite size effects, and therefore the behavior of μ in such a scenario, we consider the total density as

$$n_{\rm tot} = \frac{3}{V}\frac{1}{e^{(m-\mu)/T}-1} + \frac{3}{2\pi^2}\int p^2 dp \frac{1}{e^{(\sqrt{m^2+p^2}-\mu)/T}-1}. \tag{2.112}$$

At finite volume V, the quantization condition for $\mu = m$ leads to infinite density. Therefore, taking [115]

$$\frac{m-\mu}{T} = \delta, \quad \text{such that} \quad \delta \propto V^{-1} \quad \text{as} \quad V \to \infty,$$

we have

$$\begin{aligned} n_{\rm tot} &= \frac{3}{V\delta} + n_{\rm ex}(T,\mu) \\ &\simeq \frac{3}{V\delta} + n_{\rm ex}(T,\mu=m) - \frac{3}{\sqrt{2}\pi}(mT)^{3/2}\sqrt{\delta}. \end{aligned} \tag{2.113}$$

This can be written as

$$D_1\delta^{3/2} + D_2\delta - 1 = 0, \tag{2.114}$$

where

$$D_1 = \frac{V}{\sqrt{2}\pi}(mT)^{3/2} \equiv d_1(T)V, \qquad D_2 = \frac{V}{3}\left[n_{\rm tot} - n_{\rm ex}(T,\mu=m)\right] \equiv d_2(T)V.$$

The above equation has two complex and one real root. For large V, the asymptotic behavior of the real root can be found as follows [115]:

1. For $T < T_c$, $d_2(T) > 0 \implies \delta \simeq d_2 V^{-1}$.

2. At $T = T_c$, $d_2(T) = 0 \implies \delta \simeq \frac{1}{d_1^{2/3}} V^{-2/3}$.

3. At $T > T_c$, if T is close to T_c, $\delta \ll 1$, and $d_2(T) < 0$, one finds $\delta \simeq \frac{d_2^2}{d_1^2}$.

Finding δ helps us to study the behaviour of μ for systems with finite volume. To investigate the effects of finite-size, we assumed a spherical system of radius

R, with the corresponding volume given by $V = (4/3)\pi R^3$. Three representative systems of different sizes with corresponding radii $R = 3$, 5, and 7 fm are taken in the present study. For a fixed total number density ($n_{\rm tot} = 0.1$ fm^{-3}), the total particle number increases with system size, implying that larger systems contain a higher total particle content. This framework is used to investigate how finite-volume effects impact the formation and properties of a Bose–Einstein condensate. For these finite volumes, Eq. (2.97) is used to evaluate the condensate fraction. Through the volume parameter, the system size enters the thermodynamic relations, which in turn modify the distribution of particles between the condensate and excited states. It is essential to keep in mind that when dealing with finite volumes, the momentum spectrum becomes discretized, and the true ground state is no longer at $p = 0$. Instead, the smallest accessible momentum is fixed by the boundary conditions of the system. Consequently, the condensate occupies this lowest allowed momentum state, which still exhibits a significantly enhanced occupation. However, a true divergence in the condensate population no longer occurs, and the Bose–Einstein condensation transition becomes smoother compared to the thermodynamic limit ($R \to \infty$).

In the present analysis, it is observed that even for the smallest system considered ($R = 3$ fm), the shift in the ground-state energy relative to that in the thermodynamic limit is minimal and has a negligible influence on the overall results. Moreover, since the finite volume introduces a discretized momentum spectrum, a more rigorous treatment would involve replacing the continuous momentum integrals with discrete summations over quantized momentum states. Although this refinement would slightly modify the numerical values of the condensate fraction or transport coefficients, the qualitative behavior and overall trends discussed here would remain unchanged. Fig. 2.11 illustrates the temperature variation of the condensate fraction for a pion gas with a fixed total number density, $n_{\rm tot} = 0.1$ fm^{-3} [124]. The black solid curve represents the condensate fraction for the case of thermodynamic limit, yielding a critical temperature of

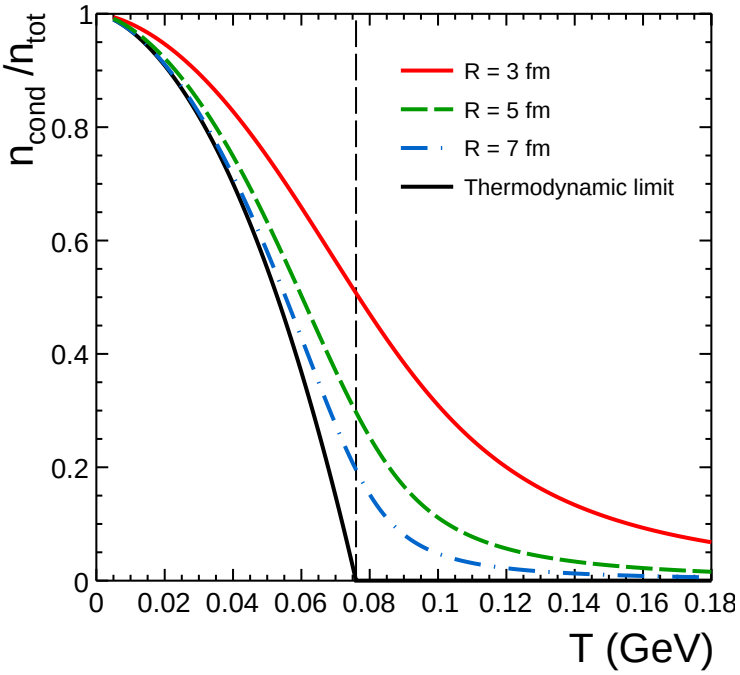

Figure 2.11: The variation of condensate fraction with temperature is shown for both the thermodynamic limit and systems of finite sizes with $R = 3$, 5, and 7 fm. The calculations are performed at a fixed total number density of $n_{\rm tot} = 0.1$ fm^{-3}, corresponding to a critical temperature of $T_c = 0.076$ GeV [124].

$T = T_C = 76$ MeV, as obtained from Eq. (2.95). This result is consistent with earlier findings, such as in Ref. [115]. To study the finite-size effects, we present the condensate fraction for a system with $R = 3$ fm, with a solid red curve. The green dashed line and the blue dotted dashed line represent systems with $R = 5$ fm and $R = 7$ fm, respectively. For a system of finite size, the condensate fraction is seen to decrease with temperature, but unlike in the thermodynamic limit, it does not vanish completely at T_c. The sharp transition observed in the thermodynamic limit is thus smeared out in finite systems, indicating that the onset of condensation is smoothened by volume effects. Throughout this analysis, the critical temperature (T_c) is therefore defined as that obtained in the thermody-

namic limit. A finite fraction of particles remains in the condensed phase even for $T > T_c$, though this fraction gradually becomes negligible with further increase in temperature. As the system volume increases (with increasing R), maintaining a fixed number density implies a larger total particle number. Consequently, the transition behavior progressively approaches that of the thermodynamic limit, where both the volume and particle number tend to infinity while keeping $n_{\rm tot}$ constant. Irrespective of the system size, the condensate fraction tends to unity as $T \to 0$, as expected. At sufficiently high temperatures, the dependence on system volume becomes negligible. Furthermore, as the number densities of both

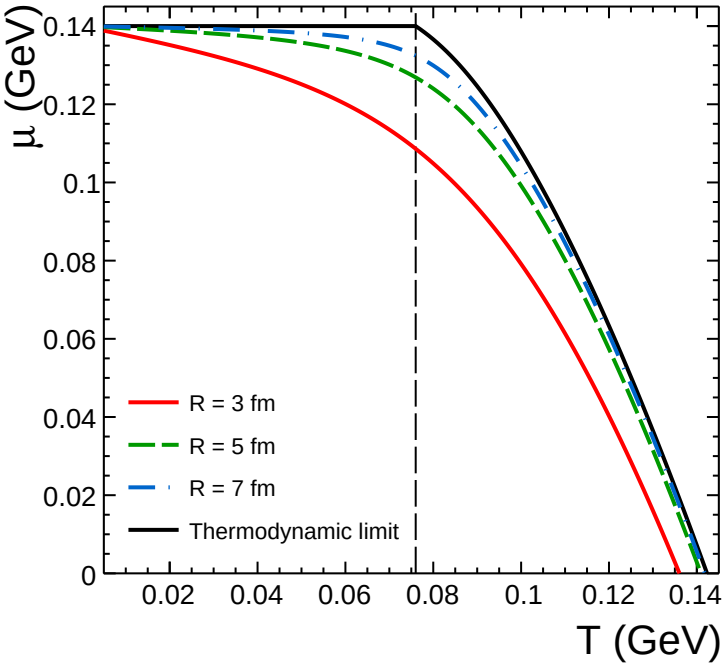

Figure 2.12: Temperature dependence of the chemical potential, μ, shown for both the thermodynamic limit and for finite systems with radii $R = 3$, 5, and 7 fm. The calculations are performed at a fixed total density of $n_{\rm tot} = 0.1$ fm^{-3}, corresponding to a critical temperature of $T_c = 0.076$ GeV [124].

the condensate and the excited states vary with temperature, a fixed total density

$n_{\rm tot}$ implies that the chemical potential must also exhibit a temperature dependence, i.e., $\mu \equiv \mu(T)$. At each temperature, the value of μ is evaluated so as to ensure that the total number density remains constant. The resulting behavior of $\mu(T)$ is illustrated in the right panel of Fig. 2.12 [124]. It can be seen that, with increasing system size, the variation of $\mu(T)$ gradually approaches that expected in the thermodynamic limit, confirming that finite-size effects become less significant for larger volumes.

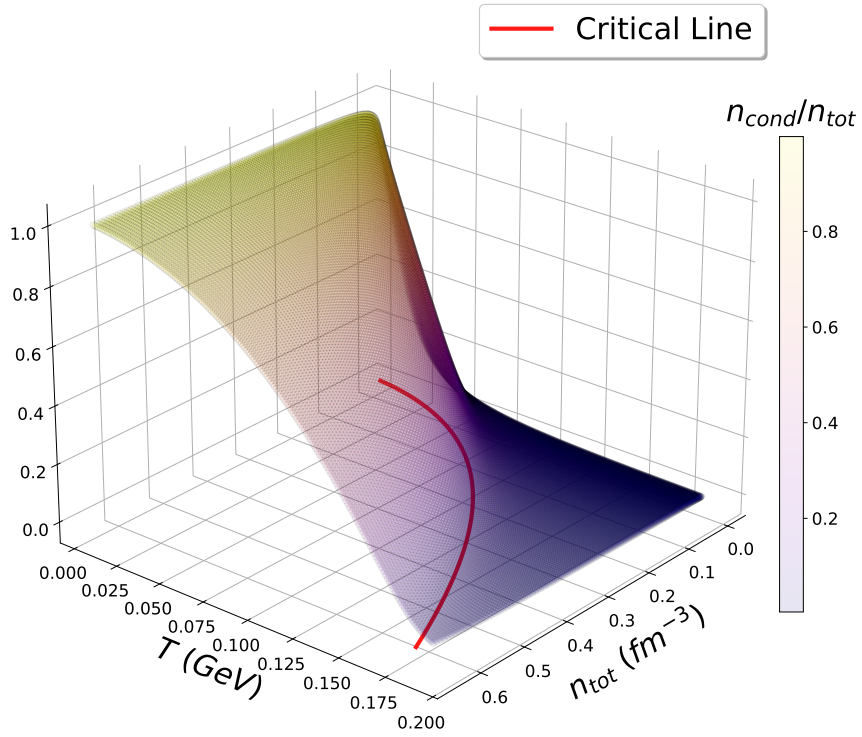

Figure 2.13: Temperature dependence of condensate fraction of pions for different total number densities considered. The BEC critical line showing the transition temperature T_c for different values of total density $n_{\rm tot}$ is represented by the solid red curve in the $T - n_{\rm tot}$ plane. The BEC phase for $T < T_c$, is described by Eq. (2.97) [124].

It is important to note that the critical temperature, T_c, varies for different

choices of total particle density, $n_{\rm tot}$. In Fig. 2.13, the condensate fraction is shown as a function of temperature for several values of $n_{\rm tot}$ in a finite volume system with radius $R = 7$ fm [124]. As expected, a higher total density corresponds to a larger critical temperature. The red solid curve in the T–$n_{\rm tot}$ plane denotes the BEC critical line obtained in the thermodynamic limit, serving as a reference to illustrate how the finite-volume cases approach the ideal behavior as $n_{\rm tot}$ increases.

In the context of heavy-ion collisions, the speed of sound plays a crucial role in characterizing the hydrodynamic evolution of the hot and dense matter produced. It also serves as a valuable probe of the degrees of freedom, as it is directly linked to the underlying equation of state [125]. From a thermodynamic perspective, the speed of sound quantifies the change in pressure to changes in energy density at constant entropy per particle (s/n). Mathematically, it can be written as

$$c_{\rm s}^2(T,\mu) = \left.\frac{\partial P}{\partial \varepsilon}\right|_{s/n}, \tag{2.115}$$

where P and ε are the pressure and energy density and for a pion gas in BEC, these are given as

$$P = -\frac{Tg}{2\pi^2}\int p^2 dp \ln\left[1 - \exp\left(-\frac{\mathrm{E}-\mu}{\mathrm{T}}\right)\right], \tag{2.116}$$

and

$$\varepsilon = \frac{gm}{V[\exp(\frac{m-\mu}{T})-1]} + \int \frac{d^3p}{(2\pi)^3}\frac{gE}{\exp\left(\frac{\sqrt{\mathbf{p}^2+m^2}-\mu}{T}\right)-1} \tag{2.117}$$

Depending on the T and μ dependence of the thermodynamic quantities, the Eq. (2.115) becomes,

$$c_{\rm s}^2(T,\mu) = \frac{\frac{\partial P}{\partial T} + \frac{\partial P}{\partial \mu}\frac{d\mu}{dT}}{\frac{\partial \varepsilon}{\partial T} + \frac{\partial \varepsilon}{\partial \mu}\frac{d\mu}{dT}}, \tag{2.118}$$

where,

$$\frac{d\mu}{dT} = \frac{s\frac{\partial n}{\partial T} - n\frac{\partial s}{\partial T}}{n\frac{\partial s}{\partial \mu} - s\frac{\partial n}{\partial \mu}}. \tag{2.119}$$

Again, the entropy density ($s = \partial P/\partial T$) and specific heat ($c_v = \partial \varepsilon/\partial T$) involved in Eq, (2.118) can be obtained for a pion gas in BEC as,

$$\begin{aligned} s = &- \frac{g}{2\pi^2}\int_0^\infty p^2 dp\Big[\ln\{1-\exp[-(E-\mu)/T]\} \\ &- \frac{T}{\exp[(E-\mu)/T]-1}\Big(\frac{E-\mu+\mu' T}{T^2}\Big)\Big], \end{aligned} \tag{2.120}$$

$$\begin{aligned} c_v = &\frac{g}{V}\frac{m\ \exp[(m-\mu)/T]}{\big(\exp[(m-\mu)/T]-1\big)^2}\Big(\frac{m-\mu+\mu' T}{T^2}\Big) \\ &+ \frac{g}{2\pi^2}\int p^2 dp\Bigg[\frac{E\ \exp[(\sqrt{p^2+m^2}-\mu)/T]}{\big(\exp[(\sqrt{p^2+m^2}-\mu)/T]-1\big)^2} \\ &\times\Big(\frac{E-\mu+\mu' T}{T^2}\Big)\Bigg], \end{aligned} \tag{2.121}$$

where $\mu' = \partial\mu/\partial T$.

Before discussing how the BEC of pion gas affects the speed of sound, let us first study the behavior of individual quantities, such as entropy density and specific heat. The entropy density is the first-order derivative of the pressure with temperature and is therefore sensitive to phase transitions, specifically to the kind of first-order transitions. It may be noted that a first-order phase transition, such as the familiar liquid–gas transition, is identified through a discontinuity in the entropy density at the critical temperature, T_c, due to the underlying interparticle interactions that drive such transitions. On the other hand, in an ideal Bose gas, the Bose–Einstein condensation (BEC) represents a purely quantum-statistical phase transition that originates from the nature of Bose–Einstein statistics rather than from direct interactions. This transition is characterized by an abrupt increase in ground-state occupation below T_c. The temperature dependence of entropy density scaled by the total number density is shown in Fig. 2.14 [124]. In our calculations, we have considered a temperature interval ranging from 5

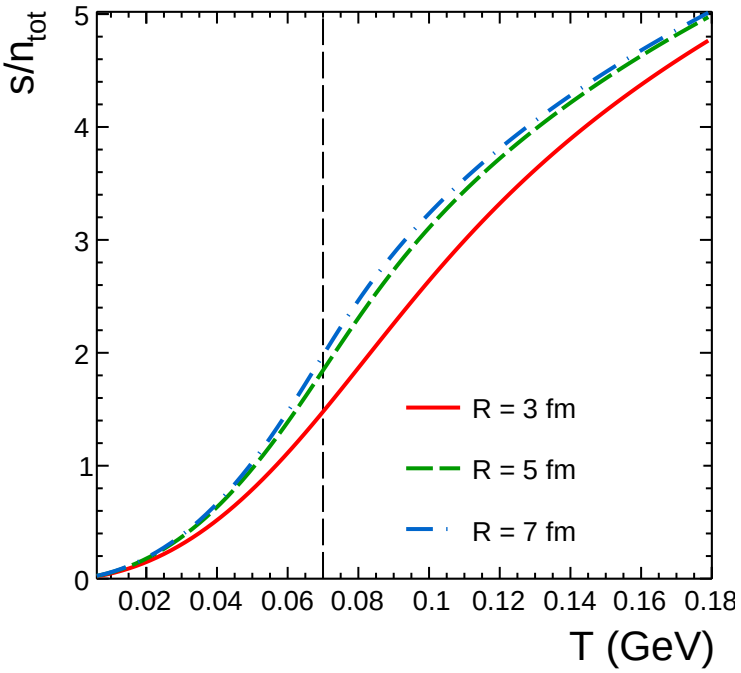

Figure 2.14: Temperature dependence of scaled entropy density, $s/n_{\rm tot}$ for different system sizes with $R = 3$, 5, and 7 fm [124].

MeV to 180 MeV. It is evident that, for all considered system sizes, the entropy density remains very small in the condensed region and increases steadily with temperature. At the critical temperature, the system undergoes a continuous transition without any discontinuity, as expected for a BEC-type phase change. The entropy calculated here corresponds exclusively to the excitations above the ground state.

A similar temperature dependence of entropy was reported in Ref. [126] for an ideal BEC in a three-dimensional trap. Although the ground state possesses a non-zero entropy, the total entropy equals that of the excited states because the contribution from correlations between the ground and excited states, arising from the constraint of fixed total particle number, exactly cancels the ground-state entropy. Thus, the entropy remains continuous across T_c, although with a

change in the slope of the curve. A similar phenomenon is observed in a two-dimensional photon gas confined in an optical cavity [127], where the entropy per photon was found to decrease with T/T_c in accordance with the third law of thermodynamics, matching the ideal Bose gas prediction. Likewise, experiments with two-dimensional atomic gases [128] have shown similar variations. These observations imply that the thermodynamic behavior of a relativistic pion gas undergoing BEC closely resembles that of low-temperature atomic or photonic condensates, reaffirming the universal nature of Bose–Einstein condensation across different physical systems and energy scales.

Another important thermodynamic observable associated with phase transitions is the specific heat per particle. For a Bose gas, the specific heat at constant volume, c_v, exhibits a distinct temperature dependence: it rises with temperature, attains a maximum near the critical point, and then gradually decreases with further increase in T. This produces a characteristic Λ-shaped curve—often referred to as the Λ-transition (as observed in liquid helium [129]). Theoretical analyses [130, 131] as well as experimental studies [127] reveal the presence of a cusp-like singularity in c_v at the critical temperature, T_c. A similar trend is observed for a relativistic pion gas in the thermodynamic limit [115], as illustrated in Fig. 2.15 [124]. For a non-relativistic Bose gas, c_v tends toward the classical limit of 3/2 at high temperatures ($T \gg T_c$) [131], whereas in the relativistic pion gas, it saturates at approximately 3 [115]. As the system volume increases, the peak near T_c becomes more pronounced, and in the thermodynamic limit, a sharp cusp is expected to emerge, consistent with the findings of Ref. [115]. By definition, the pion gas considered here undergoes a continuous (second-order) phase transition to the condensed phase, characterized by a smooth evolution of thermodynamic quantities such as entropy density, without the release or absorption of latent heat [79]. However, this transition in an ideal Bose gas does not exhibit the typical signatures of criticality, such as diverging correlation lengths or higher-order susceptibilities since no interparticle interactions are considered

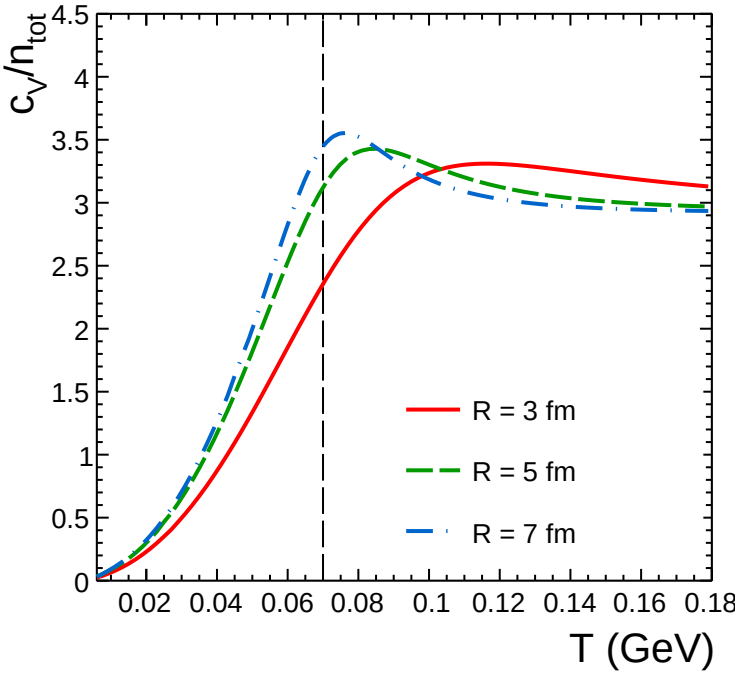

Figure 2.15: Temperature dependence of the scaled specific heat, $c_v/n_{\rm tot}$ for different systems with $R = 3$, 5, and 7 fm [124].

to mediate the long-range correlations. When interactions are introduced, however, the nature of the transition can change. For instance, in harmonically trapped Bose systems with either attractive or repulsive interactions, the condensation may become first-order [132], and similar behavior has been predicted for two-component Bose mixtures with repulsive interactions [133]. The role of interactions in modifying the thermodynamic behavior of the pion gas is further explored in Ref. [119], where the authors studied the impact of repulsive interactions on both the critical temperature and particle number fluctuations. Their analysis reveals that the BEC transition line shifts according to the interaction model, and the onset of condensation occurs at different temperatures in each case.

Let us now discuss the behavior of the speed of sound in a pion gas in the

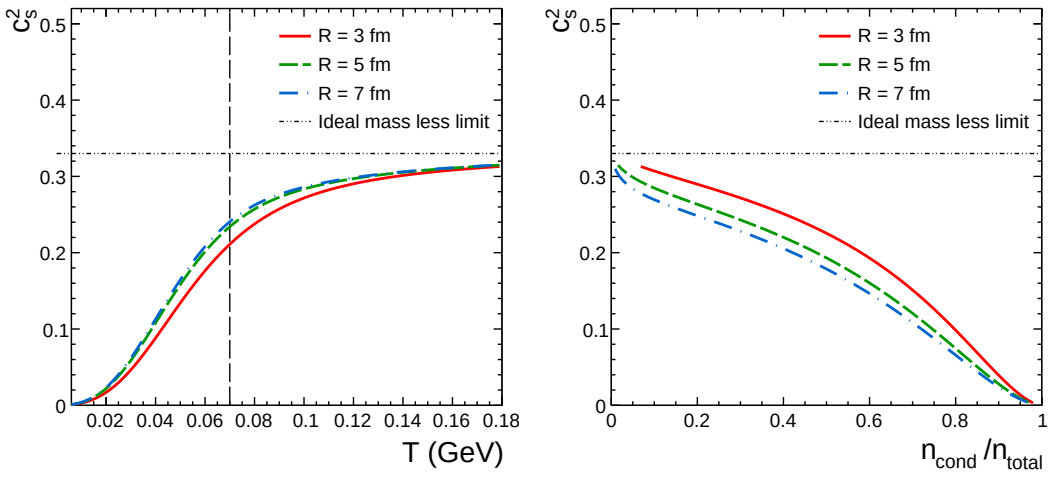

Figure 2.16: Variation of speed of sound with temperature (left panel) and also with the condensate fraction of pions (right panel) is compared for systems with radii $R = 3$, 5, and 7 fm [124].

presence of a condensate. In the left panel of Fig. 2.16, the squared speed of sound, c_s^2, is shown as a function of the temperature, while the right panel shows the variation of c_s^2 with condensate fraction, $n_{\rm cond}/n_{\rm tot}$, for different system sizes [124]. It is evident that c_s^2 decreases progressively as the condensate fraction increases (as T decreases). This behavior can be understood in terms of the softening of the equation of state (EoS) in the Bose–Einstein condensed phase. In a pion BEC, the condensed pions contribute minimally to the pressure, whereas the energy density continues to grow with increasing condensate population. As a result, the system becomes less resistant to compression, leading to a reduction in the squared speed of sound. We will discuss this further in the next section while understanding the transport coefficients in the condensed phase.

2.3.2 Shear and Bulk viscosity of the pion gas in BEC

The study of transport coefficients, specifically shear (η) and bulk (ζ) viscosities, is essential for understanding the dynamical evolution of matter created

in ultra-relativistic nuclear collisions. These quantities provide insight into how momentum and energy are dissipated within the medium. From elliptic flow measurements at RHIC, the ratio of shear viscosity to entropy density (η/s) was found to approach the well-known Kovtun–Son–Starinets (KSS) bound of $1/4\pi$, derived from the AdS/CFT correspondence [39, 41]. The existence of a minimum in η/s near the QCD transition temperature helps us to understand the properties of the exotic matter created in high-energy collisions. In contrast, the bulk viscosity to entropy density ratio (ζ/s) remains relatively less explored, particularly at high temperatures where the system is nearly conformal and $\zeta/s \to 0$. However, near the critical temperature (T_c), conformal symmetry breaks, giving rise to a sharp peak in the trace anomaly, $(\epsilon - 3P)/T^4$, and a corresponding enhancement in ζ/s. This behavior reflects the system's sensitivity to changes in degrees of freedom and the non-conformal dynamics around the QCD phase boundary.

In the context of Bose–Einstein condensation, understanding these dissipative properties becomes even more intriguing. The formation of a condensate modifies the microscopic scattering processes and alters the collective transport behavior of the medium. Previous studies, such as that by Chen *et al.* [134], have shown that in a gluon plasma, the presence of a Bose–Einstein condensate leads to a suppression of shear viscosity. Motivated by these findings, we extend this investigation to a system of pion gas that can undergo condensation under suitable thermodynamic conditions. In this section, we explore how the onset of pion condensation affects both shear and bulk viscosities. The analysis is performed using the Boltzmann transport equation [135] within the relaxation time approximation (RTA) [136], incorporating the thermodynamic features of the Bose–Einstein condensed phase. This study provides valuable insight into how Bose condensation may influence the dissipative evolution of hadronic matter in the late stages of heavy-ion collisions. The RTA simplifies the collision integral in the Boltzmann equation, with its accuracy depending on the chosen ansatz and relaxation time [137]. Other approaches include the Chapman–Enskog (CE) ex-

pansion [102], whose precision improves with higher-order corrections [137, 138], and the Kubo formalism [139], which relates transport coefficients to correlation functions. Comparative studies [137, 140] show that RTA estimates can differ from Green–Kubo or CE results, though CE generally agrees better with Kubo calculations. While the Kubo approach [141, 142] is more fundamental, the RTA offers a practical framework for parametric studies using a simplified model for the collision integral.

In the absence of external force, the relativistic Boltzmann transport equation can be expressed as [124]

$$\frac{\partial f}{\partial t} + v_p^i \frac{\partial f_p}{\partial x^i} = I\{f_p\}, \tag{2.122}$$

where $\vec{v}_p = \vec{p}/E_p$ denotes the single-particle velocity. The rate at which the non-equilibrium distribution function f_p evolves due to collisions among the particles is quantified by the collision integral $I\{f_p\}$. Within the RTA, it is assumed that the return to equilibrium occurs exponentially with a relaxation time that is approximately the order of the collision time. Consequently, the collision integral under RTA takes the simplified form

$$I\{f_p\} \backsimeq -\frac{(f_p - f_p^0)}{\tau(E_p)} = -\frac{\delta f_p}{\tau(E_p)}, \tag{2.123}$$

where $\tau(E_p)$ represents the relaxation time of a particle with energy E_p. Using this one obtains from Eq. (2.122) as

$$\delta f_p = -\tau(E_p)\left(\frac{\partial f_p^0}{\partial t} + v_p^i \frac{\partial f_p^0}{\partial x^i}\right). \tag{2.124}$$

The total distribution function for the system that is slightly away from equilibrium is given by

$$f_p = f_p^0 + \delta f_p. \tag{2.125}$$

where the local equilibrium distribution function f_p^0 for pions is given by

$$f_p^0 = \frac{1}{\exp\left(\frac{E_p - \mathbf{p}.\mathbf{v} - \mu}{T}\right) - 1}, \tag{2.126}$$

where **v** is the fluid velocity. The energy-momentum tensor for an ideal fluid is given by

$$T^{\mu\nu} = \int \frac{d^3p}{(2\pi)^3 E_p} p^\mu p^\nu f_p. \tag{2.127}$$

Extending to a system with $f_p = f_p^0 + \delta f_p$, the total energy-momentum tensor can be written as the sum of an ideal part ($T_0^{\mu\nu}$) and a dissipative part ($T_{diss}^{\mu\nu}$) as

$$T^{\mu\nu} = T_0^{\mu\nu} + T_{dissi}^{\mu\nu}. \tag{2.128}$$

The ideal part, $T_0^{\mu\nu}$ is given by

$$T^{\mu\nu} = (\varepsilon + P)v^\mu v^\nu - Pg^{\mu\nu}, \tag{2.129}$$

where ε and P denotes the energy density and pressure, respectively. The fluid four velocity is given by v^μ. The dissipative part of the energy-momentum tensor has the terms for the viscosities and is given by

$$T_{dissi}^{\mu\nu} = -\eta\big(\nabla^\mu v^\nu + \nabla^\nu v^\mu\big) + (\zeta - \frac{2}{3}\eta)\Delta^{\mu\nu}\nabla_\alpha v^\alpha \tag{2.130}$$

In the local Lorentz frame with $v^\mu = (1, \vec{0})$, the projection tensor $\Delta^{\mu\nu} = g^{\mu\nu} - v^\mu v^\nu$ = diag(0, -1, -1, -1) and $\nabla^\mu = \Delta^{\mu\alpha}\partial_\alpha = \partial^\mu$, the spatial part of the energy-momentum tensor depends linearly on the gradients of the local three-velocity as

$$T_{dissi}^{ij} = -\eta\left(\frac{\partial v^i}{\partial x^j} + \frac{\partial v^j}{\partial x^i}\right) - (\zeta - \frac{2}{3}\eta)\frac{\partial v^i}{\partial x^j}\delta^{ij} \tag{2.131}$$

The Eq. (2.127) can also be written for spatial components as

$$T_{dissi}^{ij} = \int \frac{d^3p}{(2\pi)^3 p^0} p^i p^j \delta f_p \tag{2.132}$$

For the estimation of shear viscosity, we consider a stead flow of the form $v^i = (v_x(y), 0, 0)$ with a space-time independent temperature which results the Eq. (2.131) to reduce to

$$T_{dissi}^{xy} = -\eta\frac{\partial v_x}{\partial y} \tag{2.133}$$

For such a flow, the time derivative in Eq. (2.124) vanishes and δf_p is given as

$$\delta f \simeq -\tau(E_p) v_p^y \frac{\partial f_p^0}{\partial y} = -\tau(E_p) \left(\frac{p_y}{E_p}\right) f_p^0 \frac{p_x}{T} \frac{\partial v_x}{\partial y}. \tag{2.134}$$

Substituting δf_p from this to Eq. (2.132), we obtain T^{xy}_{dissi} as

$$T^{xy}_{dissi} = \int \frac{d^3p}{(2\pi)^3} \frac{p_x p_y}{E_p} \left(-\frac{\tau(E_p)}{T} \frac{p_x p_y}{E_p} \frac{\partial v_x}{\partial y} f_p^0\right). \tag{2.135}$$

Comparing the coefficients of $\partial v_x/\partial y$ from Eq. (2.133) and Eq. (2.135), we get shear viscosity as

$$\boxed{\eta = \frac{1}{15T} \int \frac{d^3p}{(2\pi)^3} \tau(E_p) \frac{p^4}{E_p^2} f_p^0} \tag{2.136}$$

The dissipative transport coefficient that measures the resistance of a system to uniform expansion or compression is the bulk viscosity. From the trace of Eq. (2.132), we get

$$T^{ii}_{diss} = -3\zeta \frac{\partial v^i}{\partial x^i}. \tag{2.137}$$

Hence, in a similar way, Substituting Eq. (2.124) in Eq. (2.127) we get

$$(T_{dissi})^{ii} = -\int \frac{d^3p}{(2\pi)^3} \tau(E_p) \frac{p^2}{E_p} \left(\frac{\partial f_p^0}{\partial t} + v_p^i \frac{\partial f_p^0}{\partial x^i}\right) \tag{2.138}$$

Solving this in local rest frame within the condition of conservation of energy-momentum tensor ($\partial_\mu T^{\mu\nu} = 0$) , one can obtain from above Eqs. (2.137) and (2.138) as

$$\boxed{\zeta = \frac{1}{T} \int \frac{d^3p}{(2\pi)^3} \tau(E_p) f_p^0 \left[E_p c_s^2 - \frac{p^2}{3E_p}\right]^2} \tag{2.139}$$

where single particle energy is given by $E_p^2 = p^2 + m_p^2$, and $c_s^2 = \frac{\partial P}{\partial \varepsilon}$ denotes the squared speed of sound at constant baryon density.

The average relaxation time ($\tau(E_p)$) can be defined as

$$\tau^{-1}(E_a) = \sum_{bcd} \int \frac{d^3p_b}{(2\pi)^3} \frac{d^3p_c}{(2\pi)^3} \frac{d^3p_d}{(2\pi)^3} W(a, b \to c, d) f_b^0 \tag{2.140}$$

where the transition rate $W(a, b \to c, d)$ is

$$W(a, b \to c, d) = \frac{(2\pi)^4 \delta(p_a + p_b - p_c - p_d)}{2E_a 2E_b 2E_c 2E_d} \mid \mathcal{M} \mid^2 \tag{2.141}$$

with $\mid \mathcal{M} \mid$ as the transition amplitude. The Eq. (2.140) is simplified in the center of mass frame as

$$\tau^{-1}(E_a) = \sum_b \int \frac{d^3p_b}{(2\pi)^3}\sigma_{ab}\frac{\sqrt{s-4m^2}}{2E_a 2E_b}f_b^0$$

$$\equiv \sum_b \int \frac{d^3p_b}{(2\pi)^3}\sigma_{ab}v_{ab}f_b^0 \tag{2.142}$$

where the relative velocity is given by v_{ab}. the $\sqrt{s}$ and σ_{ab} are the center of mass energy, and total scattering cross section, respectively.

The $\tau(E_a)$ can be approximated to averaged relaxation time ($\tilde{\tau}$), which one can obtain by averaging Eq. (2.142) over the distribution function, f_a^0 as,

$$\begin{aligned}\tilde{\tau}_a^{-1} &= \frac{\int \frac{d^3p_a}{(2\pi)^3}\tau^{-1}(E_a)f_a^0}{\int \frac{d^3p_a}{(2\pi)^3}f_a^0} \\ &= \sum_b \frac{\int \frac{d^3p_a}{(2\pi)^3}\frac{d^3p_b}{(2\pi)^3}\sigma_{ab}v_{ab}f_a^0 f_b^0}{\int \frac{d^3p_a}{(2\pi)^3}f_a^0} \\ &= \sum_b n_b\langle\sigma_{ab}v_{ab}\rangle.\end{aligned} \tag{2.143}$$

which for a gas of single species (pion gas) can be written as

$$\tilde{\tau}_a^{-1} = n_b\langle\sigma_{ab}v_{ab}\rangle, \tag{2.144}$$

where $n_b = \int \frac{d^3p_b}{(2\pi)^3}f_b^0$ is the number density of pions. $\langle\sigma v\rangle$ is the thermal average cross-section multiplied by the relative velocity. Considering the pions as hard spheres having a constant cross-section, σ, the $\langle\sigma v\rangle$ can be calculated as follows [88, 89],

$$\langle\sigma_{ab}v_{ab}\rangle = \frac{\sigma\int d^3p_a d^3p_b v_{ab}f_a^0 f_b^0}{\int d^3p_a d^3p_b f_a^0 f_b^0} \tag{2.145}$$

where the momentum space volume elements is given as,

$$d^3p_a d^3p_b = 8\pi^2 p_a p_b dE_a dE_b\ dcos\theta. \tag{2.146}$$

The Eq. (2.145) becomes,

$$\langle \sigma_{ab} v_{ab} \rangle = \frac{\sigma \int 8\pi^2 p_a p_b dE_a dE_b \; dcos\theta f_a^0 f_b^0 \frac{\sqrt{(E_a E_b - p_a p_b cos\theta)^2 - (m_a m_b)^2}}{E_a E_b - p_a p_b cos\theta}}{\int 8\pi^2 p_a p_b dE_a dE_b \; dcos\theta f_a^0 f_b^0}. \tag{2.147}$$

σ is the hadronic collision cross-section. We use a constant value of $\sigma = 11.3$ mb [124, 143] for the calculations, which corresponds to pions with a hardcore radius of 0.3 fm. Now, we turn towards the estimation of viscosities for a pion gas in the presence of a BE condensate. The condensate alters the microscopic scattering processes, where one expects two types of collisions: collisions between two excited (non-condensed) particles and collisions between the excited particles and condensate particles. Consequently, the inverse (averaged) relaxation time receives contributions from both kinds of collisions ($\tilde{\tau}_{12}^{-1} + \tilde{\tau}_{22}^{-1}$) [124, 144].

Hence, if the condensate particle density is denoted by n_1 with n_2 for those in the excited state, then the effective relaxation time in a pion gas with BEC can be written as,

$$\tilde{\tau}^{-1} = \tilde{\tau}_{12}^{-1} + \tilde{\tau}_{22}^{-1} \tag{2.148}$$

$$\Rightarrow \boxed{\tilde{\tau}^{-1} = \Big(n_1 \langle \sigma_{12} v_{12} \rangle + n_2 \langle \sigma_{22'} v_{22'} \rangle \Big)}, \tag{2.149}$$

where

$$\langle \sigma_{12} v_{12} \rangle = \frac{\sigma \int d^3p_1 d^3p_2 v_{12} f_1^0 f_2^0}{\int d^3p_1 d^3p_2 f_1^0 f_2^0}. \tag{2.150}$$

$$\langle \sigma_{22'} v_{22'} \rangle = \frac{\sigma \int 8\pi^2 p_2 p_{2'} dE_2 dE_{2'} \; dcos\theta f_2^0 f_{2'}^0 \frac{\sqrt{(E_2 E_{2'} - p_2 p_{2'} cos\theta)^2 - (m_2 m_{2'})^2}}{E_2 E_{2'} - p_2 p_{2'} cos\theta}}{\int 8\pi^2 p_2 p_{2'} dE_2 dE_{2'} \; dcos\theta f_2^0 f_{2'}^0}. \tag{2.151}$$

To investigate the viscous behavior of a pion gas, we employ the Boltzmann transport equation within RTA. This approach can be further generalized through a quasiparticle description, wherein the relevant transport degrees of freedom correspond to thermal excitations possessing medium-modified effective masses. It is essential to note that the Boltzmann equation in RTA effectively captures

the behaviors of thermal (non-condensed) excitations where hadrons have well-defined momenta and masses. However, once the temperature drops below the condensation threshold, the macroscopic condensate behaves as a coherent quantum state. The dynamics of such a state are more appropriately governed by the Gross–Pitaevskii equation (GPE) [144], which describes the collective behavior of the macroscopic wavefunction associated with the fully condensed state. A more complete and self-consistent framework would require coupled equations that account for both condensate and non-condensate interactions, such as the generalized Gross–Pitaevskii and quantum kinetic formulations as in Ref. [144]. Incorporating such effects would lead to a two-fluid description, comprising both the superfluid and normal components, and would give a more clear picture of the properties of the condensate.

In this section, we estimate the shear (η) and bulk (ζ) viscosities of a pion gas under Bose–Einstein condensation using the Boltzmann transport equation in the RTA scheme. This treatment becomes non-trivial since, under BEC conditions, the pion system naturally separates into two interacting subsystems: (i) excited-state pions with finite momentum, and (ii) condensed pions occupying the zero or near-zero momentum ground state. Consequently, two dominant types of collisions emerge: those between excited pions and those between an excited pion and a condensate pion. Therefore, the conventional RTA framework must be modified accordingly to incorporate these two interaction channels.

The dependence of η and ζ on the condensate fraction ($n_{\rm cond}/n_{\rm tot}$), for various system sizes is shown in Fig. 2.17 [124]. These results reveal how the viscous properties evolve as the system becomes increasingly dominated by the condensate component. While the shear viscosity quantifies the resistance to any shape deformation in the fluid, the bulk viscosity measures its opposition to volume changes such as expansion or compression. Together, these transport coefficients significantly influence the anisotropic evolution of the hot matter produced in heavy-ion collisions [145]. From the figure, it can be observed that the viscosities

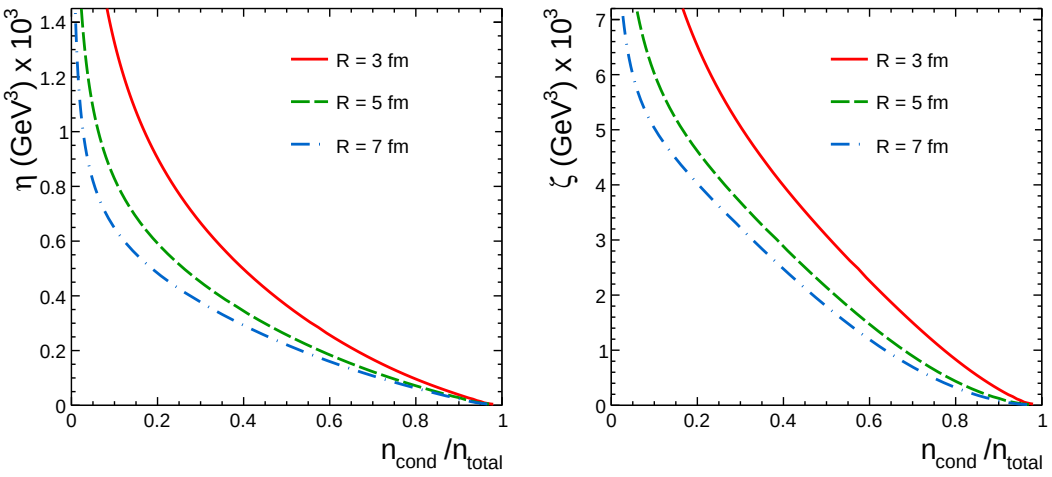

Figure 2.17: Shear viscosity (left panel) and bulk viscosity (right panel) as functions of the condensate fraction of pions compared for different system sizes having $R = 3$, 5, and 7 fm [124].

are higher when a larger fraction of pions occupy excited states. In contrast, as the condensate fraction increases, both η and ζ decrease sharply, approaching nearly zero when most of the pions are in the condensed phase. This suggests that a completely condensed pion system behaves as an inviscid fluid. This observation aligns with the behavior seen in low-temperature Bose–Einstein condensates of cold helium atoms, which are widely known to exhibit superfluidity characterized by an exceptionally small viscosity. Furthermore, an evident dependence on the system size can also be noticed, indicating that finite-size effects play a non-negligible role in determining the viscous properties of the pion condensate. Larger systems show a steeper decrease in η and ζ with increasing $n_{\rm cond}/n_{\rm tot}$, though the trends converge at high condensate fractions. It is important to note that while exploring system-size dependence, it is essential to verify the applicability of the hydrodynamic description. This can be ensured by evaluating the mean free path (λ) and Knudsen number (Kn) [146], with hydrodynamics being suitable for the case when $Kn \ll 1$. For a pion density of 0.1 fm^{-3}, systems

with radii $R = 7$ and 5 fm satisfy this criterion, whereas for $R = 3$ fm, $Kn \sim 1$, implying that such a small system should be considered only for comparative or qualitative studies of finite-size effects.

In Fig. 2.18, the ratio of shear and bulk viscosities to entropy density as a function of temperature is presented for different system sizes [124]. It is observed that for smaller systems, both η/s and ζ/s attain relatively low values in the low-temperature region, where a substantial fraction of pions are in the condensed phase. At higher temperatures, as the number of thermally excited pions increases, their contribution to the transport coefficients becomes dominant. Consequently, the influence of system size on these viscosity ratios diminishes gradually as the temperature increases. In comparison to η/s, the system size dependency is observed more distinctly for ζ/s. A system with a smaller radius corresponds to a higher density, leading to more frequent particle interactions and therefore larger absolute viscosity values, as shown in Fig. 2.17. However, since the entropy density also increases significantly (as indicated in Fig. 2.14), the net effect results in smaller η/s and ζ/s values at low T, which then rise with increasing temperature. A more realistic estimation incorporating interparticle interactions, as well as a coupled treatment using the Boltzmann transport equation and Gross–Pitaevskii framework, may further refine these results. Similar to the shear viscosity, the bulk viscosity is also sensitive to the assumptions of the ideal gas approximation. Various QCD-based models predict that ζ/s exhibits a peak around the QCD critical temperature, arising from strong deviations from conformal symmetry, before decreasing again in the hadronic phase at lower temperatures [147]. In the present study, an enhancement of ζ/s is observed near the BEC transition. However, its sharp suppression at lower temperatures highlights the need for a more detailed understanding of the dissipative behavior in the condensate phase, particularly close to zero temperature, where interactions could play a non-negligible role.

For all system sizes studied, both η/s and ζ/s display an overall increasing

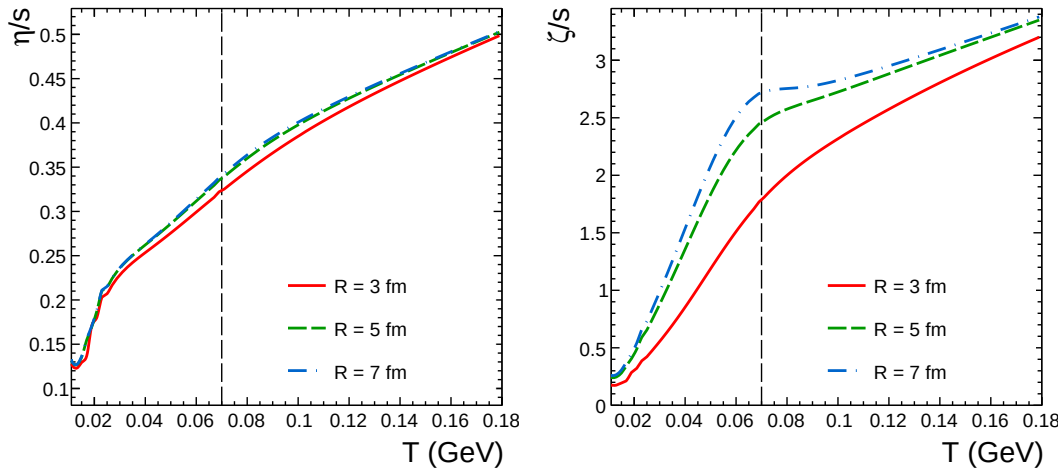

Figure 2.18: Ratio of shear viscosity to entropy density (left panel) and bulk viscosity to entropy density (right panel) as functions of temperature for a pion gas under BEC with different system sizes of $R = 3$, 5, and 7 fm [124].

trend with temperature, with ζ/s consistently having a larger magnitude. These findings suggest that Bose–Einstein condensation significantly alters the viscous behavior of the pion gas, producing a qualitatively distinct temperature dependence compared to a purely thermal (non-condensed) pion gas. The analysis here is performed at a fixed total pion density, which introduces a temperature-dependent chemical potential $\mu(T)$ that decreases with increasing T and strongly influences the observed viscosity ratios. In the absence of a condensate, the transport coefficients are entirely governed by thermal excitations. For instance, Ref. [148] reports that for a pion gas at zero chemical potential, η/s decreases with temperature and approaches the KSS bound, consistent with the findings of Refs. [149–151]. Similarly, the bulk viscosity to entropy density ratio for a pion gas with physical pion mass decreases with temperature below the QCD crossover temperature [152], whereas in the massless pion limit, it shows a peak near the crossover [153]. In another study [154], the bulk and shear viscosities of a pion gas were computed using the Chapman–Enskog formalism, incorporating a

temperature-dependent chemical potential arising from early chemical freeze-out in heavy-ion collisions. The authors found that, unlike the zero μ case where both viscosities decrease with temperature, the inclusion of a temperature-dependent chemical potential results in η/s and ζ/s increasing with T.

As already discussed, we have shown in Fig. 2.16 that the squared speed of sound, c_s^2, is found to decrease with an increasing condensate fraction, even though the viscosities simultaneously drop, as shown in Fig. 2.17. In conventional fluids, a reduction in viscosity is often associated with a stiffer equation of state (EoS) and hence a larger c_s^2, making this behavior quite non-trivial. However, in the case of a pion Bose–Einstein condensate (BEC), the condensed pions contribute minimally to the pressure, while the energy density continues to increase. This results in a softening of the equation of state, manifested as the observed suppression of c_s^2. Such a simultaneous decrease in both viscosity and sound speed, though counterintuitive from the viewpoint of classical hydrodynamics, arises naturally from the quantum statistical nature of the BEC phase. The reduction in viscosity originates from the macroscopic quantum coherence of the system, where a large number of pions occupy the lowest momentum state, thereby suppressing momentum transfer between adjacent fluid layers (affecting shear viscosity) and diminishing the resistance to volume expansion or compression (affecting bulk viscosity). As the condensate fraction grows, the available phase space for dissipative scattering processes, such as π_{excited}–π_{excited} and π_{excited}–π_{cond} collisions shrinks drastically, leading to an overall suppression of viscous effects.

On the other hand, the softening of the EoS and corresponding reduction in c_s^2 reflect the decreasing pressure contribution from the condensate component. This interplay gives rise to a distinct quantum fluid regime, where the system behaves as a nearly dissipationless medium with weakened pressure gradients that influence the propagation of density perturbations. These effects could have potential experimental implications in heavy-ion collisions, particularly in the transverse momentum (p_{T}) dependence of elliptic flow and freeze-out dynamics at LHC and

RHIC energies. A reduced pressure gradient, coupled with near-inviscid behavior, may suppress collective flow observables, such as elliptic flow (v_2). Investigating event-by-event fluctuations in the azimuthal distribution, especially in the low-p_{T} region, could provide insights into such behavior. Although the low-p_{T} part of the pion spectra is often dominated by resonance decays, high-purity pion measurements in this region may reveal enhancements linked to the presence of a condensate. These effects are expected to be particularly sensitive to finite-size modifications of the BEC critical temperature (T_c) and could offer experimental evidence of Bose–Einstein condensation in high-energy nuclear collisions.

Chapter 3

Effect of rotation on the thermodynamic properties of hadron gas

The QCD phase diagram is primarily described in terms of two thermodynamic parameters, temperature T and baryochemical potential μ_B, as discussed earlier in Chapter 1. Determining the precise location of the phase boundary separating the confined hadronic phase from the deconfined quark-gluon phase, along with identifying a possible critical point in the T–μ_B plane, remains one of the central pursuits of research among the high-energy physics community. At zero μ_B, the transition from hadronic matter to the partonic degrees of freedom is marked by a smooth but rapid change in the thermodynamic quantities as calculated using lQCD simulations. However, at higher values of μ_B, the transition is expected to become first order, characterized by a discontinuity or divergence in one or more thermodynamic quantities at a specific temperature, referred to as the critical temperature. Typical thermodynamic observables such as number density, entropy density, and specific heat exhibit sharp variations or discontinuities at this point, indicating the presence of a real phase transition. In contrast, for a crossover transition, no single temperature defines the transition. Instead, these observables display rapid variations (for densities) or pronounced peaks (for response functions such as heat capacity) over a narrow temperature range,

reflecting the broadness of the transition. External fields can further influence the nature and location of such phase transitions. For instance, the presence of a strong magnetic field modifies the particle dispersion relations and alters the density of states, thereby affecting both the phase transition behavior and the position of the critical point [155]. The recent discovery of finite vorticity (or rotation) production in peripheral heavy-ion collisions [51] adds an extra dimension to our exploration of the QCD phase diagram. Even though a great amount of angular momentum is carried by the spectator nucleons just after collision, a significant measurable rotation is still observed of the order of 10^{-2} GeV ($\sim 10^{21}$ s^{-1}) [51, 156]. The properties of QCD matter, and the phase transitions can be affected non-trivially by the system's rotation. Indeed, theoretical studies propose the existence of an additional critical point in the T–ω plane, where ω denotes the angular velocity of the rotating system [61]. This suggests revisiting the properties of QCD matter under the combined influence of rotation and magnetic fields, particularly in systems with high baryon densities.

Motivated by these developments, this chapter focuses on the role of rotation in shaping the thermodynamic behavior of a hadronic medium. The van der Waals hadron resonance gas (VDWHRG) model is employed to explore the first-order liquid–gas phase transition under rotational influence. This study aims to provide an understanding of how the presence of rotation can modify the QCD phase transition, as well as the potential shift in the QCD critical point. We first analyze the effect of rotation on the thermodynamics of a rotating hadron gas, and subsequently, we examine how rotation impacts the liquid-gas phase transition in this framework. In addition, we examine the fundamental properties of Bose–Einstein condensation in a rotating medium. Possible modifications to the conditions required for BEC in the presence of finite rotation are analyzed. In principle, this study demonstrates that rotation acts analogously to an effective chemical potential, leading to significant modifications of the phase structure and phase transitions of the QCD matter under consideration [157, 166].

3.1 Thermodynamic properties under rotation

We consider a relativistic system composed of fermionic and bosonic particles, each with spin quantum number S, confined in a large but finite volume V, and rotating uniformly with constant angular velocity $\boldsymbol{\omega}$ about a fixed axis. The local thermodynamic equilibrium is described by the rotating grand canonical ensemble, where the equilibrium density operator incorporates contributions from conserved energy, charge, and angular momentum. The presence of $\boldsymbol{\omega}$ introduces a coupling between the rotation and the intrinsic spin degrees of freedom of the particles, leading to spin polarization and a modification of the energy spectrum through the term $-\boldsymbol{\omega}\cdot\widehat{\mathbf{J}}$. Following the formalism as in Ref. [158–163], we start with the density operator for a relativistic system in global thermodynamic equilibrium with rotation, which can be written as

$$\widehat{\rho}_{\omega} = \frac{1}{Z_{\omega}} \exp[-(\widehat{H} - \mu\widehat{Q} - \boldsymbol{\omega}\cdot\widehat{\mathbf{J}})/T]\mathsf{P}_V, \tag{3.1}$$

where the $\widehat{H}$, $\widehat{Q}$, and $\widehat{\mathbf{J}}$ denote the Hamiltonian, conserved charge, and angular momentum operator, respectively. The parameter μ represents the chemical potential, whereas the angular velocity is denoted by ω. The corresponding partition function in the rotating grand canonical ensemble Z_{ω} is given as

$$Z_{\omega} = \mathrm{tr}\{\exp[(-\widehat{H} + \mu\widehat{Q} + \boldsymbol{\omega}\cdot\widehat{\mathbf{J}})/T]\mathsf{P}_V\}. \tag{3.2}$$

where the P_V is called the projector onto a localized state $|h_V\rangle$ (or localized region). In a non-relativistic system, thermodynamic equilibrium under rotation can be maintained only if the rotation is rigid [158, 160]. This condition implies that the angular velocity vector, $\boldsymbol{\omega}$, remains uniform across the entire system of characteristic size x, giving rise to a rigid body velocity field described by $\mathbf{v} = \boldsymbol{\omega}\times\mathbf{x}$. When extended to a relativistic framework, an additional requirement must be satisfied to preserve causality, expressed as $|\boldsymbol{\omega}\times\mathbf{x}| \ll 1$ in natural units. As rigid rotation at finite angular velocity ω is not possible for all space, the

projector P_V is introduced to describe such a physically meaningful state. It restricts the Hilbert space to the degrees of freedom within a finite localized volume V with $\mathsf{P}_V = \sum_{h_V} |h_V\rangle\langle h_V|$.

The partition function given in Eq. (3.2) can be factorized into a product of single-particle partition functions. Consequently, the evaluation of Eq. (3.2) reduces to computing the matrix elements of single-particle operators that are compatible with the system's conserved quantities, such as $\widehat{h}$, $\widehat{q}$, and $\widehat{\mathbf{j}}$ [158, 159]

$$\begin{aligned}&\langle p_\pm, \tau_\pm| \exp[-(\widehat{h} + \mu\widehat{q} + \omega \cdot \widehat{\mathbf{j}})/T]\mathsf{P}_V|p_\pm, \sigma_\pm\rangle \\ &= (\mathrm{e}^{(\epsilon-\mu q)/T} \pm 1)^{-1}\langle p_\pm, \tau_\pm| \exp[\omega \cdot \widehat{\mathbf{j}}/T]\mathsf{P}_V|p_\pm, \sigma_\pm\rangle,\end{aligned} \tag{3.3}$$

Here, $p_\pm$ denotes the four-momentum, while $\sigma_\pm$ and $\tau_\pm$ represent the polarization states of the particles. The symbols $\pm$ correspond to fermions and bosons, respectively. To evaluate the rotational contribution, an analytical continuation is employed from imaginary values of ω on the right-hand side of Eq. (3.3). By substituting ω/T with $-i\phi$, one obtains a rotation $\mathsf{R}_{\hat{\omega}}(\phi)$ about the axis defined by ω through an angle ϕ, the above equation becomes

$$\langle p_\pm, \tau_\pm| \exp[\omega \cdot \widehat{\mathbf{j}}/T]\mathsf{P}_V|p_\pm, \sigma_\pm\rangle = \langle p_\pm, \tau_\pm|\mathsf{R}_{\hat{\omega}}(\phi)\mathsf{P}_V|p_\pm, \sigma_\pm\rangle. \tag{3.4}$$

Let us expand the matrix element on the right-hand side of above equation. We have

$$\langle p_\pm, \tau_\pm|\mathsf{R}_{\hat{\omega}}(\phi)\mathsf{P}_V|p_\pm, \sigma_\pm\rangle = \sum_{\sigma'_\pm} \int d^3\mathrm{p}'\ \langle p_\pm, \tau_\pm|\widehat{\mathsf{R}}_{\hat{\omega}}(\phi)|p'_\pm, \sigma'_\pm\rangle\langle p'_\pm, \sigma'_\pm|\mathsf{P}_V|p_\pm, \sigma_\pm\rangle. \tag{3.5}$$

Using Dirac's Delta and Wigner matrix, the matrix element of rotation becomes

$$\langle p_\pm, \tau_\pm|\widehat{\mathsf{R}}_{\hat{\omega}}(\phi)|p'_\pm, \sigma'_\pm\rangle = \delta^3\left(\mathbf{p}_\pm - \mathsf{R}_{\hat{\omega}}(\phi)(\mathbf{p}_\pm{}')\right) D^S([\mathsf{R}_{\hat{\omega}}(\phi)(p'_\pm)]^{-1}\mathsf{R}_{\hat{\omega}}(\phi)[p'_\pm])_{\tau_\pm\sigma'_\pm}, \tag{3.6}$$

whereas determining the P_V matrix elements is not trivial, and a quantum field

theory framework is used for the calculations [158, 162] to obtain

$$\begin{aligned}&\langle p'_{\pm},\sigma'_{\pm}|\mathsf{P}_V|p_{\pm},\sigma_{\pm}\rangle\\&=\frac{1}{2}\sqrt{\frac{\varepsilon}{\varepsilon'}}\int_V d^3\mathrm{x}\,\mathrm{e}^{i\mathbf{x}\cdot(\mathbf{p}_{\pm}-\mathbf{p}_{\pm}')}\left(D^S([p'_{\pm}]^{-1}[p_{\pm}])+D^S([p'_{\pm}]^{\dagger}[p_{\pm}]^{\dagger-1})\right)_{\sigma'_{\pm}\sigma_{\pm}}\langle 0|\mathsf{P}_V|0\rangle,\end{aligned}\tag{3.7}$$

where the vacuum expectation value of the projector P_V, $\langle 0|\mathsf{P}_V|0\rangle$ tends to 1 in the large volume limit as $\mathsf{P}_V\to 1$. The $[p_{\pm}]$ is defined as a Lorentz transformation that takes the time-like component $m\hat{t}=(m,0,0,0)$ to p [158]. The $(2S+1)$ dimensional SL(2, C) matrx is denoted by D^S. Using Eqs. (3.6) and (3.7), the Eq. (3.5) can be written as

$$\begin{aligned}\langle p_{\pm},\tau_{\pm}|\widehat{\mathsf{R}}_{\hat{\omega}}(\phi)\mathsf{P}_V|p_{\pm},\sigma_{\pm}\rangle&=\frac{1}{2}\int_V d^3\mathrm{x}\,\mathrm{e}^{i\mathbf{x}\cdot(\mathbf{p}_{\pm}-\mathsf{R}_{\hat{\omega}}(\phi)^{-1}(\mathbf{p}_{\pm}))}\\&\times\left(D^S([p_{\pm}]^{-1}\mathsf{R}_{\hat{\omega}}(\phi)[p_{\pm}])+D^S([p_{\pm}]^{\dagger}\mathsf{R}_{\hat{\omega}}(\phi)[p_{\pm}]^{\dagger-1})\right)_{\tau_{\pm}\sigma_{\pm}}\end{aligned}\tag{3.8}$$

We can use the unitarity property of the Wigner rotation, i.e.,

$$D^S([\mathsf{R}_{\hat{\omega}}(\phi)(p'_{\pm})]^{-1}\mathsf{R}_{\hat{\omega}}(\phi)[p'_{\pm}])=D^S([\mathsf{R}_{\hat{\omega}}(\phi)(p'_{\pm})]^{\dagger}\mathsf{R}_{\hat{\omega}}(\phi)[p'_{\pm}]^{\dagger-1}),\tag{3.9}$$

Then the analytical continuation of Eq. (3.8) to imaginary rotation angles leads to the final form of the matrix element appearing in Eq. (3.3), and can be written as

$$\begin{aligned}\langle p_{\pm},\tau_{\pm}|\exp[\omega\cdot\widehat{\mathbf{j}}/T]\mathsf{P}_V|p_{\pm},\sigma_{\pm}\rangle&=\frac{1}{2}\int_V d^3\mathrm{x}\,\mathrm{e}^{i\mathbf{x}\cdot(\mathbf{p}_{\pm}-\mathsf{R}_{\hat{\omega}}(i\omega/T)^{-1}(\mathbf{p}_{\pm}))}\\&\times\left(D^S([p_{\pm}]^{-1}\mathsf{R}_{\hat{\omega}}(i\omega/T)[p_{\pm}])+D^S([p_{\pm}]^{\dagger}\mathsf{R}_{\hat{\omega}}(i\omega/T)[p_{\pm}]^{\dagger-1})\right)_{\tau_{\pm}\sigma_{\pm}}\end{aligned}\tag{3.10}$$

The matrix element obtained in the above Eq. (3.10) is the prime component to obtain the equilibrium single-particle phase space distribution, which underlies

the further thermodynamic description of the system. We can express the corresponding phase-space distribution using the spatial integral representation of Eq. (3.3) as

$$\begin{aligned} f(\mathbf{x},\mathbf{p})_{\tau_\pm\sigma_\pm} =& (e^{(\varepsilon-\mu q)/T}\pm 1)^{-1} \mathrm{e}^{i\mathbf{x}\cdot(\mathbf{p}_\pm - \mathsf{R}_{\hat{\omega}}(i\omega/T)^{-1}(\mathbf{p}_\pm))} \\ & \times \frac{1}{2}\left(D^S([p_\pm]^{-1}\mathsf{R}_{\hat{\omega}}(i\omega/T)[p_\pm]) + D^S([p_\pm]^\dagger \mathsf{R}_{\hat{\omega}}(i\omega/T)[p_\pm]^{\dagger-1})\right)_{\tau_\pm\sigma_\pm} \end{aligned} \tag{3.11}$$

Along with the causality condition, for a macroscopic system, and hence, for a realistic scenario, the ratio of ω to T is small, i.e., $\hbar\omega/k_BT \ll 1$. Consequently, the momentum difference appearing in the exponent of Eq. (3.11) can be approximated, to the leading order in ω/T, as

$$\begin{aligned} &\mathbf{p}_\pm - \mathsf{R}_{\hat{\omega}}(i\omega/T)^{-1}(\mathbf{p}_\pm) \\ &\quad = \mathbf{p}_\pm - \left[\cosh\frac{\omega}{T}\,\mathbf{p}_\pm - i\sinh\frac{\omega}{T}\,\hat{\omega}\times\mathbf{p}_\pm + (1-\cosh\frac{\omega}{T})\,\mathbf{p}_\pm\cdot\hat{\omega}\hat{\omega}\right] \\ &\quad \simeq i\frac{\omega}{T}\hat{\omega}\times\mathbf{p}_\pm \end{aligned} \tag{3.12}$$

Hence, using $\mathbf{v} = \omega\times\mathbf{x}$, the phase-space distribution function in Eq. (3.11) becomes

$$\begin{aligned} f(\mathbf{x},\mathbf{p}_\pm)_{\tau_\pm\sigma_\pm} =& (e^{(\varepsilon-\mu q)/T}\pm 1)^{-1} e^{-\mathbf{x}\cdot(\omega\times\mathbf{p}_\pm)/T} \\ & \times \frac{1}{2}\left(D^S([p_\pm]^{-1}\mathsf{R}_{\hat{\omega}}(i\omega/T)[p_\pm]) + D^S([p_\pm]^\dagger \mathsf{R}_{\hat{\omega}}(i\omega/T)[p_\pm]^{\dagger-1})\right)_{\tau_\pm\sigma_\pm} \\ =& (e^{(\varepsilon-\mu q)/T}\pm 1)^{-1} e^{\mathbf{p}_\pm\cdot(\omega\times\mathbf{x})/T} \\ & \times \frac{1}{2}\left(D^S([p_\pm]^{-1}\mathsf{R}_{\hat{\omega}}(i\omega/T)[p_\pm]) + D^S([p_\pm]^\dagger \mathsf{R}_{\hat{\omega}}(i\omega/T)[p_\pm]^{\dagger-1})\right)_{\tau_\pm\sigma_\pm} \\ =& (e^{(\varepsilon-\mu q)/T}\pm 1)^{-1} e^{(\mathbf{p}_\pm\cdot\mathbf{v})/\mathbf{T}} \\ & \times \frac{1}{2}\left(D^S([p_\pm]^{-1}\mathsf{R}_{\hat{\omega}}(i\omega/T)[p_\pm]) + D^S([p_\pm]^\dagger \mathsf{R}_{\hat{\omega}}(i\omega/T)[p_\pm]^{\dagger-1})\right)_{\tau_\pm\sigma_\pm} \end{aligned} \tag{3.13}$$

This is the unnormalized single-particle phase-space distribution for an ideal rotating relativistic gas of fermions and bosons. To obtain the properly normalized

phase-space distribution in $(\mathbf{x}, \mathbf{p})$ space, one must take the trace of this matrix over the spin indices as [158]

$$\boxed{f(\mathbf{x},\mathbf{p}) = \sum_{\sigma_\pm} f(\mathbf{x},\mathbf{p})_{\sigma_\pm\sigma_\pm} = (e^{(\varepsilon-\mu q)/T} \pm 1)^{-1} e^{(\mathbf{p}\cdot\mathbf{v})/\mathbf{T}} \chi\Big(\frac{\omega}{T}\Big)}, \tag{3.14}$$

with

$$\chi\Big(\frac{\omega}{T}\Big) \equiv \mathrm{tr}\left[D^S(\mathsf{R}_{\hat{\omega}}(i\omega/T))\right] = \frac{\sinh(S+\frac{1}{2})\frac{\omega}{T}}{\sinh(\frac{\omega}{2T})}, \tag{3.15}$$

Using this single-particle distribution function, we can write the pressure for a single hadronic species in a rotating hadron gas as

$$P_i^{id}(T,\omega,\mu_i) = \frac{g_i}{2\pi^2}\int_0^\infty p^2 dp \frac{p^2}{3E_i} \frac{e^{(\mathbf{p}\cdot\mathbf{v})/\mathbf{T}}}{\exp[(E_i-\mu_i)\pm 1]} \chi\Big(\frac{\omega}{T}\Big), \tag{3.16}$$

with $\chi(\frac{\omega}{T})$ as in the Eq. (3.15). In accordance with the causality condition, the spatial dependence is safely neglected by considering a fixed system size, $x = R =$ 5 fm, throughout the analysis. Additionally, for the range of ω considered here, the corresponding Lorentz factor remains very close to unity and, therefore, is neglected in the present formalism. The total pressure of the rotating hadron gas is then obtained by summing over the contributions from all hadronic species, as

$$P = \sum_i P_i^{id}. \tag{3.17}$$

Other thermodynamic quantities such as energy density ε_i, number density n_i, and entropy density s_i, for a single hadronic species can be written as

$$\varepsilon_i^{id}(T,\omega,\mu_i) = \frac{g_i}{2\pi^2}\int_0^\infty \frac{E_i\, p^2 dp\; e^{(\mathbf{p}\cdot\mathbf{v})/\mathbf{T}}}{\exp[(E_i-\mu_i)/T]\pm 1}\chi(\frac{\omega}{T}) \tag{3.18}$$

$$n_i^{id}(T,\omega,\mu_i) = \frac{g_i}{2\pi^2}\int_0^\infty \frac{p^2 dp\; e^{(\mathbf{p}\cdot\mathbf{v})/\mathbf{T}}}{\exp[(E_i-\mu_i)/T]\pm 1}\chi(\frac{\omega}{T}) \tag{3.19}$$

$$\begin{aligned} s_i^{id}(T,\omega,\mu_i) = \pm\frac{g_i}{2\pi^2}\int_0^\infty p^2 dp\; \frac{p^2}{3E_i}\frac{e^{(\mathbf{p}\cdot\mathbf{v})/\mathbf{T}}}{\exp[(E_i-\mu_i)/T]\pm 1} \\ \times\left[\frac{1}{T^2}\Big(\frac{(E_i-\mu_i)}{1\pm\exp[\frac{-(E_i-\mu_i)}{T}]} - \mathbf{p}\cdot\mathbf{v}\Big)\chi(\frac{\omega}{\mathbf{T}}) \right. \\ \left. + \frac{\partial}{\partial\omega}\chi\Big(\frac{\omega}{T}\Big)\right] \end{aligned} \tag{3.20}$$

It is noteworthy that we will estimate different thermodynamic quantities in an interacting system in the presence of rotation. The various thermodynamic observables like pressure, number density, energy density, etc., are estimated in the VDWHRG model as discussed in Chapter 2. Therefore, we can write pressure in VDWHRG as

$$P_M(T,\omega,\mu) = \sum_{i\in M} P_i^{id}(T,\omega,\mu^{*M}), \tag{3.21}$$

$$P_B(T,\omega,\mu) = \sum_{i\in B} P_i^{id}(T,\omega,\mu^{*B}) - an_B^2(T,\omega,\mu), \tag{3.22}$$

$$P_{\bar{B}}(T,\omega,\mu) = \sum_{i\in \bar{B}} P_i^{id}(T,\omega,\mu^{*\bar{B}}) - an_{\bar{B}}^2(T,\omega,\mu). \tag{3.23}$$

The pressure due to mesons, baryons, and anti-baryons is given by $P_M(T,\omega,\mu)$, $P_B(T,\omega,\mu)$, and $P_{\bar{B}}(T,\omega,\mu)$, respectively. The total pressure due to the hadron gas in VDWHRG with rotation is then written as

$$P(T,\omega,\mu) = P_M(T,\omega,\mu) + P_B(T,\omega,\mu) + P_{\bar{B}}(T,\omega,\mu), \tag{3.24}$$

The number density for mesons and (anti)baryons is given as

$$n_M(T,\omega,\mu) = \frac{\sum_{i\in M} n_i^{id}(T,\omega,\mu^{*M})}{1+b\sum_{i\in M} n_i^{id}(T,\omega,\mu^{*M})}, \tag{3.25}$$

$$n_{B(\bar{B})}(T,\omega,\mu) = \frac{\sum_{i\in B(\bar{B})} n_i^{id}(T,\omega,\mu^{*B(\bar{B})})}{1+b\sum_{i\in B(\bar{B})} n_i^{id}(T,\omega,\mu^{*B(\bar{B})})}. \tag{3.26}$$

The modified chemical potential because of interaction μ^* for mesons and baryons is given respectively as

$$\mu^{*M} = -bP_M(T,\omega,\mu), \tag{3.27}$$

$$\mu^{*B(\bar{B})} = \mu_{B(\bar{B})} - bP_{B(\bar{B})}(T,\omega,\mu) - abn_{B(\bar{B})}^2(T,\omega,\mu) + 2an_{B(\bar{B})}(T,\omega,\mu), \tag{3.28}$$

In a similar way, we can obtain entropy density ($s(T,\omega,\mu)$), energy density ($\varepsilon(T,\omega,\mu)$), as in Chapter 2, along with the specific heat ($c_V = \partial\varepsilon/\partial T$) and speed of sound ($c_s^2 = \partial P/\partial\varepsilon$) in the VDWHRG model for a rotating hadron resonance gas. All the experimentally established hadrons and resonances up to

mass 2.25 GeV from PDG [5] are employed in the analysis. We use the same VDW parameters a and b as in Chapter 2, i.e., $a = 0.926$ MeV fm^3 and $b = (16/3)\pi r^3$, r being the hardcore radius of each hadron (for mesons, $r_M = 0.2$ fm and for (anti)baryons $r_{B(\bar{B})} = 0.62$ fm). It is important to note that, in principle, the van der Waals parameters should depend on the system's rotation. However, since treating a and b as explicit functions of ω is non-trivial, this dependence is neglected in the present study. Furthermore, in a rotating medium, quantities such as pressure may, in general, exhibit anisotropy, with possible components parallel and perpendicular to the angular momentum vector. Nevertheless, for simplicity and in line with several previous works [156, 164, 165], all thermodynamic observables in this formalism are assumed to remain isotropic throughout the medium.

Figure 3.1 displays the temperature evolution of several scaled thermodynamic observables, namely P/T^4, ε/T^4, s/T^3, $(\varepsilon - 3P)/T^4$, c_v/T^3, and the squared speed of sound $c_{\rm s}^2$, evaluated at vanishing baryochemical potential for different magnitudes of the angular velocity ω [166]. The red triangles represent lQCD results from the Wuppertal–Budapest collaboration [167], whereas the shaded bands denote the corresponding calculations from the HotQCD collaboration [10], both evaluated at $\mu_B = 0.0$ GeV. All model calculations in this study are also performed for $\mu_B = 0.0$ GeV. The solid black curve shows the results obtained for $\omega = 0$ fm^{-1} and is in good agreement with the estimations from lQCD.

It is evident that P/T^4 in the upper left panel of Fig. 3.1 increases monotonically with temperature for all values of ω, with a higher angular velocity corresponding to larger P/T^4 values at a given temperature. Similar behavior is observed for ε/T^4, s/T^3, $(\varepsilon - 3P)/T^4$, and c_v/T^3, though the slopes of these quantities differ, reflecting the distinct sensitivities of each observable to rotation. A clear peak is seen for the trace anomaly ($(\varepsilon - 3P)/T^4$), which shifts towards lower temperatures as ω increases. This peak signals conformal symmetry breaking, marking the regime where the effective masses of the constituent particles

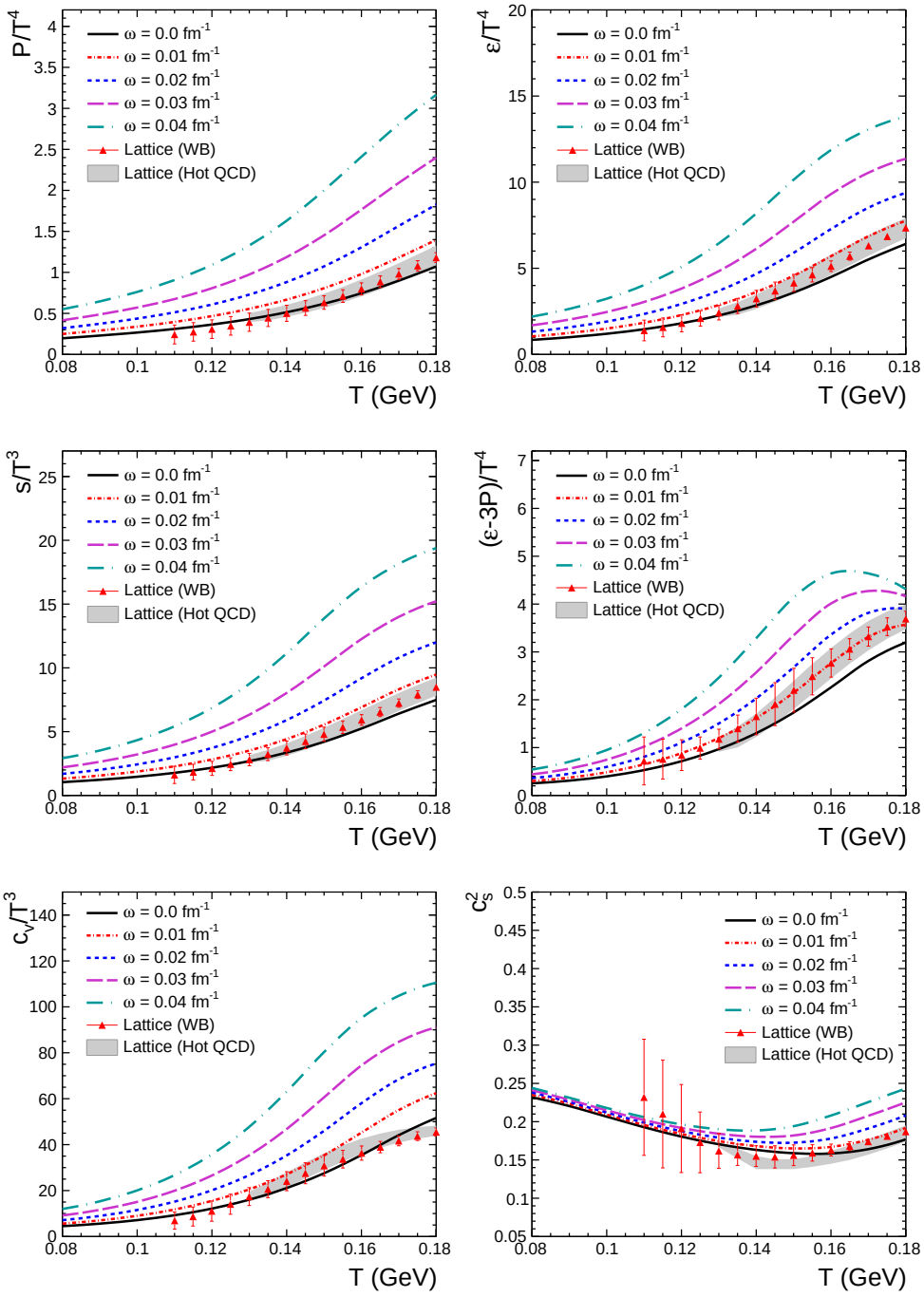

Figure 3.1: Temperature dependence of various thermodynamic observables at $\mu_B = 0$ GeV for distinct values of the rotation ω [166]. Results are compared with lQCD results from the Wuppertal–Budapest [167], and HotQCD [10] collaboration.

approach zero. The behavior of the squared speed of sound, c_s^2, provides additional insight into the phase transition dynamics. Within the VDWHRG framework, c_s^2 exhibits a distinct minimum, consistent with lQCD findings, which can be interpreted as an indicator of the transition from hadronic to partonic degrees of freedom. As the rotational chemical potential increases, the minimum systematically shifts towards lower temperatures, indicating that the effective phase transition temperature decreases in the presence of rotation.

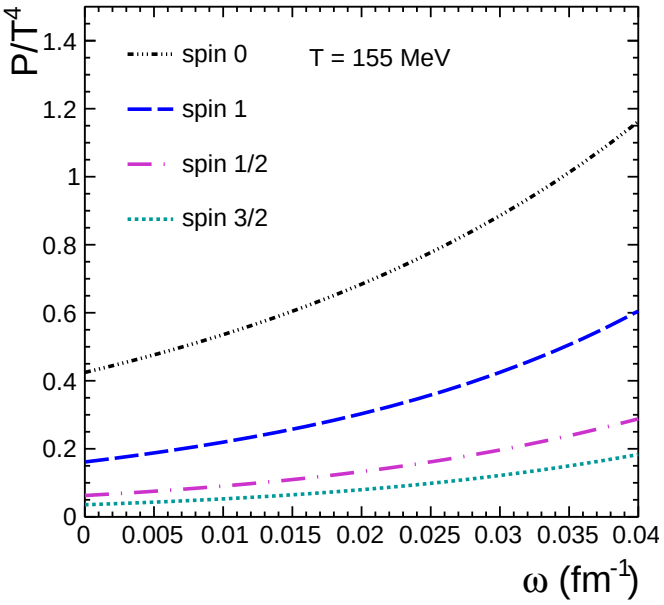

Figure 3.2: Scaled pressure as a function of angular velocity, ω, for particles with different spin values at a fixed temperature of $T = 155$ MeV [166].

To examine how spin and rotation influence the thermodynamic behavior of the system, the scaled pressure is shown as a function of ω for particles with different spin values in Fig. 3.2 at a constant temperature, $T = 155$ MeV. It can be seen that the pressure is predominantly contributed by spin-0 particles, followed in order by those with spin-1, spin-1/2, and spin-3/2. This hierarchy originates from the Boltzmann factor in the single-particle distribution, where lighter par-

ticles yield a stronger contribution. Consequently, the spin-0 mesons, such as pions and kaons, have the largest contribution to the total pressure, followed by vector mesons like ρ and η. The spin-1/2 baryons (e.g., protons and neutrons) and spin-3/2 baryons (e.g., Λ, Ξ) contribute progressively less. Furthermore, as the angular velocity ω increases, the overall pressure from each spin sector rises correspondingly, consistent with the rotational enhancement already discussed.

In addition to these, we evaluate another density associated with the system's angular velocity (the so-called rotational chemical potential, ω), referred to as the spin density. When rotation is introduced into the medium, the Euler relation connecting various thermodynamic quantities is modified as [168],

$$\varepsilon + P = sT + n\mu + \mathrm{w}\omega, \tag{3.29}$$

where w denotes the spin density. Consequently, the spin density can be obtained as

$$\begin{aligned} \mathrm{w} = \left.\frac{\partial P}{\partial \omega}\right|_{T,\mu} &= \pm\frac{g_i}{2\pi^2}\int_0^\infty p^2 dp\ \frac{p^2}{3E_i}\ \frac{e^{(\mathbf{p}\cdot\mathbf{v})/\mathbf{T}}}{\exp[(E_i-\mu_i)/T} \\ &\times \Big[\frac{1}{T}px\ \chi\Big(\frac{\omega}{T}\Big) + \frac{\partial}{\partial\omega}\chi\Big(\frac{\omega}{T}\Big)\Big]. \end{aligned} \tag{3.30}$$

Fig. 3.3 illustrates the temperature dependence of the dimensionless, normalized spin density calculated within the VDWHRG framework using Eq. (3.30). Analogous to the number density, which is obtained as the derivative of pressure (or free energy) with respect to the chemical potential, the spin density is determined by differentiating the pressure with respect to the rotational chemical potential. Physically, the net spin density represents the imbalance between hadrons whose spins are aligned parallel and antiparallel to the direction of rotation. It is evident from the figure that, similar to other thermodynamic densities such as number and entropy densities, the spin density rises with increasing temperature. Furthermore, for a fixed temperature, as the rotational chemical potential increases, the spin density also rises.

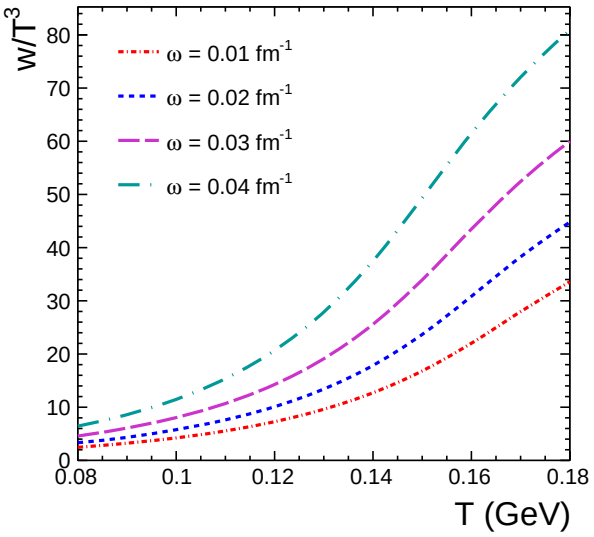

Figure 3.3: Temperature dependence of Net spin density ($W = \partial P/\partial\omega$) for distinct values of ω [166].

We further compute the susceptibilities corresponding to various conserved charges to examine how they respond to changes in the rotational chemical potential. Fluctuations of conserved charges, such as net baryon number, electric charge, and strangeness, serve as sensitive probes of the hadronization process and play a crucial role in identifying possible phase boundaries. Enhanced fluctuations in these observables are commonly regarded as a crucial indicator of proximity to the QCD critical endpoint. As rotation is expected to affect the phase transition and the position of the associated critical point, it is therefore essential to examine how rotational effects influence the fluctuations of conserved charges. The nth order susceptibilities of these conserved quantities are obtained from the successive derivatives of the VDW pressure with respect to the relevant chemical potentials and are defined as

$$\chi_x = \frac{\partial^n (P/T^4)}{\partial(\mu_x/T)^n}, \tag{3.31}$$

where x denotes the conserved charge under consideration, namely, the baryon

number, electric charge, or strangeness. We evaluate the second-order suscepti-

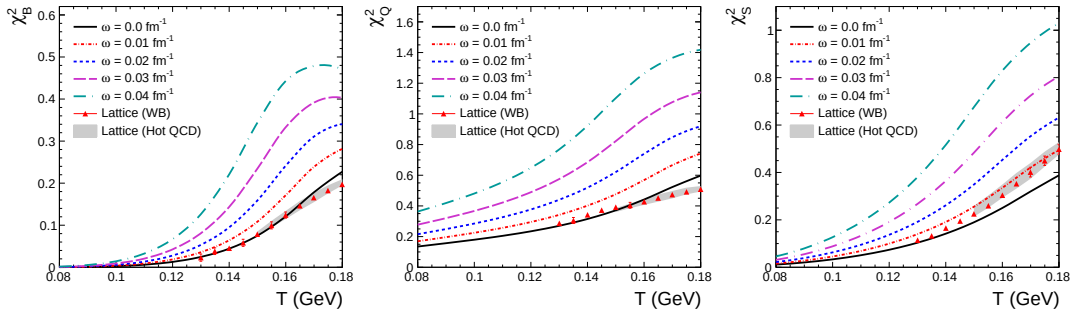

Figure 3.4: Temperature dependence of the baryon number (left), electric charge (middle), and strangeness (right) susceptibilities for various values of the rotational chemical potential, ω [166].

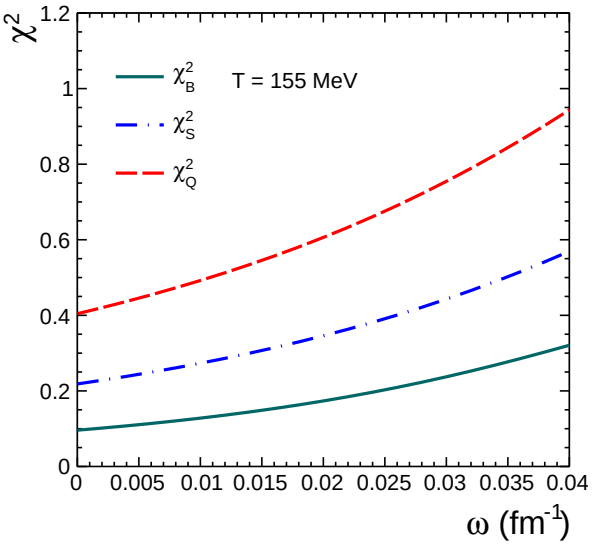

Figure 3.5: The ω dependence of conserved charge susceptibilities at a constant temperature, $T = 155$ MeV [166].

bilities for the baryon number, electric charge, and strangeness conserved charges, which are presented in Fig. 3.4 as functions of temperature for different values of angular velocity ω. The red triangles correspond to lattice QCD data from

the Wuppertal–Budapest collaboration [167], while the shaded regions represent results from the HotQCD collaboration [10]. The solid black curve represents the results obtained within the VDWHRG framework at $\mu_{\rm B} = 0$ and $\omega = 0$, and it reproduces the lattice results for baryon and charge susceptibilities quite well, whereas the strangeness susceptibility appears slightly lower than the lattice estimates. With increasing rotational chemical potential, the magnitude of all susceptibilities rises. In particular, a pronounced enhancement is observed in the baryon number susceptibility at larger ω, while the charge susceptibility tends to saturate and the strangeness susceptibility shows a steadily increasing trend across the considered range of ω.

In Fig. 3.5, we further illustrate the dependence of these susceptibilities on ω at a fixed temperature, $T = 155$ MeV. It is evident that all three susceptibilities exhibit a monotonic rise with increasing rotational chemical potential, showing similar qualitative behavior.

3.2 Phase transitions

A phase transition is defined as the change of a thermodynamic system from one state (or phase) to another state of matter at some specific thermodynamic conditions like T and μ_B. These phase transitions are often characterized by a sudden change in the system's properties. An order parameter is an observable that distinguishes the different phases of a thermodynamic system. The classifications of different orders of phase transition by Paul Ehrenfest are based on the behavior of thermodynamic free energy, where [169]

- A first-order phase transition is marked by a sudden change (discontinuity) of the first-order derivative of free energy with respect to an appropriate thermodynamic variable. Such a transition is accompanied by the absorption or release of latent heat. At the phase boundary, both the phases

coexist and are hence said to be in the mixed phase.

- When the free energy and its first-order derivative remain continuous, and the second-order derivative shows a discontinuity or divergence, it is said to be the second-order phase transition.

- For an analytic crossover transition, the free energy and its derivatives are continuous. The properties of the system change smoothly as it goes from one phase to another. These are generally marked by a rapid increase (but continuous) in densities and a peak in the derivatives of some observable, such as specific heat or susceptibilities.

The van der Waals interaction among hadrons gives rise to a liquid–gas phase transition in the hadronic medium. Therefore, in the present study, we focus on such a phase transition within the hadron gas. In Ref. [62], the authors considered a system of nuclear matter, determining the van der Waals (VDW) parameters by reproducing the ground-state properties of that nuclear matter. They predicted a first-order phase transition in a Fermi gas of nucleons, characterized by a critical temperature $T_c \sim 19$ MeV and a baryochemical potential $\mu_B \sim 908$ MeV. This framework was subsequently extended to a hadronic medium by incorporating VDW interactions among all hadronic species [81, 83]. In these studies, the VDW parameters were constrained by reproducing lQCD thermodynamic observables at vanishing baryochemical potential. Considering interactions only among pairs of baryons and anti-baryons, Ref. [81] reported a critical point at $T = 62.1$ MeV and $\mu_B = 708$ MeV. Whereas a slightly higher critical point was obtained at $T \approx 65$ MeV and $\mu_B \approx 715$ MeV [83] when interactions among the mesons are also included. It is noteworthy to mention that all these analyses consistently demonstrate the existence of a liquid–gas phase transition and an associated critical point in the T–μ_B plane.

When rotation is incorporated into the system, it is expected to act as an additional form of chemical potential, often referred to as the rotational chem-

ical potential. As discussed in the previous section, the rotation enhances the thermodynamic properties of the hadronic system, playing a similar role to the baryochemical potential. Along with pressure, energy density, and other quantities, susceptibilities also show a similar increase with an increase in rotation, as was observed in the case of high baryochemical potential. This motivates us to investigate whether rotation can affect the liquid-gas critical point, or even induce a phase transition at zero baryochemical potential. The conclusion at the end of the study may ultimately motivate the exploration of an extended QCD phase diagram in the three-dimensional parameter space spanned by temperature, baryochemical potential, and angular velocity, i.e., a phase diagram in the $T - \mu_B - \omega$ plane.

We estimate the entropy density, the first-order derivative of pressure with respect to temperature. For a first-order liquid-gas phase transition, we expect a discontinuity in this entropy density. To see if rotation can inhibit a first-order phase transition, we consider the case of zero μ_B and estimate entropy density as a function of temperature for different magnitudes of rotation, ω. The variation of the scaled entropy density in the T–ω phase plane is shown in Fig 3.7. The rotational parameter ω is expressed in units of GeV to capture fine variations, while the temperature is sampled at intervals of 0.5 MeV.

At lower rotational chemical potentials and higher temperatures, the scaled entropy density exhibits a smooth and continuous behavior. However, as ω increases, this smooth profile begins to distort, and beyond $\omega \simeq 0.019$ GeV, a discontinuity emerges around $T \simeq 113$ MeV. This distinct discontinuity signals the onset of a first-order phase transition at high angular velocities. The observation implies that the effect of rotation on the medium mimics that of baryon chemical potential in driving a liquid–gas phase transition [81]. Consequently, a hadronic gas can undergo liquefaction either by increasing the baryon density and lowering the temperature or by enhancing the angular velocity while simultaneously cooling the system. In comparison to Ref. [83], where the critical point

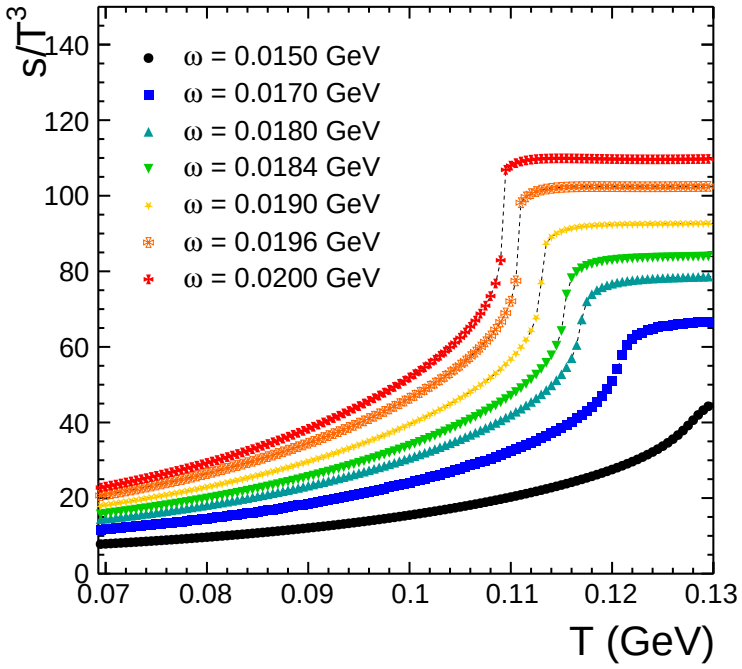

Figure 3.6: Scaled entropy density as a function of temperature at high values of rotation [166].

in the T–μ_B plane is found near $T = 65$ MeV, the present study in $T - \omega$ plane yields a higher critical temperature even with the same van der Waals parameters. This indicates that the introduction of rotational chemical potential accelerates the occurrence of the phase transition. Similar to the role of magnetic fields, which are known to elevate the chiral transition temperature [170], the angular velocity here raises the critical temperature for the liquid–gas phase transition relative to that induced by baryochemical potential.

It is important to emphasize that, in the case of a first-order phase transition, the first derivative of the free energy with respect to any thermodynamic variable should exhibit a discontinuity at the same transition point. This behavior serves as a defining characteristic of a first-order transition. For instance, if one considers the derivative of pressure with respect to the baryochemical potential μ_B, the

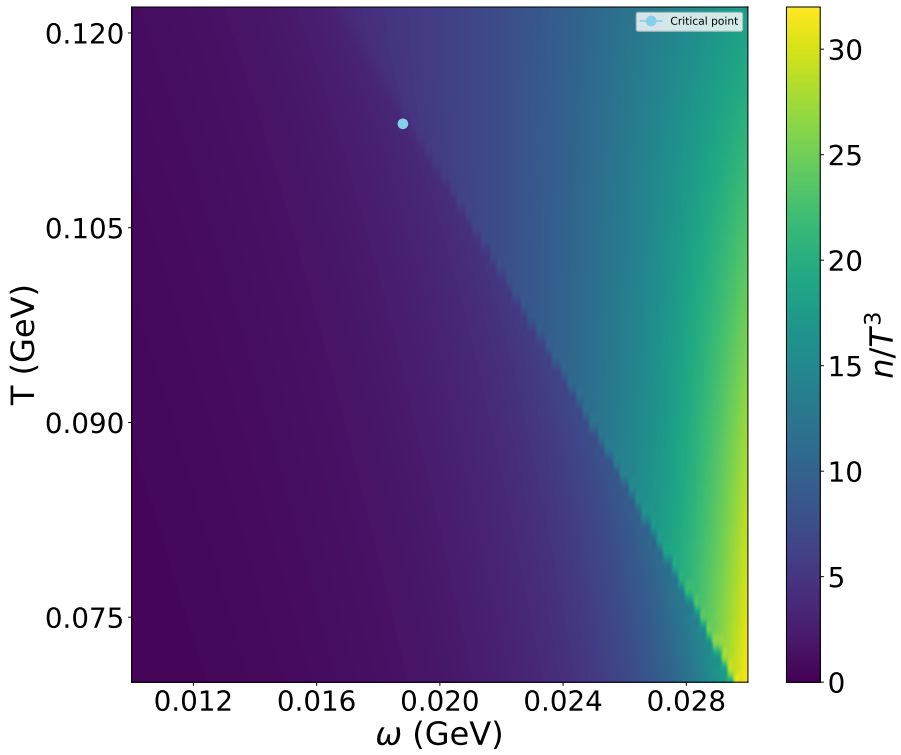

Figure 3.7: Scaled number density as a function of $T-\omega$ plane with solid marker representing the critical point of the liquid-gas phase transition in hadron gas.

so obtained number density should display a discontinuity at the same (T, μ_B) coordinates. Figure 3.7 presents the variation of the scaled number density, n/T^3, across a continuous range of ω and T. A clear phase transition is observed in the same T and ω values, where the critical point is indicated by a solid marker, followed by a clear first-order phase transition line identified through the discontinuities in the scaled number density, n/T^3.

3.2.1 Phase transition in $T-\mu_B-\omega$ plane

Now, since we understood the effect of rotation, which in many ways mimics the role of the baryochemical potential on the thermodynamic properties of the hadron gas, it will be interesting to explore how these two effects interplay with

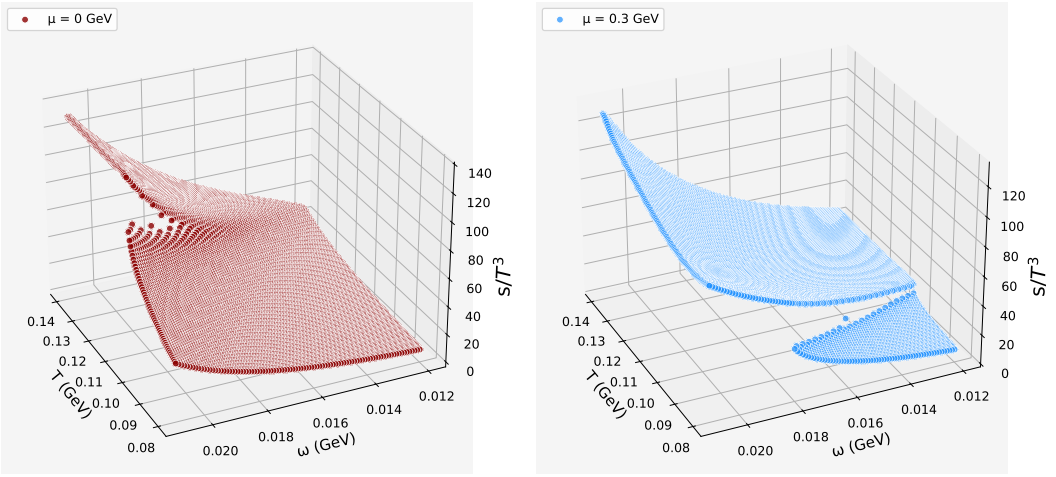

Figure 3.8: Scaled entropy density as a function of T and omega for $\mu_B = 0$ GeV (left) and $\mu_B = 0.3$ GeV (right) [171].

the characteristics of the phase transition in the hadronic medium. In Fig. 3.8, we show the effect of μ_B on the phase transition in the right panel in comparison to the vanishing μ_B case in the left panel. It is evident that the presence of a finite baryochemical potential (for instance, $\mu_B = 0.3$ GeV) causes the transition to occur at a comparatively lower temperature. Consequently, as μ_B increases, the critical point progressively shifts toward smaller T and ω values. This indicates that an enhancement in baryochemical potential effectively reduces the rotational chemical potential required to induce the phase transition. Hence, for every combination of (T, μ_B, ω), a corresponding critical point and associated first-order transition line can be defined.

Therefore, rather than having a single critical point in the $T - \mu_B$ or $T - \omega$ plane, the system exhibits a critical line in the three-dimensional $T - \mu_B - \omega$ space, accompanied by a first-order transition surface instead of a single line. The variation of scaled quantities such as s/T^3 or n/T^3 with temperature can be analyzed to trace this critical behavior. The corresponding critical temperatures

obtained in the $\mu_B - \omega$ plane are shown in Fig. 3.9. The solid red curve represents the critical line in the $T - \mu_B - \omega$ phase space, while for each individual critical point, defined by a particular set of (T_c, μ_{B_c}, ω_c), the associated first-order transition lines are indicated in the $T - \omega$ plane using colored markers.

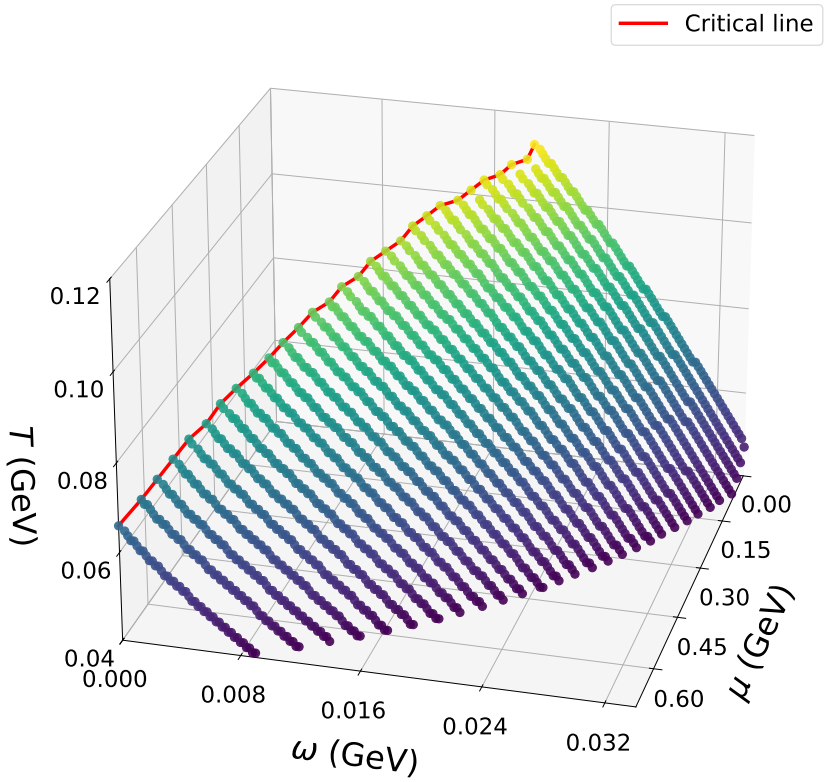

Figure 3.9: The liquid-gas phase diagram in $T - \mu_B - \omega$ plane.

We have investigated the influence of rotation on the thermodynamic properties of an interacting Hadron Resonance Gas. Our analysis reveals that the inclusion of rotation introduces effects analogous to those of a finite baryochemical potential, effectively acting as a rotational chemical potential. The presence of angular velocity enhances key thermodynamic observables such as pressure, energy density, and entropy density, indicating that rotation contributes to the overall energy content and dynamical evolution of the hadronic medium. The

analysis of fluctuations of conserved charges further indicates that rotation amplifies second-order susceptibilities, suggesting a stronger correlation among conserved quantities in a rotating hadronic system. These findings suggest that rotational motion, although often overlooked, plays a significant role in shaping the thermodynamic and microscopic behavior of the QCD matter produced in non-central heavy-ion collisions. Furthermore, we demonstrated that the rotation can induce a first-order liquid–gas phase transition in the hadronic phase. Therefore, it is essential to incorporate the effect of rotation when studying the QCD phase diagram, which must be explored by extending another axis due to rotation, i.e., mapping the QCD phase diagram in the $T - \mu_B - \omega$ plane.

3.3 Effect of rotation on the condensation of meson gas

Earlier in Chapter 2, we studied the properties of BE condensation using a pion gas, and we learned that for a relativistic meson gas, the BEC phenomenon occurs when the chemical potential approaches the lowest single-particle energy level (mass m of the meson), typically expressed as $\mu \to m$. While BEC is traditionally associated with low-temperature atomic systems, the same underlying principles also govern the behavior of bosonic excitations in strongly interacting matter at high density, such as pions, kaons, and vector mesons in hadronic or neutron-star environments.

We also observed in the previous Section of this Chapter that rotation affects the thermodynamic system by introducing another type of chemical potential, known as the rotational chemical potential. The rotation enhances all thermodynamic quantities in a similar way to the baryochemical potential. The presence of rotation leads to a first-order phase transition even for a vanishing μ_B case. By the same analogy, we can reasonably expect that the rotation can also influence

the conditions required to achieve the condensation of a meson gas. The rotational energy can shift the critical temperature and hence the chemical potential required for the onset of BEC. The strict condition of $\mu = m$ may be lowered in the presence of rotation. Therefore, it will be interesting to study the properties of a BEC in a rotating system of mesonic gas.

While the possibility of Bose–Einstein condensation of pseudoscalar pions has been widely examined in the literature [115, 116, 172–174], the possibility of condensation in the vector sector, specifically for ρ mesons, remains comparatively less explored. The non-central heavy-ion collisions at low energy, as well as the superfluid interiors of a rotating neutron star [175, 176], may achieve a suitable environment for the possible condensation of ρ mesons. Owing to their spin $S = 1$, ρ mesons offer a unique opportunity to study the combined effect of rotation, condensation, and spin polarization. Rotation introduces a coupling between the angular momentum of the medium and the intrinsic spin of particles, lifting the degeneracy among different spin states. In relativistic systems, this coupling can generate a global polarization, aligning the spins of particles along the axis of rotation. Unlike spin-zero bosons, vector mesons possess internal spin degrees of freedom, which couple directly to rotation and can lead to measurable polarization. When a Bose–Einstein condensate forms in a rotating system, the macroscopic occupation of the ground state may further amplify this spin alignment. These effects are of considerable interest not only for understanding QCD in extreme conditions but also for their potential astrophysical implications. A ρ meson condensate can soften the neutron-star equation of state, while a polarized ρ condensate may influence anisotropic neutrino emission or modify the transport properties inside strongly magnetized stellar cores.

In this section, we will examine the effect of rotation on the conditions required to achieve condensation, and subsequently, the dynamics of polarization of the ρ mesons in the presence of the BEC will be shown. This is to be noted that the formalism for the rotating hadron gas considered in the previous section has

the spin degeneracy encoded in its expression. While it is useful for studying the average thermodynamic properties of the hadron gas, it becomes necessary to consider individual spins when studying particles of a single kind with a spin. We attempt to adopt a formalism that lifts this degeneracy in the presence of rotation, enabling a more accurate description of rotational effects. This approach also enables us to compare and refine various mathematical formalisms currently used in ongoing studies of rotation and incorporate potential inputs to enhance them. We begin by deriving the critical conditions for Bose–Einstein condensation in a rotating ρ-meson gas and then proceed to analyze the resulting polarization phenomena in the presence of the condensate.

3.3.1 Critical conditions to achieve BEC in a rotating ρ meson gas

We can obtain a rotating frame by transforming the non-rotating coordinates x'^{μ} to that of rotating coordinates x^{μ} with angular velocity ω in the z direction as [164]

$$\begin{aligned} x &= x^{'}\cos\omega t + y^{'}\sin\omega t \\ y &= -x^{'}\sin\omega t + y^{'}\cos\omega t \\ z &= z^{'} \\ t &= t^{'} \end{aligned} \tag{3.32}$$

The invariant space-time interval (ds^2) in the inertial frame can be obtained as

$$\begin{aligned} ds^2 &= dt^2 - dx^{'2} - dy'^2 - dz^2 \\ &= dt^2(1-(x^2+y^2)\omega^2) + 2\omega(y\ dx - x\ dy)dt \\ &\quad - dx^2 - dy^2 - dz^2 \end{aligned} \tag{3.33}$$

The metric tensor thus obtained is given below [164]

$$g_{\mu\nu} = \eta_{\lambda\sigma}\frac{\partial x'^{\lambda}}{\partial x^{\mu}}\frac{\partial x'^{\sigma}}{\partial x^{\nu}} = \begin{pmatrix} 1-(\chi^2+y^2)\omega^2 & y\omega & -\chi\omega & 0 \\ y\omega & -1 & 0 & 0 \\ -\chi\omega & 0 & -1 & 0 \\ 0 & 0 & 0 & -1 \end{pmatrix} \tag{3.34}$$

where the $\eta_{\lambda\sigma}$ is the Minikowski metric tensor with $\eta = \text{diag}(1, -1, -1, -1)$. Further introducing vierbein, $\eta_{\lambda\sigma} = e^{\mu}_{\lambda}e^{\nu}_{\sigma}g_{\mu\nu}$, we adopt $e^{t}_{0} = e^{x}_{1} = e^{y}_{2} = e^{z}_{3} = 1$, $e^{x}_{0} = y\omega$, $e^{y}_{0} = -x\omega$ and all other components to be zero. Following the calculations [61, 177–179] involving the metric and vierbien, one can find that there is a shift in the Hamiltonian due to the rotation and is given by [164]

$$\hat{H} \to \hat{H} - \mathbf{J}\cdot\boldsymbol{\omega} \tag{3.35}$$

where we have the total angular momentum $\mathbf{J} = \mathbf{L} + \mathbf{S}$, with $\mathbf{L}$ and $\mathbf{S}$ being the orbital and spin angular momentum, respectively.

The energy dispersion relation thus gets modified in the presence of rotation and is given as

$$\varepsilon \to \varepsilon - (l+s)\omega \tag{3.36}$$

where the z components of orbital and spin angular momentum are denoted with l and s, respectively. This shift in energy behaves analogously to the chemical potential, and that is why we will have an effective chemical potential for a rotating system. This demonstrates the potential for redefining the conditions required for condensation in a rotating system in comparison to those of a non-rotating gas.

In the presence of rotation, the pressure due to the ith Bosonic species is given by [164, 165]

$$P_i = -\frac{T}{8\pi^2}\sum_{\ell=-\infty}^{\infty}\int dk_r^2\int dk_z\sum_{\nu=\ell}^{\ell+2S_i} J_{\nu}^2(k_r r)\times\log\left\{1-\exp[-(\varepsilon_{\ell,i}-\mu_i)/T]\right\}, \tag{3.37}$$

with the radial momentum k_r and the momentum along z direction, k_z, the energy of each particle is given as, $\varepsilon_{l,i} = \sqrt{k_r^2 + k_z^2 + m_i^2} - (l+s)\omega$, where m is the mass of the particle species. The radial integration in the above equation is $dk_r^2 = 2\ k_r\ dk_r$. The Bessel functions of the first kind are denoted by J_ν, whereas the radial distance from the axis of rotation is given by r. The causality condition requires imposing a boundary condition at $r = R$ with $R\omega \leq 1$ (considering natural units, $c = 1$), such that the wave functions are normalized inside the cylindrical volume of the gas (at $r \leq R$).

The imposed boundary condition results in the quantization of the radial component of the momentum as $k_r = \xi_{l,i}/R$ [164], where $\xi_{l,i}$ denotes the ith zero of the Bessel function, satisfying $J_l(\xi_{l,i}) = 0$. This discretization predominantly influences the low-momentum sector, implying that the integration over k_r acquires a nonzero lower limit, given by $k_r = \xi_{l,i}/R = \xi_{l,i}\omega$. It is also worth noting that the formalism inherently contains a radial dependence through the Bessel function $J_\nu(k_r r)$. However, in order to isolate and clearly interpret the effects arising purely from rotation, and to avoid additional complications associated with spatial variations across the radius, we eliminate this explicit r dependence by evaluating all thermodynamic quantities at a fixed radius, following the methodology adopted in [164, 165, 180]. This choice eliminates any ambiguity caused by radial inhomogeneities. Since centrifugal effects are strongest near the outer edge of the system, all numerical results are obtained by setting $r = R$ [180].

For a gas of ρ mesons, the total number density can be obtained from Eq. (3.37) as [181]

$$\begin{aligned} n_{\rm tot} &= \left(\frac{\partial P}{\partial \mu}\right)_{T,\omega} \\ &= \frac{1}{8\pi^2} \sum_{\ell=-\infty}^{\infty} \int dk_r^2 \int dk_z \sum_{\nu=\ell}^{\ell+2S_i} J_\nu^2(k_r r) \times \frac{1}{\exp[(\varepsilon_{\ell,i} - \mu_i)/T] - 1}. \end{aligned} \tag{3.38}$$

It is important to note that in Ref. [164], the summation over ν is introduced to account for spin degeneracy in a simplified manner. However, when the system is

rotating, this degeneracy is lifted, and different spin projections couple differently to the direction of the angular momentum, leading to spin-dependent modifications of the particle density. Consequently, the summation over ν is replaced by that of the individual spin states of the particle species as done in Ref. [181]. For the ρ meson, this requires summing over the three spin projections, $s = -1, 0, +1$.

Now we can focus on the critical conditions required to achieve the BEC phenomenon in a rotating gas of ρ mesons. Taking the reference from a non-rotating gas, we know that the BEC occurs when the chemical potential μ becomes equal to the ground state energy, i.e., $\mu = \varepsilon_0 = m_\rho$ (as momentum, $p = 0$). For the case of charged $\rho^\pm$, we consider the isospin chemical potential, as $\mu_\rho = \pm\mu_I$. In the presence of rotation, the single-particle energies are modified, and the boundary conditions also lead to the quantization of radial momentum. Hence, the ground state energy ε_0 is now not equal to m_ρ as $k_r \neq 0$, rather it is determined by the imposed boundary conditions. Consequently, the condensation for a rotating meson gas occurs when $\mu = \mu_c = \varepsilon_{min}$, where ε_{min} is the minimum single-particle energy in a rotating medium.

Let us start from the particle's energy given in Eq. (3.38) as

$$\varepsilon_l = \sqrt{k_r^2 + k_z^2 + m^2} - (l + s)\omega, \tag{3.39}$$

To determine the absolute ground state of the system, the single-particle energy must be minimized with respect to all available degrees of freedom. The longitudinal momentum is first eliminated by choosing $k_z = 0$, thereby removing any kinetic contribution along the rotation axis. Next, for a ρ meson having spin projections $s = -1, 0, +1$, the rotational coupling term $-(l + s)\omega$ is minimized by selecting the spin state that yields the largest energy gain from rotation. This corresponds to choosing $s = +1$. Under these considerations, the lowest accessible single-particle energy for a rotating ρ meson gas (subject to $k_z = 0$ and the constraint $\varepsilon_l - \mu \geq 0$) becomes [181]

$$\varepsilon_{\min} = \sqrt{(\xi_{l_{\max},1}, \omega)^2 + m^2} - (l_{\max} + 1)\omega, \tag{3.40}$$

where $l_{\max}$ denotes the angular momentum quantum number that minimizes the expression above.

The onset of Bose–Einstein condensation is then identified by the condition that the chemical potential reaches this minimum energy, i.e. $\mu = \varepsilon_{\min}$. The critical temperature for the emergence of a ρ meson condensate in a rotating medium is therefore given by [181]

$$n_{\rm ex}(T = T_c, \mu = \varepsilon_{\min}) = n_{\rm tot}. \tag{3.41}$$

For temperatures below T_c, the distribution of particles between the condensate and excited states follows directly as

$$n_{\rm tot} = n_{\rm cond} + n_{\rm ex}.$$

The condensate fraction can be obtained using [181]

$$\frac{n_{\rm cond}}{n_{\rm tot}} = 1 - \frac{n_{\rm ex}}{n_{\rm tot}} = 1 - \frac{n_{\rm ex}(T < T_c, \mu = \varepsilon_{\min})}{n_{\rm ex}(T = T_c, \mu = \varepsilon_{\min})}, \tag{3.42}$$

which mirrors the standard formulation for BEC [115, 124].

In this study, we consider a ρ meson gas with a fixed total number density of $n_{\rm tot} = 0.15$ fm^{-3}. This total density includes contributions from all three spin projections of the ρ meson, namely, spin-up, spin-down, and spin-zero within a cylindrically rotating system of radius $R = 5$ fm. The choice of R is motivated by experimental and phenomenological estimates of the characteristic source size in heavy-ion collisions, which typically lie in the range of 4–9 fm [120, 182, 183]. In the non-rotating limit ($\omega = 0$), the system retains full spin degeneracy, and the three spin states share the density equally, each contributing 0.05 fm^{-3}. When rotation is introduced, this degeneracy is lifted due to the coupling between the particle's spin and the medium's angular momentum. As shown in Fig. 3.10, at $\omega = 0$ GeV, all three spin states have the same density of 0.05 fm^{-3}. With an increase in the magnitude of ω, the population of the spin-up state grows, while the density in the spin-down state correspondingly decreases. The spin-zero state

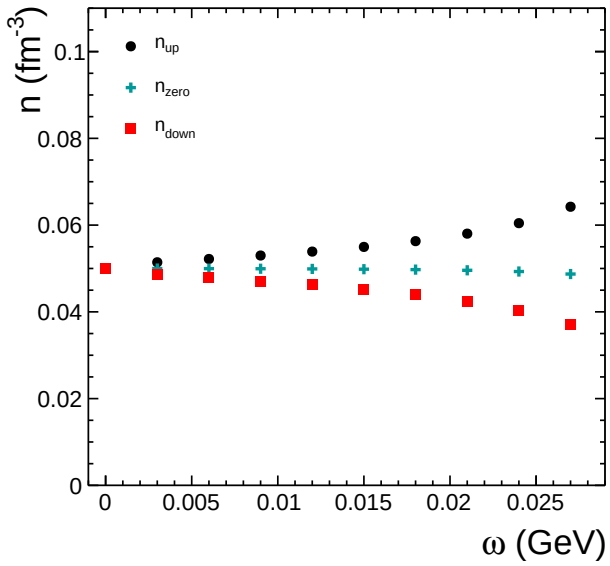

Figure 3.10: Number density of each spin projection of the ρ meson as a function of rotation. Total density being equal to 0.15 fm^{-3}.

remains nearly unaffected by rotation. Throughout this redistribution, the total density is constrained to remain fixed at 0.15 fm^{-3}.

Let us now examine how rotation influences the BEC transition in a gas of ρ mesons. From Eq. (3.42), it follows that for $T < T_c$ and in the limit $T \to 0$, the condensate fraction tends toward unity, indicating that the entire particle density considered ($n_{\rm tot} = 0.15$ fm^{-3}) resides in the condensed phase. the fraction of particles in the condensate diminishes progressively and vanishes at the critical temperature $T = T_c$, beyond which the system is entirely composed of excited states.. This behavior is illustrated in the left panel of Fig. 3.11, where the condensate fraction is plotted as a function of temperature for three representative values of the angular velocity ω, including the non-rotating limit $\omega = 0$. In each case, the condensate fraction drops to zero at T_c and rises monotonically as the temperature decreases, eventually approaching unity in the limit $T \to 0$.

An important observation can be made from Fig. 3.11 that the critical temper-

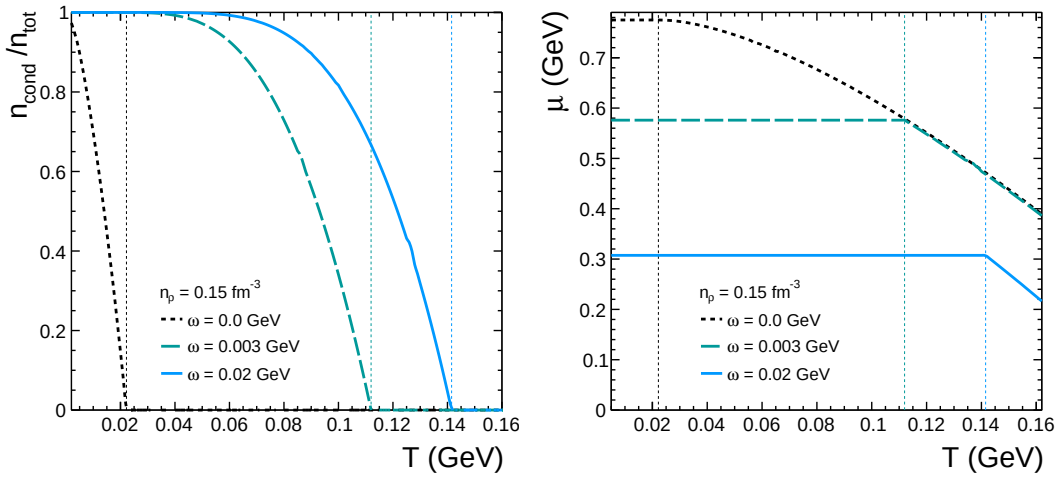

Figure 3.11: Condensate fraction (left) and chemical potential (right) as a function of temperature for different magnitudes of rotation [181].

ature T_c increases with increasing rotational chemical potential ω. This shift can be understood through the interplay among T, ω, and μ under the constraint of fixed $n_{\rm tot}$. The corresponding temperature dependence of the chemical potential is shown in the right panel of Fig. 3.11. In the absence of rotation, the system behaves as a standard relativistic Bose gas, where condensation sets in when $\mu = m$. This feature is clearly visible for $\omega = 0$, where the chemical potential saturates at $\mu = m = 0.775$ GeV for all $T < T_c$, while for $T > T_c$ the requirement of maintaining a fixed number density causes μ to decrease with temperature, consistent with the expected thermodynamic trends [115, 124].

Eq. (3.40) shows that the effective chemical potential of the system decreases in the presence of finite rotation, and this decrease is proportional to the angular velocity. This observation is significant because it suggests that rotation itself facilitates the formation of a condensate. The system requires a smaller chemical potential to achieve the BEC condition than in the non-rotating case. This mechanism also explains why the critical temperature T_c rises with increasing ω when the total density $n_{\rm tot}$ is held fixed. Moreover, we explore the behav-

ior of T_c at very high values of rotation. It is noteworthy to mention that the causality condition (following the boundary condition chosen here at $R = 5$ fm) restricts the admissible range of rotation to $\omega \lesssim 0.2$ fm^{-1} ($\sim$0.0394 GeV). The dependence of T_c on ω for several choices of $n_{\rm tot}$ is illustrated in Fig. 3.12. As expected, at any fixed ω, a larger particle density corresponds to a higher T_c, in agreement with earlier studies such as Ref. [115]. More interesting, however, is the non-monotonic response of T_c to rotation. Although T_c initially increases rapidly with ω, it eventually reaches a maximum and subsequently decreases. Remarkably, the position of this maximum is nearly independent of the value of $n_{\rm tot}$. This non-monotonic behaviour can be traced back to the structure of the

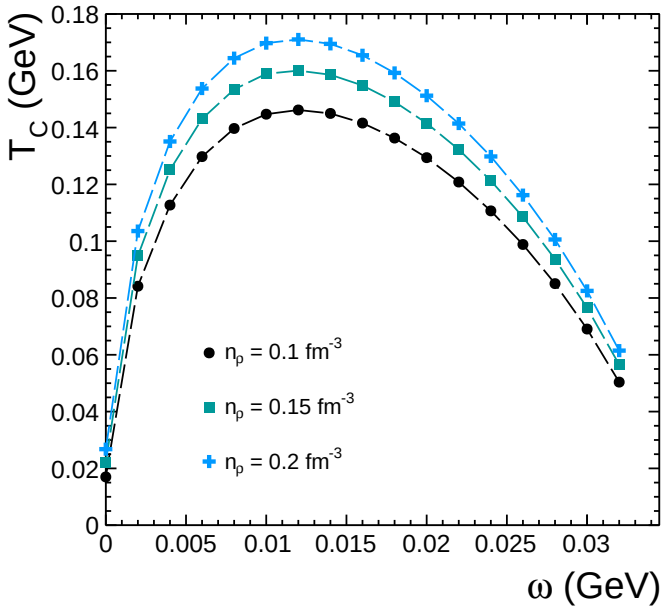

Figure 3.12: The variation of critical temperature with rotation for different cases of total densities of ρ gas [181].

minimum single-particle energy $\varepsilon_{\rm min}$ that determines the condensation condition in a rotating system. Minimizing Eq. (3.40) with respect to the orbital quantum number l reveals a competition between two contributions: (i) the term $-(l+1)\omega$,

which favors large l, tending to lower $\varepsilon_{\min}$, and (ii) the centrifugal contribution $\sqrt{(\xi_{l,1}\omega)^2 + m^2}$, which increases with l because $\xi_{l,1}$ grows with the orbital excitation. At moderate values of ω, the linear $-(l+1)\omega$ term dominates, reducing $\varepsilon_{\min}$ and driving T_c upward. At sufficiently high ω, the quadratic centrifugal term $(\xi_{l,1}\omega)^2$ exceeds the linear term, increasing $\varepsilon_{\min}$ and thereby lowering T_c. This competition yields the characteristic rise-and-fall structure of $T_c(\omega)$.

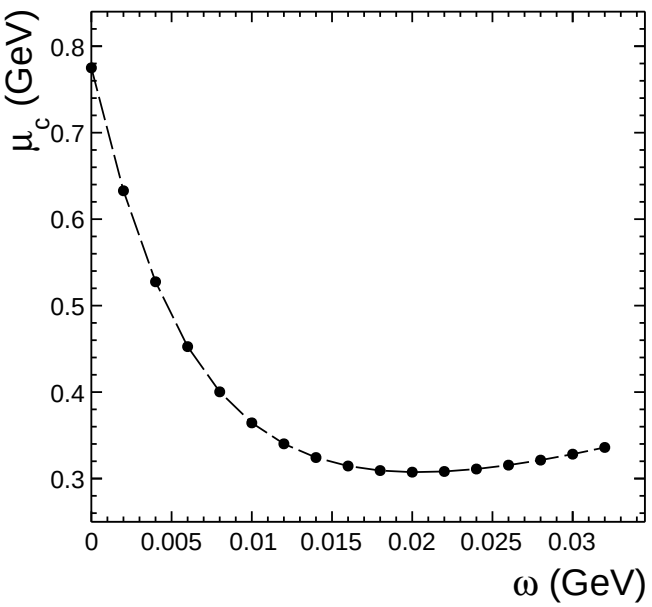

Figure 3.13: The variation of critical chemical potential with rotation. For $\omega = 0$ GeV, it reduces to a non-rotating system where BEC occurs when $\mu_c = m_\rho = 0.775$ GeV [181].

The chemical potential at the onset of condensation, $\mu_c = \varepsilon_{\min}$, exhibits a similar qualitative behaviour. As shown in Fig. 3.13, $\mu_c(\omega)$ decreases, reaches a minimum, and rises again at higher rotational speeds. We find that the μ_c is independent of n_{tot}, which is expected, for instance, at $\omega = 0$, one always has $\mu_c = m$ irrespective of the total density of the gas. We also observe that within the ω range considered, μ_c never approaches zero, even at the highest allowed

angular velocities. This implies that rotation alone cannot produce a macroscopic BEC. Instead, it enhances the condensation by reducing the required chemical potential.

Therefore, the combined interplay among temperature, rotation, and chemical potential, subject to the constraint of fixed density, gives rise to the observed structure of $T_c(\omega)$. In Ref. [184], the influence of rotation on BEC thermodynamics is examined, where the critical temperature is found to shift under rotation. In their formulation, a rotating dilute gas exhibits a lower T_c than its non-rotating counterpart, yet the temperature associated with the transition increases proportionally with the rotational drive. Despite differing physical setups, both studies consistently highlight the nontrivial role of rotation in reshaping the BEC phase boundary.

3.3.2 Spin polarization in the presence of a condensate

In a non-rotating system, all spin substates of a gas are populated equally due to spin degeneracy. However, in a rotating medium composed of ρ mesons, this degeneracy is lifted. The rotation couples to the spin degrees of freedom, producing an imbalance among these states. To quantify this polarization effect, we examine the individual spin densities.

In a quantum-statistical framework, the spin state of a vector meson ($S = 1$) is described by the spin density matrix $\rho_{mm'} = \langle S, m_s|\hat{\rho}|S, m'_s\rangle$, whose diagonal elements ρ_{11}, ρ_{00}, and ρ_{-1-1} correspond to the occupation probabilities of the substates with spin projections $m_s = +1, , 0$, and -1, respectively [163, 185]. A commonly used spin-alignment parameter is defined by $\rho_{00} \sim n_0/(n_{+1}+n_0+n_{-1})$, which measures the probability of the meson spin lying perpendicular to the chosen quantization axis. For an unpolarized gas with statistically distributed spin states, one expects $\rho_{00} = 1/3$. Any significant deviation from $1/3$ is therefore interpreted as evidence of global spin alignment induced by vorticity or other

medium-driven mechanisms [186, 187]. At the quark level, theoretical treatments relate ρ_{00} to the polarization of the constituent quark and antiquark through [185, 188]

$$\rho_{00} = \frac{1 - P_q P_{\bar{q}}}{3 - P_q P_{\bar{q}}}, \tag{3.43}$$

where the quark polarization P_q is given by

$$P_q = \frac{n_{q_\uparrow} - n_{q_\downarrow}}{n_{q_\uparrow} + n_{q_\downarrow}}, \tag{3.44}$$

with $n_{q_\uparrow}$ and $n_{q_\downarrow}$ denoting the densities of quarks with spin up and down, respectively. By analogy, the same conceptual structure can be applied at the hadronic level. A nonzero $\rho_{00} - 1/3$ indicates spin alignment of ρ mesons, while a nonvanishing polarization P characterizes the net vector polarization of the medium. Therefore, for the polarization study, we evaluate the density of each spin state in both the condensate and the excited components of the system. The overall spin alignment, i.e., the degree of vector polarization, is characterized through the normalized net spin density, defined as [181]

$$P_\rho = \frac{n_\uparrow - n_\downarrow}{n_\uparrow + n_\downarrow}, \tag{3.45}$$

where $n_\uparrow$ and $n_\downarrow$ denote the densities of ρ mesons in the spin-up and spin-down states, respectively. This quantity measures the net preference of the ensemble to align its spin along the global rotation axis and hence reflects the imbalance between the different spin projections.

For a fixed angular velocity, the total density of the ρ meson gas at any temperature is simply the sum of the contributions from all spin substates. Rotation lifts the degeneracy between the spin-up and spin-down populations, leading to $n_\uparrow \neq n_\downarrow$. However, at a given ω, their sum is fixed and remains constrained by the requirement of fixed total density. As the system passes through the BEC transition, the distribution of particles between the condensate and the excited states changes with temperature. Thus, although the total polarization P_ρ is

set entirely by the imposed rotation, its temperature dependence emerges from the distribution of each spin state between the condensed and thermal fractions. This redistribution across the transition governs how polarization manifests in the condensed and excited components of the ρ meson gas.

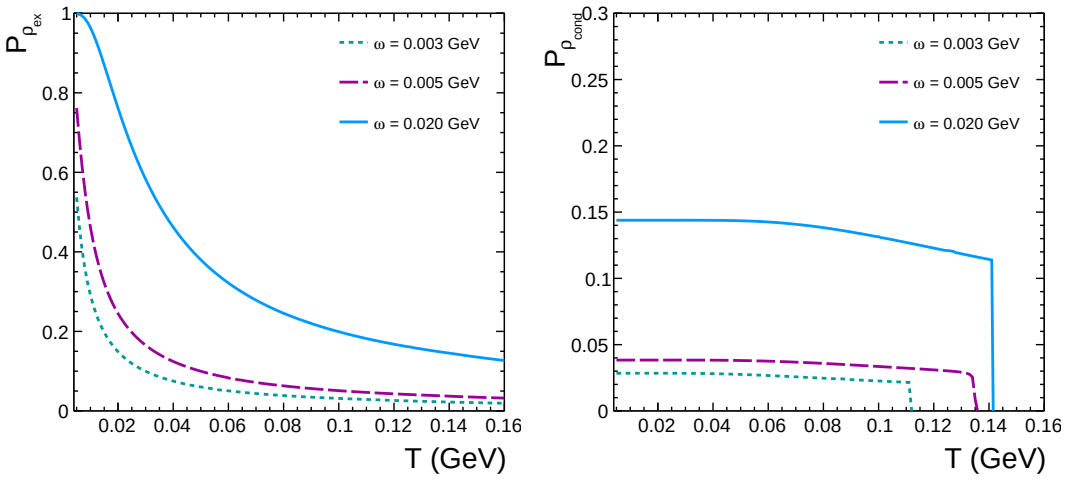

Figure 3.14: Temperature dependence of the spin polarization of thermal (left) and condensate rho mesons (right) for different values of ω [181].

We use Eq. (3.45) to evaluate the polarization of the ρ meson gas separately for the excited ($P_{\rm ex}$) and the condensate components ($P_{\rm cond}$) in order to clarify how each responds to the onset of BEC. We consider three distinct values for rotation, $\omega = 0.003$, 0.005, and 0.02 GeV. The Fig. 3.14 displays the temperature dependence of $P_{\rm ex}$ and $P_{\rm cond}$. For the excited states, a nonzero polarization is observed across all finite ω, reaching its maximum at low temperatures and gradually diminishing as temperature increases. As expected, larger angular velocities enhance the magnitude of this polarization, with the strongest effect appearing for $\omega = 0.02$ GeV. In the limit $T \to 0$, $P_{\rm ex}$ becomes largest, although the excited fraction is extremely small in this region (see Fig. 3.11). Since the total excited density diminishes at very low T, and because of the large value of ω, the excited spin-down states are even more suppressed, the thermal population

becomes almost entirely dominated by the spin-up state. Consequently, at low temperatures and high ω, the excited sector approaches a nearly fully polarized configuration. The condensate exhibits a somewhat different behavior. At the moment of condensation ($T \approx T_c$), the condensate already carries a finite polarization that grows in magnitude with increasing ω. As the temperature decreases further, the condensate polarization continues to increase gradually owing to the rising condensate fraction.

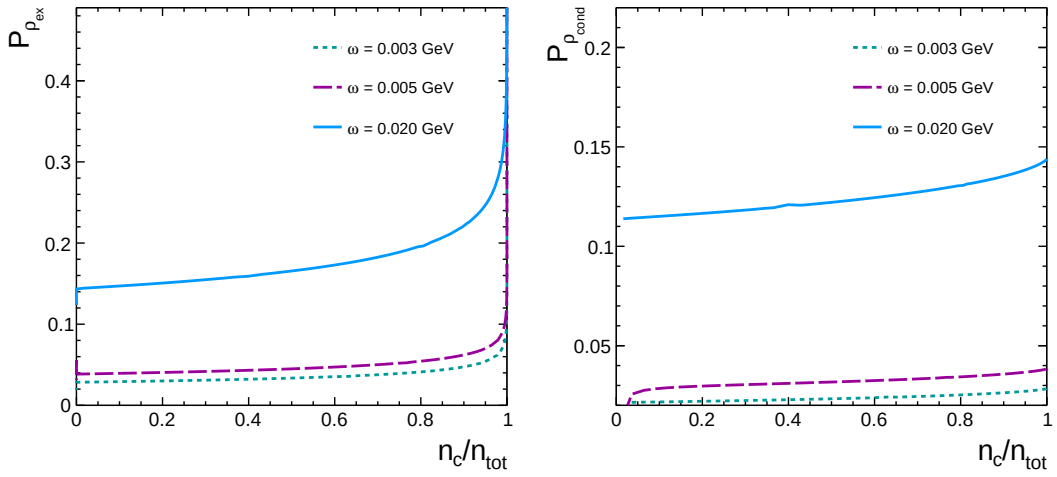

Figure 3.15: Spin polarization of thermal (left) and condensate rho mesons (right) as a function of condensate fraction for different values of ω [181].

We must emphasize that $n_{\rm ex}$ and $n_{\rm cond}$ correspond to two physically distinct components of the system, each capable of exhibiting different polarization behavior. The excited population $n_{\rm ex}$ acquires polarization through the combined influence of rotation and temperature, whereas the condensate fraction $n_{\rm cond}$ is governed by the coherent macroscopic occupation of the ground state. The condensate is characterized by a collective wavefunction, and its polarization $P_{\rm cond}$ mainly represents the intrinsic spin alignment of this coherent state. Fig. 3.15 presents the polarization of both the excited and condensate components as functions of the total condensate fraction. Our analysis reveals that the polarization of

both $n_{\rm cond}$ and $n_{\rm ex}$ increases smoothly as $n_{\rm cond}/n_{\rm tot}$ grows. This behavior clearly demonstrates that the onset of Bose–Einstein condensation strengthens global spin alignment beyond what would arise from a thermal population of polarized states alone. Once formed, the condensate introduces a coherent mean field that explicitly breaks spin-rotation symmetry. As a result, the condensate not only develops intrinsic polarization but also exerts an aligning influence on the surrounding thermal component, thereby enhancing the polarization. Consequently, the condensate fraction $n_{\rm cond}/n_{\rm tot}$ acts as a powerful control parameter regulating the overall polarization of the system, linking the behavior of both condensed and non-condensed components.

It should be noted that the present analysis considers a non-interacting ρ meson gas. Interactions, if included, would modify the chemical potential and could shift the critical temperature T_c away from the ideal-gas prediction. Moreover, in a dense interacting medium, the in-medium mass of vector mesons may decrease, leading to a reduced μ_c for the onset of BEC [175, 189]. Nonetheless, the qualitative rotational mechanisms identified here, such as the enhancement of $T_{\rm c}$ and its influence on spin alignment, are expected to remain the same. The present work, therefore, establishes a foundational, ideal gas framework that isolates and demonstrates the essential interplay between rotation, Bose–Einstein condensation, and spin polarization.

Our study provides the first systematic exploration of how rotation, Bose-Einstein condensation, and spin polarization collectively shape the behavior of a dense ρ meson gas. We find that global rotation substantially lowers the critical chemical potential μ_c, thereby enhancing the probability of ρ meson condensation. The rotation also simultaneously induces strong spin alignment in both the thermal and condensed components. The condensate acts as a coherent polarized medium, further amplifying the overall polarization of the system. These results have direct implications for heavy-ion collisions and neutron star physics. In low-energy collisions, where both baryon density and vorticity are high, the combined

conditions may enable the onset of ρ condensation and produce measurable polarization signatures in decay observables. In neutron stars, a spin-polarized ρ condensate could soften the equation of state and generate anisotropic pressure, potentially influencing stellar deformation. Together, these findings highlight rotation as a key driver of mesonic condensation and polarization in strongly interacting matter.

Chapter 4

Extension to the conventional VDWHRG model

The hadron resonance gas model offers one of the most promising alternatives to the first-principles lattice QCD approach for studying the properties of hot and dense hadronic matter. It shows quite good agreement with the thermodynamic quantities obtained using lQCD simulations for the case of vanishing μ_B at low temperature ($T \lesssim 150$ MeV) [10, 11]. Apart from this, the ideal HRG model is also able to explain the hadronic abundances measured in experiments, describing the particle ratios obtained in high-energy collisions [190]. For a realistic picture, one needs to take into account the interaction among the hadrons. This is supported by the fact that the ideal HRG model diverges significantly from high-temperature lattice lQCD calculations. In addition, the model is unable to explain the higher-order conserved charge fluctuations observed in lQCD [191] as well as in experimental data [70]. Incorporating a finite size to the hadrons solves one of the crude assumptions of ideal HRG, which assumes the hadrons and resonances to be point particles. The so-called excluded volume HRG (EVHRG) model incorporates repulsive interactions by assigning a finite eigenvolume to each hadronic species, effectively preventing them from overlapping in space [33, 192]. Alternatively, the mean-field HRG (MFHRG) framework introduces repulsion through an interaction potential acting between hadrons [193, 194]. Several extensions of the HRG approach appear in the literature, including the Lorentz-modified

excluded volume HRG (LMEVHRG) model [195], which accounts for Lorentz contraction of hadrons at high momenta, and the thermal effective-mass HRG (THRG) model [196], where hadrons acquire a temperature-dependent effective mass.

Among these approaches, the van der Waals HRG (VDWHRG) model has emerged as the most successful in reproducing lattice QCD thermodynamics. In this formulation, hadrons experience both short-range repulsion and long-range attraction of van der Waals type [62, 82, 197]. The VDWHRG model reproduces lattice QCD results up to temperatures of approximately $T \simeq 180$ MeV [80, 198], suggesting that van der Waals interactions may play a crucial role in hot hadronic matter. An important feature of this model is that it naturally accommodates a first-order (liquid–gas) phase transition, which is anticipated to appear in the QCD phase diagram [199].

The VDWHRG framework has been extensively applied to study thermodynamic and transport properties of hadronic matter [81, 83, 96], and fluctuations of conserved charges have also been evaluated at vanishing baryochemical potential [70, 80]. However, despite its relevance for the physics of dense baryonic matter, the behavior of the VDWHRG model at large μ_B has received comparatively little attention. When this model is used to estimate the higher-order conserved charge cumulants, which are used for probing the critical point in the QCD phase diagram, it is observed that it fails to explain the experimental data, especially at low center-of-mass energy, corresponding to the high μ_B regime. This provides us with another opportunity to examine the potential drawbacks and refine the model to make it reliable for use in the high μ_B region, thereby enabling it to be applied at the energies available in experiments such as FAIR and NICA [200].

4.1 Limitations of the VDWHRG model

The analysis in Ref. [80] demonstrates that the VDWHRG framework reproduces lattice QCD thermodynamics to a great extent, which originates from the interplay of repulsive and attractive interactions: while repulsion tends to suppress thermodynamic observables, attraction counterbalances this suppression, leading to a more realistic description of hadronic matter at $\mu_B = 0$. A subsequent refinement of the model was proposed in Ref. [196], where the hadrons were assigned temperature-dependent effective masses within the VDWHRG scheme. In most existing VDWHRG studies, however, the van der Waals forces are taken to act exclusively between (anti)baryon–(anti)baryon pairs, neglecting meson–meson and meson–(anti)baryon interactions for simplicity. For instance, Ref. [81] investigates the liquid–gas critical point assuming VDW interactions only among (anti)baryons, whereas Ref. [83] extends the formulation by including meson–meson interactions. A common limitation that we observed in these works [81, 83] is the assumption of constant VDW parameters a and b throughout the entire (T, μ_B) plane, which is likely an oversimplification.

The van der Waals (VDW) parameters used in these studies are largely based on two approaches, obtained either by reproducing the properties of ground-state nuclear matter [80, 82], or from the fitting of different thermodynamic variables obtained from the lattice QCD calculations [81]. In all previous considerations, the VDW parameters are taken to be constants throughout the thermodynamic phase space. For example, Ref. [80] determines the VDW parameters by reproducing the saturation properties of nuclear matter, namely the saturation density $n_0 = 0.16$ fm^{-3} and the binding energy per nucleon $E/A = 16$ MeV. This yields $a = 329$ MeV and $b = 3.42$ fm^3 [80, 82], and leads to the prediction of a first-order nuclear liquid–gas phase transition with a critical point at $T_c \approx 19.7$ MeV and $\mu_B \approx 908$ MeV. An alternative set of VDW parameters was obtained in Ref. [81],

where the pressure and energy density calculated within the VDWHRG formulation are used to fit the lQCD data of the same quantities at zero baryon chemical potential (μ_B). These obtained values of a and b were then employed to explore the model at finite baryon chemical potential, calculations involving higher values of μ_B. However, the current study argues that this assumption is oversimplified and requires modification.

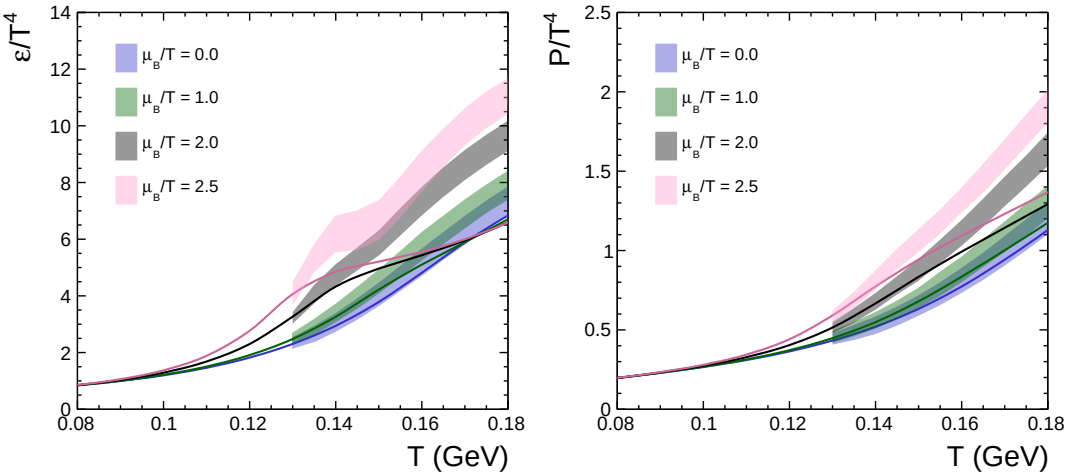

Figure 4.1: Temperature dependence of scaled energy density and pressure [201]. Solid lines are the results obtained in VDWHRG using constant parameters, a = 1.25 GeV fm^3 and r_B = 0.7 fm [81], which are compared to the lQCD data [84] shown in coloured bands. At high μ_B/T values, the model deviates from the lQCD predictions.

As shown in Fig. 4.1, the use of fixed VDW parameters extracted at μ_B = 0 does not explain lattice QCD thermodynamics once we move towards larger values of μ_B. The noticeable deviation from lQCD results at high μ_B/T suggests that the standard VDWHRG formulation, with constant attractive and repulsive couplings, may be missing essential physics in regions of high baryon density. Although some exploration of the possibility of temperature or density-dependent VDW parameters [202] has been conducted, a systematic investigation of such

dependencies is still lacking in the literature. Motivated by this, the present study proposes that the VDW interaction parameters a and b should not be treated as universal constants, but rather as quantities that may vary with both temperature and baryochemical potential. Allowing a (T, μ_B) dependence in these parameters provides a more realistic description of lQCD thermodynamics, particularly in the high-density regime where the constant-parameter approach breaks down.

We use a standard χ^2 minimization procedure [81] to extract the values of the van der Waals parameters a and b by fitting the temperature-dependent lQCD results at fixed $\mu_{\rm B}/T$. Once these optimal values are obtained for each available $\mu_{\rm B}/T$ data, we parametrize both a and b as smooth functions of $\mu_{\rm B}/T$, allowing their use over a continuous range of $(T, \mu_{\rm B})$ through a reasonable extrapolation. This construction effectively introduces a $\mu_{\rm B}$ and T dependent VDW parameter set, thereby improving the behavior of the VDWHRG model in the high–baryon-density regime where the original constant-parameter formulation begins to fail. This leads to the modification of the conventional VDWHRG (which uses constant parameters) to obtain the new Modified van der Waals HRG model incorporating the $T - \mu_B$ dependence of the VDW parameters.

4.2 The modified van der Waals HRG (MVDWHRG) model

We discussed the formulation of the conventional VDWHRG model in Chapter 2, where we obtained the thermodynamic quantities, such as VDW pressure and energy density, given by

$$\begin{aligned} P(T,\mu) &= P^{id}(T,\mu^*) - an^2(T,\mu), \\ \epsilon(T,\mu) &= \frac{\sum_i \epsilon_i^{id}(T,\mu^*)}{1 + b\sum_i n_i^{id}(T,\mu^*)} - an^2(T,\mu). \end{aligned} \tag{4.1}$$

where $n(T,\mu)$ is the VDW number density and μ^* is the modified chemical

potential, given by

$$\mu^* = \mu - bP(T,\mu) - abn^2(T,\mu) + 2an(T,\mu). \tag{4.2}$$

The quantities $P^{id}(T,\mu^*)$ and $\epsilon_i^{id}(T,\mu^*)$ are the pressure and energy density in the ideal HRG model, which for an ith species can be written as

$$\begin{aligned} P_i^{id}(T,\mu_i) &= \pm\frac{Tg_i}{2\pi^2}\int_0^\infty p^2dp\ \ln\{1\pm\exp[-(E_i-\mu_i)/T]\}, \\ \varepsilon_i^{id}(T,\mu_i) &= \frac{g_i}{2\pi^2}\int_0^\infty \frac{E_i\ p^2dp}{\exp[(E_i-\mu_i)/T]\pm 1} \end{aligned} \tag{4.3}$$

Our methodology involves simultaneously fitting our results for pressure and energy density, obtained using Eq. (4.1), to the available lattice lQCD data for a particular value of μ_B/T. From the fitting, we extract the two free parameters, the VDW a and b parameters. We then repeat the fitting procedure for the data available for other μ_B/T values. Thus, for each value of μ_B/T, we have a set of VDW parameters.

In our calculations, we have considered a fixed hardcore radius for mesons (r_M) over all values of μ_B/T. This is under the assumption that changes of μ_B/T should affect only baryons and not mesons. In order to extract the VDW parameters a and b_B, we use the χ^2 minimization technique to obtain the best fit to available lQCD data [84] using the relation [81, 192];

$$\chi^2 = \frac{1}{N_{dof}}\sum_{i,j}\frac{\left(X_{i,j}^{lQCD}(T_j) - X_{i,j}^{model}(T_j)\right)^2}{\left(\Delta_{i,j}^{lQCD}(T_j)\right)^2}, \tag{4.4}$$

where the $X_{i,j}^{lQCD}(T_j)$ and $X_{i,j}^{model}(T_j)$ are respectively the values of i^{th} thermodynamic observable from lQCD calculations and VDWHRG model calculations at a given j^{th} temperature. The $\Delta_{i,j}^{lQCD}(T_j)$ are the values of error involved in the corresponding lQCD calculations. The number of degrees of freedom N_{dof} is given by the number of lQCD data points minus the number of fitting parameters. For different values of μ_B/T, we fit the lQCD results of pressure and energy density with VDWHRG model calculations to obtain the a and b_B parameters.

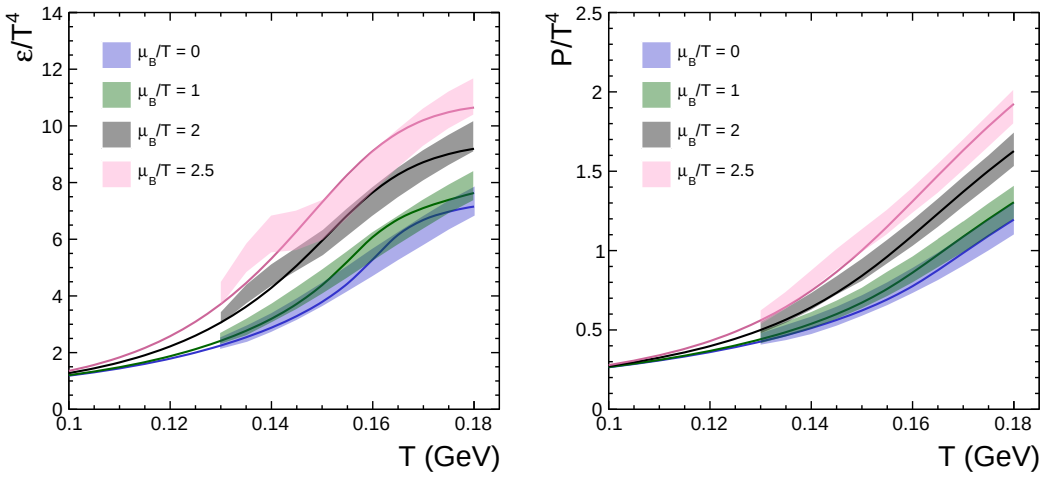

Figure 4.2: Illustration of the χ^2 fitting of the model results (solid line) to the available lQCD data (color bands) for different cases of μ_B/T values [201].

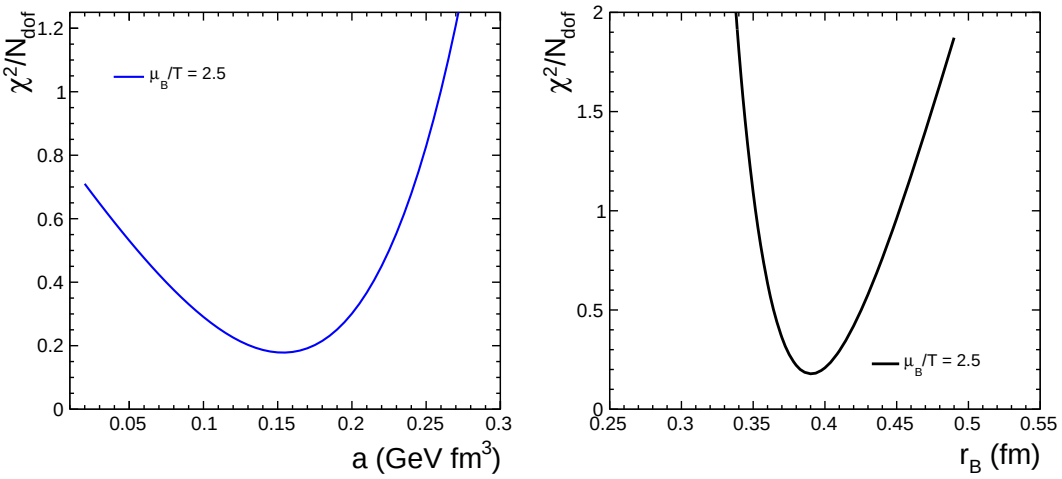

Figure 4.3: The values of χ^2/N_{dof} is shown for the fitting of parameters a and r_B when $\mu_B/T = 2.5$ [201].

Fig. 4.2 shows the comparison of lQCD data (colour band) with corresponding fit values (solid line) of scaled pressure and energy density, calculated using the Eqs. (4.1), for certain values of μ_B/T. Table 4.1 lists the obtained fit parameters

a and r_B and the corresponding χ^2/N_{dof} values for each μ_B/T considered. The Fig. 4.3 illustrates the values of χ^2/N_{dof} obtained for one case of $\mu_B/T = 2.5$ for which the best fit for the parameters is obtained for $a = 0.15$ GeV, and $r_B = 0.385$ fm.

μ_B/T	a (GeV fm^3)	r_B (fm)	$\chi^2/N_{\rm dof}$
0.0	1.650 ± 0.050	0.635 ± 0.050	1.06/20
1.0	0.786 ± 0.064	0.515 ± 0.050	0.91/20
2.0	0.275 ± 0.025	0.425 ± 0.050	1.88/20
2.5	0.150 ± 0.050	0.385 ± 0.150	3.50/20

Table 4.1: The van der Waals parameters extracted via χ^2 minimization fitting for different cases μ_B/T values. Here, r_B denotes the baryon hard-core radius, which gives the VDW repulsive parameter through the relation $b_B = (16/3)\pi r_B^3$ [201].

The extracted attractive and repulsive van der Waals parameters, a and b, are displayed as functions of μ_B/T in Fig. 4.4. Both parameters show a decreasing trend with increasing μ_B/T, indicating that higher baryon density or lower temperature progressively weakens the effective VDW interaction. This reduction of interaction strength with density is qualitatively consistent with observations reported in Ref. [202]. To parameterize this dependence, we perform fits to the obtained VDW parameters a and b values using two functional forms, a negative exponential and a quadratic polynomial, given by [201]

$$a = c_1 \exp\left(c_2 \frac{\mu_B}{T}\right), \; b = d_1 \exp\left(d_2 \frac{\mu_B}{T}\right), \tag{4.5}$$

and

$$a = e_1\left(\frac{\mu_B}{T}\right)^2 + e_2\left(\frac{\mu_B}{T}\right) + e_3, \; b = f_1\left(\frac{\mu_B}{T}\right)^2 + f_2\left(\frac{\mu_B}{T}\right) + f_3. \tag{4.6}$$

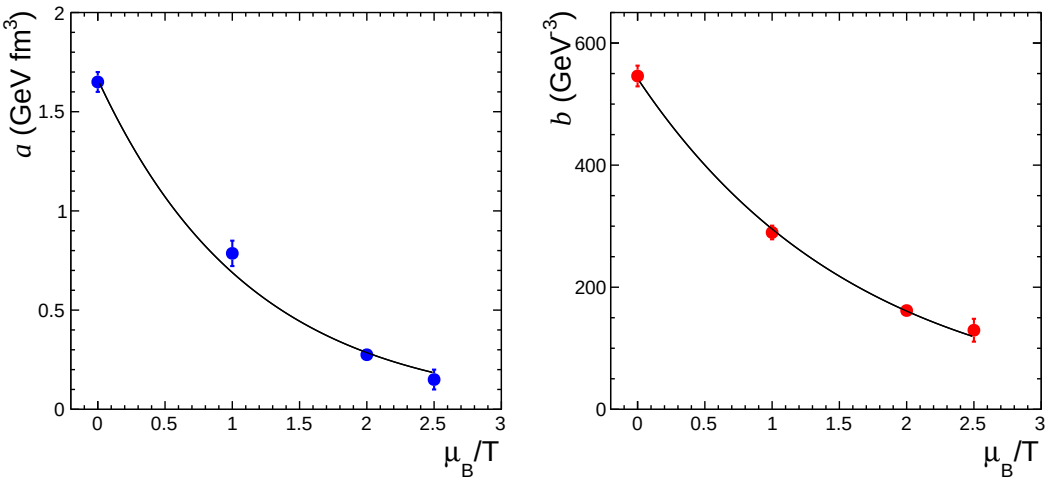

Figure 4.4: The extracted van der Waals parameters a and b, obtained from the χ^2 fits to lattice QCD data, shown as functions of μ_B/T. The solid black curves represent the corresponding negative exponential function fit to the extracted a and b values [201].

The best fit coefficients for both parametrizations are summarized in Table 4.2. To limit the number of free parameters and maintain a compact model structure, the present analysis proceeds using only the exponential parametrization in Eq. (4.5). As Fig. 4.4 clearly shows, at sufficiently large μ_B/T (i.e., high baryon density or low temperature), the interaction parameters approach very small values, driving the system toward an almost ideal HRG limit.

Since the VDW parameters now acquire an explicit dependence on μ_B/T, the resulting framework is referred to as the modified VDWHRG (MVDWHRG) model. For any fixed value of μ_B/T, however, the parameters remain constant, and the model effectively reduces to the standard VDWHRG formulation. To demonstrate the reliability of the model, we examine the fluctuations of conserved charges at chemical freeze-out, utilizing the MVDWHRG framework. Consistent with earlier analyses [203, 204], the thermodynamic parameters (T, μ_B) relevant for a given collision energy are taken at the chemical freeze-out boundary derived

Table 4.2: Functional fit to VDW parameters a and b as functions of μ_B/T and the corresponding parameters [201].

$\boldsymbol{a}$ (GeV fm^3)	$\boldsymbol{b}$ (GeV^{-3})
Exponential:	**Exponential:**
$\boldsymbol{a = c_1 \exp\left(c_2 \frac{\mu_B}{T}\right)}$	$\boldsymbol{b = d_1 \exp\left(d_2 \frac{\mu_B}{T}\right)}$
$c_1 = 1.66 \pm 0.05$ GeV fm^3	$d_1 = 541.93 \pm 15.98$ GeV^{-3}
$c_2 = -0.88 \pm 0.04$	$d_2 = -0.61 \pm 0.03$
Quadratic:	**Quadratic:**
$\boldsymbol{a = e_1\left(\frac{\mu_B}{T}\right)^2 + e_2\left(\frac{\mu_B}{T}\right) + e_3}$	$\boldsymbol{b = f_1\left(\frac{\mu_B}{T}\right)^2 + f_2\left(\frac{\mu_B}{T}\right) + f_3}$
$e_1 = 1.65 \pm 0.05$ GeV fm^3	$f_1 = 543.74 \pm 16.54$ GeV^{-3}
$e_2 = -1.04 \pm 0.09$ GeV fm^3	$f_2 = -309.55 \pm 28.44$ GeV^{-3}
$e_3 = 0.18 \pm 0.04$ GeV fm^3	$f_3 = 58.72 \pm 11.08$ GeV^{-3}

from hadron-yield systematics. So, for a given center of mass energy, we have a pair of freeze-out parameters T and μ_B, and for each of these values, a pair of VDW parameters, which works the same as the conventional VDWHRG model.

4.3 Proton number cumulants in the modified VDWHRG framework

The search for the QCD critical point, and thus the mapping of the QCD phase diagram, remains one of the major goals of various heavy-ion collision programs. Fluctuations of conserved charges provide highly sensitive probes of critical phenomena. Near the critical end point (CEP), the correlation length increases.

Since the higher-order cumulants of conserved-charge distributions scale with large powers of this length [205–209], they exhibit exceptional sensitivity to critical dynamics, even when the growth of correlations is constrained by finite system size and critical slowing down [210, 211]. The experimental conserved-charge fluctuations are directly related to the corresponding thermodynamic susceptibilities [35], and are expected to show non-monotonic behavior in the vicinity of the CEP. This has motivated extensive theoretical and experimental efforts to measure event-by-event fluctuations of net baryon number, electric charge, and strangeness. The RHIC Beam Energy Scan (BES) program has reported cumulants of net protons [15, 212–215], net charge [216], and net kaons [217] over a broad range of collision energies. Future facilities such as FAIR (CBM) and NICA aim to explore even higher values of μ_B, where signatures of the CEP are expected to be more pronounced.

As the lightest baryons and hence the most copiously produced baryonic species in heavy-ion collisions, protons serve as practical experimental proxies for net-baryon-number fluctuations. Previous studies have demonstrated that incorporating van der Waals interactions into the HRG framework significantly affects its thermodynamic behavior, producing marked deviations in higher-order cumulants relative to the ideal HRG [70, 204]. This motivates a re-examination of proton number fluctuations within our Modified VDWHRG (MVDWHRG) model, in which the interaction parameters a and b depend explicitly on μ_B and T. Such a dependence modifies the equation of state across the baryon-rich region, providing a more realistic baseline for interpreting fluctuation measurements from experiments.

To compare the model predictions with experimental data, it is essential to map the thermodynamic variables (T, μ_B) to the experimental variable, i.e., the collision energies $\sqrt{s_{\rm NN}}$. In practice, the values of T and μ_B at chemical freeze-out are obtained by fitting hadron yields measured in experiments using statistical thermal models, and a parametrization is employed to estimate these values for

a given center of mass energy. The extracted T and μ_B also determine the corresponding interaction parameters in the MVDWHRG framework, allowing for a consistent evaluation of proton-number cumulants and their ratios along the freeze-out line. In the following sections, we first derive a parametric relation connecting the thermodynamic parameters T and μ_B to the collision energy, and then we proceed to calculate the cumulant ratios for comparison with the latest available experimental data.

4.3.1 The chemical freeze-out parameters

An analysis of particle yields and their ratios from AA collisions at AGS, SPS, and RHIC energies [218–225] is performed to obtain the corresponding chemical freeze-out parameters. The estimation of chemical freeze-out parameters may depend upon the hadronic model and interactions used, as well as on the conditions, like the hadronic mass cut-off, considered in the calculations [200]. Thus, to maintain consistency across different model assumptions, we performed independent fits of the hadron yield data using the ideal HRG, VDWHRG, and MVDWHRG frameworks, employing an identical particle list in each case. This procedure allows us to extract and compare the corresponding chemical freeze-out parameters in each model. We include all hadrons and resonances listed by the PDG up to a mass cut-off of 2.25 GeV [5].

For a meaningful comparison with experimental yields of stable hadrons, the contributions from resonance decays are explicitly incorporated, with each resonance treated using its Breit–Wigner mass distribution. This procedure ensures that the model-predicted particle yields account for feed-down from higher resonances and thus reflect the experimentally measurable hadron multiplicities. In the ideal HRG framework, the primordial yield ($N_i^{\rm prim}$) of the ith hadron species can be written as [201]

$$\langle N_i^{\rm prim}(T,\mu_i)\rangle = \frac{V g_i}{2\pi^2}\int_0^\infty \frac{p^2 dp}{\exp[(E_i-\mathbf{q}_i\cdot\boldsymbol{\mu})/T]\gamma_S^{-n_S}\pm 1}, \tag{4.7}$$

where V is the system volume. The conserved charge vector and the corresponding chemical potential are given by $\mathbf{q_i}$ ($= Q_i, B_i, S_i$) and $\boldsymbol{\mu}$ ($= \mu_Q, \mu_B, \mu_S$). To account for the observed suppression of strange hadron production, a strangeness non-equilibrium factor (commonly referred to as the strangeness suppression factor) $\gamma_S \neq 1$ is introduced [67, 68, 226], where n_S denotes the number of valence strange plus anti-strange quarks in the ith hadron. The total yield of ith species including the contributions from heavier resonance decays [67, 68, 227–229] given as

$$\langle N_i \rangle = \langle N_i \rangle^{\rm prim} + \sum_R \langle N_R \rangle^{\rm prim} \langle N_i \rangle_R. \tag{4.8}$$

Here, the $\langle N_R \rangle$denotes the primordial multiplicity of resonance R, and $\langle N_i \rangle_R$ is the average number of stable daughter hadrons of type i produced from its decay and is given by $\langle N_i \rangle_R = \sum_j Br_j^R(R \to i) N_{i,j}^R$, with $Br_j^R(R \to i)$ as the branching ratio of j^{th} decay channel, and $N_{i,j}^R$ is the number of daughter hadrons (of type i) produced. All the branching ratios are taken from the PDG [5]. Incorporating the finite resonance widths by considering a Breit-Wigner (BW) distribution, Eq. (4.7) can be written as [68],

$$\begin{aligned} \langle N_i^{prim}(T, \mu_i) \rangle = \frac{V g_i}{2\pi^2} \int_{m_i^{min}}^{m_i^{max}} dm\ \rho_i^{BW}(m) \\ \int_0^\infty \frac{p^2 dp}{\exp[(\sqrt{p^2+m^2} - \mathbf{q_i}.\boldsymbol{\mu})/T] \gamma_S^{-n_s} \pm 1}, \end{aligned} \tag{4.9}$$

where the relativistic BW distribution $\rho_i^{BW}(m)$ for i^{th} resonance is given by

$$\rho_i^{BW}(m) = C_i \frac{2 m m_i \Gamma_i}{(m^2 - m_i^2)^2 + m_i^2 + \Gamma_i^2}. \tag{4.10}$$

where the BW width of ith resonance is given by Γ_i. C_i is the normalization constant so as to have $\int_{m_i^{min}}^{m_i^{max}} dm\ \rho_i^{BW}(m) = 1$. The integration is carried out over a mass interval of $[m - \delta m_l, m + \delta m_u]$, where $\delta m_l = \min[m - m_{threshold}, 2\Gamma]$ and $\delta m_u = 2\Gamma$ [67]. The weighted average of individual threshold masses over all the decay channels of i^{th} resonance, with the corresponding branching ratios as weights, gives the threshold mass $m_{threshold}$.

To reproduce the experimental hadron multiplicities, we use Eq. (4.9) together with the decay contribution from Eq. (4.8). Eq. (4.9) contains several free parameters, such as the volume V, T, γ_s, and μ_B, which are determined by fitting the model to the measured particle yields. The remaining parameters, μ_Q and μ_S, are fixed by imposing global conservation laws consistent with the initial conditions of the colliding system. For overall charge conservation, the ratio of net electric charge to net baryon number, Q/B, is required to match the corresponding ratio of participating protons to nucleons in the colliding nuclei [67, 204]. For Au–Au and Pb–Pb collisions, this ratio is approximately 0.4. Strangeness neutrality is implemented by demanding that the total net strangeness vanish. Thus, μ_Q and μ_S are obtained by solving the coupled constraints

$$\frac{N_Q}{N_B} = \frac{Q}{B} = 0.4,$$
$$N_S = 0, \tag{4.11}$$

where N_Q, N_B, and N_S denote the net charge, net baryon number, and net strangeness, respectively. Solving these relations simultaneously yields μ_Q and μ_S for each collision energy.

The experimental hadron yields measured in central Pb–Pb and Au–Au collisions by the NA49 and STAR collaborations at $\sqrt{s_{NN}}$ = 6.3, 7.7, 8.8, 12.3, 17.3, and 130 GeV [219–225] are used as inputs to extract the chemical freeze-out parameters. These parameters are obtained by minimizing the χ^2 function [201],

$$\chi^2 = \frac{1}{N_{dof}} \sum_i \frac{\left(N_i^{exp} - N_i^{model}\right)^2}{\sigma_i^2}, \tag{4.12}$$

where N_{dof} is the number of degrees of freedom, N_i^{exp} and N_i^{model} denote the experimentally measured and model-predicted multiplicities for species i, and $\sigma_i^2 = (\sigma_i^{stat})^2 + (\sigma_i^{syst})^2$ includes both statistical and systematic uncertainties.

To extend the analysis toward lower beam energies, we also include hadron yields from Au–Au collisions at $\sqrt{s_{NN}}$ = 2.7 and 4.86 GeV measured at AGS

Table 4.3: Estimated chemical freeze-out parameters in ideal HRG, VDWHRG, and MVDWHRG models for different energies [201].

$\sqrt{s_{NN}}$ (GeV)	IHRG		VDWHRG		MVDWHRG	
	T (GeV)	μ_B (GeV)	T (GeV)	μ_B (GeV)	T (GeV)	μ_B (GeV)
130	0.177	0.037	0.174	0.042	0.149	0.021
17.3	0.165	0.313	0.164	0.311	0.151	0.250
12.3	0.176	0.414	0.162	0.345	0.152	0.328
8.77	0.159	0.458	0.155	0.422	0.146	0.411
7.62	0.156	0.509	0.135	0.548	0.144	0.471
6.27	0.152	0.543	0.128	0.604	0.137	0.511
4.86	0.136	0.664	0.114	0.671	0.122	0.604
2.7	0.046	0.881	0.053	0.812	0.057	0.894

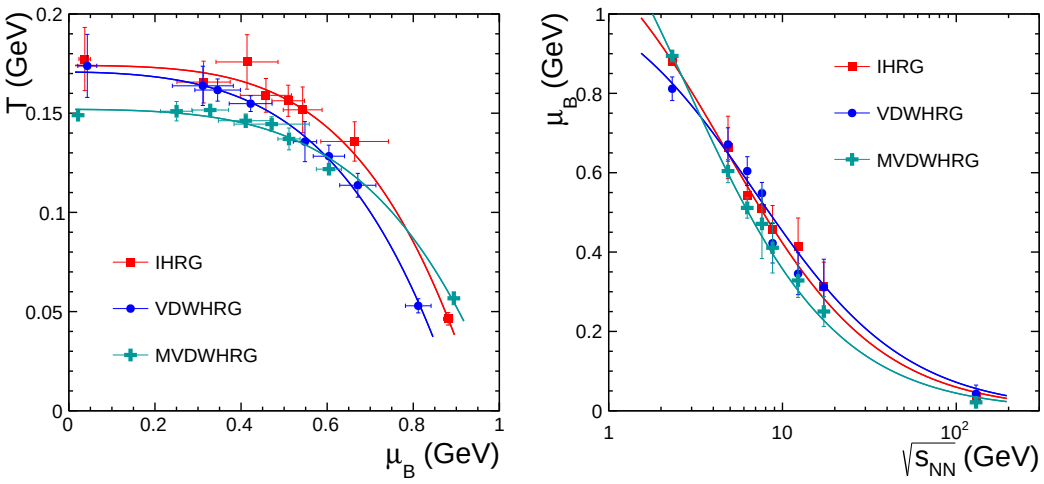

Figure 4.5: (Color Online) The freeze-out parameters obtained from the statistical fit to the experimental measurements of hadron multiplicities. The polynomial fit is shown using colored solid lines [201].

Table 4.4: Parameters relating T, μ_B and with $\sqrt{s_{NN}}$ [201].

	p_1 (GeV)	p_2 (GeV^{-1})	p_3 (GeV^{-3})	p_4 (GeV)	p_5 (GeV^{-1})
IHRG	0.174 ± 0.012	0.019 ± 0.076	0.187 ± 0.082	1.310 ± 0.071	0.210 ± 0.032
VDWHRG	0.171 ± 0.010	0.051 ± 0.073	0.189 ± 0.108	1.099 ± 0.076	0.143 ± 0.024
MVDWHRG	0.152 ± 0.002	0.021 ± 0.023	0.125 ± 0.031	1.644 ± 0.112	0.360 ± 0.049
IHRG (Cleymans et al.[203])	0.166 ± 0.002	0.139 ± 0.016	0.053 ± 0.021	1.308 ± 0.028	0.273 ± 0.008
IHRG (Poberezhnyu et al.[204])	0.152 ± 0.001	0.026 ± 0.003	0.219 ± 0.004	1.310 ± 0.006	0.278 ± 0.003
VDWHRG (Poberezhnyu et al.[204])	0.157 ± 0.002	0.0032 ± 0.0027	0.259 ± 0.004	1.094 ± 0.004	0.157 ± 0.002

energies [67, 230–233]. At such energies, the production of strange hadrons becomes highly suppressed, making exact strangeness conservation essential. Consequently, the statistical description of the grand canonical ensemble includes exact conservation of strangeness, known as the strangeness canonical ensemble (SCE) [203].

For each collision energy, the experimental yields are independently fitted using the ideal HRG, VDWHRG, and MVDWHRG models. The resulting freeze-out parameters extracted from these fits are listed in Table 4.3 and illustrated in Fig. 4.5.

The collision-energy dependence of the freeze-out temperature (T) and baryochemical potential (μ_B) is extracted following the parametrizations proposed in Refs. [200, 204]. The resulting chemical freeze-out curve is described by

$$\begin{aligned} T(\mu_B) &= p_1 - p_2\mu_B^2 - p_3\mu_B^4, \\ \mu_B(\sqrt{s}) &= \frac{p_4}{1 + p_5\sqrt{s}}. \end{aligned} \tag{4.13}$$

The fitted freeze-out trajectories for the ideal HRG, VDWHRG, and MVDWHRG models are presented through colored solid lines in Fig. 4.5. The corresponding parameters are listed in Table 4.4, where they are also compared with earlier extractions from the literature [203, 204]. These parametrizations are subsequently employed to compute the model predictions at the $\sqrt{s_{NN}}$ values relevant for comparison with experimental measurements.

4.3.2 Proton number cumulants

Cumulants are used to quantify the non-Gaussian behavior of a distribution. In the context of heavy-ion collisions and QCD, strong deviations of higher-order cumulants from baseline expectations can be interpreted as signatures of phase transitions or the vicinity of a critical point, where correlations grow, and the distribution becomes strongly non-Gaussian. Considering the distribution of an observable N (say, net proton number in an event), the average of this observable

from all the events is given by the mean, $M = \langle N \rangle$. This is the first order cumulant. The spread of the distribution is given by the second-order cumulant, the variance, $\sigma^2 = \langle (N - \langle N \rangle)^2 \rangle$. Skewness ($S$) is the third-order cumulant that quantifies the asymmetry of the distribution and reveals if fluctuations are biased towards higher or lower values. The fourth-order cumulant, known as kurtosis (κ), determines how flat or peaked a distribution is in comparison to a normal distribution. Cumulants up to fourth order (with $\Delta N = N - \langle N \rangle$) are given below [35]

$$\begin{aligned} C_1 &= \langle N \rangle, \\ C_2 &= \langle (\Delta N)^2 \rangle, \\ C_3 &= \langle (\Delta N)^3 \rangle, \\ C_4 &= \langle (\Delta N)^4 - 3\langle (\Delta N)^2 \rangle^2 \rangle, \end{aligned} \tag{4.14}$$

For a system in thermal equilibrium, these cumulants can be related to the thermodynamic susceptibilities of the corresponding conserved charge. The nth order susceptibility corresponding to a conserved charge Q can be calculated by taking the nth derivative of pressure with respect to the corresponding chemical potential as

$$\kappa_n = \frac{\partial^n}{\partial(\mu_Q/T)^n} \frac{P}{T^4}, \tag{4.15}$$

where P is the pressure of the system given by $P = \frac{1}{VT^3} \ln Z(V, \mu_Q, T)$. One can relate the number susceptibilities to the cumulants, which can be written as [35, 229]

$$\begin{aligned} k_1 &= \frac{1}{VT^3} \langle N \rangle_c = \frac{1}{VT^3} \langle N \rangle, \\ k_2 &= \frac{1}{VT^3} \langle (\Delta N)^2 \rangle_c = \frac{1}{VT^3} \langle (\Delta N)^2 \rangle, \\ k_3 &= \frac{1}{VT^3} \langle (\Delta N)^3 \rangle_c = \frac{1}{VT^3} \langle (\Delta N)^3 \rangle, \\ k_4 &= \frac{1}{VT^3} \langle (\Delta N)^4 \rangle_c = \frac{1}{VT^3} \Big(\langle (\Delta N)^4 - 3\langle (\Delta N)^2 \rangle^2 \rangle \Big), \end{aligned} \tag{4.16}$$

To remove volume dependencies and ensure a reliable comparison with experimental measurements, it is best practice to construct the ratio of these cumulants.

In this Chapter, we will look into the net proton number cumulant ratios, which are described as

$$S\sigma = \frac{\kappa_3}{\kappa_2}, \quad \frac{S\sigma^3}{M} = \frac{\kappa_3}{\kappa_1}, \quad \kappa\sigma^2 = \frac{\kappa_4}{\kappa_2}. \tag{4.17}$$

To enable a meaningful comparison with experimentally measured fluctuations, the calculations must also incorporate the effects of experimental acceptance cuts. This is implemented by transforming the momentum components (p_x, p_y, p_z) to the experimentally relevant variables of transverse momentum, rapidity, and azimuthal angle (p_T, y, ϕ). The kinematic acceptance is then imposed through appropriate cuts on y and p_T, while assuming full azimuthal coverage ($\phi = 2\pi$). With these considerations, the phase-space integration appearing in the pressure expression is written as [234].

$$\begin{aligned} P_i^{id}(T, \mu_i) = \pm \frac{T g_i}{4\pi^2} \int_{-y_{max}}^{y_{max}} dy \int_{p_T^{min}}^{p_T^{max}} dp_T \\ \times p_T \sqrt{p_T^2 + m^2} \cosh(y) \\ \times \ln\{1 \pm \exp[-\frac{(\sqrt{p_T^2 + m_i^2}\cosh(y) - \mu_i)}{T}]\}. \end{aligned} \tag{4.18}$$

The same kinematic acceptance cuts are imposed on both the primordial hadrons and the decay products originating from resonances. In the present analysis, we adopt the experimental acceptance window of $0.4 < p_T < 2.0$ GeV/c and $|y| < 0.5$, consistent with the STAR Collaboration measurements [213, 215]. This ensures a direct and reliable comparison between the model calculations and the experimental data.

Resonance decays contribute significantly to the final state proton yield and, consequently, influence proton number fluctuations. The mean proton multiplicity in the final state, $\langle \tilde{N_p} \rangle$, can be expressed as the sum of primordial protons and those originating from resonance decays [229],

$$\langle \tilde{N_p} \rangle = \langle N_p \rangle + \sum_R \langle N_R \rangle \langle N_p \rangle_R, \tag{4.19}$$

where $\langle N_p \rangle$ and $\langle N_R \rangle$ denote the primordial yields of protons and the R^{th} resonance, respectively. The average number of protons produced from the decay of resonance R is given by $\langle N_p \rangle_R = \sum_j Br_j^R N_{p_j}^R$, where Br_j^R represents the branching ratio of the j^{th} decay channel and $N_{p_j}^R$ is the number of protons produced in that channel. The total higher-order cumulants can be written as [229],

$$\begin{aligned}
\langle (\Delta \tilde{N}_p)^2 \rangle &= \langle (\Delta N_p)^2 \rangle + \sum_R \langle (\Delta N_R)^2 \rangle \langle N_p \rangle_R^2, \\
\langle (\Delta \tilde{N}_p)^3 \rangle &= \langle (\Delta N_p)^3 \rangle + \sum_R \langle (\Delta N_R)^3 \rangle \langle N_p \rangle_R^3, \\
\langle (\Delta \tilde{N}_p)^4 \rangle_c &= \langle (\Delta N_p)^4 \rangle_c + \sum_R \langle (\Delta N_R)^4 \rangle_c \langle N_p \rangle_R^4.
\end{aligned} \tag{4.20}$$

Hence, including the effects of resonance decays on higher-order moments, the generalized relation for the higher-order susceptibilities can be written as [227, 229]

$$(\kappa_n)_p = (\kappa_n)_p^{prim} + \sum_R (\kappa_n)_R^{prim} \langle N_p \rangle_R^n. \tag{4.21}$$

Thus, the total proton fluctuation receives contributions from both primordial protons and resonance decays. Moreover, since resonance decays are inherently probabilistic, the average proton yield from resonances, $\langle N_p \rangle_R$, depends on branching ratios of multiple decay channels. This stochastic nature introduces additional fluctuations in the final proton distribution, which must be accounted for in a realistic description of proton number cumulants [229]. Accounting for this probabilistic nature of resonance decays, the proton number cumulants in the final state are correspondingly modified as [229, 235, 236]

$$\langle \tilde{N}_p \rangle = \langle N_p \rangle + \sum_R \langle N_R \rangle \langle N_p \rangle_R \tag{4.22}$$

$$\begin{aligned}
\langle (\Delta \tilde{N}_p)^2 \rangle =& \langle (\Delta N_p)^2 \rangle + \sum_R \langle (\Delta N_R)^2 \rangle \langle N_p \rangle_R^2 \\
&+ \sum_R \langle N_R \rangle \langle (\Delta N_p)^2 \rangle_R,
\end{aligned} \tag{4.23}$$

$$\begin{aligned}\langle(\Delta\tilde{N}_p)^3\rangle =&\langle(\Delta N_p)^3\rangle + \sum_R \langle(\Delta N_R)^3\rangle\langle N_p\rangle_R^3 \\ &+ 3\sum_R \langle(\Delta N_R)^2\rangle\langle N_p\rangle_R\langle(\Delta N_p)^2\rangle_R \\ &+ \sum_R \langle N_R\rangle\langle(\Delta N_p)^3\rangle),\end{aligned} \tag{4.24}$$

$$\begin{aligned}\langle(\Delta\tilde{N}_p)^4\rangle_c =&\langle(\Delta N_p)^4\rangle_c + \sum_R \langle(\Delta N_R)^4\rangle_c\langle N_p\rangle_R^4 \\ &+ 6\sum_R \langle(\Delta N_R)^3\rangle\langle N_p\rangle_R^2\langle(\Delta N_p)^2\rangle_R \\ &+ \sum_R \langle(\Delta N_R)^2\rangle\Big[3\langle(\Delta N_p)^2\rangle_R^2 \\ &+ 4\langle N_p\rangle_R\langle(\Delta N_p)^3\rangle_R\Big] \\ &+ \sum_R \langle N_R\rangle\langle(\Delta N_p)^4\rangle_{R,c}.\end{aligned} \tag{4.25}$$

It is important to note that, for any specific decay channel, a resonance R can produce either zero or one (anti-)proton. This situation differs from that of lighter mesons, such as pions, for which a single decay channel may yield multiple pions. Consequently, for resonances that either decay through a single channel or for which all decay channels produce exactly one proton so that, $\langle N_p\rangle_R = 1$, the higher-order fluctuation terms, such as $\langle(\Delta N_p)^2\rangle_R$, $\langle(\Delta N_p)^3\rangle_R$, and $\langle(\Delta N_p)_c^4\rangle_R$, vanish identically [229].

Another important aspect to consider while confronting theoretical calculations of cumulants with measurements from experiments is to properly account for the effect of global baryon number conservation. Within the Grand Canonical Ensemble (GCE), conserved charges are allowed to fluctuate with an external thermal bath, as conservation is enforced only on average. In contrast, the total charge in a heavy-ion collision remains fixed. Experimentally, GCE-like conditions are effectively realized by restricting the analysis to a limited region of phase space, thereby probing only a fraction of the total system and reducing the influence of exact global conservation laws. Several studies [237–239] have dis-

cussed the role of a finite rapidity acceptance window, ΔY_{acc}. The choice of this acceptance window is crucial. For example, if $\Delta Y_{acc} \ll \Delta Y_{4\pi}$, the number of detected particles becomes too small and genuine dynamical fluctuations could get suppressed. Conversely, if the acceptance is too large, correlations arising from global baryon number conservation dominate the measured fluctuations. Therefore, even after applying experimental acceptance cuts, the residual contribution from global baryon conservation must be subtracted explicitly. We need to generalize the susceptibilities in GCE for a reliable comparison with experimental fluctuation measurements.

Various approaches have been proposed in the literature to correct fluctuation observables for conservation effects [237, 238, 240–242]. In Ref. [242], a binomial acceptance prescription was introduced within the framework of an ideal HRG. A more general treatment, known as the subensemble acceptance method (SAM), was later developed in Ref. [237], which is applicable to any arbitrary equations of state and reduces to binomial acceptance sampling in the ideal HRG limit.

Introducing an acceptance factor α, we consider a subsystem of volume $V_1 = \alpha V$ embedded within the full system of volume V. The remaining part of the system occupies a volume $V_2 = \beta V$, where $\beta = 1 - \alpha$. Both subvolumes are assumed to be sufficiently large so that intrinsic physical correlations are preserved, while total charge conservation is strictly enforced only in the full volume V. The parameter α can be related to the experimental acceptance by interpreting it as the fraction of observed charged particles [239]. For proton number fluctuations, we follow the prescription of Refs. [243, 244] and define α as the ratio of the mean proton number within the experimental acceptance to the mean baryon number in the full phase space, i.e., $\alpha = \langle N_B^{acc} \rangle / \langle N_B^{4\pi} \rangle$. The cumulants $\tilde{\kappa}_n$ evaluated within the accepted subvolume are then related to the corresponding GCE cumulants

κ_n through the SAM formalism [237–239].

$$\begin{aligned}
\tilde{\kappa}_1 &= \alpha V T^3 \kappa_1, \\
\tilde{\kappa}_2 &= \alpha V T^3 \beta \kappa_2, \\
\tilde{\kappa}_3 &= \alpha V T^3 \beta (1-2\alpha) \kappa_3, \\
\tilde{\kappa}_4 &= \alpha V T^3 \beta \Big[(1-3\alpha\beta)\kappa_4 - 3\alpha\beta \frac{\kappa_3^2}{\kappa_2} \Big], \\
\tilde{\kappa}_5 &= \alpha V T^3 \beta (1-2\alpha) \Big[(1-2\alpha\beta)\kappa_5 - 10\alpha\beta \frac{\kappa_3 \kappa_4}{\kappa_2} \Big], \\
\tilde{\kappa}_6 &= \alpha V T^3 \beta \Big[[1-5\alpha\beta(1-\alpha\beta)]\kappa_6 + 45\alpha^2\beta^2 \frac{\kappa_3^2 \kappa_4}{\kappa_2^2} \\
&\quad - 15\alpha^2\beta^2 \frac{\kappa_3^4}{\kappa_2^3} - 10\alpha\beta(1-2\alpha)^2 \frac{\kappa_4^2}{\kappa_2} \\
&\quad - 15\alpha\beta(1-3\alpha\beta) \frac{\kappa_3 \kappa_5}{\kappa_2} \Big].
\end{aligned} \tag{4.26}$$

The cumulant ratios obtained in the framework of SAM are then related to those in GCE as

$$\begin{aligned}
\frac{\tilde{\kappa}_2}{\tilde{\kappa}_1} &= (1-\alpha)\frac{\kappa_2}{\kappa_1}, \\
\frac{\tilde{\kappa}_3}{\tilde{\kappa}_1} &= \beta(1-2\alpha)\frac{\kappa_3}{\kappa_1}, \\
\frac{\tilde{\kappa}_3}{\tilde{\kappa}_2} &= (1-2\alpha)\frac{\kappa_3}{\kappa_2}, \\
\frac{\tilde{\kappa}_4}{\tilde{\kappa}_2} &= (1-3\alpha\beta)\frac{\kappa_4}{\kappa_2} - 3\alpha\beta\Big(\frac{\kappa_3}{\kappa_2}\Big)^2, \\
\frac{\tilde{\kappa}_5}{\tilde{\kappa}_1} &= \beta(1-2\alpha)\Big[(1-2\alpha\beta)\frac{\kappa_5}{\kappa_1} - 10\alpha\beta\frac{\kappa_3\kappa_4}{\kappa_2\kappa_1}\Big], \\
\frac{\tilde{\kappa}_6}{\tilde{\kappa}_2} &= [1-5\alpha\beta(1-\alpha\beta)]\frac{\kappa_6}{\kappa_2} + 45\alpha^2\beta^2\frac{\kappa_3^2\kappa_4}{\kappa_2^3} - 15\alpha^2\beta^2\frac{\kappa_3^4}{\kappa_2^4} \\
&\quad - 10\alpha\beta(1-2\alpha)^2\frac{\kappa_4^2}{\kappa_2^2} - 15\alpha\beta(1-3\alpha\beta)\frac{\kappa_3\kappa_5}{\kappa_2^2},
\end{aligned} \tag{4.27}$$

where $\beta = 1-\alpha$. In the limiting case $\alpha \to 0$, the influence of global baryon number conservation vanishes, and the resulting cumulants smoothly approach their corresponding GCE values.

Finally, we have our interacting hadron resonance gas model, the MVDWHRG, where we have incorporated the T and μ_B dependence of the VDW

parameters. We consider the experimental acceptance cuts, resonance decay contribution along with the global baryon conservation effect into the model and then calculate higher order cumulant ratios, specifically $S\sigma = \frac{\kappa_3}{\kappa_2}$, $\frac{S\sigma^3}{M} = \frac{\kappa_3}{\kappa_1}$, and $\kappa\sigma^2 = \frac{\kappa_4}{\kappa_2}$. In the Boltzmann limit, the Skellam limit for these ratios are given as

$$S\sigma = \tanh\,(\mu_B/T), \qquad \frac{S\sigma^3}{M} = 1, \qquad \kappa\sigma^2 = 1. \tag{4.28}$$

Any deviation from this limit is a potential indication of new physics that could possibly hints the vicinity of a critical point.

Fig. 4.6 illustrates the energy dependence of the cumulant ratios as functions of $\sqrt{s_{NN}}$. The net-proton fluctuation measurements from the RHIC Beam Energy Scan are shown by solid blue markers for BES-I [213–215] and solid red markers for BES-II [15]. The BES-II results correspond to $\sqrt{s_{NN}}$ = 7.7, 9.2, 11.5, 14.6, 17.3, and 27 GeV, while the BES-I program provides data at $\sqrt{s_{NN}}$ = 39, 54.4, 62.4, and 200 GeV. The black dashed curve represents the Skellam baseline, whereas the solid blue curve corresponds to predictions from the ideal HRG (IHRG) model. Results obtained within the VDWHRG framework using constant van der Waals parameters, a = 329 MeV fm^3 and b = 3.42 fm^3 [82], are shown by the solid green line. These are compared with the modified VDWHRG (MVDWHRG) results, shown by the solid red line, where the parameters a and b depend on μ_B/T according to Eq. (4.5).

It was demonstrated in Ref. [245] that deviations from the Skellam limit in the IHRG model at large baryon densities originate from quantum statistical effects. However, such quantum correlations alone are insufficient to reproduce the proton cumulant data measured in the BES-I program, indicating that their contribution is relatively small [246, 247]. In Ref. [248], a hybrid approach incorporating additional effects such as excluded volume interactions and global baryon number conservation was shown to significantly influence the cumulant ratios. That study suggested that repulsive interactions dominate the description at high $\sqrt{s_{NN}}$, whereas the observed deviations at $\sqrt{s_{NN}} \leq 20$ GeV point toward the significance

of attractive interactions. Although the VDWHRG model provides a natural

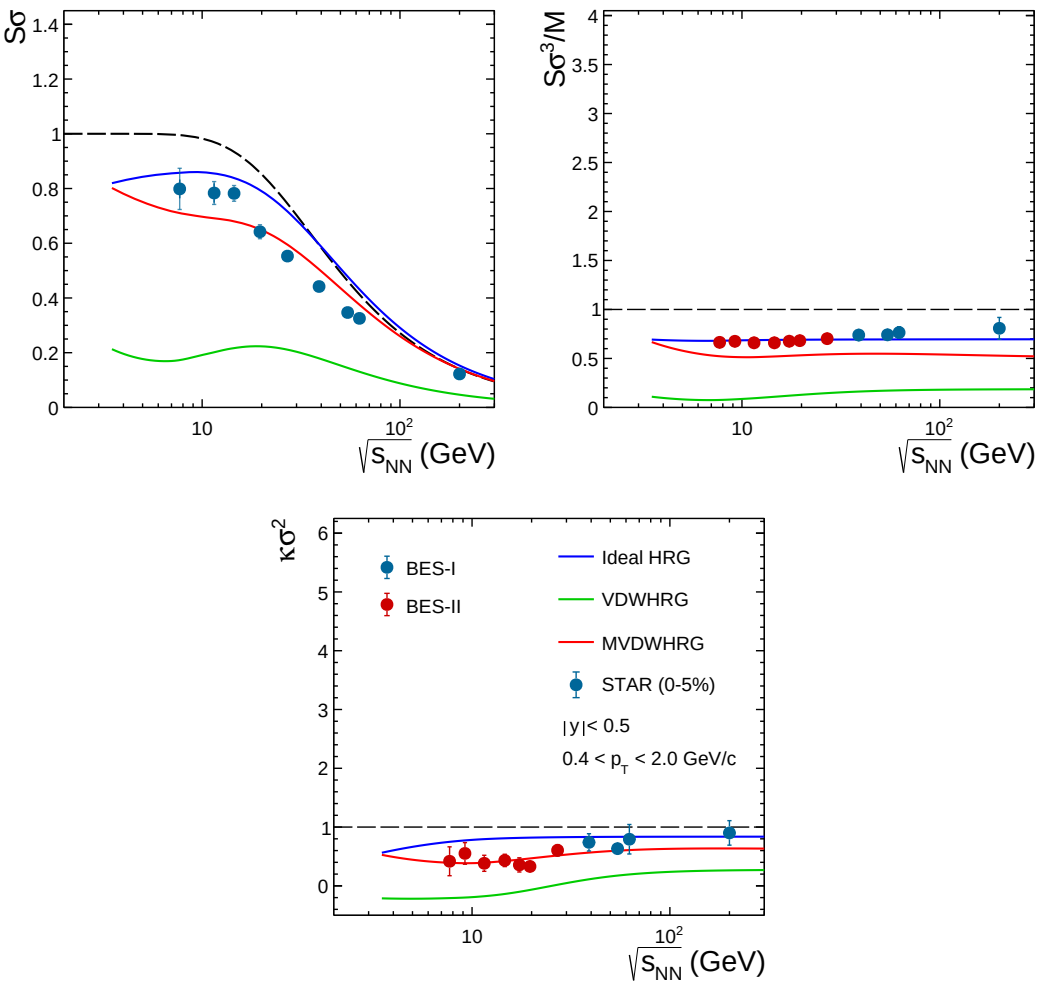

Figure 4.6: Net proton number cumulant ratios as functions of centre-of-mass energies obtained with IHRG, VDWHRG, and MVDWHRG [201], and are compared with the experimental results from STAR BES-I (blue) and BES-II (red) [15, 213] shown by the solid markers.

framework to investigate this interplay, it fails to reproduce the experimental trends quantitatively. In contrast, the MVDWHRG formulation adopted in the present work yields a substantially improved description of both BES-I data and the recent BES-II measurements. A noteworthy feature is that at low centre-

of-mass energies (corresponding to high μ_B), the MVDWHRG results gradually converge toward the IHRG baseline. This behavior can be traced back to the progressive suppression of both van der Waals parameters at large μ_B (a and b $\rightarrow 0$ at high μ_B or low $\sqrt{s_{NN}}$), effectively driving the system toward an ideal gas limit.

Several experimentally relevant effects are incorporated into our hadronic model calculations to enable a meaningful comparison with experimental measurements of fluctuation observables. These include the impact of limited kinematic acceptance [70, 249], contributions from resonance decays [227, 229], and corrections arising from global baryon number conservation [241]. The influence of these effects on the cumulant ratios is systematically examined in Fig. 4.7 for both the case of ideal HRG and MVDWHRG, and the results are also compared with experimental data. The black dotted curve in Fig. 4.7 represents the baseline cumulant ratios obtained without including any of the above-mentioned corrections. The cyan dashed curve corresponds to the results after implementing the kinematic acceptance cuts in rapidity and transverse momentum, consistent with the STAR experimental conditions [15, 213–215]. While these acceptance effects are found to be negligible in the case of the ideal HRG, they lead to noticeable modifications in all cumulant ratios within the MVDWHRG framework across the entire $\sqrt{s_{\rm NN}}$ range considered.

In accordance with earlier studies [227, 229], identical acceptance cuts are applied to both primordial (anti)protons and resonances. Although, in principle, different cuts may be expected for decay products, it has been argued in Ref. [250] that such differences introduce corrections smaller than 1% and can therefore be safely neglected. The inclusion of resonance decay contributions, shown by the blue dashed curve, results in a substantial deviation from the simple HRG expectations. This behavior can be understood from the appearance of the factor $\langle N_p \rangle_R$ in Eq. (4.21), which takes values between zero and one. Consequently, higher powers of this factor lead to a strong suppression of higher-order cumulants. As

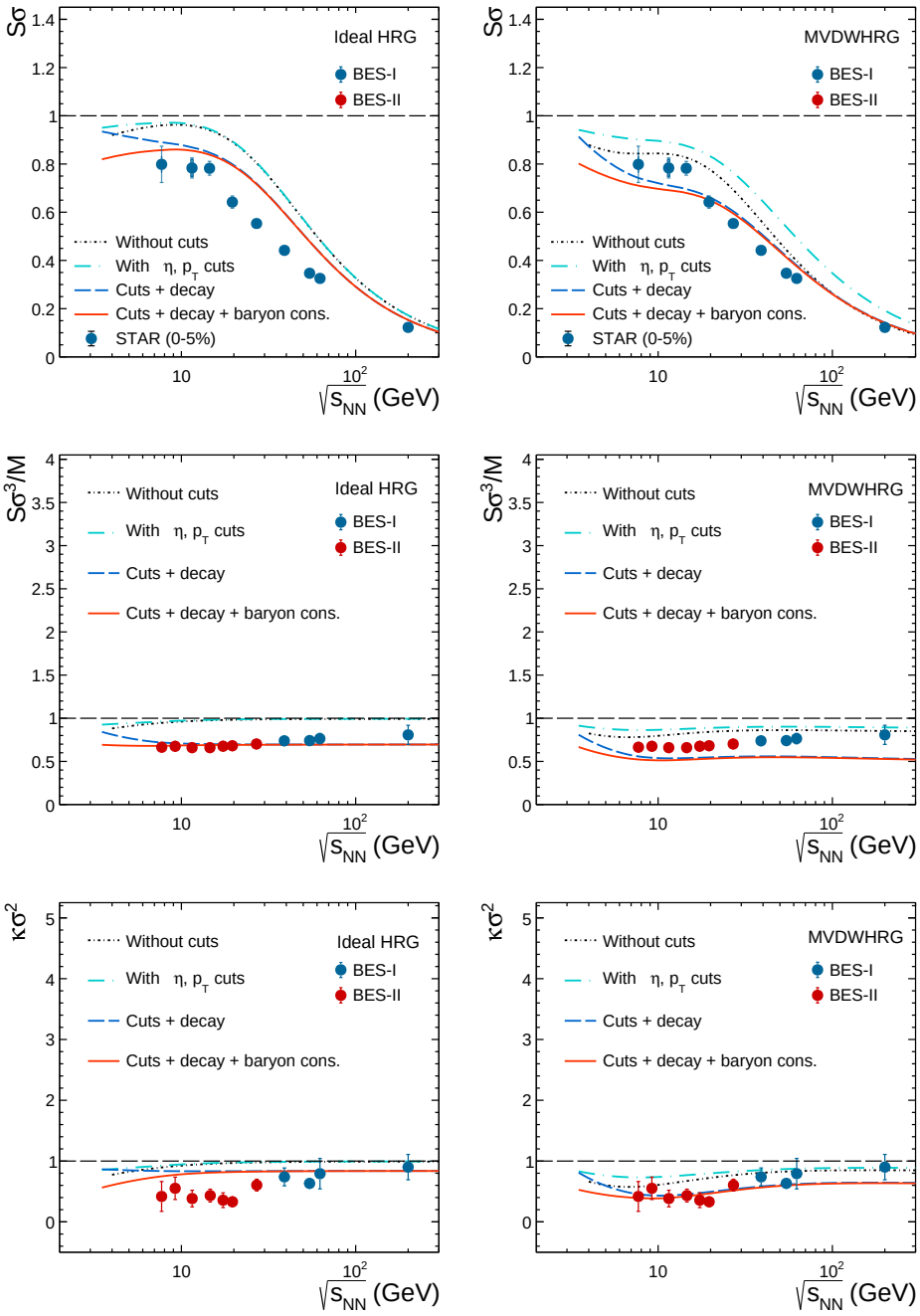

Figure 4.7: The effect of applying acceptance cuts, resonance decay contribution, and corrections due to global baryon conservation for the cumulant ratios is presented for ideal HRG (left) and MVDWHRG (right) [201], and is compared with measurements from STAR BES-I (blue) and BES-II (red) programs [15, 213].

a result of resonance decays, the observable $S\sigma$ moves closer to the experimental measurements at high $\sqrt{s_{\rm NN}}$ within the MVDWHRG model. In contrast, for $S\sigma^3/M$, the deviation from the Skellam baseline becomes more pronounced in MVDWHRG compared to IHRG, and this deviation is further enhanced once decay effects are included. The correction due to global baryon conservation is implemented through the acceptance factor α, as discussed earlier in this section. The solid red curve in Fig. 4.7 represents the full calculation, incorporating acceptance cuts, resonance decays, and baryon conservation simultaneously. The influence of global baryon conservation is found to be most significant at lower collision energies for all cumulant ratios in both the ideal HRG and MVDWHRG models. This behavior arises because, at low $\sqrt{s_{\rm NN}}$, a substantial fraction of the total baryon number is transported to the midrapidity region [248], making midrapidity measurements particularly sensitive to baryon number conservation effects.

We further extend our analysis to higher-order fluctuation observables by evaluating the cumulant ratios κ_5/κ_1 and κ_6/κ_2, and compare our results with the most recent measurements reported by the STAR collaboration [214]. The comparison is presented in Fig. 4.8. For the 0–40% centrality class, the experimental data for κ_5/κ_1 are found to oscillate around zero, exhibiting only a weak dependence on the collision energy, except at the lowest values of $\sqrt{s_{NN}}$. Both the ideal HRG and MVDWHRG frameworks reproduce the overall trend of the data reasonably well, although neither model is able to describe the measurements at $\sqrt{s_{NN}} = 3$ and 7.7 GeV. A notable distinction between the two models is observed across the explored energy range. The ideal HRG results, shown by the solid blue curve, remain positive for all $\sqrt{s_{NN}}$ and gradually approach zero as the collision energy decreases. In contrast, the MVDWHRG predictions, represented by the solid red curve, yield negative values at higher energies and smoothly converge toward the ideal HRG behavior at lower $\sqrt{s_{NN}}$. For the same centrality selection, the ratio κ_6/κ_2 is also compatible with zero except for $\sqrt{s_{NN}} = 7$ GeV, where

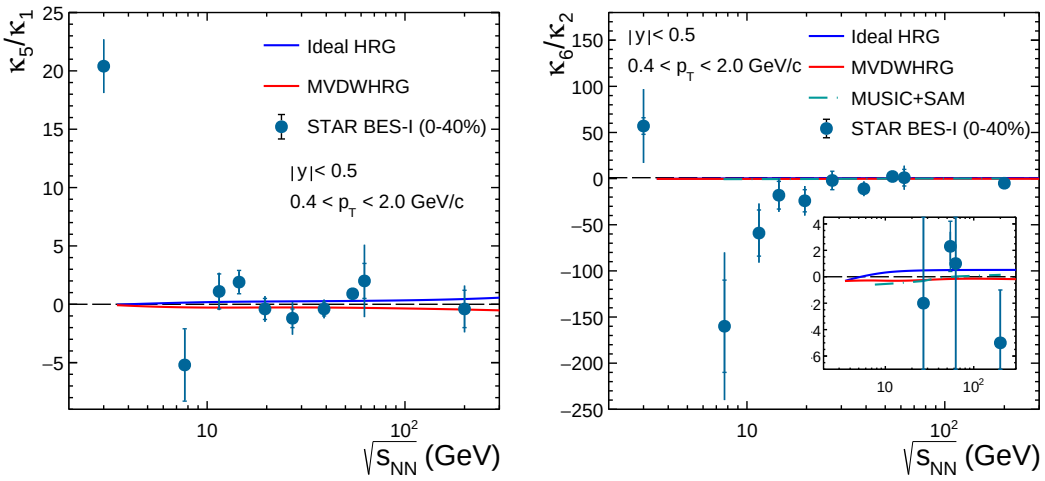

Figure 4.8: The centre-of-mass energy dependence of higher-order cumulant ratios for the ideal HRG, shown by a blue solid curve, and for MVDWHRG, shown by a red solid curve [201]. Ratios obtained using hydrodynamic calculation [248] are shown in dotted-dashed lines. Solid markers are for the BES-I results from STAR [214] .

it becomes negative with large uncertainty and turns positive only at $\sqrt{s_{NN}} = 3$ GeV. Within the ideal HRG framework, the qualitative behavior of κ_6/κ_2 closely resembles that of κ_5/κ_1, showing a monotonic decrease toward lower collision energies while remaining positive over most of the considered $\sqrt{s_{NN}}$ range, except at the lowest energies where it turns negative. On the other hand, the MVDWHRG results for κ_6/κ_2 remain negative throughout the entire energy interval and gradually merge with the ideal HRG estimates at low $\sqrt{s_{NN}}$. It is worth emphasizing that the trends obtained within the MVDWHRG model show qualitative consistency with the hydrodynamic calculations reported in Ref. [248], adding further support to the role of interaction effects and medium modifications in shaping higher-order baryon number fluctuations.

In this work, we obtain a T and μ_B dependent parametrization for the van der Waals (VDW) attractive (a) and repulsive (b) interaction parameters. Using

these modified interaction strengths, we investigate proton number fluctuations within the framework of the modified van der Waals HRG (MVDWHRG) model across a wide range of centre of mass energies. Our analysis demonstrates that the MVDWHRG approach provides an improved description of the proton fluctuation measurements reported by the RHIC BES-I and BES-II programs. We further extend the study to higher-order cumulants and perform a direct comparison with available experimental data. It is, however, to be noted that the conventional liquid–gas phase transition expected from VDW-type interactions does not manifest within the present formulation. This behavior arises because both a and b decrease exponentially with increasing μ_B/T, causing the interacting system to gradually approach the ideal HRG limit at large μ_B/T. However, comparisons with χEFT results at $T = 0$ GeV [251] indicate that the VDW parameters at extremely high μ_B may exceed the minimum values obtained from our lattice-based fits. This suggests that the interaction parameters likely attain a minimum and subsequently increase at larger μ_B/T, thereby deviating from the simple exponential behavior assumed here and potentially signaling the emergence of critical dynamics. At present, a quantitative investigation of this regime is limited by the scarcity of lattice QCD data at high μ_B and by the restricted availability of χEFT results. Exploring alternative theoretical strategies to bridge these first-principles approaches would therefore be highly valuable for achieving a comprehensive understanding of the QCD phase structure in the full $T - \mu_B$ plane.

Chapter 5

Upsilon production and polarization measurements in pp collisions at $\sqrt{s} = 13.6$ TeV with ALICE

The production of quarkonium in high-energy collisions is of particular interest for study, as it offers a unique opportunity to investigate the dynamics of QCD in both the vacuum and a medium. A bound state comprising a heavy quark and an anti-quark pair is known as a quarkonium, such as a charmonium ($c\bar{c}$) and bottomonium ($b\bar{b}$). They are produced in the initial stages of a collision through the hard scatterings, where the momentum transfer among the partons is very high. Although the production mechanism of quarkonium states, such as the J/ψ, in hadronic collisions, like pp collisions, is not fully understood, it has been utilized as a probe of the deconfined medium created in heavy-ion collisions. It is expected that if a medium is created in a heavy-ion collision, it can modify the potential between the quark-antiquark pair of the quarkonium through color screening and can lead to the dissociation of bound states at sufficiently high temperatures. This leads to a significant suppression in the yield of these quarkonium states in heavy-ion collisions in comparison to a single pp collision. The dissociation temperature depends upon the binding energy (or the size) of the quarkonium. Consequently, in both the charmonium and bottomonium families,

excited states dissociate at a lower temperature than the corresponding ground state. However, it is noteworthy to mention that at higher colliding energies, another interesting phenomenon, the recombination of the quark and anti-quark that are close in the phase space, can occur. This can enhance the yield of the quarkonia, especially in the low transverse momentum region.

Moreover, the measurements of quarkonium production in pp collisions can enhance our understanding of both perturbative and non-perturbative aspects of QCD. The production of heavy quarks and anti-quarks occurs at very high energies and requires a large momentum transfer, where perturbative QCD can be applied. Further evolution of a bound state out of these quark-antiquark pair involves non-perturbative QCD, in which the typical momentum scale is of the order of their relative momentum in the range of $\sim$ 1 GeV [27]. Therefore, the theoretical description of quarkonium production is commonly formulated within a factorized framework that separates short-distance perturbative processes from long-distance non-perturbative dynamics. The perturbative component is calculated using leading order (LO) and/or next-to-leading order (NLO) pQCD matrix elements that include heavy quark–antiquark pair production, gluon excitation, and gluon splitting, and is typically implemented in event generators such as PYTHIA and EPOS [27]. Several phenomenological models have been proposed to understand the non-perturbative nature of quarkonium formation. This includes the Color-Evaporation Model (CEM), where the heavy quark-antiquark pair, produced in any color or spin state, interacts with the surrounding color field and produces a colorless quarkonium state with a probability factor F derived from experimental data [252, 253]. It treats quarkonium formation as a fixed fraction of all heavy quark pairs produced below the open heavy-flavor threshold. A more rigorous and systematic approach is provided by Non-Relativistic QCD (NRQCD), which employs an effective field theory expansion in the heavy-quark relative velocity and factorizes quarkonium production into short-distance coefficients calculable in perturbative QCD and nonperturbative long-distance

matrix elements [254]. Depending on the sub-process considered into account, the quarkonium production in the NRQCD model can follow two different mechanisms, such as the Color-Singlet model (CSM) and Color-Octet Mechanism (COM) [253, 254]. The CSM assumes that the heavy quark–antiquark pair is produced directly in a color-singlet state with the same quantum numbers as the final quarkonium, with the hadronization process treated perturbatively, i.e., there is no evolution of the quantum state of the pair from the production to its hadronization [253]. On the other hand, the COM involves Long-Distance Matrix Elements (LDMEs) for the hadronization probability of a heavy quark-antiquark pair to a stable quarkonium [253, 255].

Despite decades of extensive experimental and theoretical efforts, a unified and quantitatively consistent description of quarkonium production within QCD remains elusive. Early measurements of differential quarkonium cross sections at high transverse momentum (p_{T}) revealed large discrepancies with leading-order predictions of the CSM, highlighting the inadequacy of simple production mechanisms [31, 256]. The introduction of the NRQCD framework, which allows quarkonia to form via intermediate color-octet states [254], significantly improved agreement with production yields. However, this success relies on long-distance matrix elements that are not calculable from first principles and must be obtained by fitting to experimental data, leading to sizable theoretical uncertainties and limited predictive power. Subsequent next-to-leading-order calculations in the color-singlet channel enhanced the yields and reduced the apparent need for large color-octet contributions [31, 257], thereby demonstrating the inconsistencies among various competing theoretical approaches. As a result, differential cross-section measurements alone are insufficient to uniquely constrain quarkonium production mechanisms. In this context, polarization measurements of vector quarkonium states ($J^{PC} = 1^{--}$), measured through their decay daughters, is expected to provide essential and independent observables that are highly sensitive to the underlying production dynamics and offer a powerful means to

discriminate between theoretical models.

5.1 Quarkonia polarization

The angular distribution of decay products is governed by the intrinsic properties of the decaying particle and its interaction dynamics. In particular, it encodes information on the particle's polarization, namely the angular momentum state in which it is produced, which is determined by the underlying production mechanism and the specific kinematic and experimental conditions. Polarization measurements therefore provide direct access to the internal production dynamics of the particle and constitute a sensitive probe of the fundamental interactions responsible for its formation [32]. Vector particles occupy a central role in polarization studies, as their spin alignment directly reflects the mechanism of their couplings to fermions and gauge bosons. Experimentally, vector particles are particularly advantageous since they can be reconstructed through their dilepton decay channels, which provides clean experimental detection and theoretical interpretations. However, it has been seen that different approaches to production mechanism models have very different predictions for polarization of the produced quarkonium states. In NRQCD calculations dominated by color-octet contributions, quarkonia, such as J/ψ and $\psi(2S)$ are expected to become increasingly transversely polarized at high transverse momentum. In contrast, next-to-leading-order color-singlet calculations predict a strong longitudinal polarization over a wide p_{T} range. It is expected that the experimental measurements can be easily used to discriminate between the two descriptions. However, experimental results are again surprising to both these models. As illustrated in Fig. 5.1, the LHCb results for pp collisions at $\sqrt{s}$=7 TeV [258] show that the measured polarization parameter λ_θ remains close to zero, indicating an almost unpolarized or weakly longitudinally polarized J/ψ, is clearly not in line with any of the theoretical expectations. This discrepancy highlights the incomplete understanding of

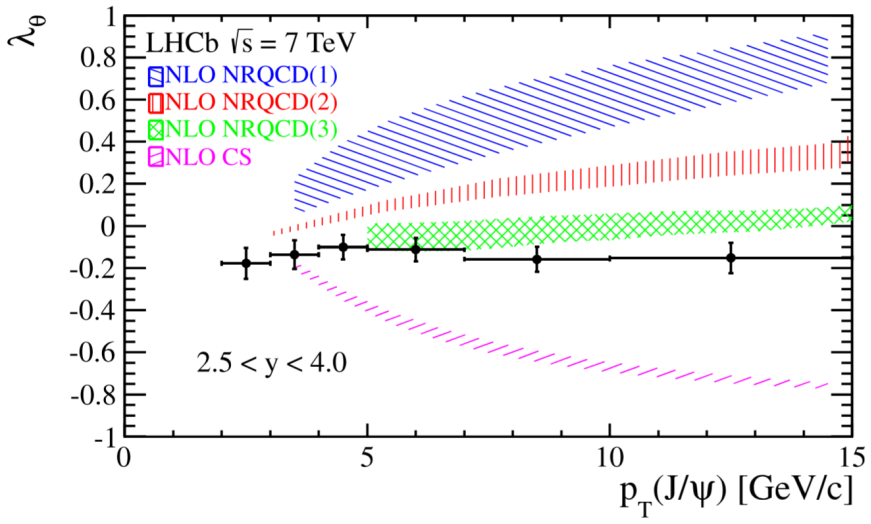

Figure 5.1: Polarization parameter λ_θ measurements for prompt J/ψ from LHCb is compared with different NRQCD predictions [258].

quarkonium production dynamics and underlines the critical role of polarization measurements in constraining and discriminating between competing theoretical models.

Being massive, the bottomonium (Υ) states (comprising $b\bar{b}$) are expected to satisfy the non-relativistic approximation better than the charmonium states, making the Υ system a particularly stringent test of NRQCD. However, existing polarization measurements of the Υ (1S) state remain inconclusive. Results from the Tevatron indicate either unpolarized (from CDF collaboration [259]) or longitudinally polarized (from $D\varnothing$ collaboration [260]) production for $p_T <$ 25 GeV/c in helicity frame. At lower energies, fixed-target measurements [261] reveal yet strange behavior. While the combined Υ (2S) and Υ (3S) states exhibit strong transverse polarization, the Υ (1S) is only weakly polarized, despite sharing identical quantum numbers. This behavior suggests a possible role of feed-down contributions [31]. Moreover, the latest polarization measurements of Υ (nS) (n = 1, 2, 3) at $\sqrt{s}$ = 7 TeV by CMS [262] and at $\sqrt{s}$ = 7 and 8 TeV by LHCb [263] shows no polarization. Overall, the lack of a consistent and pre-

cise description of bottomonium polarization limits our further understanding of quarkonium production and polarization dynamics. In this thesis, we attempt to measure the Υ (nS) polarization in pp collisions at $\sqrt{s} = 13.6$ TeV to obtain high precision results as well as to investigate if there is any effect of high energy collisions on the production and polarization dynamics of the Upsilon states.

5.1.1 Angular distribution and polarization

Polarization arises when a particle is preferentially produced in a specific state out of the possible eigenstates of the angular momentum projection J_z along a chosen quantization axis, following the angular momentum conservation and the symmetries of the strong and electromagnetic interactions. Vector particles like J/ψ, $\psi(2S)$, Υ (nS), with $J^{PC} = 1^{--}$, can be in any of the eigenstates $J_z =$ +1, -1, or 0, or a superposition of these three states. The polarization describes the relative population of the three spin eigenstates that combine to form the observed state of a vector particle. This composition is determined by the underlying production mechanism and the specific experimental conditions [31, 32]. Experimentally, polarization corresponds to the average J_z content of the particle ensemble, and is measured through the angular distribution of decay products in the particle's rest frame. By collecting a large sample of decays and performing a shape analysis of these angular distributions, the average spin alignment of the produced particles can be extracted. An isotropic distribution corresponds to an ensemble that is, on average, unpolarized, whereas any observed anisotropy indicates the presence of polarization in the production process.

Vector quarkonia can acquire polarization through several production mechanisms governed by helicity conservation, a fundamental property of both QED and QCD in the relativistic (massless) limit. The helicity operator, defined as the projection of the spin along the momentum direction, coincides with chirality for massless fermions, implying that chirality conservation enforces helicity con-

servation [31, 32]. In electron–positron annihilation via an intermediate virtual photon, helicity conservation in the relativistic limit requires the annihilating leptons to have opposite helicities. In the laboratory frame, with antiparallel momenta, their spins are aligned, and angular momentum conservation then leads to the production of a $c\bar{c}$ pair with a dominant angular momentum projection of $J_z = \pm 1$ (assuming orbital angular momentum $L = 0$ for ground state). A similar argument holds in QCD. In the massless limit, quark helicity is conserved, and charmonia produced via quark–antiquark annihilation through an intermediate gluon are therefore expected to be transversely polarized. At higher transverse momenta, quarkonium production is increasingly dominated by gluon fragmentation processes, in which an almost on-shell gluon fragments into a heavy quark–antiquark pair. Since the fragmenting gluon is predominantly transversely polarized, helicity conservation implies that the resulting quarkonium should inherit this transverse polarization, leading again to a preference for $J_z = \pm 1$ at asymptotically large p_{T} [31, 32].

In this thesis, we measure the production of Υ (nS) states and the resonance ratio as a function of p_{T}. In addition to this, the major focus is on the polarization measurement of the $\Upsilon(1S)$ state. The leptonic decay channel of Υ (1S), in particular $\Upsilon(1\mathrm{S}) \to \mu^+\mu^-$ with a branching fraction of 2.48 ± 0.05 %, provides a clean signal for experimental measurements of polarization of the parent particle as well as for theoretical interpretations. Let us consider a Υ (1S) meson (same holds true for any other vector meson with $J^{PC} = 1^{--}$), where it is formed as a superposition of the three $J = 1$ eigenstates, namely, $J_z = +1$, -1, 0 with respect to polarization axis z as [31]

$$|\Upsilon(1S)\rangle = b_{+1}|{+1}\rangle + b_{-1}|{-1}\rangle + b_0|0\rangle \tag{5.1}$$

The analysis is carried out in the Υ (1S) rest frame, where the common emission axis of the two decay leptons defines the reference z' axis, conventionally chosen along the direction of the positively charged lepton (here μ^+).

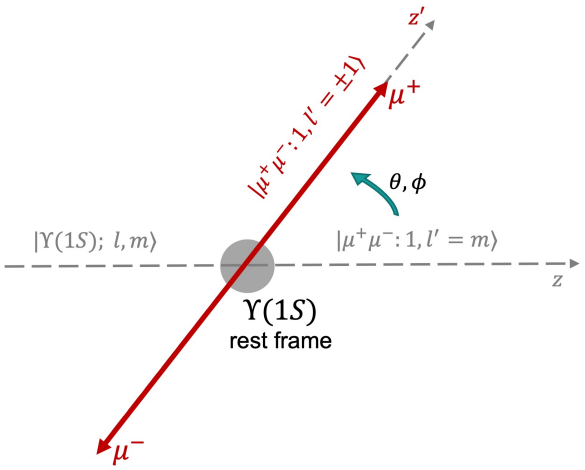

Figure 5.2: Schematic representation showing the decay of ϒ (1S) in its rest frame [31].

The dilepton decay $\Upsilon(1S) \to \mu^+\mu^-$ is studied in the ϒ (1S) rest frame. For massless leptons, helicity conservation implies that the lepton pair produced via an intermediate virtual photon carries angular momentum projection ±1 along the lepton emission axis (z'), so that we can represent it as an eigenstate of $J_{z'}$, $|\mu^+\mu^-; 1, l'\rangle$, with $l' = \pm 1$. In order to relate this natural decay axis to the chosen polarization axis, where we can express this state as a superposition of eigenstates of J_z, $|\mu^+\mu^-; 1, l\rangle$ (where $l = 0, \pm 1$), a rotation of the angular momentum eigenstates is performed using Wigner rotation matrices. The transformation using rotation $R(\alpha, \beta, \gamma)$ from a set of axes (x, y, z) to (x', y', z') is given by [31]

$$|J, M'\rangle = \sum_M D^J_{MM'}(R)\,|J, M\rangle, \tag{5.2}$$

where the rotation matrix elements $D^J_{MM'}$ are given by

$$D^J_{MM'}(\alpha, \beta, \gamma) = e^{-iM\alpha}\, d^J_{MM'}(\beta)\, e^{-iM'\gamma} \tag{3}$$

in terms of reduced matrix elements

$$d^J_{MM'}(\beta) = \sum_{t=\max(0,M-M')}^{\min(J+M,J-M')} (-1)^t \times \frac{\sqrt{(J+M)!(J-M)!(J+M')!(J-M')!}}{(J+M-t)!(J-M'-t)!\,t!\,(t-M+M')!} \times \left(\cos\frac{\beta}{2}\right)^{2J+M-M'-2t} \left(\sin\frac{\beta}{2}\right)^{2t-M+M'}. \quad (5.3)$$

In the present case, the required rotation aligns the original quantization axis z with the dilepton emission axis z'. The most general rotation accomplishing this transformation is parameterized by the Euler angles $\beta = \theta$ and $\alpha = -\gamma = \phi$. Consequently, the dilepton angular momentum state can be expressed as a superposition of the eigenstates of the J_z operator as [31]

$$|\mu^+\mu^-; 1, l'\rangle = \sum_{l=0,\pm1} D^1_{ll'}(\phi, \theta, -\phi)\, |\mu^+\mu^-; 1, l\rangle \quad (5)$$

The decay amplitude corresponding to a given spin projection, Υ(1S) (m) $\rightarrow$ $\mu^+\mu^-$ (l′) can be written as

$$B_{ml'} = \sum_{l=0,\pm1} D^{1*}_{ll'}(\phi, \theta, -\phi)\, \langle \mu^+\mu^-;\, 1, l \,|\, \mathcal{B} \,|\, \Upsilon(1S);\, 1, m\rangle = B\, D^{1*}_{ml'}(\phi, \theta, -\phi). \quad (5.4)$$

where the transition operator $\mathcal{B}$ is of the form $\langle \mu^+\mu^-;\, 1, l \,|\, \mathcal{B} \,|\, \Upsilon(1S);\, 1, m\rangle = B\ \delta_{ml}$ because of angular momentum conservation, with the constant B being independent of m as a consequence of rotational invariance. The total amplitude for $\Upsilon(1S) \rightarrow \mu^+\mu^-(l')$, where Υ (1S) is given by the superposition as in Eq. 5.1 is given by [31]

$$B_{l'} = \sum_{m=0,\pm1} b_m B\ D^{1*}_{ml'}(\phi, \theta, -\phi) = \sum_{m=0,\pm1} a_m\ D^{1*}_{ml'}(\phi, \theta, -\phi) \quad (5.5)$$

The probability of transition is then obtained by squaring and summing over the unobserved spin alignments ($l' = \pm 1$). Using Eq. (3), together with the explicit expressions of the Wigner d-functions, $d^1_{0,\pm1} = \pm\sin\theta/\sqrt{2}$, $d^1_{\pm1,\pm1} = (1+\cos\theta)/2$, and $d^1_{\pm1,\mp1} = (1-\cos\theta)/2$ (from Eq. (5.3), the most general angular distribution for the decay of a vector quarkonium into a lepton pair can be written as [31, 32]

$$\begin{aligned} W(\cos\theta,\phi) &\propto \sum_{l'=\pm1} |B_{l'}|^2 \\ &\propto \frac{\mathcal{N}}{3+\lambda_\theta}\Big(1 + \lambda_\theta \cos^2\theta \\ &\quad + \lambda_\phi \sin^2\theta\cos 2\phi + \lambda_{\theta\phi}\sin 2\theta\cos\phi \\ &\quad + \lambda^\perp_\phi \sin^2\theta \sin 2\phi + \lambda^\perp_{\theta\phi}\sin 2\theta \sin\phi\Big), \end{aligned} \tag{5.6}$$

with

$$\mathcal{N} = |a_0|^2 + |a_{+1}|^2 + |a_{-1}|^2,$$

and

$$\begin{aligned} \lambda_\theta &= \frac{\mathcal{N} - 3|a_0|^2}{\mathcal{N} + |a_0|^2}, \\ \lambda_\phi &= \frac{2\,\mathrm{Re}[a^*_{+1}a_{-1}]}{\mathcal{N} + |a_0|^2}, \\ \lambda_{\theta\phi} &= \frac{\sqrt{2}\,\mathrm{Re}[a^*_0(a_{+1} - a_{-1})]}{\mathcal{N} + |a_0|^2}, \\ \lambda^\perp_\phi &= \frac{2\,\mathrm{Im}[a^*_{+1}a_{-1}]}{\mathcal{N} + |a_0|^2}, \\ \lambda^\perp_{\theta\phi} &= \frac{-\sqrt{2}\,\mathrm{Im}[a^*_0(a_{+1} + a_{-1})]}{\mathcal{N} + |a_0|^2}. \end{aligned} \tag{5.7}$$

It is important to note that no choice of the decay amplitudes a_m, and hence of the production amplitudes b_m, can make all polarization parameters in Eq. (5.6) vanish simultaneously. This implies that the decay angular distribution of a $J = 1$ state is never intrinsically isotropic [31]. Even if a special superposition of different production mechanisms were to accidentally cancel all anisotropies, such a case

would still correspond to a non-trivial physical polarization scenario, for example, arising from spin-randomization effects or from (semi-)exclusive production topologies involving correlated final-state particles. Polarization is therefore an intrinsic property of quarkonium states. This observation is particularly relevant given that most Monte Carlo event generators assume isotropic dilepton decays for quarkonium production in hadronic collisions, an assumption that directly affects acceptance corrections and, in turn, the normalization and kinematic dependence of measured cross sections.

In this work, only inclusive production is considered. The experimentally accessible xz plane therefore coincides with the production plane defined by the momenta of the colliding particles and the decaying quarkonium [31]. Although the last two terms in Eq. (5.6) introduce reflection asymmetries at the level of individual events with respect to the production plane, these terms vanish after averaging when only parity-conserving processes contribute. Consequently, the terms proportional to $\sin^2\theta \sin 2\phi$ and $\sin 2\theta \sin\phi$ are not observable.

Hence, the polarization of the Υ (1S) state can be measured by analyzing the angular distribution of the leptons that are produced from its decay, $\Upsilon(1S) \to \mu^+\mu^-$, using [31, 32]

$$\boxed{W(\cos\theta, \phi) \propto \frac{1}{3+\lambda_\theta}\left(1 + \lambda_\theta \cos^2\theta + \lambda_\phi \sin^2\theta \cos 2\phi + \lambda_{\theta\phi} \sin 2\theta \cos\phi\right)}. \quad (5.8)$$

where the polarization parameters are given by λ_θ, λ_ϕ, and $\lambda_{\theta\phi}$. These shape parameters altogether determine if the parent particle is polarized. For instance, (λ_θ, λ_ϕ, $\lambda_{\theta\phi}$) = (0, 0, 0) shows that the particle is unpolarized. On the other hand, (λ_θ, λ_ϕ, $\lambda_{\theta\phi}$) = (+1, 0, 0) or (-1, 0, 0) indicates a pure transverse or pure longitudinal polarization, respectively.

For the precision of measurement, an alternative to the multi-parameter fit to the function in Eq. (5.8) is done by taking one-dimensional angular distributions, obtained by integrating over ϕ and $\cos\theta$, so as to have

$$W(\cos\theta) \propto \frac{1}{3+\lambda_\theta}\left(1 + \lambda_\theta \cos^2\theta\right), \quad (5.9)$$

and

$$W(\phi) \propto 1 + \frac{2\lambda_\phi}{3+\lambda_\theta}\cos 2\theta. \tag{5.10}$$

The diagonal term $\lambda_{\theta\phi}$ can be extracted by defining a variable $\tilde{\phi}$ as

$$\tilde{\phi} = \phi - \frac{3}{4}\pi, \quad (\cos\theta < 0)$$
$$\tilde{\phi} = \phi + \frac{1}{4}\pi, \quad (\cos\theta > 0)$$

which results in the $\tilde{\phi}$ distribution as

$$W(\tilde{\phi}) \propto 1 + \frac{\sqrt{2}\lambda_{\theta\phi}}{3+\lambda_\theta}\cos 2\tilde{\phi}. \tag{5.11}$$

5.1.2 Reference frames

In the two-body decay of a vector particle, the angular distribution of the back-to-back decay products provides direct information on the polarization of the parent state. The extraction of the shape parameters λ_θ, λ_ϕ, and $\lambda_{\theta\phi}$ of the distribution Eq. (5.8) requires the definition of a reference coordinate system in the particle rest frame, in which the momentum of one decay product is described by spherical angles. Although this choice is, in principle, arbitrary, it can significantly affect the numerical values of the measured polarization parameters and, therefore, their physical interpretation [31, 32].

In the helicity (HE) frame of reference, the quantization axis is taken along the momentum direction of the quarkonium produced in the center-of-mass frame of the colliding system. In the Collin-Soper (CS) frame, the quantization axis is defined as the bisector of the momenta of the two incoming hadrons (the colliding beams) in the quarkonium rest frame, providing a symmetric treatment of the projectile and target and reducing sensitivity to initial-state transverse momentum effects. Another frame of reference, also used for quarkonium polarization studies, is the Gottfried-Jackson (GJ) frame. In this frame, the momentum direction of one of the colliding beams is taken as the quantization axis. As one can

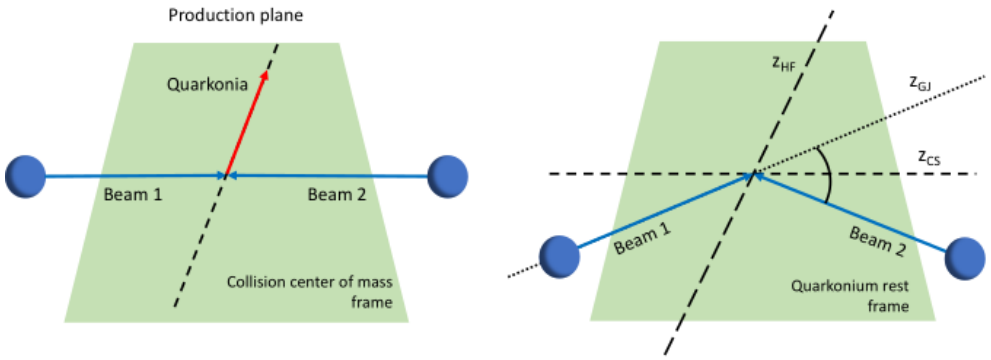

Figure 5.3: Illustration of the three standard choices for the polarization axis z, namely the helicity (HE), Collins–Soper (CS), and Gottfried–Jackson (GJ) frames [264].

see in Fig. 5.3, since the GJ axis represents an intermediate situation between the HE and CS frame of references, the latter two frames are mostly used to study quarkonium polarization, allowing for two extreme cases to interpret the polarization results.

In this thesis, we measure the production of Υ resonances and the polarization of the $\Upsilon(1S)$ state using the ALICE experiment at the LHC. The analysis is performed on pp collision data at a center-of-mass energy of $\sqrt{s} = 13.6$ TeV, collected in the forward rapidity region $2.5 < \eta < 4.0$. The Υ resonances are reconstructed via the dimuon decay channel using the ALICE Muon Spectrometer. The angular distributions of dimuons from the $\Upsilon(1S)$ state are analyzed in both the helicity (HE) and Collins–Soper (CS) reference frames to study its polarization pattern. The following sections present the detector description, followed by the analysis methodology, and the results.

5.2 The ALICE Experiment at LHC

The Large Hadron Collider (LHC) at CERN, Switzerland, a circular accelerator with a circumference of approximately 27 kilometers, is the world's largest and

most powerful particle accelerator ever built [265]. It is designed to explore fundamental interactions at the highest achievable energies in the laboratory. Since its operation began in 2008, the LHC has enabled precision tests of the Standard Model, the discovery of the Higgs boson, and extensive studies of strongly interacting matter under extreme conditions of temperature and energy density. By colliding beams of protons and heavy ions, the LHC provides access to energy densities far exceeding those of normal nuclear matter. In the case of nucleus–nucleus collisions, these extreme conditions are expected to lead to the formation of a deconfined medium of quarks and gluons, commonly referred to as the QGP. An experimental investigation of this state of matter provides crucial insight into the non-perturbative regime of QCD, and the early Universe phase that is believed to have existed just a few microseconds after the Big Bang.

The LHC is designed to accelerate two beams traveling in opposite directions within separate vacuum beam pipes and to bring them into collision at several designated interaction points along the accelerator ring. Four of the interaction points host major experiments, each specifically designed to address distinct physics objectives. The ATLAS (A Toroidal LHC ApparatuS) [266] is a general-purpose detector focusing on the study of the Higgs boson and physics beyond the standard model, such as supersymmetry. The CMS (Compact Muon Solenoid) [267] is characterized by a powerful superconducting solenoidal magnet and shares a similar physics aim with the ATLAS experiment. The LHCb (Large Hadron Collider beauty) [268] experiment, located in the forward rapidity region, focuses on beauty particles for studies of CP violation. The ALICE (A Large Ion Collider Experiment) [269] is uniquely dedicated to the study of heavy-ion collisions at the LHC, with the primary goal of investigating the properties of the quark–gluon plasma.

The ALICE experiment was designed with the primary objective of studying the properties of strongly interacting matter produced in ultra-relativistic heavy-ion collisions. It is specifically designed to operate efficiently in environments

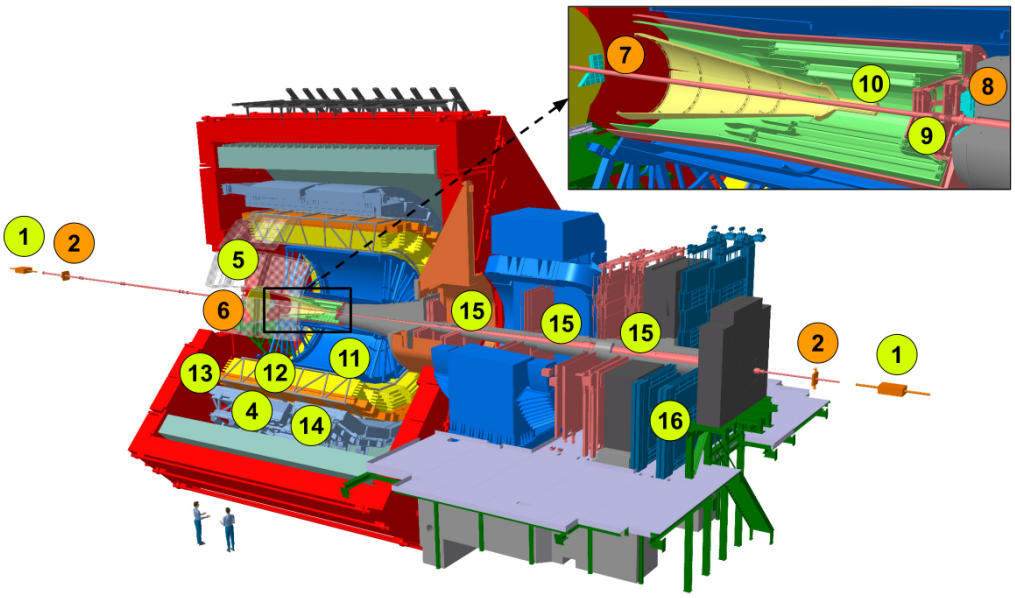

1. **ZDC** – Zero Degree Calorimeter
2. **FDD** – Forward Diffractive Detector
3. **EMCal** – Electromagnetic Calorimeter
4. **DCal** – Di-jet Calorimeter
5. **HMPID** – High Momentum Particle Identification Detector
6. **FV0** – FVzero
7. **FT0-A** – FTzero A-side
8. **FT0-C** – FTzero C-side
9. **MFT** – Muon Forward Tracker
10. **ITS** – Inner Tracking System
11. **TPC** – Time Projection Chamber
12. **TRD** – Transition Radiation Detector
13. **TOF** – Time-of-Flight Detector
14. **PHOS** – Photon Spectrometer
15. **MCH** – Muon Tracking Chambers
16. **MID** – Muon Identifier

Figure 5.4: Schematic view of the ALICE detector configuration during LHC Run 3 [270].

characterized by extremely high particle multiplicities. In addition to heavy-ion collisions, ALICE also records proton–proton and proton–nucleus interactions, which serve as essential reference systems for isolating genuine medium-induced effects. A schematic layout of the ALICE detector with the Run 3 configuration is shown in Fig. 5.4. It consists of several subdetectors, which can be grouped into two major parts, namely, the central barrier detectors and the forward detectors, as

- **The central barrel detectors** of the ALICE detector are located around

the interaction point and cover the mid rapidity ($|\eta| < 0.9$) region with complete azimuthal acceptance. It is specifically designed to perform high-precision tracking, vertexing, and particle identification. Starting from the innermost region, the Inner Tracking System (ITS) provides precise vertex reconstruction and tracking close to the collision point. It is followed by the Time Projection Chamber (TPC), which serves as the primary tracking detector, enabling the measurement of charged-particle momentum as well as particle identification through specific energy loss. Additional particle identification at intermediate and high momenta is achieved using the Time-of-Flight detector (TOF), the High Momentum Particle Identification Detector (HMPID), and the Transition Radiation Detector (TRD). Electromagnetic probes, such as photons and electrons, are measured using two electromagnetic calorimeters, namely PHOS and EMCal, which offer complementary acceptance and energy resolution. All central barrel detectors are housed within a large solenoidal magnet with a uniform magnetic field of 0.5 T. This magnetic field is crucial for the identification of charged particles and their momenta.

- **The forward detectors** in ALICE consist of several detectors that are employed to provide global event information. Event characterization and luminosity-related measurements are primarily performed by the Forward Multiplicity Detector (FMD), Zero Degree Calorimeter (ZDC), and the Fast Interaction Trigger (FIT) system. The FIT detector is composed of three sub-detectors, FT0, FV0, and FDD, based on different technologies and located at forward and backward rapidities. In addition, the Muon Forward Tracker (MFT), positioned upstream of the muon spectrometer, significantly improves the pointing and vertexing resolution of muon tracks, thereby enhancing the separation of prompt and non-prompt muon sources. The muon spectrometer itself constitutes a key forward detector system in

ALICE, dedicated to muon tracking and triggering. It enables measurements of quarkonium and heavy-flavor resonances, as well as light vector mesons.

The coordinate system used in the ALICE detector is defined with its origin at the interaction point [271]. The longitudinal axis (z) is aligned with the beam direction, where the positive z direction corresponds to the A-side and the negative z direction to the C-side, on which the muon spectrometer is located. The transverse plane is defined by the x and y axes, with x pointing radially toward the center of the LHC ring and y oriented vertically upward. The current analysis of Υ resonances is based on the dimuon decay channel, for which the primary detector in use is the muon spectrometer, briefly described below.

5.2.1 Muon spectrometer

The ALICE Forward Muon Spectrometer [272] is a dedicated detector system designed for measuring muons at forward rapidity. Its primary physics objective is the study of heavy quarkonium production, including charmonium and bottomonium states such as J/ψ, $\psi(2S)$, and Υ (nS), as well as low-mass vector mesons (ρ, ω, ϕ) through their dimuon ($\mu^+\mu^-$) decay channels. The spectrometer covers the pseudorapidity interval of $2.5 < \eta < 4.0$, corresponding to polar angles between 171° and 178°. This forward acceptance allows measurements down to zero transverse momentum, which is essential for studying prompt quarkonium production, which is dominant at low p_{T}, while maintaining a reduced background from hadronic decays and a smaller contribution from non-prompt J/ψ originating from B-hadron decay. Due to the high particle flux in heavy-ion collisions, a thick hadron absorber is used to filter out hadrons and photons from reaching the spectrometer, thereby reducing the background. A schematic representation of the ALICE muon spectrometer, highlighting its principal subsystems, is displayed in Fig. 5.5

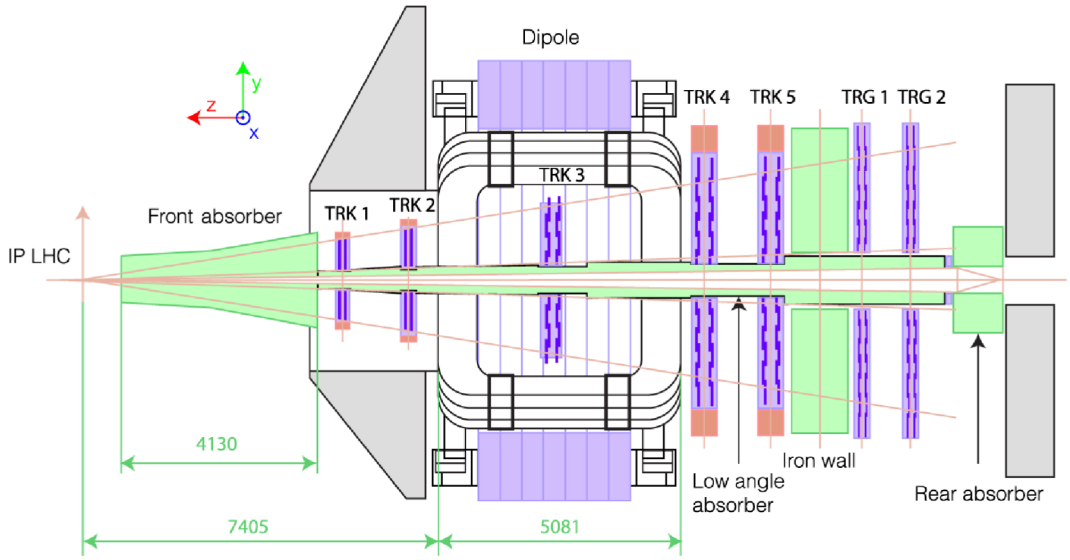

Figure 5.5: Schematic view of ALICE muon spectrometer [272]

The spectrometer is composed of three major components, namely the absorber system, the tracking chambers, and the trigger chambers. To suppress the large background of hadrons and electromagnetic particles, the spectrometer incorporates both front and rear absorber systems. The front absorber, positioned approximately 90 cm from the interaction point and surrounding the beam pipe in a conical geometry, is designed to absorb hadrons, photons, and muons from the decay of pions and kaons. Additional shielding of the beam pipe passing through the spectrometer is provided by a conical structure composed of tungsten, lead, and stainless steel, which reduces background originating from secondary interactions at small polar angles. Downstream of the tracking system, a thick iron wall (the muon filter), approximately 1.2 m thick, separates the tracking and trigger stations. A rear absorber made of iron further shields the trigger chambers from backgrounds associated with beam–gas interactions. Muon trajectory reconstruction is achieved using a tracking system, the Muon Tracking Chamber (MCH), which consists of five detector stations with two Cathode Pad Chambers in each station, arranged along the beam direction. Two stations are located immediately after the front absorber, one inside the dipole magnet, and two downstream

of the magnet, upstream of the muon filter. The Muon Identifier (MID) is placed behind the iron wall filter, is designed to efficiently select events containing high p_{T} muons originating from heavy-flavor decays and quarkonium production, while rejecting the dominant background from low p_{T} muons produced in pion and kaon decays. The trigger chambers are equipped with four planes of Resistive Plate Chambers (RPCs), which are placed one meter apart and are situated immediately after the muon filter. The primary function of the RPCs is to provide fast timing information and (x, y) coordinates of the hit points.

For our analysis, we collect muons using the muon spectrometer in ALICE, and then study the dimuon decay channel of the Υ mesons to study their production and polarization. The analysis method, along with the data sample and various configurations, is discussed in the following section.

5.3 Analysis method

5.3.1 Data sample

The data sample used for this analysis comprises data collected during Run 3 LHC operation in 2024 for pp collisions at $\sqrt{s} = 13.6$ TeV. The runs for the muon tracks are assigned as GOOD or BAD based on the quality of the detectors MCH and MID for the corresponding run. The complete list of GOOD runs used in this analysis is reported [273].

- **LHC24af_apass1_skimmed**: 550916, 550889, 550858, 550852, 550848, 550843, 550824, 550819, 550784, 550781, 550778, 550774, 550760, 550756, 550742, 550731, 550728, 550711, 550707, 550691, 550690, 550654, 550634, 550632, 550630, 550439, 550425, 550424, 550421, 550417, 550412, 550375, 550369, 550367.

- **LHC24ag_apass1_skimmed**: 551504, 551498, 551468, 551463, 551427,

551418, 551398, 551394, 551392, 551391, 551389, 551387, 551365, 551296, 551290, 551272, 551260, 551257, 551255, 551232, 551230, 551229, 551221, 551219, 551149, 551127, 551122, 551107, 551105, 551083, 551066, 551027, 551023, 551013, 551008, 551007, 551005, 550997.

LHC24aj_apass1_skimmed: 552403, 552402, 552401, 552400, 552384, 552383, 552382, 552381, 552369, 552353, 552341, 552340, 552304, 552285, 552283, 552206, 552205, 552204, 552203, 552201, 552200, 552198, 552197, 552179, 552178, 552177, 552176, 552156, 552142, 552141, 552140, 552139, 552138, 552103, 552102, 552080, 552029, 552005, 551997, 551993, 551992, 551989, 551983, 551982, 551979, 551977, 551958, 551943, 551931, 551926, 551925, 551924, 551923, 551922, 551921, 551894, 551890, 551889, 551877, 551875, 551874, 551856, 551843, 551780, 551761, 551760, 551759.

LHC24al_apass1_skimmed: 555308, 555270, 555267, 555259, 555254, 555232, 555226, 555208, 555202, 555187, 555172, 555166, 555160, 555156, 555152, 555150, 555124, 555122, 555121, 555073, 555071, 555047, 555023, 555022, 555020, 554998, 554973, 554970, 554968, 554920, 554898, 554880, 554873, 554837, 554835, 554808, 554791, 554774, 554772, 554768, 554752, 554736, 554732, 554728, 554714, 554703, 554633, 554615, 554613, 554603, 554588, 554569, 554564, 554558, 554538, 554526, 554524, 554507, 554504, 554495, 554494, 554471, 554462, 554427, 554413, 554408, 554404, 554394, 554354, 554323, 554322, 554316, 554295, 554293, 554261, 554247, 554223, 554208, 554207, 554203, 554201, 554198, 554194, 554098, 554095, 554094, 554092, 553903, 553880, 553862, 553844, 553825, 553824, 553821, 553819, 553816, 553807, 553785, 553756, 553739, 553702, 553700, 553663, 553660, 553655, 553633, 553610, 553590, 553588, 553555, 553536, 553530, 553512, 553486, 553305, 553299, 553297, 553294, 553274, 553255, 553253, 553250, 553225, 553219, 553193, 553189, 553188, 553187, 553185.

LHC24am_apass1_skimmed: 555976, 555967, 555965, 555960, 555958,

555933, 555917, 555900, 555883, 555860, 555853, 555850, 555801, 555798, 555790, 555789, 555763, 555761, 555759, 555742, 555740, 555723, 555707, 555705, 555695, 555693, 555676, 555651, 555649, 555612, 555596, 555591, 555575, 555546, 555543, 555540, 555504, 555482, 555478, 555476, 555451, 555443, 555435, 555411, 555408, 555401, 555374, 555370, 555345, 555344.

LHC24an_apass1_skimmed: 557926, 557913, 557897, 557876, 557862, 557749, 557744, 557726, 557723, 557717, 557691, 557681, 557659, 557613, 557547, 557531, 557509, 557482, 557481, 557444, 557425, 557415, 557374, 557350, 557339, 557336, 557321, 557299, 557291, 557271, 557251, 557233, 557226, 557149, 557138, 557119, 557118, 557112, 557104, 557074, 557026, 557021, 557019, 557012, 556997, 556981, 556979, 556958, 556954, 556939, 556923, 556913, 556909, 556907, 556889, 556872, 556834, 556816, 556767, 556741, 556734, 556716, 556680, 556664, 556562, 556542, 556517, 556497, 556491, 556485, 556482, 556461, 556454, 556437, 556412, 556372, 556370, 556284, 556269, 556248, 556237, 556218, 556210, 556182, 556164, 556160, 556152.

LHC24an_apass1_skimmed: 558801, 558783, 558757, 558752, 558750, 558744, 558726, 558685, 558676, 558656, 558633, 558627, 558615, 558606, 558604, 558602, 558551, 558535, 558482, 558449, 558437, 558433, 558422, 558410, 558409, 558406, 558390, 558387, 558383, 558369, 558354, 558330, 558329, 558327, 558291, 558288, 558284, 558275, 558273, 558247, 558244, 558221, 558217, 558215, 558182, 558179, 558155, 558153, 558150, 558126, 558124, 558122.

In the new O2 framework for Run 3, the analysis is performed in three different steps:

1. Event filtering: selection of required events from the original AO2D file to create a reduced dataset, the task **ppfilter** is used.

2. Muon selection: the **table-maker** task is performed on the reduced AO2D to select the muon track candidates. For all the data passes listed above, the skimming configuration is done (https://alimonitor.cern.ch/hyperloop/train-run/410589/general), and the output is then combined to create a reduced dataset, **DQ_LHC24_pass1_skimmed_DiMuon_time_assoc**.

3. Dimuon selection: Finally, the **table-reader** task is used on the obtained reduced dataset to build the dimuon observables. Further selections at the track level are applied here. The merged output, consisting of the required histograms, can be found at https://alimonitor.cern.ch/hyperloop/train-run/401413/general [273].

5.3.2 Monte Carlo (MC) production

For the determination of tail parameters required for signal extraction as well as the acceptance-efficiency (A $\times$ ε) correction of the obtained number of Υ states, the MC dataset anchored to Run 3 data period 2022 pass 7 with production tag LHC24l4 is used (https://its.cern.ch/jira/browse/O2-5644).

5.3.3 Event selection

The events are selected using the combined configuration under **eventStandarSel8ppQuality**. This selection removes ambiguous reconstructed tracks at the event level. Minimum-bias events are selected using the **sel8** trigger, while events located at time-frame boundaries are excluded to prevent track splitting across adjacent time frames coming from the same event. Additionally, a selection is applied to the primary vertex position (**VtxZ**), which selects events with an SPD vertex reconstructed within $|v_z| < 10$ cm. This is to ensure reliable vertex reconstruction and consistency with the Monte Carlo description. The details of the event selection cut are described in the Table 5.1.

eventStandardSel8ppQuality	
Variable	**Description**
`isSel8`	Requires the event to satisfy the minimum-bias trigger condition.
`VtxZ: -10 to 10`	Selects events with the primary vertex position constrained within ±10 cm along the beam (z) axis.
`isNoTFBorder`	Rejects events with vertices located near the Time Frame boundaries to suppress edge effects.
`isNoITSROFBorder`	Discards events close to the ITS readout-frame boundary to avoid potential timing inconsistencies.
`isNoSameBunch`	Removes events originating from the same bunch crossing (identical T0 BC).
`isGoodZvtxFT0vsPV`	Imposes $\lvert Z_{\mathrm{PV}} - Z_{\mathrm{FT0\text{-}C}} \rvert < 1$ cm to ensure consistency between FT0-C and reconstructed primary vertex positions.
`isVertexITSTPC`	Requires a primary vertex reconstructed using combined ITS and TPC track information.
`isVertexTOFmatched`	Ensures the presence of tracks associated with the vertex that are matched to the TOF detector.

Table 5.1: Event selection for the analysis [274].

5.3.4 Muon selection

The muon candidates are selected with the following criteria:

- Single muon track within the muon spectrometer acceptance, i.e., -4.0 $< \eta_{\mu}$ $<$ -2.5.
- The MCH-MID track match requirement: track type 3
- To remove the tracks crossing the thicker part of the absorber, the radial position, R_{abs} of the muon track is kept in 17.6 $< R_{abs} <$ 89.5 cm.
- To remove the tracks not pointing to the vertex, the momentum times the distance to the closest approach ($p\times$ DCA) is within the 6σ of the distribution.
- A p_{T} cut of 0.7 GeV/c is applied at the single muon level using the trigger **muonLowPt2**.

Dimuon pairs are formed from the single muons satisfying the above criteria. Those dimuons are selected using two additional criteria:

- The total charge of the dimuon pair is zero.
- The dimuon rapidity is within the range -4.0 $< y_{\mu^+\mu^-} <$ -2.5.

5.3.5 Signal extraction

In the present analysis, the inclusive Υ (nS) yields are extracted in the dimuon decay channel using the invariant mass method. For each selected opposite-sign dimuon pair, the invariant mass is calculated as [50]

$$M_{\mu^+\mu^-} = \sqrt{(E_1^2 + E_2^2) - |\vec{p_1} + \vec{p_2}|^2}, \tag{5.12}$$

where E_1 and E_2 denote the energies, and $\vec{p_1}$ and $\vec{p_2}$ represent the momenta of the two decay muons. The quantity $M_{\mu^+\mu^-}$ corresponds to the invariant mass of the dimuon pair. The raw Υ yield is obtained from the resulting invariant mass distribution. This is achieved by fitting the spectrum with a superposition

of signal and background components. The fitting functions are selected empirically and typically consist of dedicated terms to model the Υ signal peak, along with additional components to describe the underlying background and the long continuum extending on either side of the signal region, commonly referred to as the tails.

5.3.5.1 Signal function

The signal is modelled by a sum of 3 Double Crystal Ball Functions (DCB): one for each Υ state [262, 263]. The DCB consists of a Gaussian core extended with two tails, one on each side. The tails are composed of an exponential and a power law term. The DCB is a C_1 function; the function and its first derivative are continuous. The analytical form of a DCB function is given below [275–277]:

$$f(x;\mu,\sigma,\alpha_L,n_L,\alpha_R,n_R) = N \cdot \begin{cases} \exp\left(-\frac{(x-\mu)^2}{2\sigma^2}\right), & \text{for } \alpha_R > \frac{x-\mu}{\sigma} > -\alpha_L \\ A \times \left(B - \frac{x-\mu}{\sigma}\right)^{-n_L}, & \text{for } \frac{x-\mu}{\sigma} \leq -\alpha_L \\ C \times \left(D + \frac{x-\mu}{\sigma}\right)^{-n_R}, & \text{for } \frac{x-\mu}{\sigma} \geq \alpha_R \end{cases} \tag{5.13}$$

where

$$\begin{aligned} A &= \left(\frac{n_L}{|\alpha_L|}\right)^{n_L} \exp\left(-\frac{|\alpha_L|^2}{2}\right), \\ B &= \frac{n_L}{|\alpha_L|} - |\alpha_L|, \\ C &= \left(\frac{n_R}{|\alpha_R|}\right)^{n_R} \exp\left(-\frac{|\alpha_R|^2}{2}\right), \\ D &= \frac{n_R}{|\alpha_R|} - |\alpha_R|. \end{aligned} \tag{5.14}$$

Here, N is the normalization factor, μ and σ are the mean and the width of the Gaussian function. The α_L, n_L (α_R, n_R) represent the tail parameters

on the left (right) side. A DCB function, in general, has a Gaussian core with exponential tails on either side. This tail structure arises in the invariant mass distribution because of multiple scattering of muons in the front absorber and residual misalignment, among other effects [275]. Hence, for the three DCB functions, there are in total $3 \times 4 = 12$ tail parameters. However, to limit the complexity of the fit arising from a large number of free parameters, a common set of tail parameters is employed for all three double Crystal Ball (DCB) functions. As a result, the effective number of independent tail parameters is reduced to four.

For background modelling, the following functions are commonly used:

- **Sum of two exponentials (DE):**

$$A \times e^{a_1 x} + B \times e^{b_1 x} \tag{5.15}$$

- **Sum of two power laws (DP):**

$$A \times x^{a_1} + B \times x^{b_1} \tag{5.16}$$

- **Variable width Gaussian (VWG):**

$$A \exp\left[-0.5\left(\frac{x-a}{\sqrt{\mathrm{Var}(\sigma)}}\right)^2\right], \qquad \text{where} \quad \mathrm{Var}(\sigma) = b + c \times \frac{x-a}{a} \tag{5.17}$$

Consequently, even after enforcing common tail parameters for the three Υ (nS) states, the combined signal and background fit involves approximately 10–12 free parameters. To avoid excessive complexity in the fitting due to the large number of parameters, the tail parameters cannot be left free, as this leads to a systematic overestimation of the tail contribution and a non-physical shape of the extended tails. Therefore, the tail parameters are fixed either through MC simulations or via data-driven estimation, both of which are discussed in this thesis.

5.3.5.2 Tail parameters

The tail parameters are determined using two complementary methods: Monte Carlo (MC) simulations and a data-driven approach. In the present work, the MC-based method is employed using a pure $\Upsilon(1S)$ signal sample. The LHC24l4 MC production, containing only $\Upsilon(1S)$ dimuon decays, is used to construct the invariant mass distribution after applying the same single-muon and dimuon selection criteria described in Sec. 5.3.4. The resulting invariant mass spectrum is

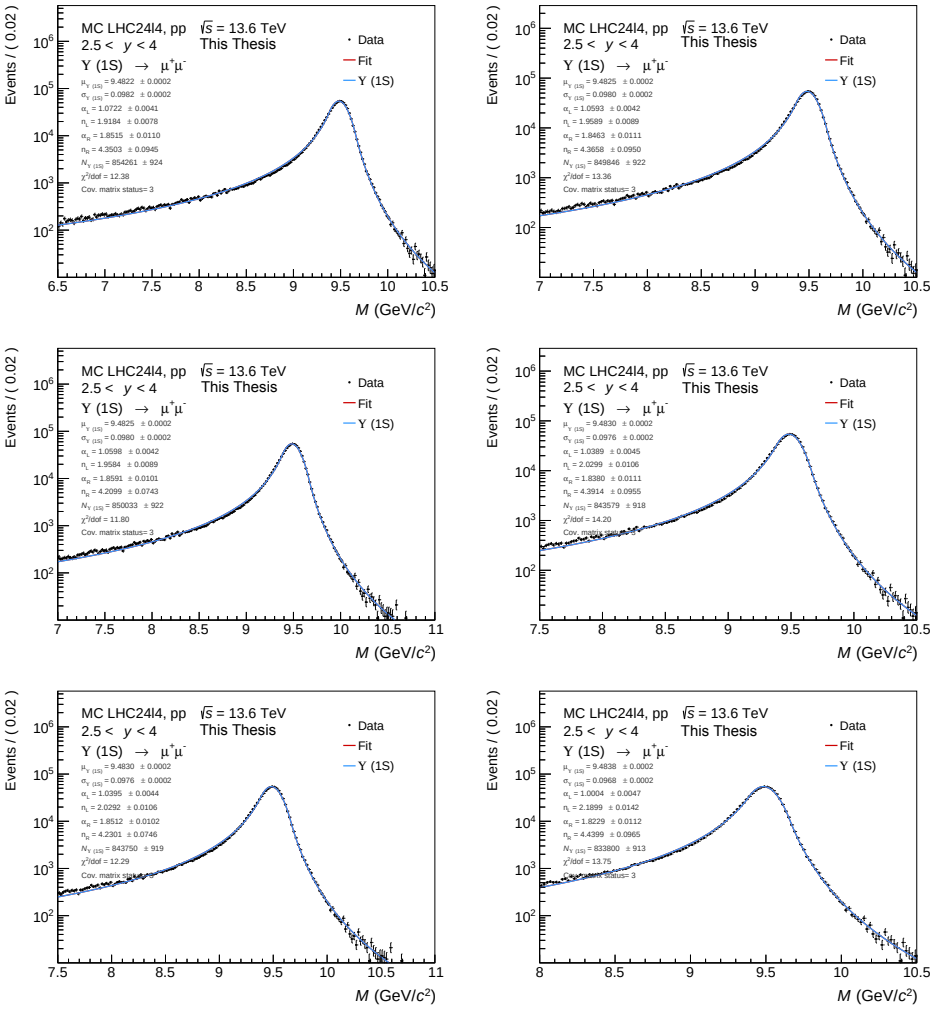

Figure 5.6: An illustration of fit to Υ (1S) mass peak with a DCB function in six different fitting ranges [273].

fitted with a single double Crystal Ball (DCB) function, with all parameters left free. To assess the stability of the extracted tail parameters, the fit is performed in six different dimuon mass ranges, as illustrated in Fig. 5.6. The tail parameters obtained from each fit range are shown in Fig. 5.7. The average of these values is used as the fixed MC tail parameters for the rest of the analysis, unless otherwise specified for any changes. The mean value is followed by the statistical error and systematic error (discussed in the next sections).

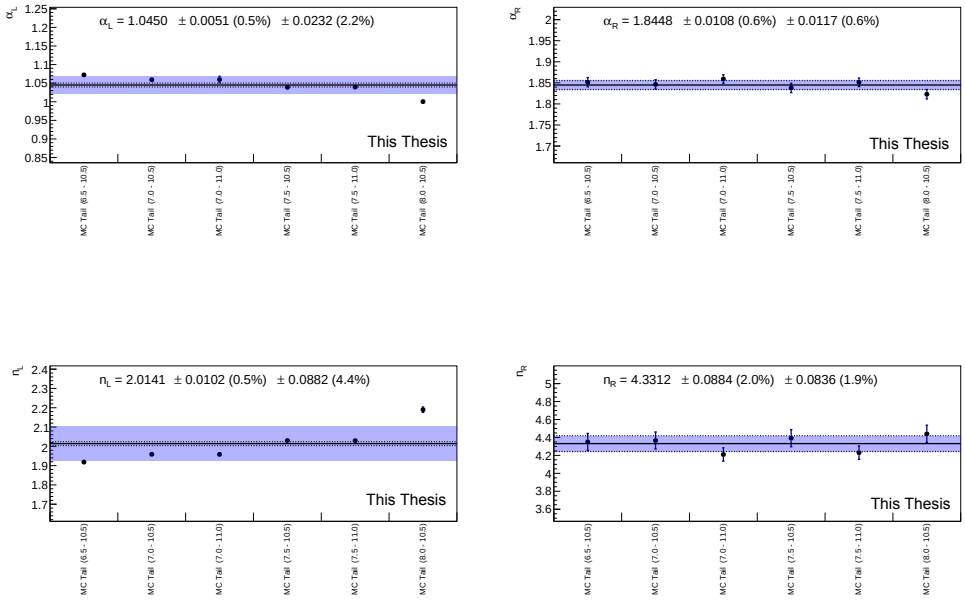

Figure 5.7: The obtained tail parameters using different fitting ranges are shown [273].

To obtain the tail parameters using the experimental data, we fit the dimuon invariant mass spectra to reconstruct the Υ resonances. All the parameters, including the tail parameters, are kept free. For the signal function, we use the Double Crystal Ball function, whereas for the background, three functions, namely DE, DP, and VWG, as described in Sec. 5.3.5.1, are employed. Six different fitting ranges are used. The complete fitting method is described in the

next section. The systematic error due to different background functions and fitting ranges considered is listed in Table 5.2.

Table 5.2: Invariant mass fitting configurations used for tail parameter estimation [273].

Fitting ranges (GeV/c^2)	**Background functions**	**Signal function**
(6.0 – 11.5), (7.0 – 11.5)	VWG	DCB
(6.0 – 12.0,) (7.0 – 12.0)	DE	
(6.5 – 12.0,) (7.5 – 12.0)	DP	

The obtained fitting parameters using experimental data for each configuration are shown in Fig. 5.8.

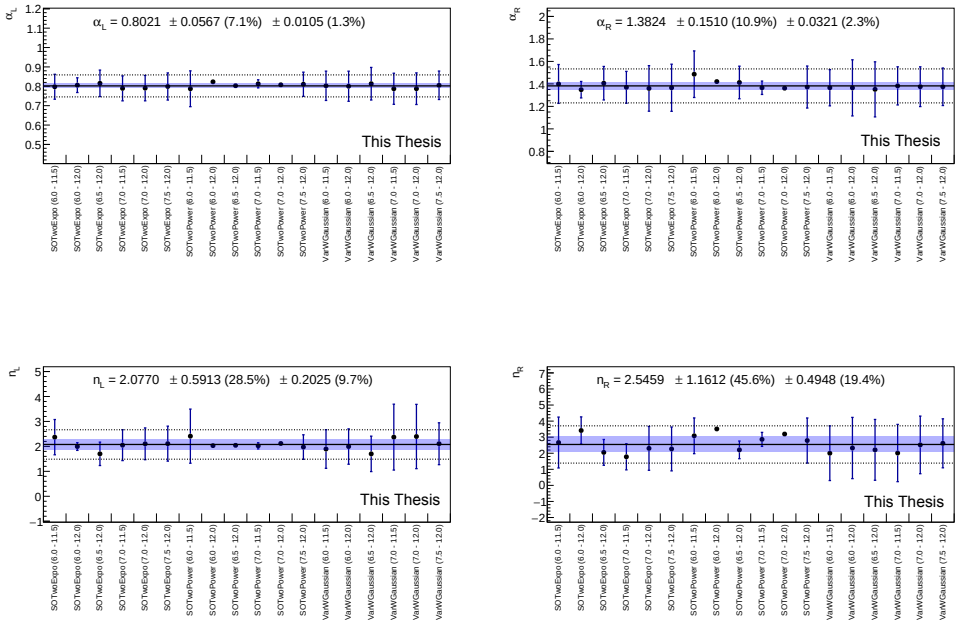

Figure 5.8: The obtained tail parameters using different fitting ranges in the data are shown [273].

Finally, the estimated values of the tail parameters using MC simulations and

a data-driven approach are then summarized in Table 5.3, where they are also compared with those from the Run 2 analysis [275].

Tail Parameters	**Run 2**		**Run 3**	
	MC	Data-driven	**MC**	**Data-driven**
α_L	1.016	0.807	**1.045**	**0.802**
n_L	2.035	3.369	**2.014**	**2.077**
α_R	2.063	1.228	**1.845**	**1.382**
n_R	2.247	3.738	**4.331**	**2.546**

Table 5.3: The tail parameter values obtained in this analysis in Run 3 [273], extracted using the LHC24l4 MC sample and corresponding data are compared with Run 2 results [275].

5.3.5.3 p_{T} integrated raw yield

The fitting procedure to obtain p_T integrated yield involves following methods:

- The dimuon invariant mass distribution is fitted with three DCB functions for each Υ state.
- The background is fitted with the VWG function, and later also with DE and DP functions.
- The fitting range is taken as 6.5 to 12.0 GeV/c^2.
- The fitting is done using both the MC and data-driven tail parameters.
- All the parameters except the tail parameters are kept free. The mass and width of Υ (2S) and Υ (3S) are kept fixed to a value in proportion to those of Υ (1S) from the fit through the relation [273, 275]

$$M_{\Upsilon(2S,3S)} = M^{\mathrm{fit}}_{\Upsilon(1S)} + M^{\mathrm{PDG}}_{\Upsilon(2S,3S)} - M^{\mathrm{PDG}}_{\Upsilon(1S)} \tag{5.18}$$

$$\sigma_{\Upsilon(2S,3S)} = \sigma^{\text{fit}}_{\Upsilon(1S)} \times \frac{\sigma^{\text{MC}}_{\Upsilon(2S,3S)}}{\sigma^{\text{MC}}_{\Upsilon(1S)}} \tag{5.19}$$

In Fig. 5.9, we present the results of fitting the dimuon invariant mass spectra with the above configurations.

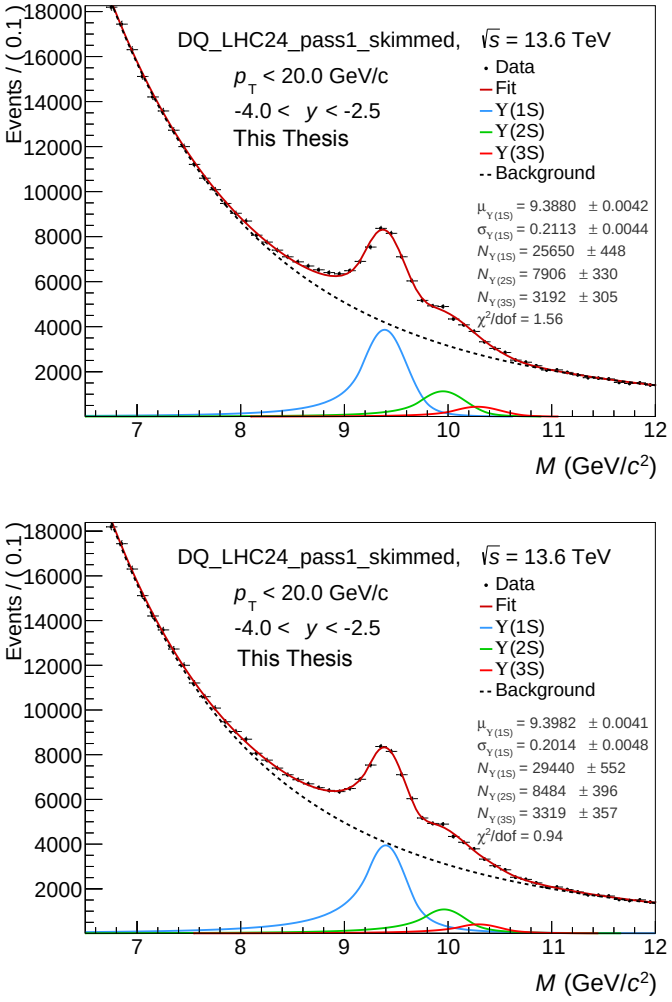

Figure 5.9: The dimuon invariant mass spectra fitted with DCB function for signal and VWG for background. The upper and the lower ones are obtained using the MC and data-driven tail parameters, respectively. The raw number of Υ states is shown in the figures [273].

5.3.5.4 Systematic uncertainty on signal extraction

The extraction of the Υ (nS) yields presented above is performed by fitting the dimuon invariant mass spectrum in the range 6.5 GeV/c^2 to 12.0 GeV/c^2 using a double Crystal Ball (DCB) function for the signal and a variable width Gaussian (VWG) function for the background. Alternatively, the signal can also be extracted by employing different functional forms for both the signal and background, as well as by varying the fitting range. These variations introduce systematic effects in the extracted yields. The primary sources of systematic uncertainty considered in this analysis are summarized below.

1. **Background functions:** For background, the functional forms that are commonly used are the VWG, DE, and DP.

2. **Tail parameters:** The tail parameters of the signal function are determined either from Monte Carlo simulations at $\sqrt{s}$ = 13.6 TeV or using data-driven methods applied to the available integrated data sample.

3. **Fitting range:** To assess the sensitivity of the extracted yields to the chosen mass interval, six different fitting ranges are considered: (6.0–11.5), (6.0–12.0), (6.5–12.0), (7.0–11.5), (7.0–12.0), and (7.5–12.0) GeV/c^2.

Therefore, considering three background functions, two sets of tail parameters, and 6 fitting ranges, the total number of tests, $n_{\text{test}} = 36$. So, if x is our quantity of interest (say raw yield of Υ (nS)), the statistical ($\sigma^{\text{stat}}_{\langle x \rangle}$) and systematic ($\sigma^{\text{syst}}_{\langle x \rangle}$) errors can be estimated using [275]

$$\sigma^{\text{stat.}}_{\langle x \rangle} = \frac{1}{n_{\text{tests}}} \sum_{i=1}^{n_{\text{tests}}} \sigma_{x_i}, \tag{5.20}$$

$$\sigma^{\text{sys.}}_{\langle x \rangle} = \sqrt{\frac{\sum_{i=1}^{n_{\text{tests}}} \left(x_i - \langle x \rangle\right)^2}{n_{\text{tests}} - 1}}. \tag{5.21}$$

where the mean is given by $\langle x \rangle = \sum_{i=1}^{n_{\text{tests}}} x_i$. The raw yields of each of the Υ states are shown in Fig. 5.10. It is observed that the major contribution to systematic error comes from the two sets of tail parameters.

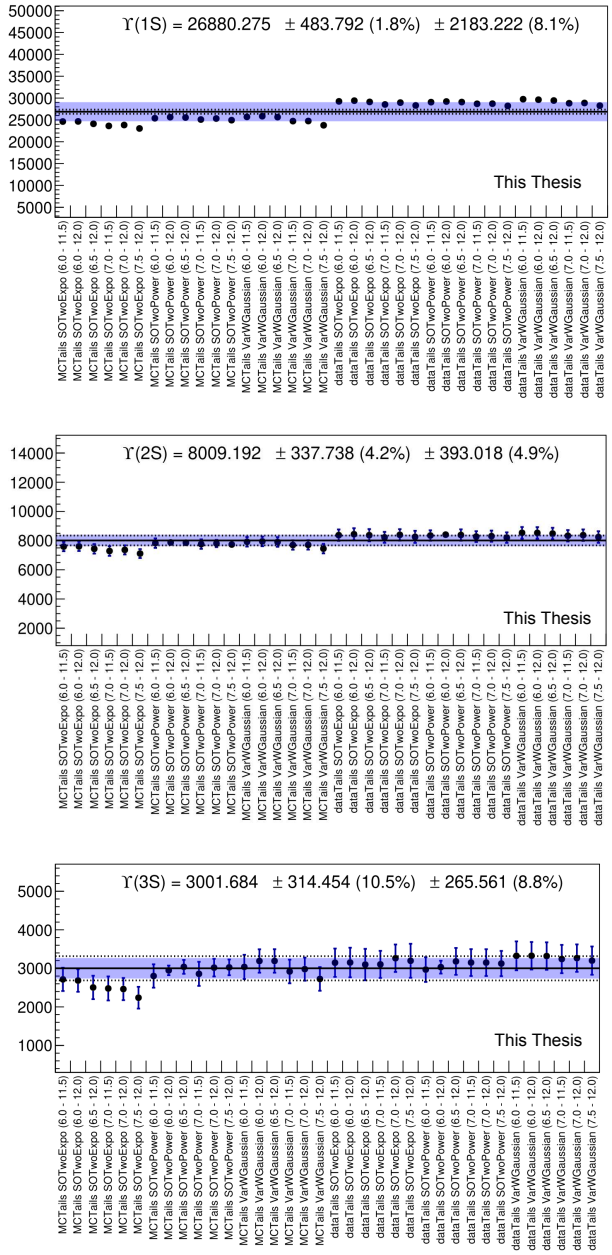

Figure 5.10: Systematic results of fitting the integrated statistics to get the raw yield of Υ (nS) states [273].

5.3.5.5 p_{T} differential yield

We then proceed to fit the dimuon invariant mass distribution in different p_{T} bins. With the available statistics, we currently consider only four p_{T} bins: 0-2, 2-4, 4-8, and 8-20 GeV/c. Following the same procedure, we fit the signal and background with DCB and VWG functions, respectively, in the fitting range of 6.5-12.0 GeV/c^2. The fitting results using MC tail parameters are shown in Fig. 5.11, and those of using data-driven tail parameters are shown in Fig. 5.12

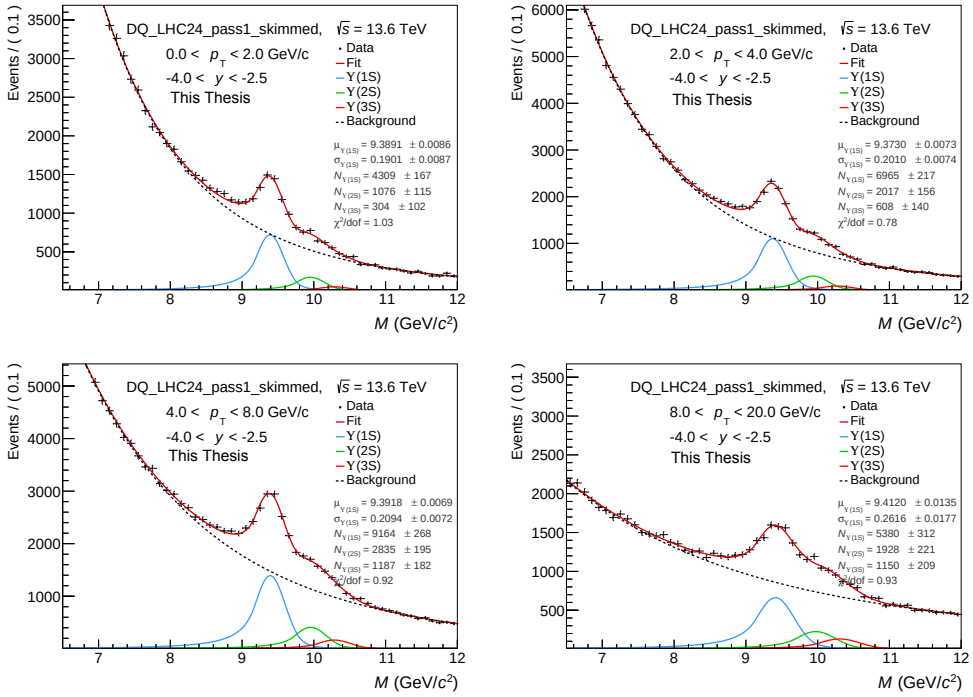

Figure 5.11: Illustration of p_{T} differential fitting of dimuon invariant mass spectra using MC tail parameters [273].

The fitting procedure is repeated using other background functions and fitting ranges to estimate the systematic uncertainties. The final yield in different p_{T} bins as well as in the p_{T} integrated case is obtained by correcting the raw yields using an acceptance-efficiency factor, which is described the next section.

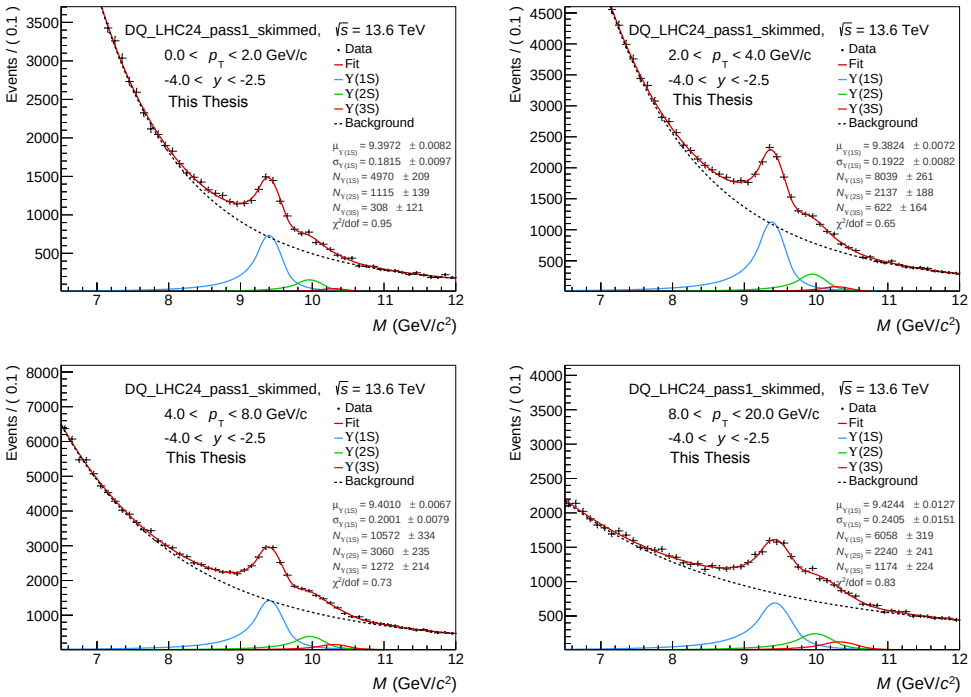

Figure 5.12: Illustration of p_{T} differential fitting of dimuon invariant mass spectra using data-driven tail parameters [273].

5.3.5.6 The Acceptance × Efficiency correction

The acceptance–efficiency factor ($A \times \varepsilon$) corrects for the loss of signal arising due to the limited acceptance and inefficiency of the detectors. The acceptance accounts for the geometrical constraints of the ALICE muon spectrometer and the decay kinematics of the dimuon channel, while the efficiency reflects the detector and reconstruction performance. In the muon spectrometer, this efficiency includes contributions from the trigger response, tracking efficiency, and track–trigger matching.

The determination of $A \times \varepsilon$ relies on detailed Monte Carlo (MC) simulations, which are performed in three main steps. First, the Υ(nS) state is generated with transverse momentum (p_T) and rapidity (y) distributions, tuned to reproduce experimental data. Second, the generated Υ(nS) is decayed into a $\mu^+\mu^-$ pair.

Finally, the decay muons are transported through the full detector geometry, and the detector response is simulated. The resulting signals are then reconstructed using the same algorithms and selection criteria as those applied to real data. The MC output provides both the number of generated Υ(nS) states, $N^{\rm gen}_{\Upsilon({\rm nS})}$, and the number of reconstructed ones, $N^{\rm rec}_{\Upsilon({\rm nS})}$, after applying all analysis cuts. The acceptance times efficiency factor is thus obtained as

$$A \times \varepsilon = \frac{N^{rec}_{\Upsilon({\rm nS})}}{N^{gen}_{\Upsilon({\rm nS})}} \tag{5.22}$$

Finally, the corrected number ($N^{\rm corr}$) of Υ (nS) is then obtained by using the relation $N^{\rm corr}_{\Upsilon({\rm nS})} = N^{\rm raw}_{\Upsilon({\rm nS})}/(A \times \varepsilon)$. We fit the reconstructed dimuon invariant mass spectra with the DCB function to get $N^{\rm rec}_{\Upsilon({\rm nS})}$. The acceptance times efficiency as a function of $p_{\rm T}$ is shown in Fig. 5.13. The corrected yield in different $p_{\rm T}$ ranges, as well as the whole $p_{\rm T}$ range, incorporating systematic uncertainties, is listed in Table 5.3.

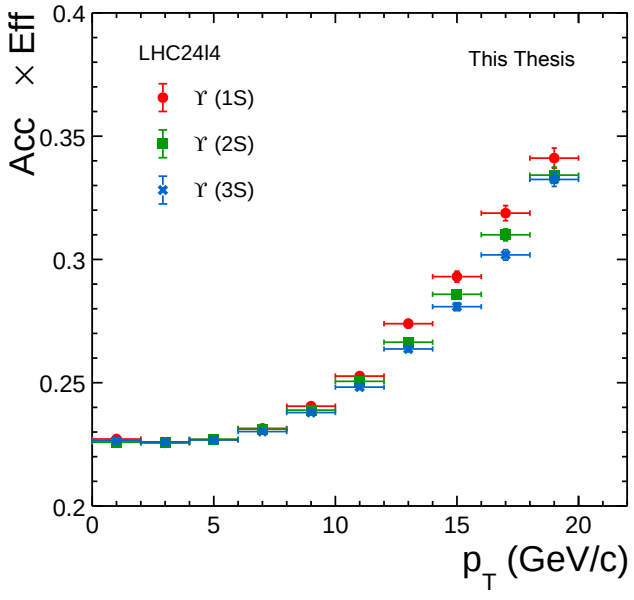

Figure 5.13: The acceptance-efficiency factor as a function of $p_{\rm T}$ for each of the Υ state [273].

p_{T} bins	$N_{\Upsilon(1S)}$	$N_{\Upsilon(2S)}$	$N_{\Upsilon(3S)}$
0–2 GeV/c	$19803.889 \pm 752.829 \pm 1693.270$	$4643.940 \pm 497.284 \pm 229.394$	$1200.829 \pm 445.448 \pm 225.633$
2–4 GeV/c	$32240.853 \pm 915.976 \pm 2720.101$	$8853.438 \pm 633.486 \pm 436.459$	$2361.357 \pm 562.996 \pm 484.082$
4–8 GeV/c	$42149.841 \pm 1171.262 \pm 3710.013$	$12490.029 \pm 825.976 \pm 663.889$	$4755.684 \pm 768.530 \pm 622.352$
8–20 GeV/c	$21217.615 \pm 1013.157 \pm 1524.664$	$7902.911 \pm 747.056 \pm 589.219$	$4166.502 \pm 733.139 \pm 460.299$
SUM	$\mathbf{115412.198 \pm 1950.412 \pm 5133.703}$	$\mathbf{33890.318 \pm 1153.617 \pm 826.962}$	$\mathbf{12484.372 \pm 1051.678 \pm 820.102}$
p_{T} Integrated	$\mathbf{113119.140 \pm 2038.890 \pm 2566.852}$	$\mathbf{33424.837 \pm 1409.847 \pm 413.481}$	$\mathbf{12476.243 \pm 1307.055 \pm 410.051}$

Table 5.4: Corrected yields of Υ(1S), Υ(2S), and Υ(3S) states in different p_T intervals compared with the p_{T} integrated yield [273].

5.4 Upsilon resonances ratio

We estimate the ratios of number of excited states produced to that of ground state Υ, specifically the ratio of Υ (2S) to Υ (1S), Υ (3S) to Υ (1S), and the combined Υ (2S) plus Υ (3S) to Υ (1S). We extract the raw yield of Υ (nS) using the fit to the dimuon invariant mass fit and correct the yield by multiplying the $A \times \varepsilon$ factor as discussed in previous section. A total of 36 tests are made to estimate the systematic uncertainties by considering fitting in 6 fitting ranges $\times$ 3 background functions $\times$ 2 sets of tail parameters. The ratio obtained as a function of p_{T} is shown in Fig. 5.14 [273].

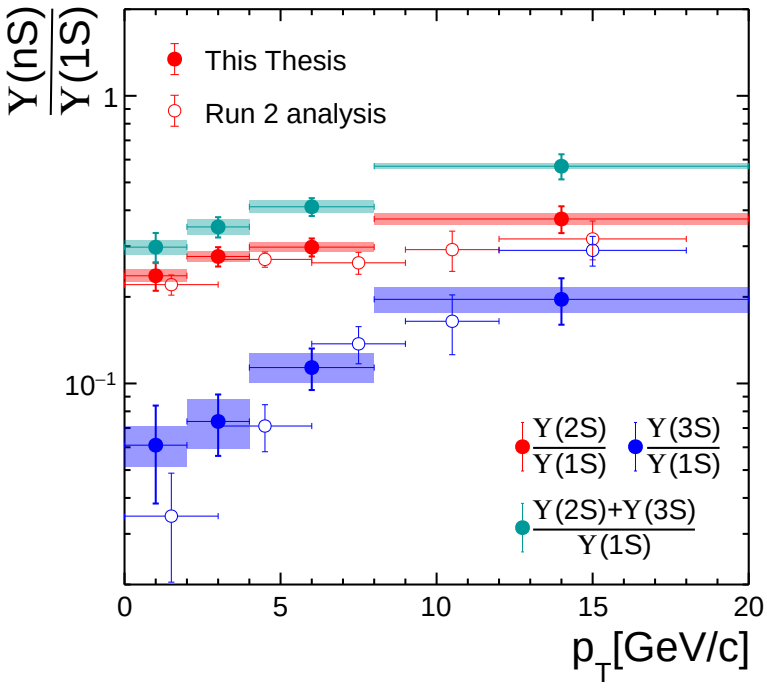

Figure 5.14: Excite to ground state yield ratio of Υ states as a function of p_{T} [273].

It is observed that the resonance ratio is increasing with p_{T} and is relatively consistent with the measurement done in Run 2 at center of mass energy 13 TeV [275].

5.5 ϒ (1S) polarization

As discussed in Sec. 5.1.1, measuring the polarization requires determining the shape parameters λ_θ, λ_ϕ, and $\lambda_{\theta\phi}$ from the angular distributions. We obtain the dimuon invariant mass spectra in angular bins of $\cos\theta$, ϕ, and $\tilde{\phi}$, and following a similar procedure as done for the angular-integrated case, we fit with signal and background functions to obtain ϒ (1S) yield. After obtaining the corrected angular distributions of ϒ (1S), the corresponding distribution functions, $W(\cos\theta)$, $W(\phi)$, and $W(\tilde{\phi})$ are used to fit and obtain the polarization parameters λ_θ, λ_ϕ, and $\lambda_{\theta\phi}$, respectively.

In the MC simulation, we observe that the width of the $\Upsilon(1S)$ exhibits an angular dependence. As shown in Fig. 5.15, the width of the $\Upsilon(1S)$, obtained by fitting the dimuon invariant-mass spectra in each $|\cos\theta|$ bin in the HE reference frame, varies systematically with $|\cos\theta|$.

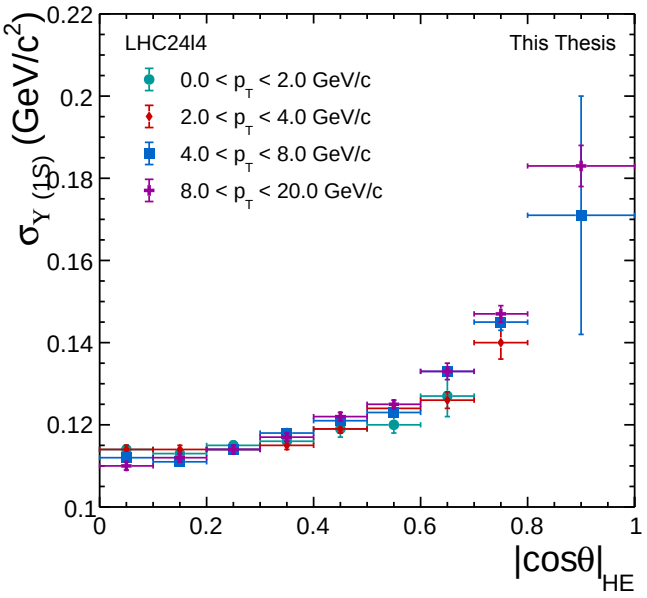

Figure 5.15: The width of ϒ (1S) as a function of $|\cos\theta|$ in the Helicity frame, obtained using MC simulation [273].

Therefore, the width of Υ (1S) in each bin i (refer to any of the $\cos\theta$, ϕ, or $\tilde{\phi}$ bin) is fixed by scaling the measured width for the angle-integrated spectrum with the MC ratio between the widths for the bin i and for the integrated spectrum. Hence, it can be written as [273, 275]

$$\sigma^{i,\mathrm{Data}}_{\Upsilon(1S)} = \sigma^{i,\mathrm{MC}}_{\Upsilon(1S)} \times \left(\frac{\sigma^{\mathrm{Data}}_{\Upsilon(1S)}}{\sigma^{\mathrm{MC}}_{\Upsilon(1S)}} \right)_{\mathrm{Integrated}}. \tag{5.23}$$

5.5.1 Angular distribution of Υ (1S) yield

5.5.1.1 Raw yield

The raw yield of Υ (1S) is obtained by fitting the dimuon invariant mass spectra in different angular bins in both the Helicity and Collins-Soper frame of reference. We have considered four different p_{T} bins of 0-2, 2-4, 4-8, and 8-20 GeV/c. An example fits in 6 different $|\cos\theta|$ bins for the case of $2.0 < p_{\mathrm{T}} < 4.0$ GeV/c is shown in Fig. 5.16.

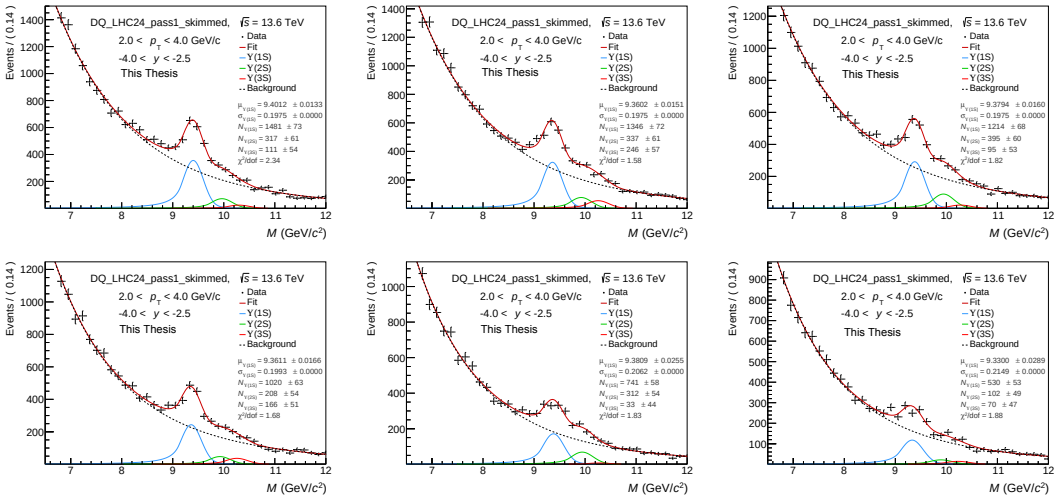

Figure 5.16: Illustration of fit to obtain Υ (1S) yield as in $|\cos\theta|$ bins of (0.0-0.1) to (0.5-0.6) from left to right and to bottom. The fitings are done for the $2.0 < p_{\mathrm{T}} < 4.0$ GeV/c in the Helicity frame [273].

Repeating the procedure, we obtain the raw yields of $\Upsilon(1S)$ as a function of $|\cos\theta|$ for the HE and CS frame of reference, as shown in Fig. 5.17. Similarly, the raw yield of ϒ (1S) is obtained as a function of $|\phi|$ and $|\tilde{\phi}$ in the two frames of reference and is shown in Fig. 5.18 and Fig. 5.19, respectively.

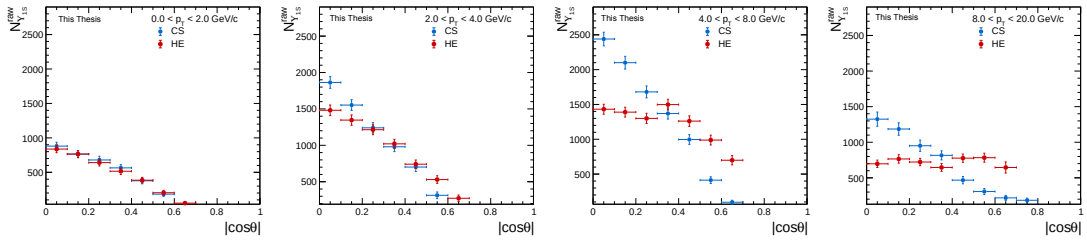

Figure 5.17: Raw yield of ϒ (1S) as a function of $|\cos\theta|$ in different p_{T} bins in CS and HE frame of references [273].

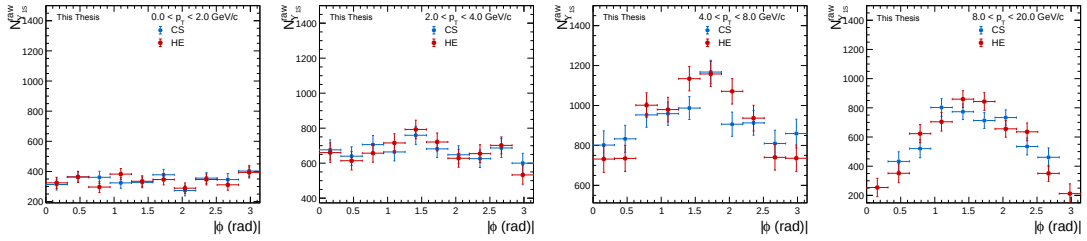

Figure 5.18: Raw yield of ϒ (1S) as a function of $|\phi|$ in different p_{T} bins in CS and HE frame of references [273].

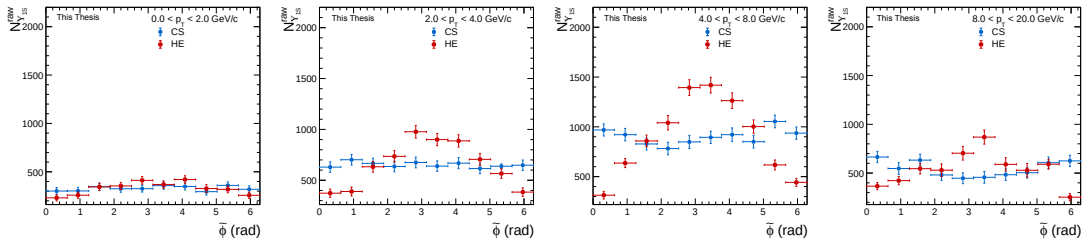

Figure 5.19: Raw yield of ϒ (1S) as a function of $\tilde{\phi}$ in different p_{T} bins in CS and HE frame of references [273].

5.5.1.2 $A \times \varepsilon$ correction

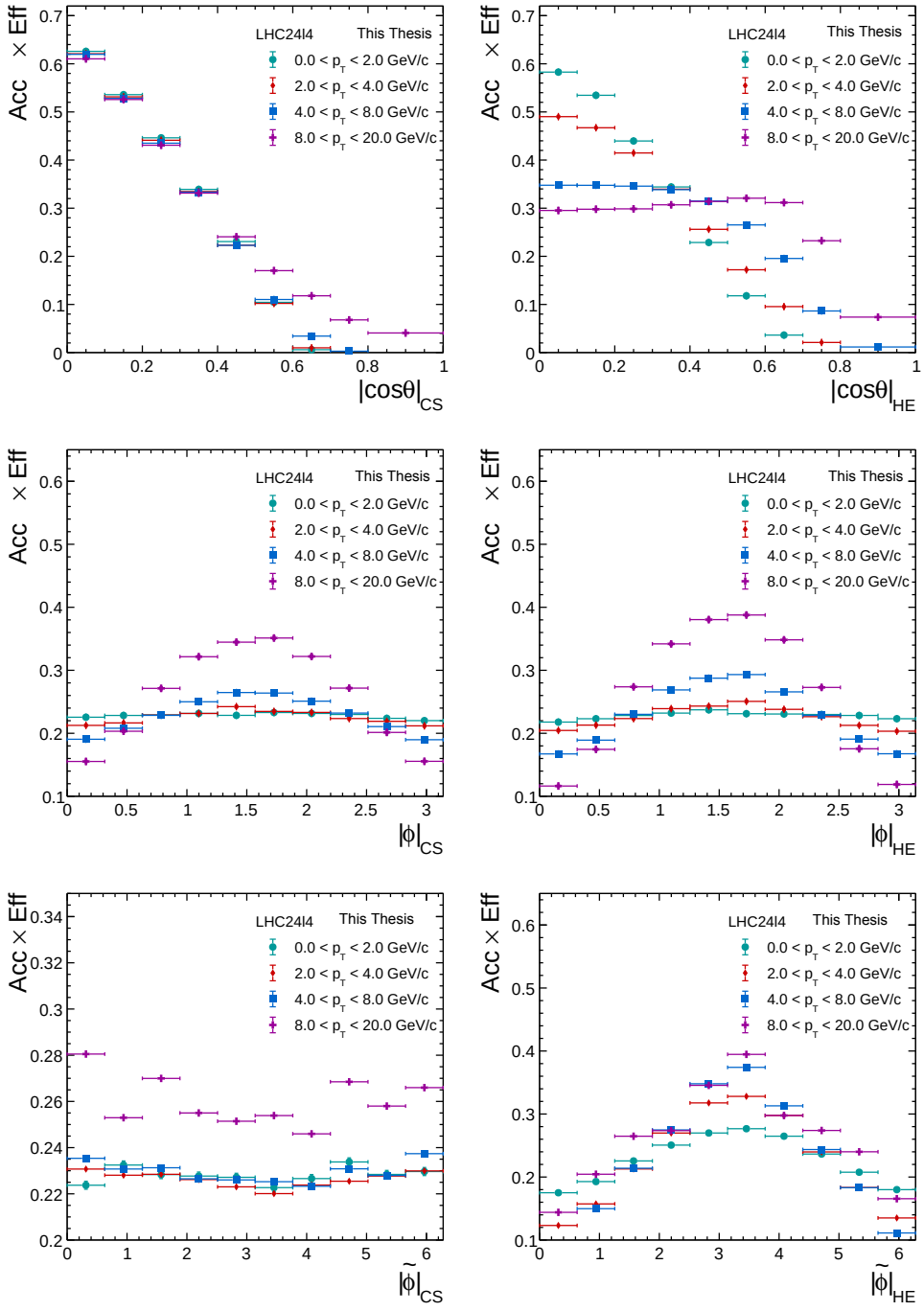

Figure 5.20: $A \times \varepsilon$ as a function of $|\cos\theta|$, $|\phi|$, and $|\tilde{\phi}|$ in CS and HE frames for different p_{T} bins [273].

In each p_{T} and angular bin i, the $A \times \varepsilon$ factor is evaluated by taking the ratio of reconstructed ϒ (1S) ($N^{rec}_{\Upsilon(1S)}$) to the generated ϒ (1S) number ($N^{gen}_{\Upsilon(1S)}$) in that particular bin. Therefore, we have

$$A \times \varepsilon(p_{\mathrm{T}}, i) = \frac{N^{rec}_{\Upsilon(1S)}(p_{\mathrm{T}}, i)}{N^{gen}_{\Upsilon(1S)}(p_{\mathrm{T}}, i)} \tag{5.24}$$

where i corresponds to any angular bin of $|\cos\theta|$, $|\phi|$. or $|\tilde{\phi}|$. The estimated $A \times \varepsilon$ as a function of $|\cos\theta|$, $|\phi|$, and $\tilde{\phi}$ in both CS and HE frames is shown in Fig. 5.20.

5.5.1.3 Corrected yield

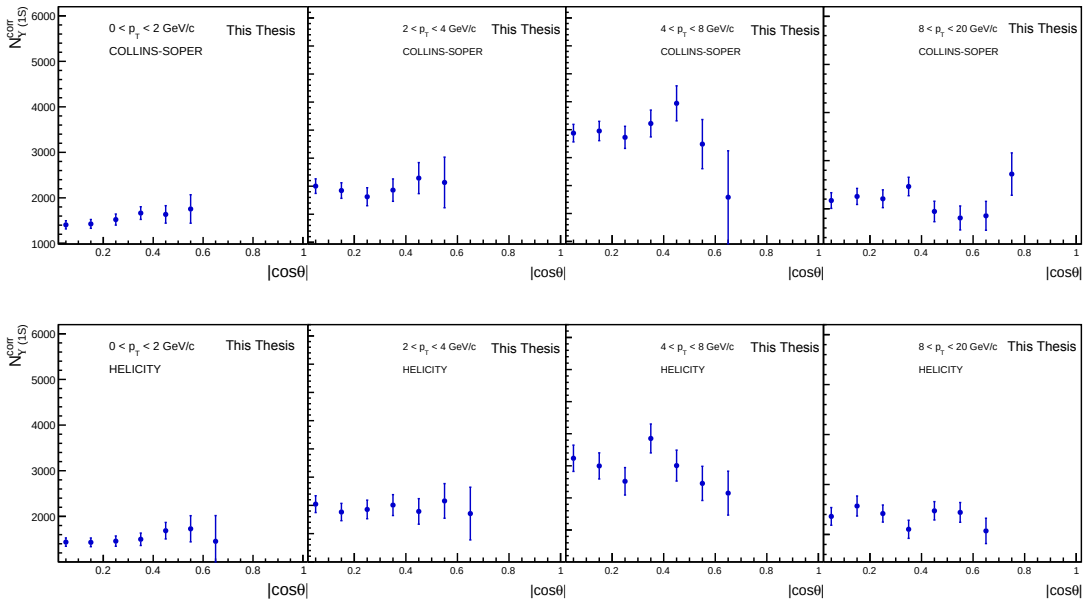

Figure 5.21: Corrected number of ϒ (1S) as a function of $|\cos\theta|$ in CS and HE frames for different p_{T} bins [273].

In each dimuon p_{T} and angular bin i, the raw number of ϒ (1S) is corrected by the $A \times \varepsilon$ factor, and hence the corrected number of ϒ (1S) ($N^{corr}_{\Upsilon(1S)}$) can be defined as

$$N^{rec}_{\Upsilon(1S)} = \frac{N^{raw}_{\Upsilon(1S)}(p_{\mathrm{T}}, i)}{A \times \varepsilon\ (p_{\mathrm{T}}, i)} \tag{5.25}$$

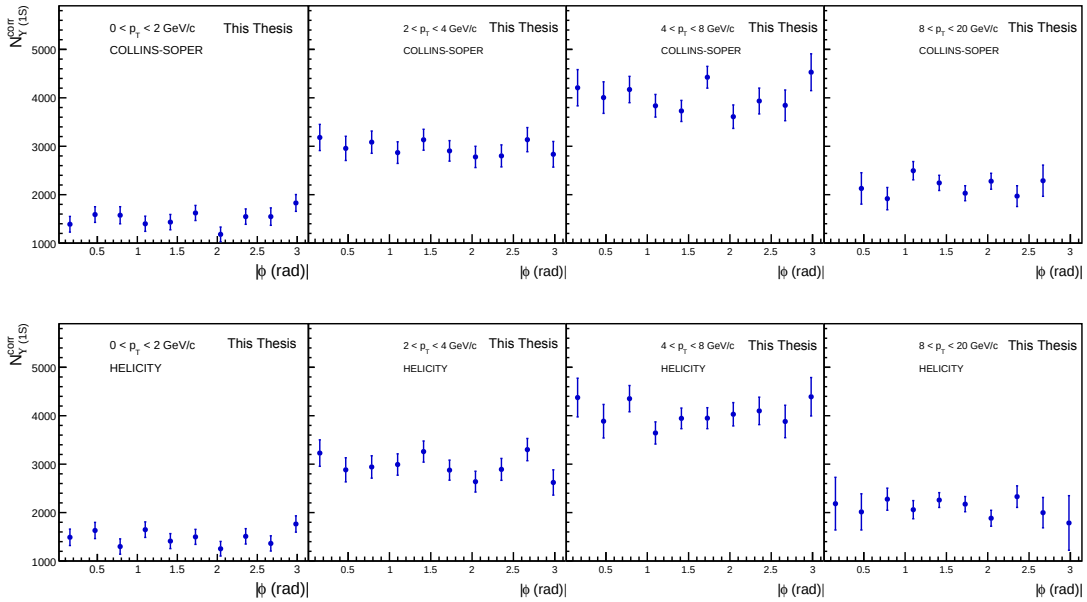

Figure 5.22: Corrected number of Υ (1S) as a function of $|\phi|$ in CS and HE frames for different p_{T} bins [273].

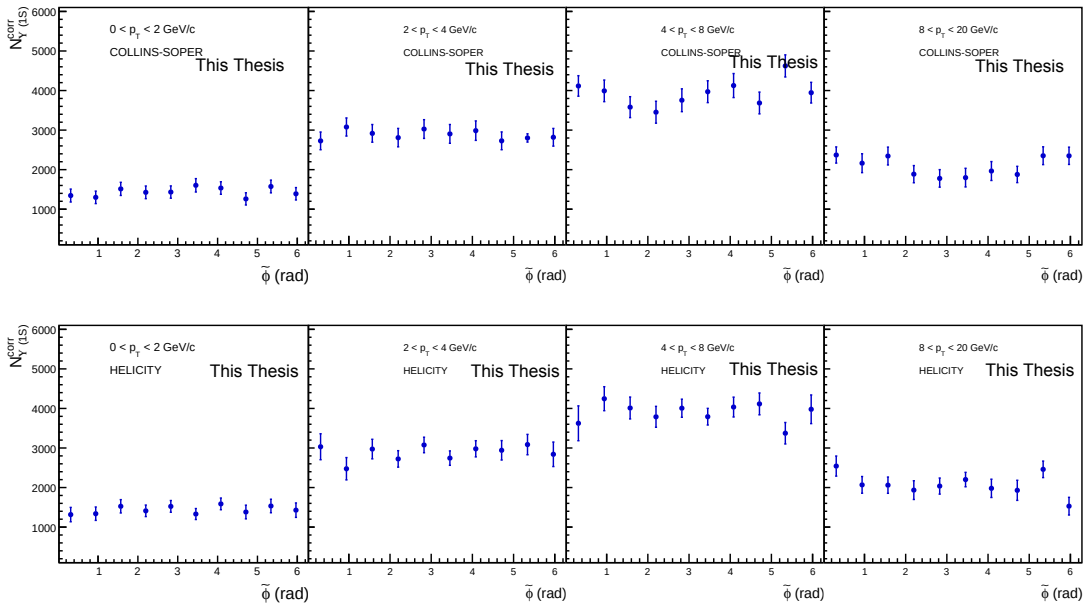

Figure 5.23: Corrected number of Υ (1S) as a function of $\tilde{\phi}$ in CS and HE frames for different p_{T} bins [273].

The corrected yield are then shown as a function of $|\cos\theta|$, $|\phi|$, and $\tilde{\phi}$ in HE and CS frames in Fig. 5.21, Fig. 5.22, and Fig. 5.23, respectively.

5.5.2 Polarization parameters

Finally, we fit the corrected angular yield of $\Upsilon(1S)$ with its corresponding angular distribution function to obtain the polarization parameters. The $\cos\theta$ distribution in both the HE and CS frames is fitted with the $W\ (\cos\theta)$ function given by

$$W(\cos\theta) \propto \frac{1}{3+\lambda_\theta}\left(1+\lambda_\theta\cos^2\theta\right), \tag{5.26}$$

and the corresponding fittings are shown in Fig. 5.24

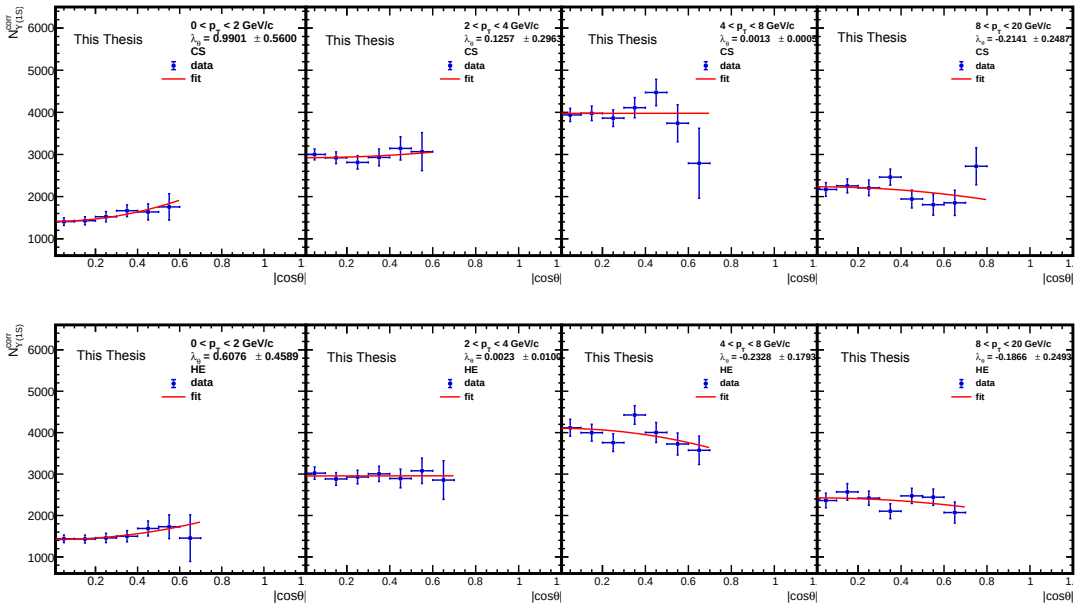

Figure 5.24: Fits to $|\cos\theta|$ distribution in CS and HE frame for different p_{T} bins [273].

Next, the ϕ distribution in both the HE and CS frames is fitted with the $W\ (\phi)$ function given by

$$W(\phi) \propto 1+\frac{2\lambda_\phi}{3+\lambda_\theta}\cos 2\theta. \tag{5.27}$$

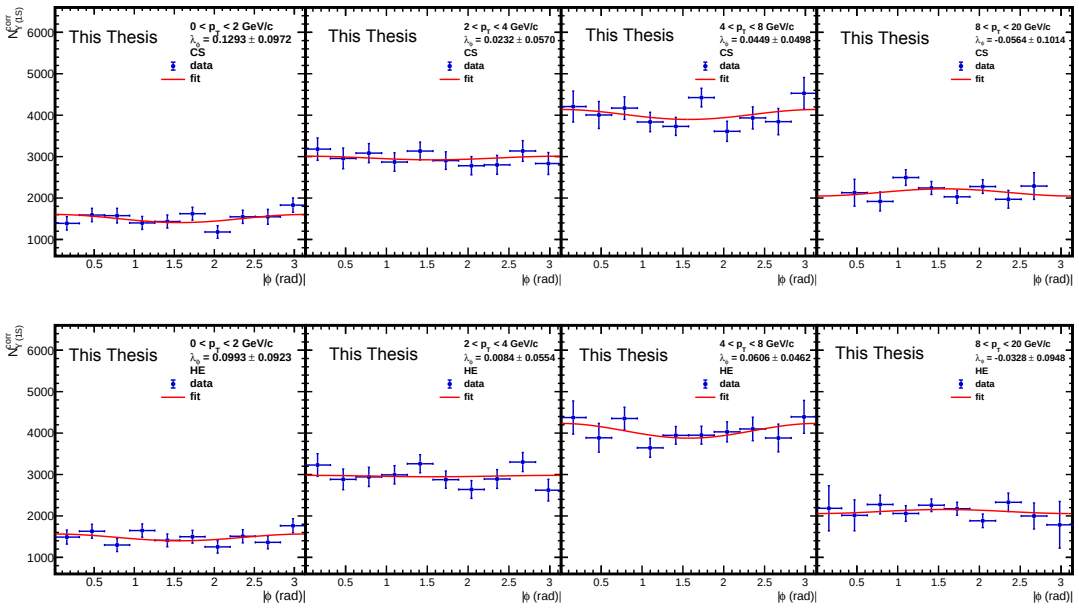

Figure 5.25: Fits to $|\phi|$ distribution in CS and HE frame for different p_{T} bins [273].

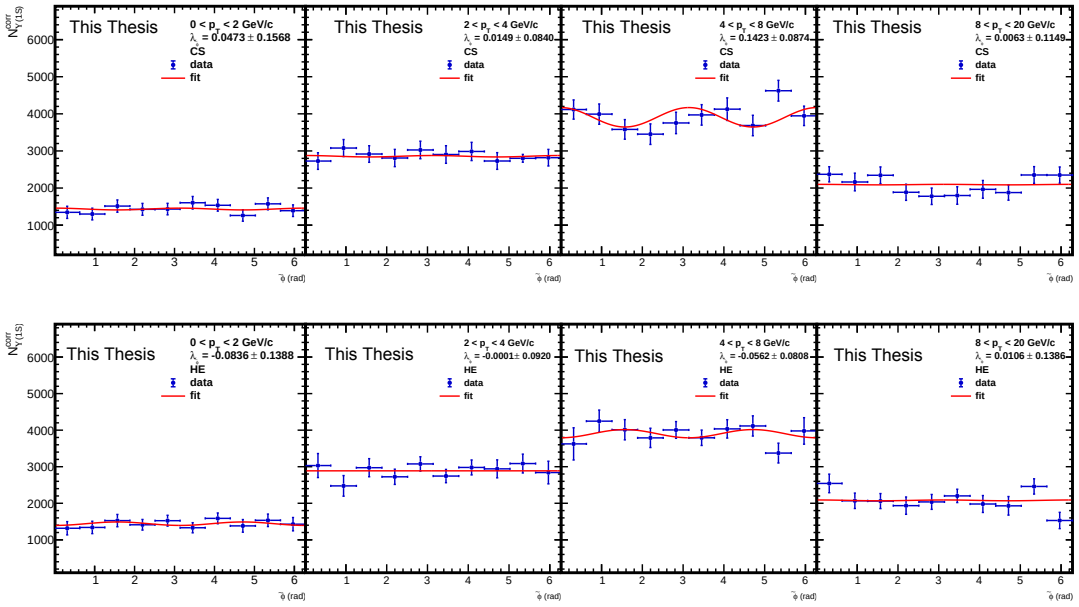

Figure 5.26: Fits to $\tilde{\phi}$ distribution in CS and HE frame for different p_{T} bins [273].

The fittings in both the frames for different p_{T} bins are shown in Fig. 5.25. Finally, the $\tilde{\phi}$ distribution in both the CS and HE frames is fitted with the W $(\tilde{\phi})$

function given by

$$W(\tilde{\phi}) \propto 1 + \frac{\sqrt{2}\lambda_{\theta\phi}}{3+\lambda_\theta} \cos 2\tilde{\phi}. \tag{5.28}$$

The fittings in both the frames for $\tilde{\phi}$ for different p_{T} bins are shown in Fig. 5.26.

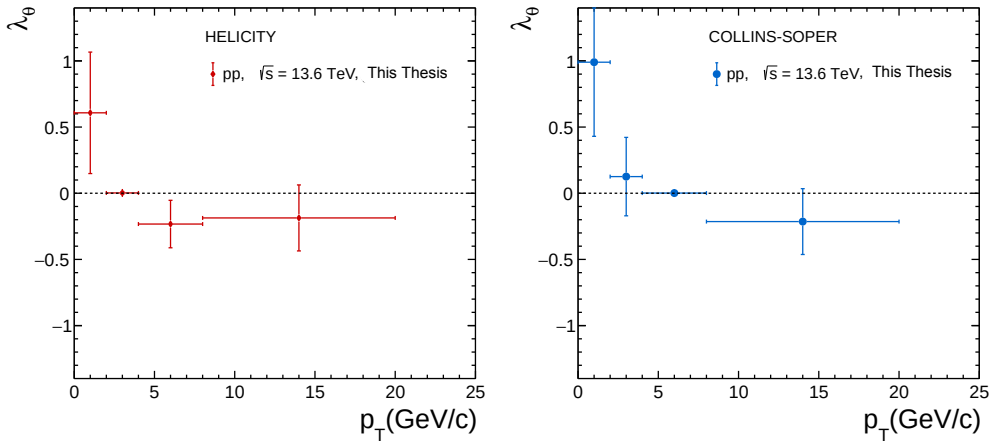

Figure 5.27: Polarization parameter λ_θ as a function of p_{T} in HE and CS frame [273].

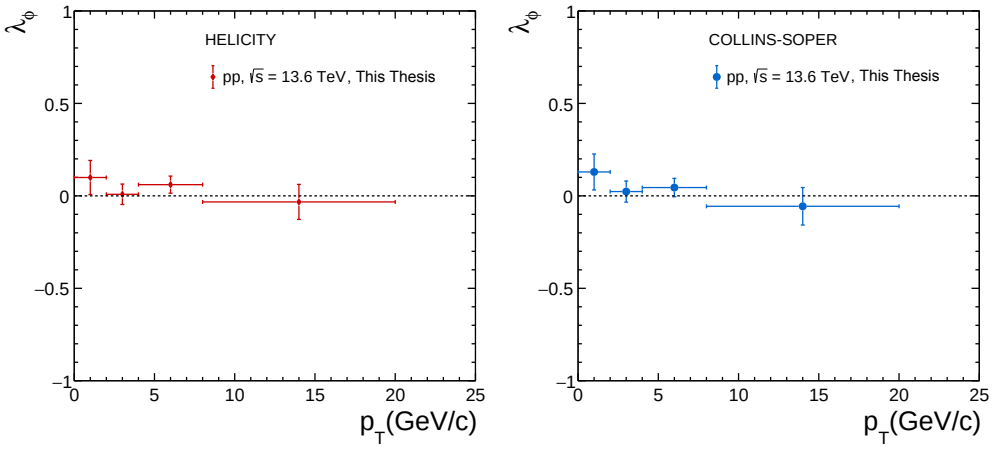

Figure 5.28: Polarization parameter λ_ϕ as a function of p_{T} in HE and CS frame [273].

The polarization parameters λ_θ, λ_ϕ, and $\lambda_{\tilde{\phi}}$ are then obtained from these fits for both the case of HE and CS frame of references. In Fig. 5.27, the λ_θ is shown

for both the HE and CS frames as a function of p_{T}. Whereas, the λ_{ϕ} and $\lambda_{\tilde{\phi}}$ are shown in Fig. 5.28 and Fig. 5.29, respecively, in both frames of reference.

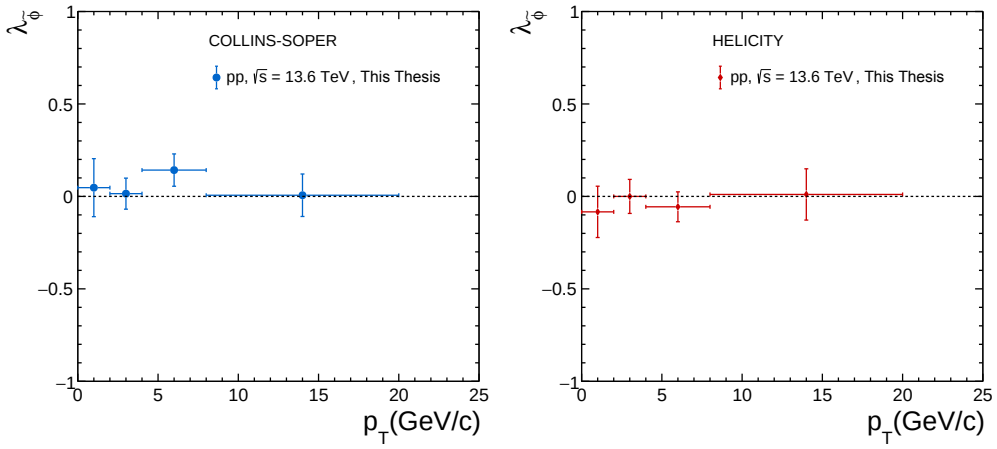

Figure 5.29: Polarization parameter $\lambda_{\tilde{\phi}}$ as a function of p_{T} in HE and CS frame [273].

We observe that the polarization parameter λ_{θ} is close to zero within large statistical uncertainties in both the HE and CS frames. For the case of $0.0 < p_{\mathrm{T}} < 2.0$ GeV/c, a deviation from zero is observed in both cases. Due to the low statistics, the fitting procedure, the tail parameters chosen, and the fitting ranges, among other factors, can significantly affect the results. Therefore, our physics interpretation would require further correction to the plots along with the systematic uncertainties. Essentially, a systematic study can identify the source of error in the analysis and thereby allow a more accurate physical interpretation. The ongoing analysis is currently focused on obtaining various sources of systematic uncertainties.

From Fig. 5.28, we observe that the λ_{ϕ} is consistent with zero for both frames of reference. Furthermore, the $\lambda_{\tilde{\phi}}$ is also found to be consistent with zero within uncertainties, as shown in Fig. 5.29.

The polarization parameters λ_{θ}, λ_{ϕ}, and $\lambda_{\tilde{\phi}}$ obtained are then compared with the measurements from the Run 2 analysis at $\sqrt{s} = 13$ TeV [278]. Fig. 5.30 shows

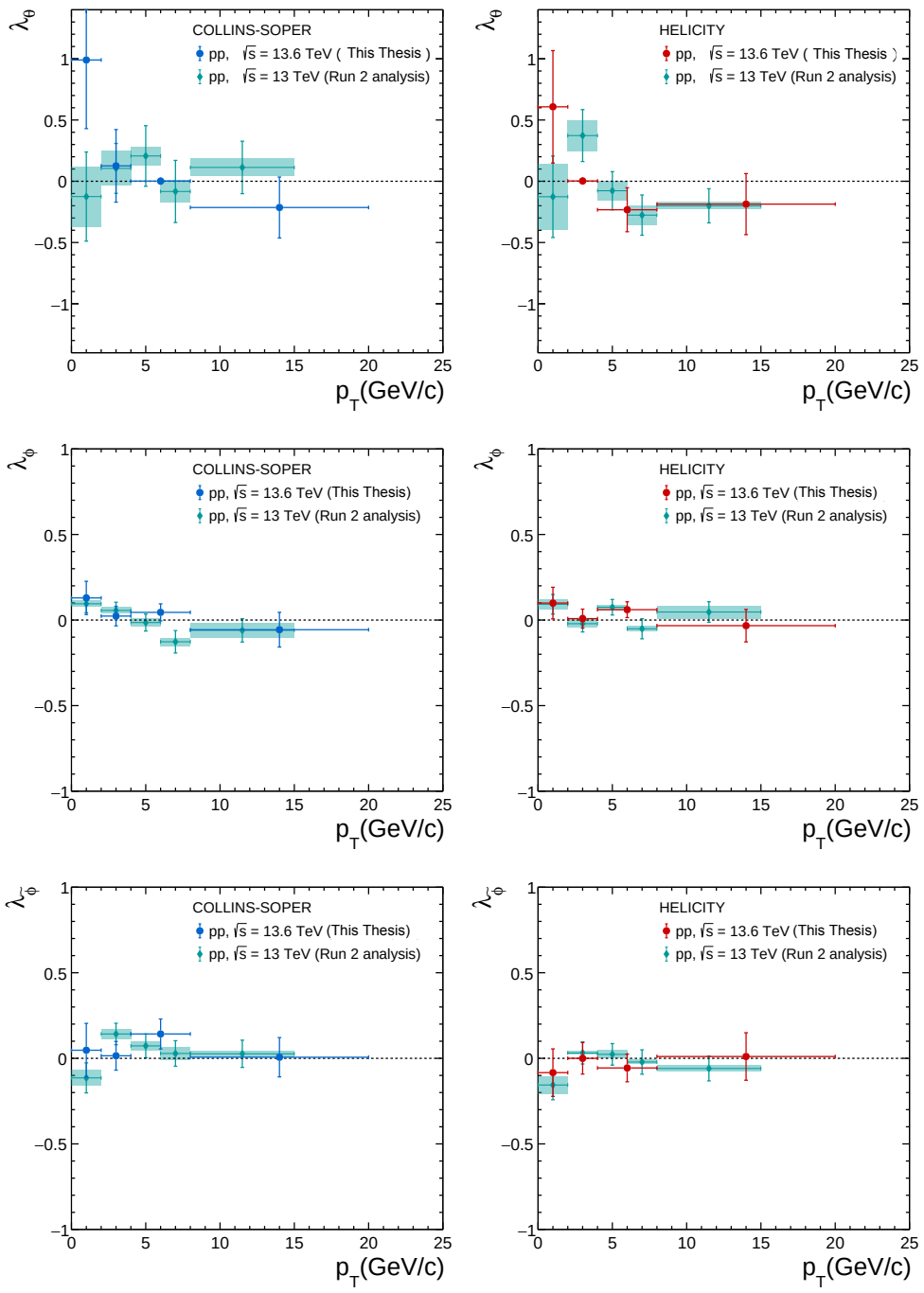

Figure 5.30: Polarization parameter λ_θ, λ_ϕ, and $\lambda_{\tilde{\phi}}$ as a function of p_{T} in CS (left) and HE (right) frame of references [273] compared with Run 2 measurements at $\sqrt{s} = 13$ TeV [278].

the λ_θ, λ_ϕ, and $\lambda_{\tilde{\phi}}$ as a function of p_{T} in CS frame and HE frames. The color band indicates the systematic error estimated in Run 2, whereas the vertical bars represent the statistical error in both Run 2 and Run 3 analyses.

Within the current statistical precision, the polarization parameter λ_θ is consistent with zero in both the HE and CS frames and agrees relatively with the Run 2 measurements at $\sqrt{s} = 13$ TeV. An apparent deviation is observed in the lowest transverse-momentum interval ($0.0 < p_{\mathrm{T}} < 2.0$ GeV/c); however, this region is affected by limited statistics. In such cases, the extracted values can be sensitive to the fitting strategy, the choice of tail parameters, and the selected mass ranges. A reliable physics interpretation, therefore, requires a detailed evaluation of systematic uncertainties. Ongoing studies aim to quantify the various sources of systematic effects in order to achieve a more robust determination of the polarization parameters.

5.5.3 Systematic uncertainties for polarization parameters

Several sources can contribute to the systematic uncertainties in the polarization measurement. This may arise from the signal extraction procedure, including variations in the chosen signal and background parameterizations, the fitting ranges, and other methodological choices. To account for these effects, multiple signal-extraction tests are performed, allowing the associated systematic uncertainties in the polarization measurements to be evaluated. Among others, the main contributions considered in this analysis include

- Signal extraction (choice of background functions and fitting ranges)
- Variation of the Υ(1S) width in the fit to the dimuon invariant mass distribution
- $A \times \varepsilon$: dependence on the MC input shape

It should be noted that the MC sample (LHC24l4) used to compute the acceptance–efficiency correction for the yield as a function of p_{T} and angular bins is anchored to the LHC22 pass 7 data period [273]. Therefore, its applicability to the LHC24 data periods needs to be checked. With the updated MC productions, these corrections will be recalculated and incorporated into the measurements of the polarization parameters. In the present study, we first focus on the systematic uncertainties associated with signal extraction to assess the stability and reliability of the fitting procedure. The different tests considered for this purpose are listed in Table 5.2.

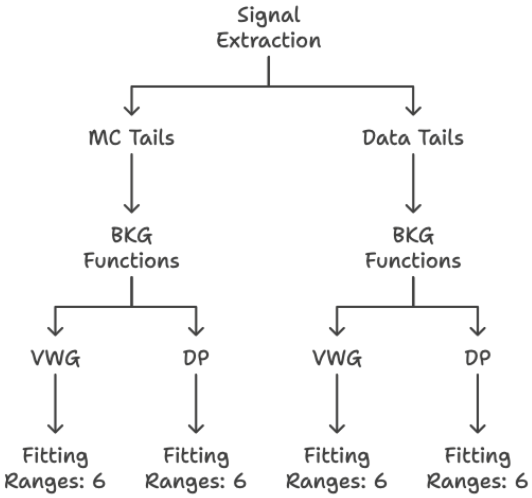

Figure 5.31: Different tests for each angular bin corresponding to a given p_{T} bin for the polarization measurements.

Only one signal parametrization, the Double Crystal Ball (DCB) function, is used, while two background functions, VWG and DP, are considered. In addition, two sets of tail parameters, obtained from data and MC, are employed. Six different fitting ranges, discussed in Table 5.2, are also used to evaluate the sensitivity of the extracted yields to the chosen mass interval. The full set of tests performed for each angular bin within a given p_{T} interval is summarized in the flow chart shown in Fig. 5.31.

5.5.3.1 Signal extraction with MC tails

For a given p_{T} bin, we are considering ~ 6 bins for $\cos\theta$ and 10 bins each for ϕ and $\tilde{\phi}$. For each bin, we consider 6 tests over different fitting ranges and different BKG functions. This is repeated in both CS and HE frames.

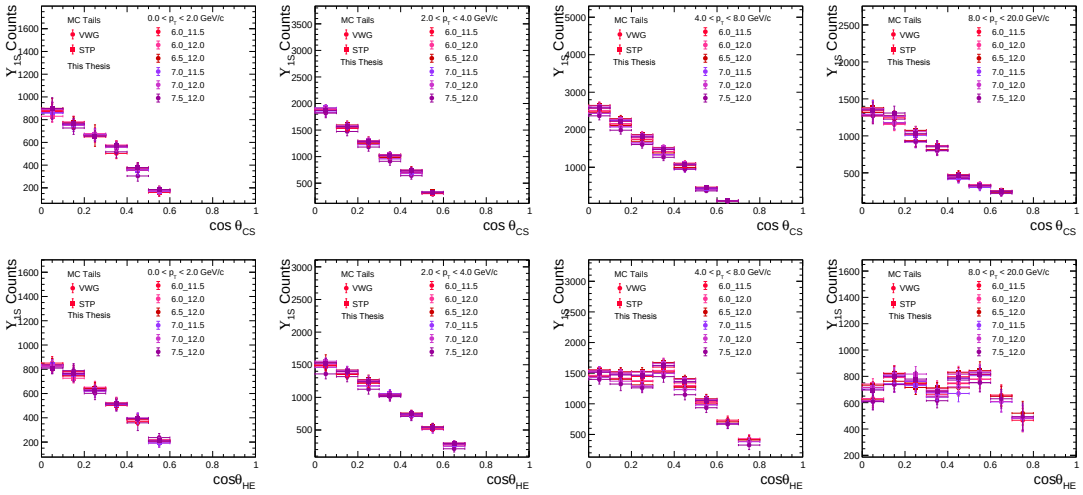

Figure 5.32: Distribution of raw numbers of Υ (1S) as a function of $\cos\theta$ in CS frame (upper panel) and HE frame (lower panel).

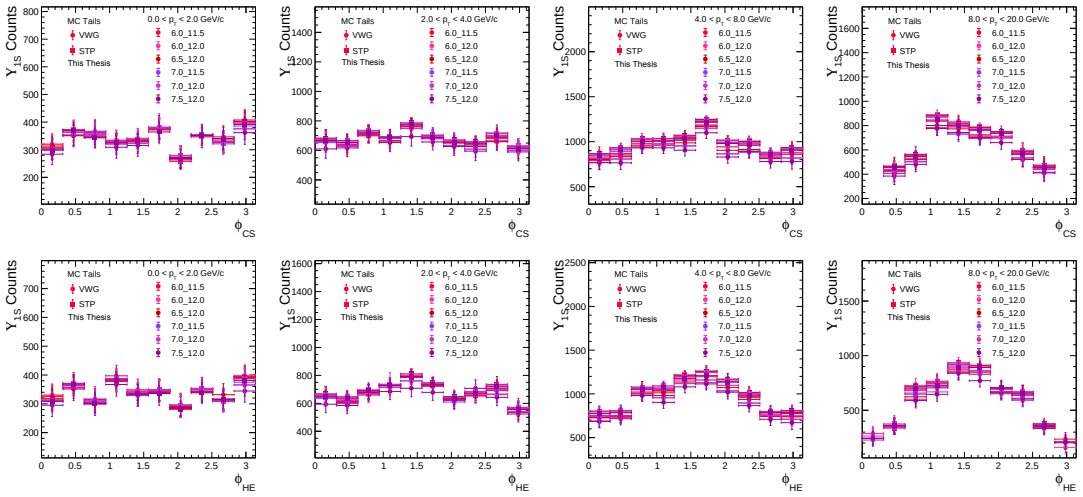

Figure 5.33: Distribution of raw numbers of Υ (1S) as a function of ϕ in CS frame (upper panel) and HE frame (lower panel).

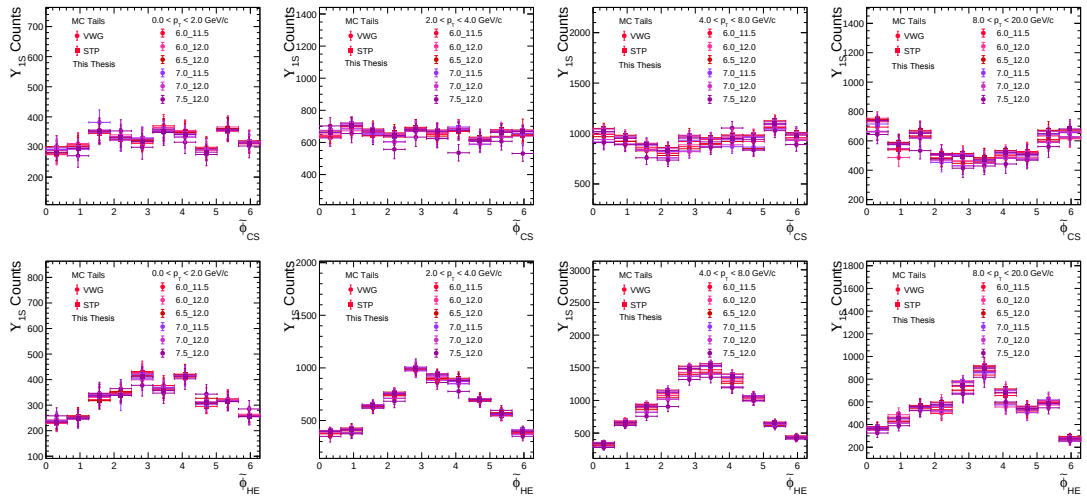

Figure 5.34: Distribution of raw numbers of Υ (1S) as a function of $\tilde{\phi}$ in CS frame (upper panel) and HE frame (lower panel).

We use the $A \times \varepsilon$ factor as obtained using Eq. (5.24) to obtain the corrected spectra of Υ (1S) as a function of $\cos\theta$, ϕ, and $\tilde{\phi}$ in CS and HE frames as shown in the following figures.

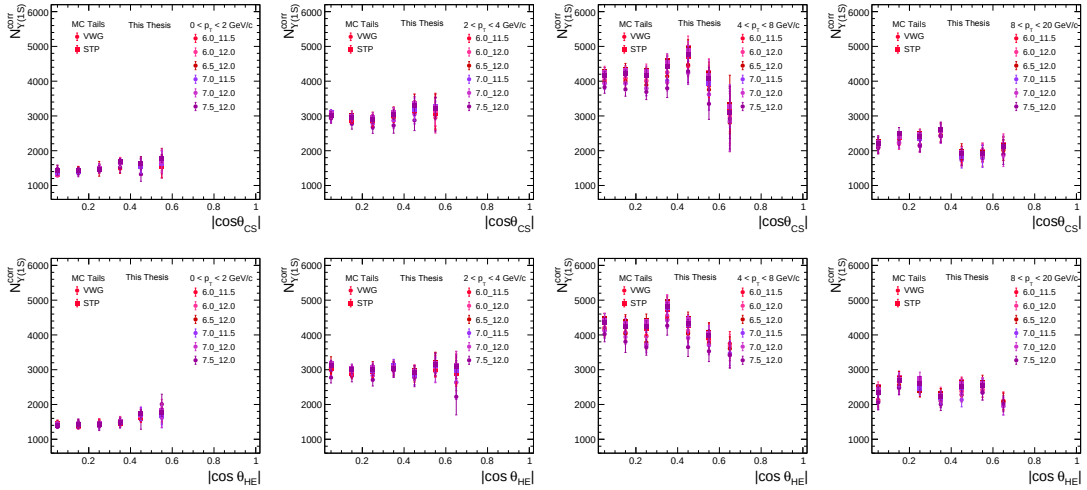

Figure 5.35: Distribution of corrected numbers of Υ (1S) as a function of $\cos\theta$ in CS frame (upper panel) and HE frame (lower panel).

The corrected spectra are then fitted with the corresponding angular distri-

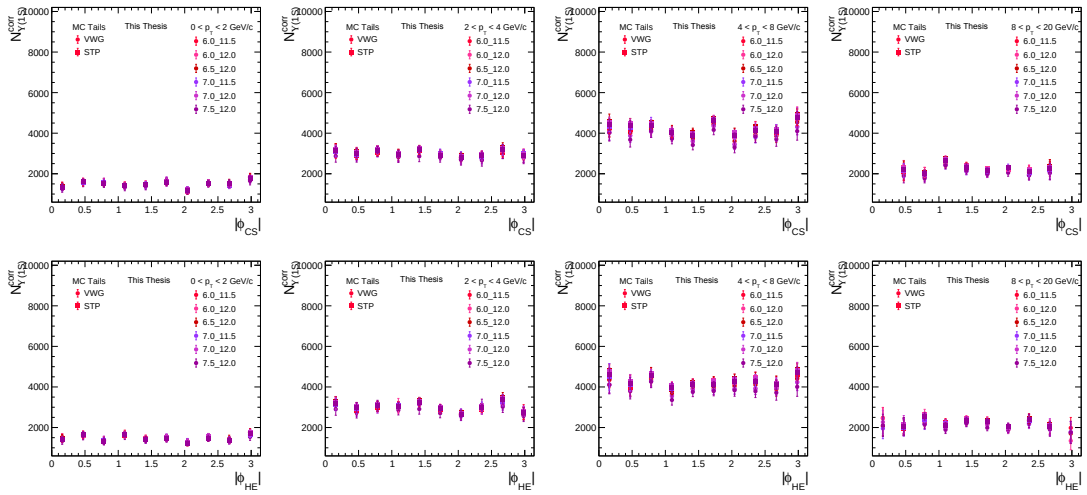

Figure 5.36: Distribution of corrected numbers of Υ (1S) as a function of ϕ in CS frame (upper panel) and HE frame (lower panel).

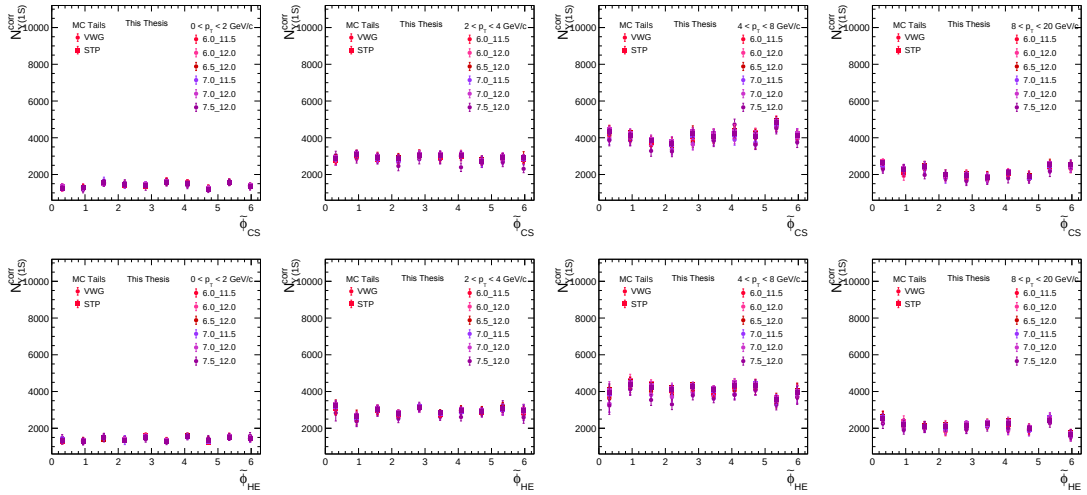

Figure 5.37: Distribution of corrected numbers of Υ (1S) as a function of $\tilde{\phi}$ in CS frame (upper panel) and HE frame (lower panel).

bution functions to obtain the polarization parameters in each p_{T} bin for both cases of CS and HE frames. For illustration, we present the case of the $\cos\theta$ distribution for CS, and HE frames in $2.0 < p_{\mathrm{T}} < 2.0$ GeV/c in Fig. 5.48. Similar procedures for fitting are considered for all four p_{T} bins considered in this analysis for $\cos\theta$, ϕ, and $\tilde{\phi}$ in CS and HE frames.

5.5 Υ (1S) polarization

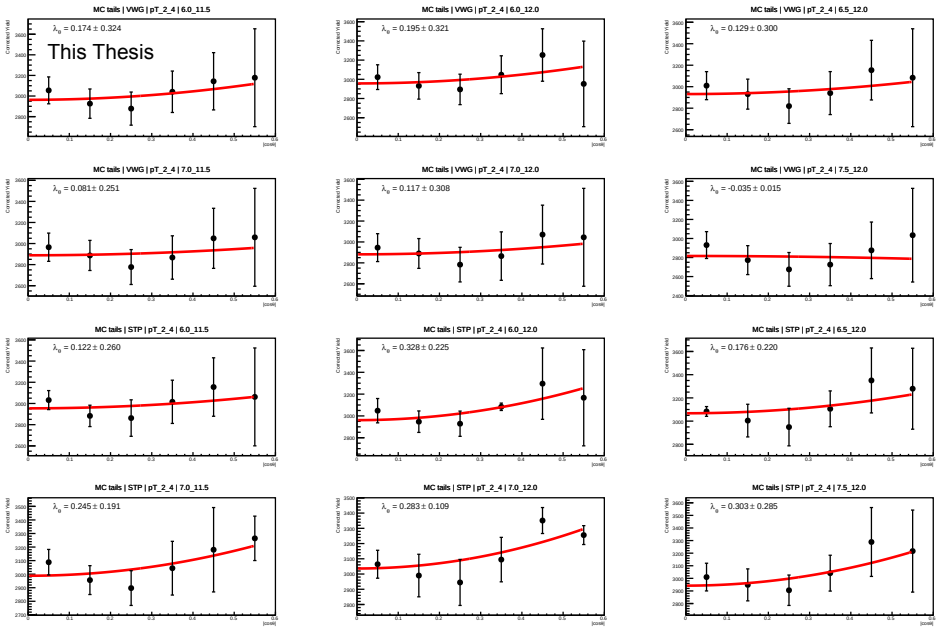

Figure 5.38: Illustration of determining polarization parameter, λ_θ in different tests for the case of $2.0 < p_{\mathrm{T}} < 4.0$ GeV/c in CS frame.

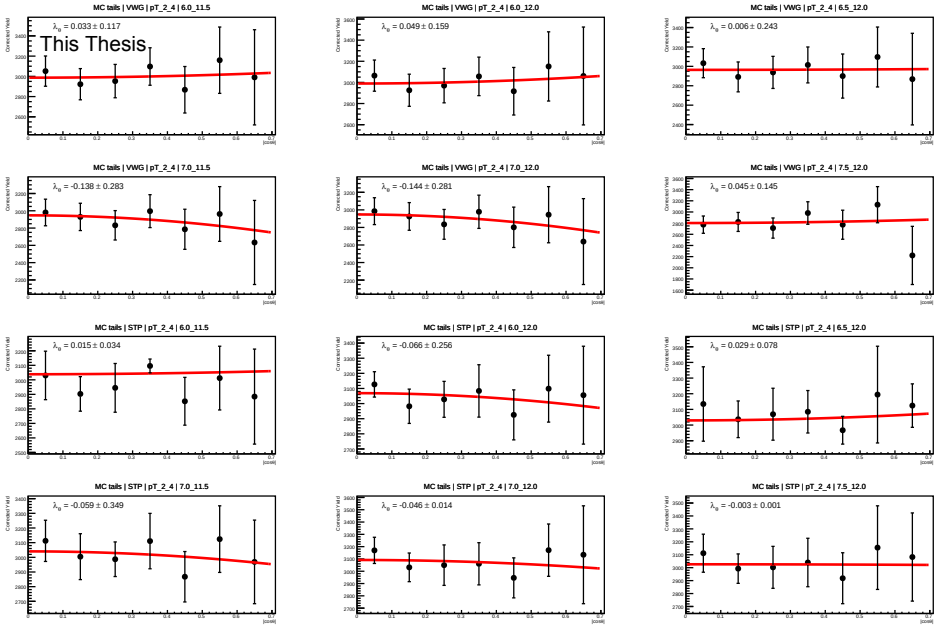

Figure 5.39: Illustration of determining polarization parameter, λ_θ in different tests for the case of $2.0 < p_{\mathrm{T}} < 4.0$ GeV/c in HE frame.

After extracting the fit parameters from all the tests, we plot them as a function of p_{T} and is shown in Fig. 5.40.

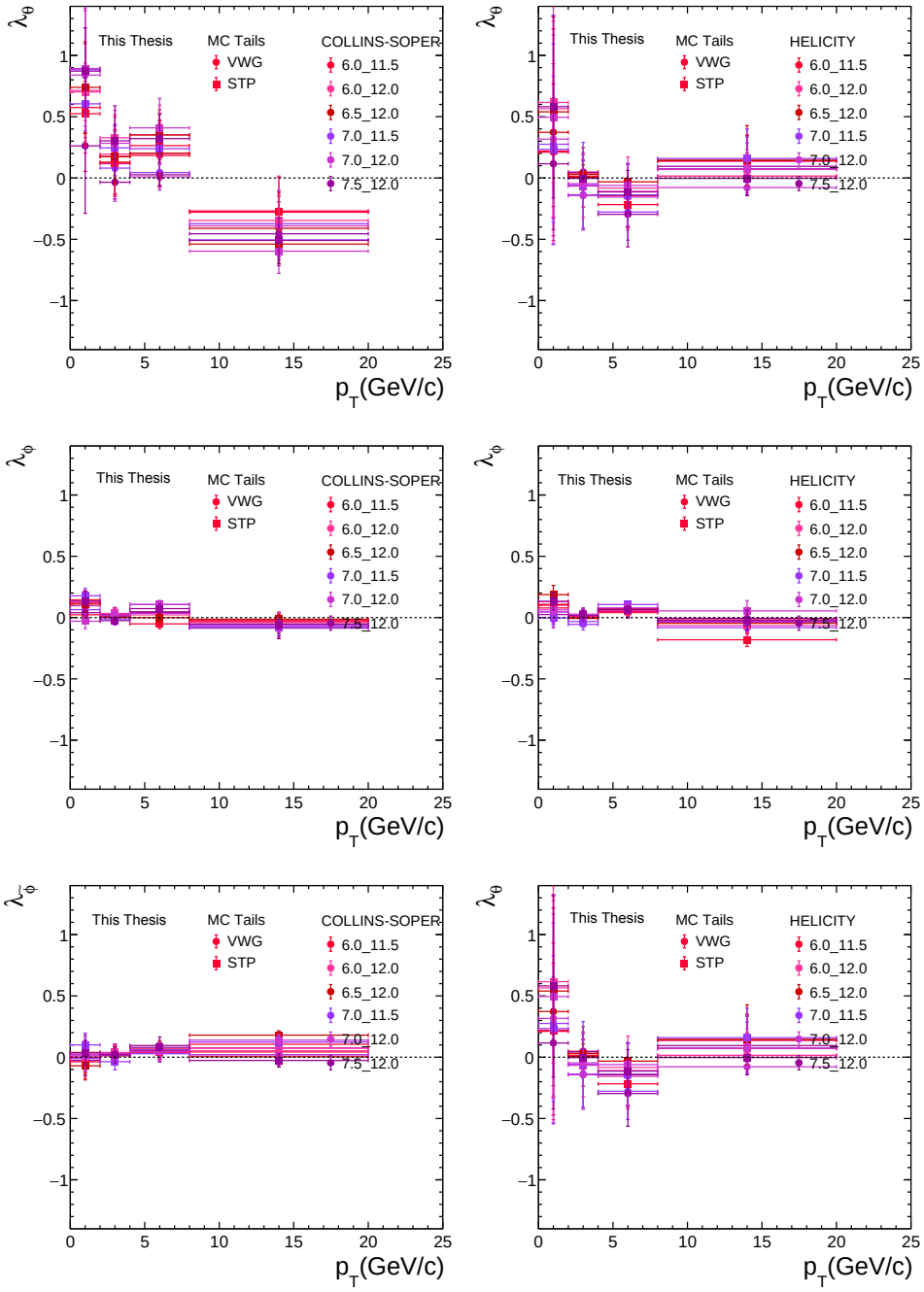

Figure 5.40: Polarization parameter λ_θ, λ_ϕ and $\lambda_{\tilde{\phi}}$ as a function of p_{T} in CS frame (left) and HE frame (right) for different tests made using MC tail parameters.

5.5.3.2 Signal extraction with data tails

The same analysis is now repeated by using tail parameters obtained from real data. For each bin, we consider 6 tests over different fitting ranges with 2 different BKG functions. This is repeated in both CS and HE frames.

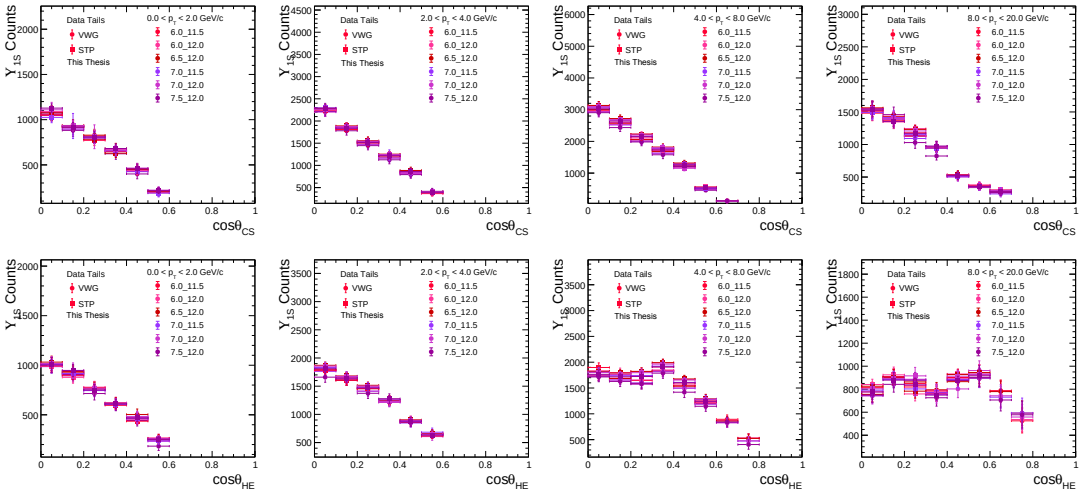

Figure 5.41: Distribution of raw numbers of ϒ (1S) as a function of $\cos\theta$ in CS frame (upper panel) and HE frame (lower panel).

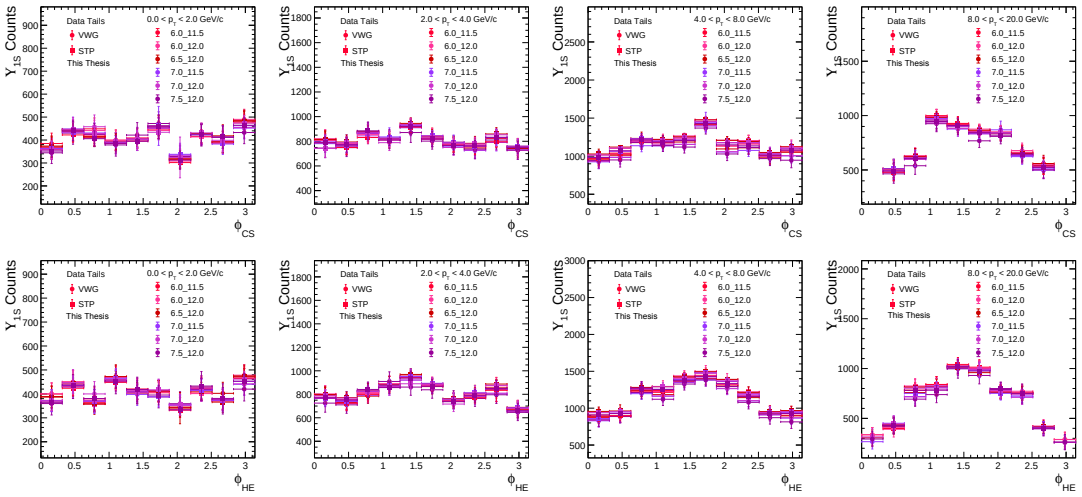

Figure 5.42: Distribution of raw numbers of ϒ (1S) as a function of ϕ in CS frame (upper panel) and HE frame (lower panel).

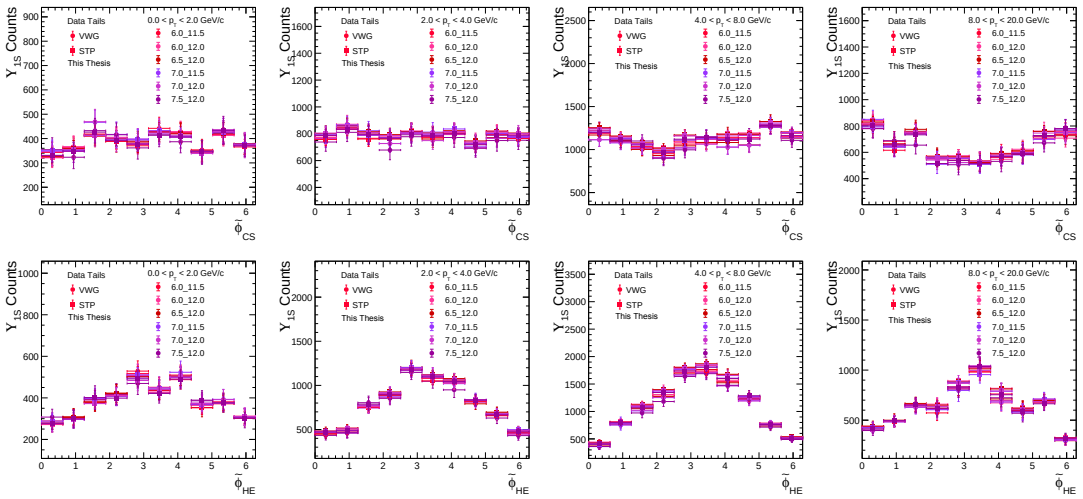

Figure 5.43: Distribution of raw numbers of Υ (1S) as a function of $\tilde{\phi}$ in CS frame (upper panel) and HE frame (lower panel).

The acceptance-efficiency corrected spectra of Υ (1S) are then obtained as a function of $\cos\theta$, ϕ, and $\tilde{\phi}$ in CS and HE frames, as shown in the following figures.

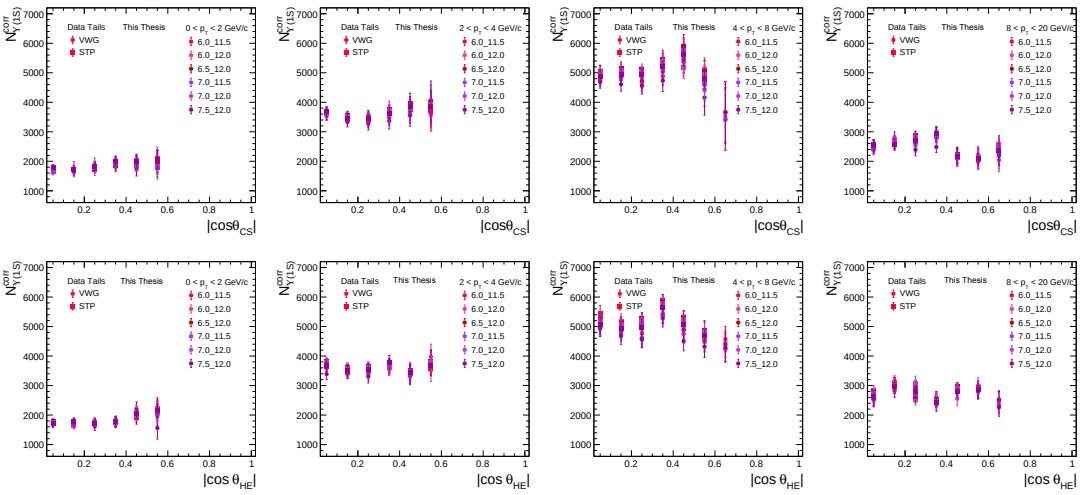

Figure 5.44: Distribution of corrected numbers of Υ (1S) as a function of $\cos\theta$ in CS frame (upper panel) and HE frame (lower panel).

The corrected spectra are subsequently fitted with the appropriate angular distribution functions to extract the polarization parameters in each p_{T} interval

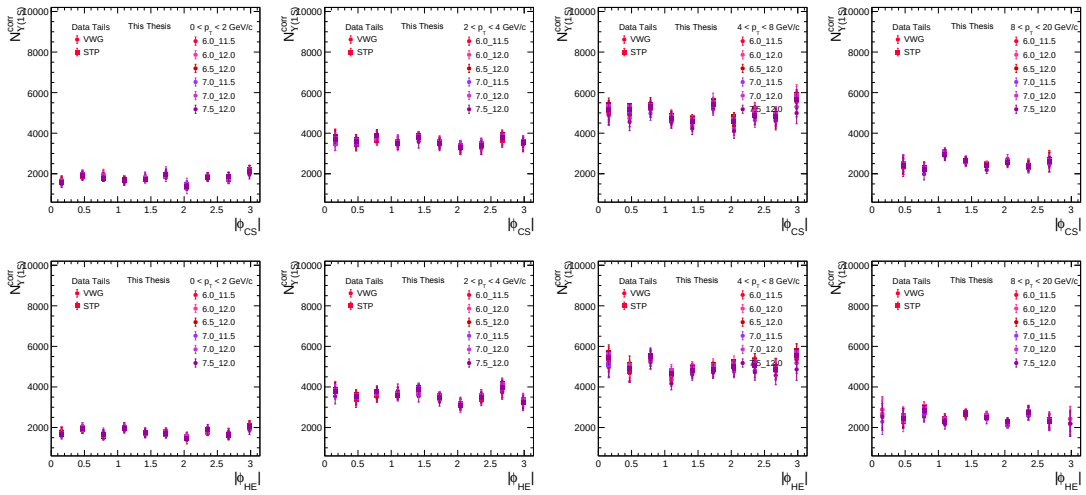

Figure 5.45: Distribution of corrected numbers of Υ (1S) as a function of ϕ in CS frame (upper panel) and HE frame (lower panel).

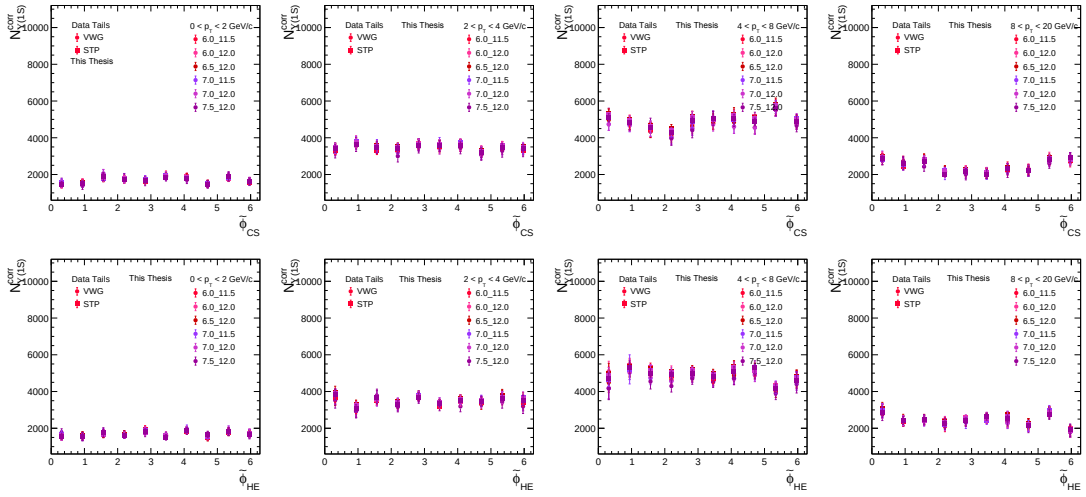

Figure 5.46: Distribution of corrected numbers of Υ (1S) as a function of $\tilde{\phi}$ in CS frame (upper panel) and HE frame (lower panel).

for both the CS and HE reference frames. As an example, the $\cos\theta$ distributions in the CS and HE frames for the $2.0 < p_{\mathrm{T}} < 4.0$ GeV/c interval are shown in Fig. 5.48. The same fitting procedure is applied to all four p_{T} bins considered in this analysis for the $\cos\theta$, ϕ, and $\tilde{\phi}$ distributions in both reference frames. After extracting the fit parameters from all the tests (with data tails), we plot them as

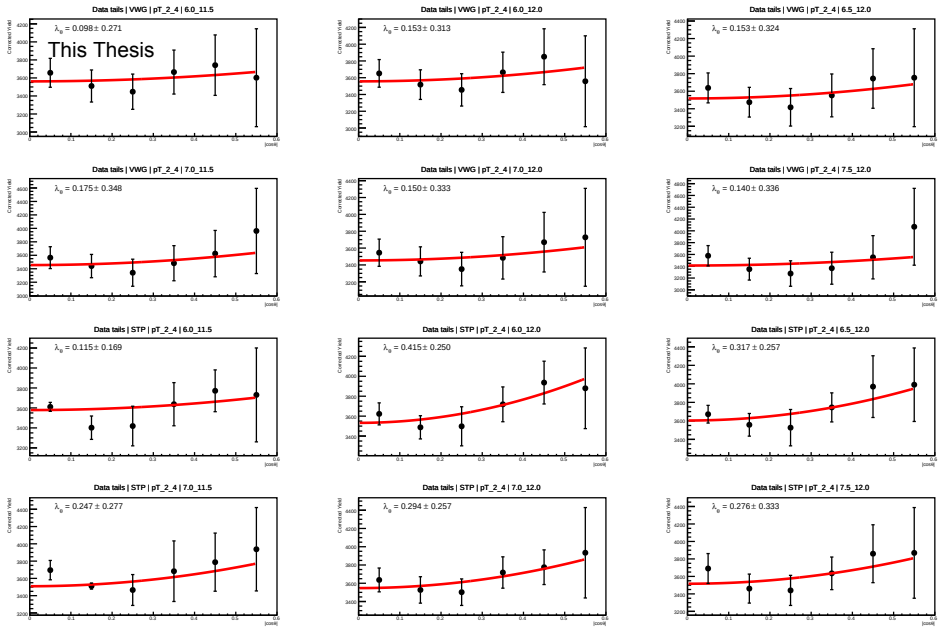

Figure 5.47: Illustration of determining polarization parameter, λ_θ in different tests for the case of $2.0 < p_{\mathrm{T}} < 4.0$ GeV/c in CS frame.

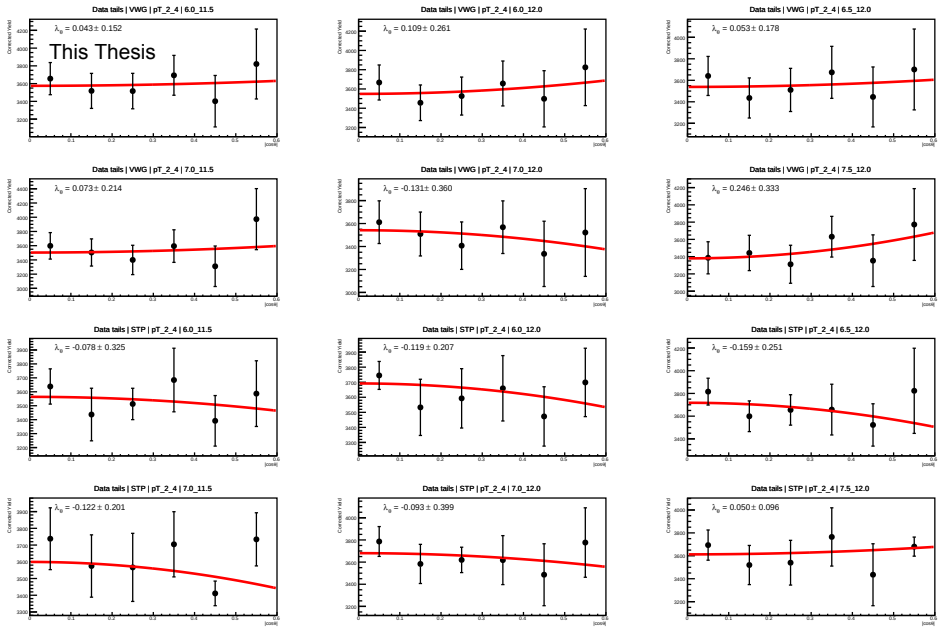

Figure 5.48: Illustration of determining polarization parameter, λ_θ in different tests for the case of $2.0 < p_{\mathrm{T}} < 4.0$ GeV/c in HE frame.

a function of p_{T} and show it in Fig. 5.49.

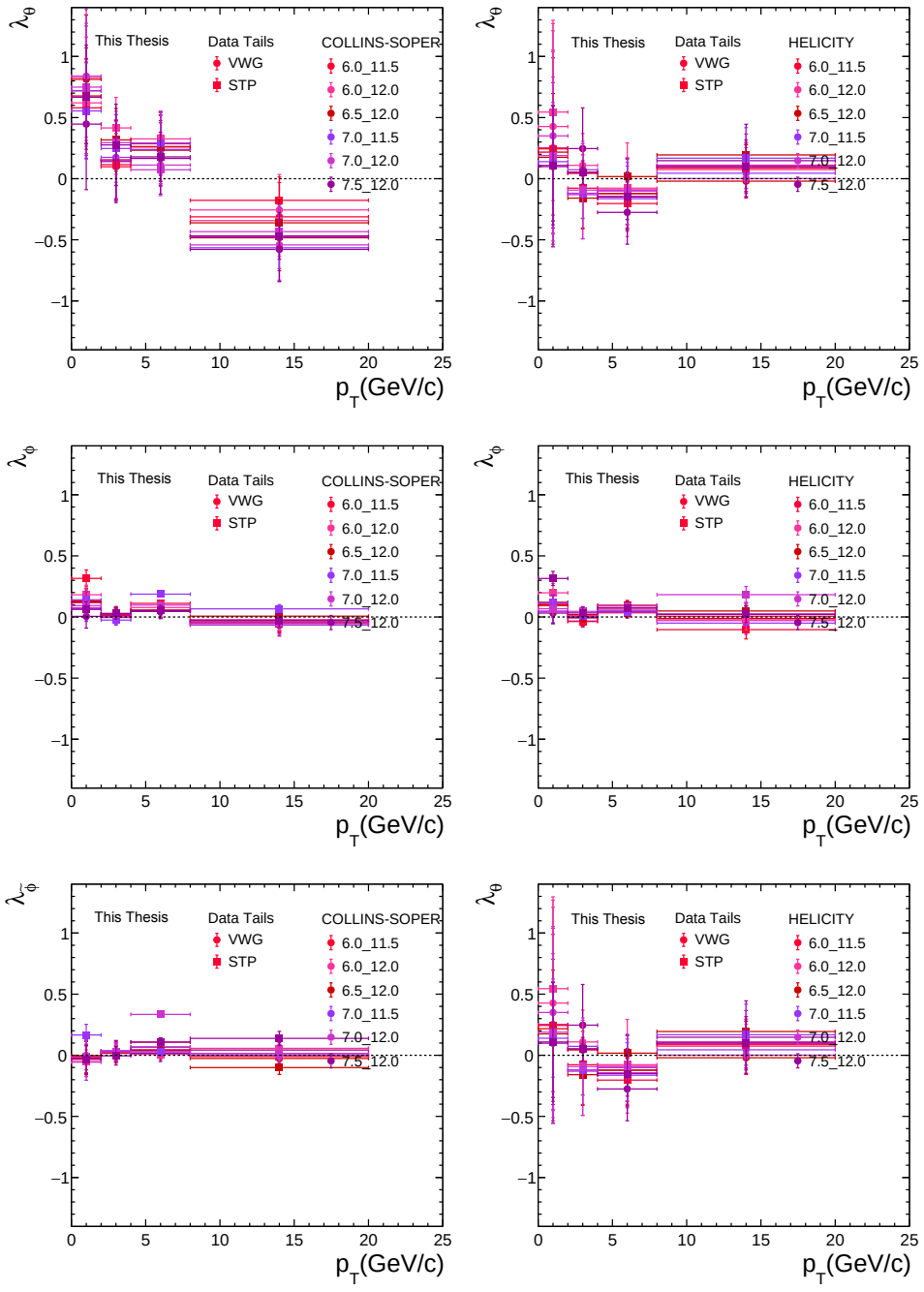

Figure 5.49: Polarization parameter λ_θ, λ_ϕ and $\lambda_{\tilde{\phi}}$ as a function of p_{T} in CS frame (left) and HE frame (right) for different tests made using MC tail parameters.

Finally, considering the results using MC and data tail parameters, we obtain

the systematics due to signal extraction. The details are given in the analysis note [273]. The polarization parameters λ_θ, λ_ϕ, and $\lambda_{\tilde{\phi}}$ with statistical and systematic uncertainties are then shown in Fig. 5.50.

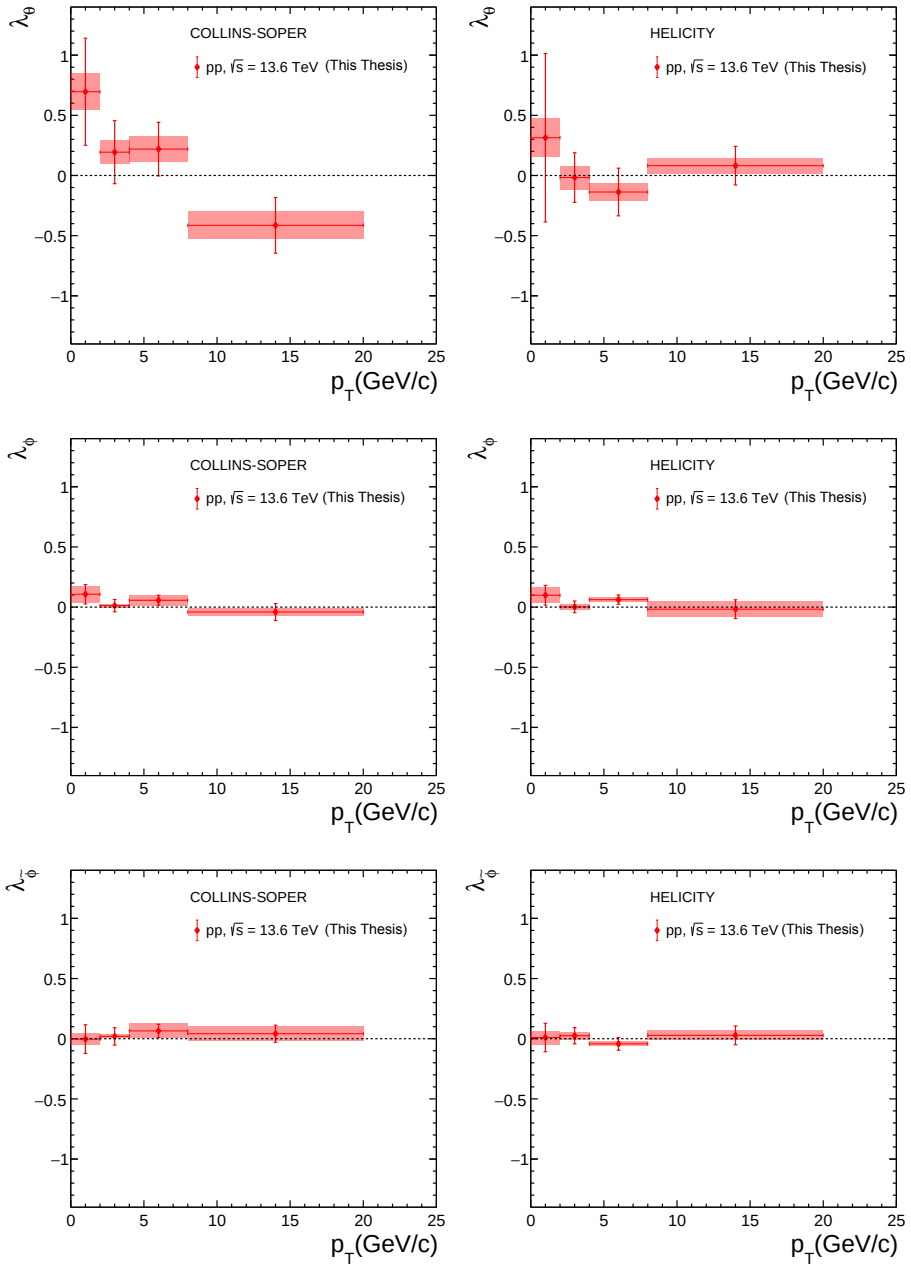

Figure 5.50: Polarization parameter λ_θ, λ_ϕ and $\lambda_{\tilde{\phi}}$ as a function of p_{T} in CS frame (left) and HE frame (right) in Run 3 at $\sqrt{s}$ 13.6 TeV.

In Fig. 5.51, the results are compared with the Run 2 measurements in pp collisions at 13 TeV [276]. The vertical bars represent the statistical uncertainty, whereas the color bands represent the systematic uncertainty.

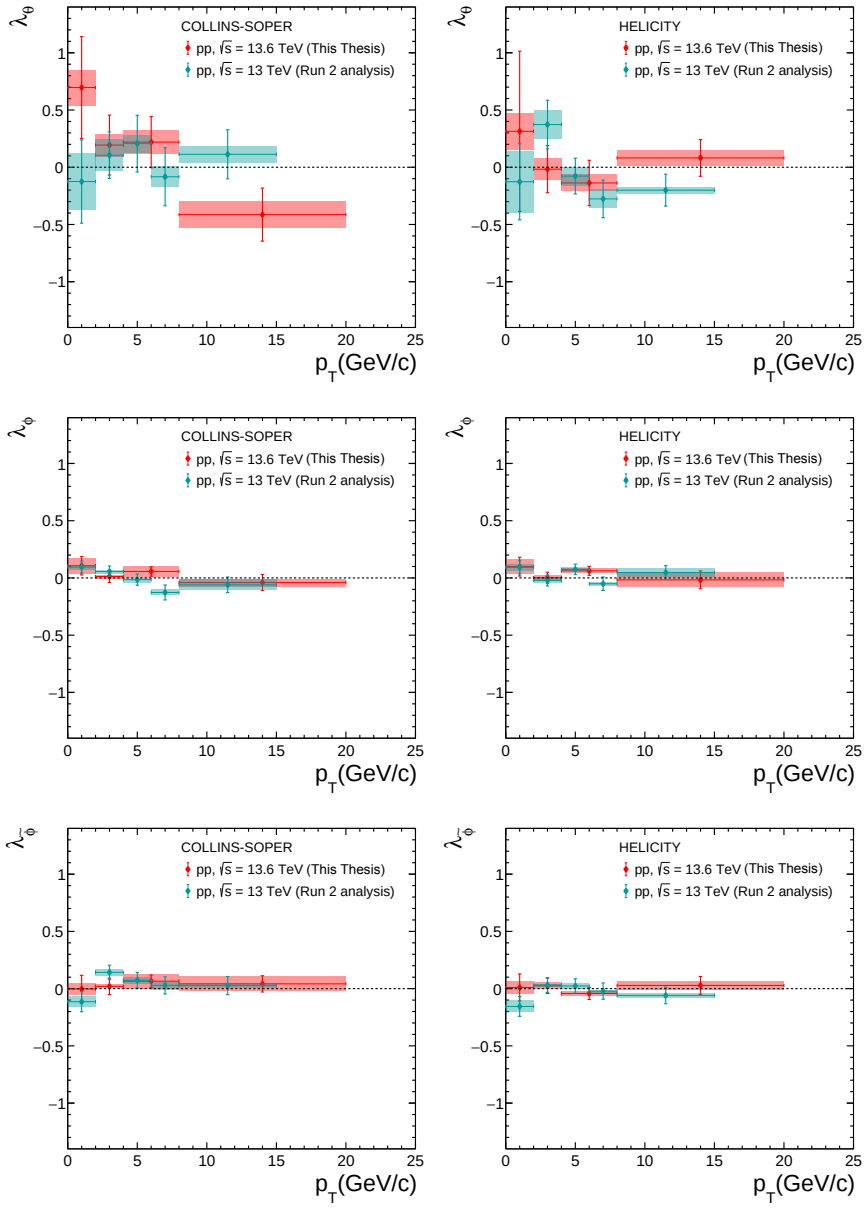

Figure 5.51: Polarization parameter λ_θ, λ_ϕ and $\lambda_{\tilde{\phi}}$ as a function of p_{T} in CS frame (left) and HE frame (right) obtained pp collisions in 13.6 TeV [273] and are compared with those from Run 2 at 13 TeV [278].

In this chapter, we analyzed the 2024 skimmed pp collisions data to reconstruct the Upsilon resonances and hence to measure the polarization of the Υ (1S) meson. First, we obtained the Upsilon resonances ratio as a function of p_{T} and compared it with those from Run 2 measurements. Both the statistical and systematic errors were obtained. Then, moving on to the polarization measurements, we analyzed the angular distributions of the decay daughters (muons) from Υ (1S) in both the Collins-Soper and Helicity frames of reference. The acceptance-efficiency corrected ditributions of Υ (1S) is obained as a function of $\cos\theta$, ϕ, and $\tilde{\phi}$ and fitted with corresponding functions to obtain the polarization parameters λ_θ, λ_ϕ, and $\lambda_{\tilde{\phi}}$ as a function of p_{T}. We observe the polarization consistent with zero within large uncertainties. At low p_{T}, the measurement shows a finite transverse polarization (λ_θ), showing deviation from previous Run 2 measurements. The λ_ϕ and $\lambda_{\tilde{\phi}}$ are found to be consistent with zero within uncertainties and in agreement with the results obtained in Run 2 measurements. The immediate next step is to repeat the analysis with new MC data anchored to 2024 data passes for more accurate results, which can help us to obtain more precise polarization parameters, especially at low p_{T}. Apart from this, the systematic uncertainties arising from the varying width of Υ (1S), the MC input shapes, simultaneous fits of polarization parameters, etc., will be addressed and will be updated in the upcoming version of ALICE Analysis Note [273]. It is noteworthy to mention that the current analysis is performed using data available from the 2024 year of pp collisions. The next step is to utilize all the available data to obtain high-precision polarization measurements. With the high statistics, the analysis will also be extended to obtain the polarization parameters for Υ (2S) and Υ (3S).

Chapter 6

Summary

The research work discussed in this PhD thesis have been carried out at the Indian Institute of Technology (IIT) Indore, India, within the ALICE collaboration at the LHC, CERN, Geneva. This thesis presents a comprehensive investigation of strongly interacting matter from both phenomenological and experimental perspectives, with the aim of advancing our understanding of Quantum Chromodynamics (QCD) matter under extreme conditions of temperature, density, and angular momentum. In high-energy collisions, the hadronic phase constitutes the final stage of the collision evolution, occurring just before the produced particles decouple and are detected by the detectors. This thesis explores this hadronic phase by considering interacting models to study the thermodynamics and transport properties of the hadrons. The thesis further addresses the early stages of the collision, where heavy quarkonium states are produced. Due to their large masses and early formation times, quarkonia serve as valuable probes of the medium created in heavy-ion collisions, providing insight into the space–time evolution of the system. Therefore, it becomes necessary to understand their production mechanism in extreme conditions. Motivated by this, the thesis attempts to make precision measurements of quarkonium production and polarization in proton–proton collisions using the ALICE experiment at the Large Hadron Collider (LHC). Understanding their production mechanism will enhance our understanding of the

QCD dynamics in both the vacuum and in a medium.

The ideal hadron resonance gas (IHRG) model was successful in describing lattice lQCD (lQCD) calculations at low temperatures (T) and zero baryochemical potential (μ_B). However, it fails at high T and also fails when compared with higher-order fluctuation results from lattice lQCD, as well as experimental measurements. The van der Waals hadron resonance gas (VDWHRG) model has emerged as one of the most reliable interacting hadron gas models, which improves the results and extends the applicability of the HRG model to high T and μ_B region. In this thesis, we explore the effect of VDW interaction on the transport properties of the hadron gas, namely, the thermal and electrical conductivities. We observe that the interplay of both the attractive and repulsive interactions plays a significant role in these quantities, especially at high T and μ_B region. The Wiedemann-Franz law is also examined for an interacting hadron gas and found to be violated for the hadronic matter at extreme conditions. Moreover, the study is further extended to systems exhibiting Bose–Einstein condensation (BEC) at high temperature, focusing on bosonic hadronic matter. The transport coefficients, such as shear and bulk viscosities, are obtained for a pion gas in the presence of a BEC and are found to be suppressed at temperatures below the BEC transition temperature, approaching an inviscid behavior.

The discovery of finite vorticity (rotation) in heavy-ion collisions opens a new door to investigate the interesting feature of QCD. In this thesis, the effects of rotation on interacting hadronic matter are systematically explored. The thermodynamic properties of an interacting hadron gas are studied by considering a rotating grand canonical ensemble. It is observed that rotation plays a similar role to the baryochemical potential by enhancing all thermodynamic quantities, such as pressure, energy density, and specific heat. It behaves as an additional chemical potential, known as the rotational chemical potential. This further motivates us to study the phase transition under the effect of rotation. At vanishing μ_B, the scaled entropy density is estimated as a function of T at high magnitudes of

rotation. Interestingly, a liquid-gas phase transition is observed in the VDWHRG model in $T-\omega$ space. This result suggests that the current study of the QCD phase diagram in $T-\mu_B$ space must be extended to consider rotation as another axis. Therefore, similar to the results obtained for a liquid-gas phase transition, a critical line (instead of a single point) and hence a first-order phase transition plane must be the future goal of the QCD phase diagram in the $T-\mu_B-\omega$ plane. The effect of rotation as a chemical potential is also explored by studying the BEC mechanism for the ρ meson. The study demonstrates that the rotation can significantly affect the conditions for the onset of condensation. The strict condition of $\mu \to m$ (m is the mass of the boson) gets relaxed in the presence of rotation (say, rotational chemical potential). This study also demonstrates how the presence of condensation enhances the polarization of the vector meson in the presence of rotation, thereby extending our understanding of the coupled effects of rotation, Bose–Einstein condensation, and spin polarization.

Although the VDWHRG model is the most reliable interacting model for the hadronic phase, this thesis demonstrated its failure in the very high μ_B region. This is essential while studying and interpreting the low-energy (corresponding to high μ_B) experimental results from heavy-ion collisions. We formulated a simple yet significant modification to the conventional VDWHRG model by incorporating the T and μ_B dependence of the VDW parameters a and b for attractive and repulsive interactions, respectively. Following this, the modified VDWHRG (MVDWHRG) is used to estimate proton number cumulant ratios, experimental observables that probe the QCD critical point. A comparison was made of the results with those obtained from the ideal HRG and the existing VDWHRG model, as well as with the experimental results. It is observed that the MVDWHRG model exhibits better agreement with the experimental results, particularly at low energies.

Precise experimental measurements of quarkonium production cross sections and polarization provide essential constraints on their underlying production

mechanisms and, consequently, offer valuable insights into the behavior of Quantum Chromodynamics (QCD) under extreme conditions. This thesis focuses on measuring the Υ(1S) polarization through its dimuon decay channel in proton–proton collisions at $\sqrt{s} = 13.6$ TeV, recorded with the ALICE detector at the LHC. After a brief overview of the current theoretical and experimental understanding of quarkonium production and polarization, the motivation for studying bottomonium polarization is presented. A concise mathematical formulation of polarization observables is introduced, followed by a detailed description of the ALICE experimental apparatus, with primary focus on the muon spectrometer, which was used for the analysis. The Υ resonances are reconstructed in the forward rapidity region through their dimuon decay channel. The Υ resonance ratios are then evaluated as a function of transverse momentum (p_{T}) and compared with corresponding measurements from Run 2 at $\sqrt{s} = 13$ TeV. The acceptance times efficiency correction factors are determined in each angular bin, allowing the extraction of corrected Υ(1S) yields as functions of $|\cos\theta|$, $|\phi|$, and $\tilde{\phi}$. One-dimensional fits to the corrected angular distributions are then performed to extract the polarization parameters. The transverse-momentum dependence of the polarization coefficients λ_θ, λ_ϕ, and $\lambda_{\tilde{\phi}}$ is studied, and the results are found to be consistent with zero within uncertainties, also in agreement with previous Run 2 measurements. The systematic uncertainties due to signal extraction are also calculated. As an outlook, the analysis will be extended to extract the complete set of polarization parameters, λ_θ, λ_ϕ, and $\lambda_{\tilde{\phi}}$, with a comprehensive evaluation of systematic uncertainties, such as those arising due to MC input shape, due to varying width, simultaneous fit, etc. The inclusion of additional datasets from ALICE Run 3 is expected to significantly improve the precision of the measurements and provide stronger constraints on bottomonium production and polarization mechanisms.

Bibliography

[1] E. Hubble, Proc. Nat. Acad. Sci. **15**, 168 (1929).

[2] G. Lemaitre, Annales Soc. Sci. Bruxelles A **47**, 49 (1927).

[3] https://www.amnh.org/learn-teach/curriculum-collections/cosmic-horizons-book/georges-lemaitre-big-bang

[4] N. Aghanim *et al.* [Planck], Astron. Astrophys. **641**, A6 (2020) [erratum: Astron. Astrophys. **652**, C4 (2021)].

[5] R. L. Workman *et al.* [Particle Data Group], PTEP **2022**, 083C01 (2022).

[6] Introduction to High Energy Heavy Ion Collision. C.Y. Wong, World Scientific (1994).

[7] H. Perkins, Introduction to High Energy Physics, Cambridge University Press (2012)

[8] https://webific.ific.uv.es/web/en/content/lattice-qcd-numerical-approach-strong-force

[9] K. Yagi, T. Hatsuda and Y. Miake, Camb. Monogr. Part. Phys. Nucl. Phys. Cosmol. **23**, 1 (2005)

[10] A. Bazavov *et al.* [HotQCD], Phys. Rev. D **86**, 034509 (2012).

[11] R. Bellwied, S. Borsanyi, Z. Fodor, S. D. Katz and C. Ratti, Phys. Rev. Lett. **111**, 202302 (2013).

[12] A. Bzdak, S. Esumi, V. Koch, J. Liao, M. Stephanov and N. Xu, Phys. Rept. **853**, 1 (2020).

[13] A. Bazavov *et al.* [HotQCD], Phys. Rev. D **90**, 094503 (2014).

[14] S. Borsanyi, Z. Fodor, C. Hoelbling, S. D. Katz, S. Krieg and K. K. Szabo, Phys. Lett. B **730**, 99 (2014).

[15] B. E. Aboona *et al.* [STAR], Phys. Rev. Lett. **135**, 142301 (2025).

[16] X. Luo, Nucl. Phys. A **956**, 75 (2016).

[17] https://particlesandfriends.wordpress.com/2016/10/14/evolution-of-collisions-and-qgp/

[18] V. Khachatryan *et al.* [CMS], JHEP **04**, 039 (2017).

[19] K. Aamodt *et al.* [ALICE], Phys. Lett. B **696**, 30 (2011).

[20] R. S. Bhalerao, "Relativistic heavy-ion collisions", arXiv:1404.3294, doi:10.5170/CERN-2014-001.219.

[21] U. Heinz and R. Snellings, Ann. Rev. Nucl. Part. Sci. **63**, 123 (2013).

[22] J. Rafelski and B. Muller, Phys. Rev. Lett. **48**, 1066 (1982) [erratum: Phys. Rev. Lett. **56**, 2334 (1986)].

[23] J. Rafelski, Phys. Rept. **88**, 331 (1982).

[24] T. Matsui and H. Satz, Phys. Lett. B **178**, 416 (1986).

[25] P. Braun-Munzinger and K. Redlich, Eur. Phys. J. C **16**, 519 (2000).

[26] B. W. Zhang, C. M. Ko and W. Liu, Phys. Rev. C **77**, 024901 (2008).

[27] T. Song, J. Aichelin, J. Zhao, P. B. Gossiaux and E. Bratkovskaya, Phys. Rev. C **108**, 054908 (2023).

[28] S. Acharya *et al.* [ALICE], Phys. Lett. B **849**, 138451 (2024).

[29] S. Acharya *et al.* [ALICE], Phys. Lett. B **822**, 136579 (2021).

[30] S. Digal, P. Petreczky and H. Satz, Phys. Rev. D **64**, 094015 (2001).

[31] P. Faccioli, C. Lourenco, J. Seixas and H. K. Wohri, Eur. Phys. J. C **69**, 657 (2010).

[32] P. Faccioli and C. Lourenço, Particle Polarization in High Energy Physics, Lect. Notes Phys. 1002 (2022), doi:10.1007/978-3-031-08876-6

[33] A. Andronic, P. Braun-Munzinger, J. Stachel and M. Winn, Phys. Lett. B **718**, 80 (2012).

[34] P. Moreau, O. Soloveva, L. Oliva, T. Song, W. Cassing and E. Bratkovskaya, Phys. Rev. C **100**, 014911 (2019).

[35] A. Pandav, D. Mallick and B. Mohanty, Prog. Part. Nucl. Phys. **125**, 103960 (2022).

[36] S. S. Adler *et al.* [PHENIX], Phys. Rev. Lett. **91**, 182301 (2003).

[37] J. Adams *et al.* [STAR], Phys. Rev. Lett. **92**, 112301 (2004).

[38] K. Adcox *et al.* [PHENIX], Phys. Rev. C **69**, 024904 (2004).

[39] J. Adams *et al.* [STAR], Nucl. Phys. A **757**, 102 (2005).

[40] G. P. Kadam and H. Mishra, Phys. Rev. C **92**, 035203 (2015).

[41] P. Kovtun, D. T. Son and A. O. Starinets, Phys. Rev. Lett. **94**, 111601 (2005).

[42] P. Romatschke and U. Romatschke, Phys. Rev. Lett. **99**, 172301 (2007).

[43] W. Schmidt, U. Katscher, B. Waldhauser, J. A. Maruhn, H. Stocker and W. Greiner, Phys. Rev. C **47**, 2782 (1993).

[44] P. Danielewicz, Acta Phys. Polon. B **33**, 45 (2002).

[45] A. Nakamura and S. Sakai, Phys. Rev. Lett. **94**, 072305 (2005).

[46] R. A. Lacey, N. N. Ajitanand, J. M. Alexander, P. Chung, W. G. Holzmann, M. Issah, A. Taranenko, P. Danielewicz and H. Stoecker, Phys. Rev. Lett. **98**, 092301 (2007).

[47] J. D. Jackson, Classical Electrodynamics, Wiley (1998)

[48] K. Tuchin, Adv. High Energy Phys. **2013**, 490495 (2013).

[49] X. Wang and I. Shovkovy, Eur. Phys. J. C **81**, 901 (2021).

[50] Raghunath Sahoo, "Relativistic Kinematics: A Journey in Spacetime," Lect. Notes in Phys. **1046**. (2025), Springer.

[51] L. Adamczyk *et al.* [STAR], Nature **548**, 62 (2017).

[52] N. Sass *et al.* [SMASH], Phys. Rev. C **108**, 4 (2023).

[53] D. E. Kharzeev, J. Liao and P. Tribedy, Int. J. Mod. Phys. E **33**, 2430007 (2024).

[54] Y. Feng, S. A. Voloshin and F. Wang, Phys. Rev. Res. **7**, 031001 (2025).

[55] K. Fukushima, D. E. Kharzeev and H. J. Warringa, Phys. Rev. D **78**, 074033 (2008).

[56] J. Mei, R. Wen, S. Mao, M. Huang and K. Xu, Phys. Rev. D **110**, 034024 (2024).

[57] J. Alexandre, K. Farakos and G. Koutsoumbas, Phys. Rev. D **63**, 065015 (2001).

[58] F. Preis, A. Rebhan and A. Schmitt, Lect. Notes Phys. **871**, 51 (2013).

[59] D. E. Kharzeev, J. Liao, S. A. Voloshin and G. Wang, Prog. Part. Nucl. Phys. **88**, 1 (2016).

[60] O. Rogachevsky, A. Sorin and O. Teryaev, Phys. Rev. C **82**, 054910 (2010).

[61] Y. Jiang and J. Liao, Phys. Rev. Lett. **117**, 192302 (2016).

[62] V. Vovchenko, D. V. Anchishkin and M. I. Gorenstein, Phys. Rev. C **91**, 064314 (2015).

[63] J. Letessier and J. Rafelski, Eur. Phys. J. A **35**, 221 (2008).

[64] J. Cleymans and H. Satz, Z. Phys. C **57**, 135 (1993).

[65] J. Cleymans and K. Redlich, Phys. Rev. Lett. **81**, 5284 (1998).

[66] J. Cleymans and K. Redlich, Phys. Rev. C **60**, 054908 (1999).

[67] F. Becattini, J. Cleymans, A. Keranen, E. Suhonen and K. Redlich, Phys. Rev. C **64**, 024901 (2001).

[68] F. Becattini, M. Gazdzicki, A. Keranen, J. Manninen and R. Stock, Phys. Rev. C **69**, 024905 (2004).

[69] A. Andronic, P. Braun-Munzinger and J. Stachel, Nucl. Phys. A **772**, 167 (2006).

[70] S. P. Behera and D. K. Mishra, Nucl. Phys. A **1024**, 122475 (2022).

[71] R. Venugopalan and M. Prakash, Nucl. Phys. A **546**, 718-760 (1992)

[72] O. Savchuk, V. Vovchenko, R. V. Poberezhnyuk, M. I. Gorenstein and H. Stoecker, Phys. Rev. C **101**, 035205 (2020)

[73] S. Pal, G. Kadam, H. Mishra and A. Bhattacharyya, Phys. Rev. D **103**, 054015 (2021).

[74] B. Borderie and J. D. Frankland, Prog. Part. Nucl. Phys. **105**, 82 (2019).

[75] H. Jaqaman, A. Z. Mekjian and L. Zamick, Phys. Rev. C **27**, 2782 (1983).

[76] J. Pochodzalla, T. Mohlenkamp, T. Rubehn, A. Schuttauf, A. Worner, E. Zude, M. Begemann-Blaich, T. Blaich, H. Emling and A. Ferrero, *et al.* Phys. Rev. Lett. **75**, 1040 (1995).

[77] Kerson Huang, *Statistical mechanics*, 2nd ed., Wiley, New York (1987).

[78] W. Greiner, L. Neise, and H. Stöcker, Thermodynamics and Statistical Mechanics, Springer-Verlag, New York (1995).

[79] L. D. Landau and E. M. Lifshitz, *Course of Theoretical Physics: Statistical Physics*, Part 1, Vol. 5, Pergamon Press, Oxford (1980).

[80] V. Vovchenko, M. I. Gorenstein and H. Stoecker, Phys. Rev. Lett. **118**, 182301 (2017).

[81] S. Samanta and B. Mohanty, Phys. Rev. C **97**, 015201 (2018).

[82] V. Vovchenko, D. V. Anchishkin, M. I. Gorenstein and R. V. Poberezhnyuk, Phys. Rev. C **92**, 054901 (2015).

[83] N. Sarkar and P. Ghosh, Phys. Rev. C **98**, 014907 (2018).

[84] A. Bazavov, H. T. Ding, P. Hegde, O. Kaczmarek, F. Karsch, E. Laermann, Y. Maezawa, S. Mukherjee, H. Ohno and P. Petreczky, *et al.* Phys. Rev. D **95**, 074505 (2017).

[85] R. S. Bhalerao, Pramana **75**, 247 (2010).

[86] G. Aarts and A. Nikolaev, Eur. Phys. J. A **57**, 118 (2021).

[87] G. P. Kadam, H. Mishra and L. Thakur, Phys. Rev. D **98**, 114001 (2018).

[88] Mirco Cannoni, Phys. Rev. D **89**, 103533 (2014).

[89] P. Gondolo and G. Gelmini, Nucl. Phys. B **360**, 145 (1991).

[90] G. P. Kadam and H. Mishra, Phys. Rev. C **92**, 035203 (2015).

[91] C. Patrignani *et al.* [Particle Data Group], Chin. Phys. C **40**, 100001 (2016).

[92] N. A. Tawfik, L. I. Abou-Salem, A. G. Shalaby, M. Hanafy, A. Sorin, O. Rogachevsky, and W. Scheinast, Eur. Phys. J. A **52**, 324 (2016).

[93] P. Braun-Munzinger, D. Magestro, K. Redlich, and J. Stachel, Phys. Lett. B **518**, 41 (2001).

[94] J. Cleymans, H. Oeschler, K. Redlich and S. Wheaton, Phys. Rev. C **73**, 034905 (2006).

[95] A. Khuntia, S. K. Tiwari, P. Sharma, R. Sahoo and T. K. Nayak, Phys. Rev. C **100**, 014910 (2019).

[96] K. K. Pradhan, D. Sahu, R. Scaria and R. Sahoo, Phys. Rev. C **107**, 014910 (2023).

[97] W. Cassing, O. Linnyk, T. Steinert and V. Ozvenchuk, Phys. Rev. Lett. **110**, 182301 (2013).

[98] M. Greif, C. Greiner and G. S. Denicol, Phys. Rev. D **93**, 096012 (2016).

[99] D. Fernandez-Fraile and A. Gomez Nicola, Phys. Rev. D **73**, 045025 (2006).

[100] P. Sahoo, S. K. Tiwari and R. Sahoo, Phys. Rev. D **98**, 054005 (2018).

[101] A. Hosoya and K. Kajantie, Nucl. Phys. B **250**, 666 (1985).

[102] S. R. De Groot, W. A. Van Leeuwen and C. G. Van Weert, Relativistic Kinetic Theory (North Holland, Amsterdam, 1980).

[103] R. Marty, E. Bratkovskaya, W. Cassing, J. Aichelin and H. Berrehrah, Phys. Rev. C **88**, 045204 (2013).

[104] S. Mitra and S. Sarkar, Phys. Rev. D **89**, 054013 (2014).

[105] S. Mitra and V. Chandra, Phys. Rev. D **96**, 094003 (2017).

[106] S. Borsanyi *et al.* [Wuppertal-Budapest], JHEP **09** (2010), 073.

[107] G. Aarts, C. Allton, A. Amato, P. Giudice, S. Hands and J. I. Skullerud, JHEP **02**, 186 (2015).

[108] L.P. Kadanoff and P.C. Martin, Annals of Physics **24**, 419 (1963).

[109] S. N. Bose, Z. Phys. 26, 178 (1924).

[110] Quantentheorie des einatomigen idealen Gases. https://doi.org/10.1002/3527608958.ch27

[111] A. Einstein, Zeitschr. für Physik, (2024) and (2025). https://www.uni-muenster.de/imperia/md/content/physik_ap/demokritov/mbecfornonphysicists/einstein_1924_1925.pdf

[112] M. H. Anderson, J. R. Ensher, M. R. Matthews, C. E. Wieman and E. A. Cornell, Science **269**, 198 (1995).

[113] G. N. Fowler, N. Stelte and R. M. Weiner, Nucl. Phys. A **319**, 349 (1979).

[114] J. Letessier and J. Rafelski, Phys. Rev. C **59**, 947 (1999).

[115] V. V. Begun and M. I. Gorenstein, Phys. Rev. C **77**, 064903 (2008).

[116] V. Begun and W. Florkowski, Phys. Rev. C **91**, 054909 (2015).

[117] V. V. Begun, M. I. Gorenstein and O. A. Mogilevsky, Phys. Rev. C **82**, 024904 (2010).

[118] S. Deb, D. Sahu, R. Sahoo and A. K. Pradhan, Eur. Phys. J. A **57**, 158 (2021).

[119] O. Savchuk, Y. Bondar, O. Stashko, R. V. Poberezhnyuk, V. Vovchenko, M. I. Gorenstein and H. Stoecker, Phys. Rev. C **102**, 035202 (2020).

[120] B. B. Abelev *et al.* [ALICE], Phys. Rev. C **89**, 024911 (2014).

[121] Yamamoto, Y. *QIS385: Bose-Einstein Condensation and Matter-Wave Lasers*, National Institute of Informatics, Quantum Information Lecture Series. Available at: https://www.nii.ac.jp/qis/first-quantum/e/forStudents/lecture/pdf/qis385/QIS385_chap3.pdf.

[122] E. Megías, V. S. Timóteo, A. Gammal, and A. Deppman, Physica A **585**, 126440 (2022).

[123] Schwartz, M. *Lecture 12: Bose–Einstein Condensation.* Statistical Mechanics (Spring 2019), Harvard University. Available at: https://schwartz.scholars.harvard.edu/sites/g/files/omnuum7046/files/schwartz/files/12-bec_0.pdf

[124] K. K. Pradhan, D. Sahu, C. R. Singh and R. Sahoo, Phys. Rev. D **112**, 074031 (2025).

[125] A. Khuntia, P. Sahoo, P. Garg, R. Sahoo and J. Cleymans, Eur. Phys. J. A **52**, 292 (2016).

[126] M. B. Kim, A. Svidzinsky, G. S. Agarwal, and M. O. Scully, Phys. Rev. A **97**, 013605 (2018).

[127] T. Damm, J. Schmitt, Q. Liang, D. Dung, F. Vewinger, M. Weitz, & J. Klaers, Nature Commun. **7**, 11340 (2016).

[128] T. Yefsah, R. Desbuquois, K. J. Günter, and J. Dalibard, Phys. Rev. Lett. **107**, 130401 (2011).

[129] R.J. Thorn, The Journal of Chemical Thermodynamics, **34**, 973 (2002).

[130] C. J. Pethick and H. Smith, *Bose-Einstein Condensation in Dilute Gases*, 2nd ed., Cambridge University Press, Cambridge (2008).

[131] R. K. Pathria and P. D. Beale, *Statistical Mechanics*, 3rd ed., Academic Press, Boston (2011).

[132] Hui Hu, Zeng-Qiang Yu, Jia Wang, and Xia-Ji Liu, Phys. Rev. A **104**, 043301 (2021).

[133] P. Jakubczyk, K. Myśliwy, and M. Napiórkowski, Phys. Rev. A **109**, 013312 (2024).

[134] Z. Chen, C. Greiner, Z. Xu and P. Zhuang, Phys. Rev. C **100**, 014906 (2019).

[135] S. Gavin, Nucl. Phys. A **435**, 826 (1985).

[136] F. Reif, Fundamentals of Statistical and Thermal Physics, McGraw-Hill, New York (1965).

[137] S. Plumari, A. Puglisi, F. Scardina and V. Greco, Phys. Rev. C **86**, 054902 (2012).

[138] A. Wiranata and M. Prakash, Phys. Rev. C **85**, 054908 (2012).

[139] X. G. Huang, A. Sedrakian and D. H. Rischke, Annals Phys. **326**, 3075 (2011).

[140] A. Wiranata, M. Prakash and P. Chakraborty, Central Eur. J. Phys. **10**, 1349 (2012).

[141] G. P. Kadam and H. Mishra, Nucl. Phys. A **934**, 133 (2014).

[142] F. Karsch, D. Kharzeev and K. Tuchin, Phys. Lett. B **663**, 217 (2008).

[143] S. K. Tiwari, S. Tripathy, R. Sahoo and N. Kakati, Eur. Phys. J. C **78**, 938 (2018).

[144] M. A. Shahzamanian and H. Yavary, Ann. Phys. **321**, 1063 (2006).

[145] G. S. Denicol, T. Kodama, T. Koide and P. Mota, Phys. Rev. C **80**, 064901 (2009).

[146] R. Scaria, D. Sahu, C. R. Singh, R. Sahoo and J. e. Alam, Eur. Phys. J. A **59**, 140 (2023).

[147] H. Song and U. W. Heinz, J. Phys. G **36**, 064033 (2009).

[148] S. Ghosh, G. Krein and S. Sarkar, Phys. Rev. C **89**, 045201 (2014).

[149] R. Lang, N. Kaiser and W. Weise, Eur. Phys. J. A **48**, 109 (2012).

[150] D. Fernandez-Fraile and A. Gomez Nicola, Eur. Phys. J. A **31**, 848 (2007).

[151] P. Kalikotay, S. Ghosh, N. Chaudhuri, P. Roy and S. Sarkar, Eur. Phys. J. A **60**, 71 (2024).

[152] E. Lu and G. D. Moore, Phys. Rev. C **83**, 044901 (2011).

[153] J. W. Chen and J. Wang, Phys. Rev. C **79**, 044913 (2009).

[154] S. Mitra and S. Sarkar, Phys. Rev. D **87**, 094026 (2013).

[155] B. Sahoo, K. K. Pradhan, D. Sahu and R. Sahoo, Phys. Rev. D **108**, 074028 (2023).

[156] X. Wang, M. Wei, Z. Li and M. Huang, Phys. Rev. D **99**, 016018 (2019).

[157] N. Padhan, K. K. Pradhan, A. Chatterjee and R. Sahoo, [arXiv:2603.27267 [hep-ph]].

[158] F. Becattini and F. Piccinini, Annals Phys. **323**, 2452 (2008).

[159] F. Becattini and L. Tinti, Annals Phys. **325**, 1566 (2010).

[160] L. Landau, L. Lifshitz, *Statistical Physics*, Pergamon Press (1980).

[161] F. Becattini and L. Ferroni, Eur. Phys. J. C **51**, 899 (2007).

[162] F. Becattini and L. Ferroni, Eur. Phys. J. C **52**, 597 (2007).

[163] F. Becattini, V. Chandra, L. Del Zanna and E. Grossi, Annals Phys. **338**, 32 (2013).

[164] Y. Fujimoto, K. Fukushima and Y. Hidaka, Phys. Lett. B **816**, 136184 (2021).

[165] G. Mukherjee, D. Dutta and D. K. Mishra, Phys. Lett. B **846**, 138228 (2023).

[166] K. K. Pradhan, B. Sahoo, D. Sahu and R. Sahoo, Eur. Phys. J. C **84**, 936 (2024).

[167] R. Bellwied, S. Borsanyi, Z. Fodor, S. D. Katz, A. Pasztor, C. Ratti and K. K. Szabo, Phys. Rev. D **92**, 114505 (2015).

[168] W. Florkowski, B. Friman, A. Jaiswal and E. Speranza, Phys. Rev. C **97**, 041901 (2018).

[169] C. Ratti and R. Bellwied, Lect. Notes Phys. **981**, 1 (2021), doi:10.1007/978-3-030-67235-5

[170] A. J. Mizher, M. N. Chernodub and E. S. Fraga, Phys. Rev. D **82**, 105016 (2010).

[171] K. K. Pradhan, B. Sahoo, D. Sahu and R. Sahoo, J. Subatomic Part. Cosmol. **4**, 100134 (2025).

[172] V. V. Begun and M. I. Gorenstein, Phys. Lett. B **653**, 190 (2007).

[173] B. B. Brandt, G. Endrodi and S. Schmalzbauer, Phys. Rev. D **97**, 054514 (2018).

[174] V. A. Kuznietsov, O. S. Stashko, O. V. Savchuk and M. I. Gorenstein, Phys. Rev. C **104**, 055202 (2021).

[175] R. Mallick, S. Schramm, V. Dexheimer and A. Bhattacharyya, Mon. Not. Roy. Astron. Soc. **449**, 1347.

[176] D. N. Voskresensky, Phys. Lett. B **392**, 262(1997).

[177] A. Vilenkin, Phys. Rev. D **21**, 2260 (1980).

[178] H. L. Chen, K. Fukushima, X. G. Huang and K. Mameda, Phys. Rev. D **93**, 104052 (2016).

[179] S. Ebihara, K. Fukushima and K. Mameda, Phys. Lett. B **764**, 94 (2017).

[180] G. Mukherjee, D. Dutta and D. K. Mishra, Eur. Phys. J. C **84**, 258 (2024).

[181] K. K. Pradhan, D. Sahu and R. Sahoo, Phys. Lett. B **872**, 140090 (2026).

[182] S. Acharya *et al.* [ALICE], Phys. Lett. B **813**, 136030 (2021).

[183] D. Sahu, S. Tripathy, G. S. Pradhan and R. Sahoo, Phys. Rev. C **101**, 014902 (2020).

[184] E. Siri and N. Sadooghi, Phys. Rev. D **111**, 036011 (2025).

[185] Z. T. Liang and X. N. Wang, Phys. Lett. B **629**, 20 (2005).

[186] S. Acharya *et al.* [ALICE Collaboration], Phys. Rev. Lett. **125**, 012301 (2020).

[187] M. S. Abdallah *et al.* [STAR Collaboration], Nature **614**, 244 (2023).

[188] F. Sun, J. Shao, R. Wen, K. Xu and M. Huang, Phys. Rev. D **109**, 116017 (2024).

[189] O. Aharony, K. Peeters, J. Sonnenschein and M. Zamaklar, JHEP **02**, 071 (2008).

[190] S. Acharya *et al.* [ALICE], Eur. Phys. J. C **84**, 813 (2024).

[191] S. Borsanyi, Z. Fodor, J. N. Guenther, S. K. Katz, K. K. Szabo, A. Pasztor, I. Portillo and C. Ratti, JHEP **10**, 205 (2018).

[192] V. Vovchenko, D. V. Anchishkin and M. I. Gorenstein, Phys. Rev. C **91**, 024905 (2015).

[193] J. I. Kapusta and K. A. Olive, Nucl. Phys. A **408**, 478 (1983).

[194] K. A. Olive, Nucl. Phys. B **190**, 483 (1981).

[195] S. Pal, A. Bhattacharyya and R. Ray, Nucl. Phys. A **1010**, 122177 (2021).

[196] H. X. Zhang, J. W. Kang and B. W. Zhang, Phys. Rev. D **101**, 114033 (2020).

[197] V. Vovchenko, D. V. Anchishkin and M. I. Gorenstein, J. Phys. A **48**, 305001 (2015).

[198] V. Vovchenko, Phys. Rev. C **96**, 015206 (2017).

[199] A. Mukherjee, J. Steinheimer and S. Schramm, Phys. Rev. C **96**, 025205 (2017).

[200] J. Cleymans, H. Oeschler, K. Redlich and S. Wheaton, Phys. Rev. C **73**, 034905 (2006).

[201] K. K. Pradhan, R. Scaria, D. Sahu and R. Sahoo, [arXiv:2308.09337].

[202] M. Dutra, B. M. Santos and O. Lourenço, J. Phys. G **47**, 035101 (2020).

[203] J. Cleymans, H. Oeschler and K. Redlich, Phys. Rev. C **59**, 1663 (1999).

[204] R. Poberezhnyuk, V. Vovchenko, A. Motornenko, M. I. Gorenstein and H. Stoecker, Phys. Rev. C **100**, 054904 (2019).

[205] M. A. Stephanov, K. Rajagopal and E. V. Shuryak, Phys. Rev. Lett. **81**, 4816 (1998).

[206] M. A. Stephanov, Phys. Rev. Lett. **102**, 032301 (2009).

[207] M. A. Stephanov, K. Rajagopal and E. V. Shuryak, Phys. Rev. D **60**, 114028 (1999).

[208] M. A. Stephanov, Phys. Rev. Lett. **107**, 052301 (2011).

[209] Y. Hatta and M. A. Stephanov, Phys. Rev. Lett. **91**, 102003 (2003) [erratum: Phys. Rev. Lett. **91**, 129901 (2003)].

[210] M. Stephanov and Y. Yin, Phys. Rev. D **98**, 036006 (2018).

[211] B. Berdnikov and K. Rajagopal, Phys. Rev. D **61**, 105017 (2000).

[212] L. Adamczyk *et al.* [STAR], Phys. Rev. Lett. **112**, 032302 (2014).

[213] M. Abdallah *et al.* [STAR], Phys. Rev. C **104**, 024902 (2021) [erratum: Phys. Rev. C **111**, 029902 (2025)].

[214] B. Aboona *et al.* [STAR], Phys. Rev. Lett. **130**, 082301 (2023) [erratum: Phys. Rev. Lett. **134**, 139901 (2025)].

[215] J. Adam *et al.* [STAR], Phys. Rev. Lett. **126**, 092301 (2021).

[216] L. Adamczyk *et al.* [STAR], Phys. Rev. Lett. **113**, 092301 (2014).

[217] L. Adamczyk *et al.* [STAR], Phys. Lett. B **785**, 551 (2018).

[218] S. Chatterjee, S. Das, L. Kumar, D. Mishra, B. Mohanty, R. Sahoo and N. Sharma, Adv. High Energy Phys. **2015**, 349013 (2015).

[219] C. Adler *et al.* [STAR], Phys. Rev. Lett. **86**, 4778 (2001) [erratum: Phys. Rev. Lett. **90**, 119903 (2003)].

[220] P. Braun-Munzinger, D. Magestro, K. Redlich and J. Stachel, Phys. Lett. B **518**, 41 (2001).

[221] S. V. Afanasiev *et al.* [NA49], Phys. Rev. C **66**, 054902 (2002).

[222] M. van Leeuwen, S. V. Afanasiev, T. Anticic, B. Baatar, D. Barna, J. Bartke, R. A. Barton, M. Behler, L. Betev and H. Białkowska, *et al.* Nucl. Phys. A **715**, 161 (2003).

[223] C. Alt *et al.* [NA49], Phys. Rev. Lett. **94**, 192301 (2005).

[224] C. Alt *et al.* [NA49], Phys. Rev. C **77**, 024903 (2008).

[225] C. Alt *et al.* [NA49], Phys. Rev. C **78**, 034918 (2008).

[226] J. Rafelski, Eur. Phys. J. A **51**,114 (2015).

[227] D. K. Mishra, P. Garg, P. K. Netrakanti and A. K. Mohanty, Phys. Rev. C **94**, 014905 (2016).

[228] J. Noronha-Hostler, R. Bellwied, J. Gunther, P. Parotto, A. Pasztor, I. Portillo Vazquez and C. Ratti, [arXiv:1607.02527 [hep-ph]].

[229] M. Nahrgang, M. Bluhm, P. Alba, R. Bellwied and C. Ratti, Eur. Phys. J. C **75**, 573 (2015).

[230] L. Ahle *et al.* [E866 and E917], Phys. Lett. B **476**, 1 (2000).

[231] J. L. Klay *et al.* [E-0895], Phys. Rev. C **68**, 054905 (2003)

[232] L. Ahle *et al.* [E866 and E917], Phys. Lett. B **490**, 53 (2000).

[233] J. L. Klay *et al.* [E895], Phys. Rev. Lett. **88**, 102301 (2002).

[234] P. Alba, W. Alberico, R. Bellwied, M. Bluhm, V. Mantovani Sarti, M. Nahrgang and C. Ratti, Phys. Lett. B **738**, 305 (2014).

[235] J. Fu, Phys. Lett. B **722**, 144 (2013).

[236] V. V. Begun, M. I. Gorenstein, M. Hauer, V. P. Konchakovski and O. S. Zozulya, Phys. Rev. C **74**, 044903 (2006).

[237] V. Vovchenko, O. Savchuk, R. V. Poberezhnyuk, M. I. Gorenstein and V. Koch, Phys. Lett. B **811**, 135868 (2020).

[238] V. Vovchenko, R. V. Poberezhnyuk and V. Koch, JHEP **10**, 089 (2020).

[239] V. Vovchenko, PoS **CPOD2021**, 013 (2022).

[240] P. Braun-Munzinger, B. Friman, K. Redlich, A. Rustamov and J. Stachel, Nucl. Phys. A **1008**, 122141 (2021).

[241] R. V. Poberezhnyuk, O. Savchuk, M. I. Gorenstein, V. Vovchenko, K. Taradiy, V. V. Begun, L. Satarov, J. Steinheimer and H. Stoecker, Phys. Rev. C **102**, 024908 (2020).

[242] A. Bzdak, V. Koch and V. Skokov, Phys. Rev. C **87**, 014901 (2013).

[243] P. Braun-Munzinger, A. Rustamov and J. Stachel, Nucl. Phys. A **960**, 114 (2017).

[244] S. Acharya *et al.* [ALICE], Phys. Lett. B **807**, 135564 (2020).

[245] K. Fukushima, Phys. Rev. C **91**, 044910 (2015).

[246] M. Kitazawa and M. Asakawa, Phys. Rev. C **85**, 021901 (2012).

[247] M. Kitazawa and M. Asakawa, Phys. Rev. C **86**, 024904 (2012) [E: Phys. Rev. C **86**, 069902 (2012)].

[248] V. Vovchenko, V. Koch and C. Shen, Phys. Rev. C **105**, 014904 (2022).

[249] P. Garg, D. K. Mishra, P. K. Netrakanti, B. Mohanty, A. K. Mohanty, B. K. Singh and N. Xu, Phys. Lett. B **726**, 691 (2013).

[250] S. Jeon and V. Koch, Phys. Rev. Lett. **83**, 5435 (1999).

[251] Y. Fujimoto, K. Fukushima, Y. Hidaka, A. Hiraguchi and K. Iida, Phys. Lett. B **835**, 137524 (2022).

[252] H. Fritzsch, Phys. Lett. B **67**, 217 (1977).

[253] A. Andronic, F. Arleo, R. Arnaldi, A. Beraudo, E. Bruna, D. Caffarri, Z. Conesa del Valle, J. G. Contreras, T. Dahms and A. Dainese, *et al.* Eur. Phys. J. C **76**, 107 (2016).

[254] G. T. Bodwin, E. Braaten and G. P. Lepage, Phys. Rev. D **51**, 1125 (1995) [erratum: Phys. Rev. D **55**, 5853 (1997)].

[255] S. Acharya *et al.* [ALICE], Eur. Phys. J. C **78**, 562 (2018).

[256] F. Abe *et al.* [CDF], Phys. Rev. Lett. **79**, 572 (1997).

[257] J. P. Lansberg, Eur. Phys. J. C **61**, 693 (2009).

[258] R. Aaij *et al.* [LHCb], Eur. Phys. J. C **73**, 2631 (2013)].

[259] D. Acosta *et al.* [CDF], Phys. Rev. Lett. **88**, 161802 (2002).

[260] V. M. Abazov *et al.* [D0], Phys. Rev. Lett. **101**, 182004 (2008).

[261] C. N. Brown *et al.* [NuSea], Phys. Rev. Lett. **86**, 2529 (2001).

[262] S. Chatrchyan *et al.* [CMS], Phys. Rev. Lett. **110**, 081802 (2013).

[263] R. Aaij *et al.* [LHCb], JHEP **12**, 110 (2017).

[264] B. Sahoo, D. Sahu, S. Deb, C. R. Singh and R. Sahoo, Phys. Rev. C **109**, 034910 (2024).

[265] L. Evans and P. Bryant, JINST **3**, S08001 (2008),

[266] G. Aad *et al.* [ATLAS], JINST **19**, P05063 (2024).

[267] M. Masciovecchio [CMS], Nucl. Part. Phys. Proc. **273**, 2378 (2016).

[268] A. A. Alves, Jr. *et al.* [LHCb], JINST **3**, S08005 (2008).

[269] K. Aamodt *et al.* [ALICE], JINST **3**, S08002 (2008).

[270] S. Upadhyaya, Int. J. Mod. Phys. A **40**, 2444006 (2025).

[271] S. Acharya *et al.* [ALICE], JINST **19**, P05062 (2024).

[272] [ALICE Collaboration], "ALICE technical design report of the dimuon forward spectrometer, "CERN-LHCC-99-22.

[273] K. K. Pradhan and R. Sahoo, "Relative Upsilon production in pp collisions in forward rapidity at $\sqrt{s}$ = 13.6 TeV with ALICE", Analysis note ID number: ANA-1645, https://alice-notes.web.cern.ch/node/1645 (ALICE Internal).

[274] https://github.com/AliceO2Group/O2Physics/blob/master/PWGDQ/Core/CutsLibrary.cxx

[275] ALICE analysis note on Υ (nS) cross section in pp collisions at $\sqrt{s}$ = 13 TeV: https://alice-notes.web.cern.ch/system/files/notes/analysis/1371/2023-03-03-UnS_pp_13TeV_AN_v2.pdf.

[276] ALICE analysis note on Υ (nS) production as a function of multiplicity in pp collisions at $\sqrt{s} = 13$ TeV: https://alice-notes.web.cern.ch/system/files/notes/analysis/839/2022-10-29-AliUpsilonMultipp_v9.pdf.

[277] ALICE Analysis Note on Υ production cross section in pp collisions at $\sqrt{s} = 13$ TeV: https://alice-notes.web.cern.ch/system/files/notes/analysis/931/2019-05-16-ALICE_analysis_note.pdf.

[278] ALICE Analysis Note on Υ (1S) polarization in pp collisions at $\sqrt{s} = 13$ TeV https://alice-notes.web.cern.ch/system/files/notes/analysis/1297/2024-10-28-UpsPolarization_pp13TeV_r3_0.pdf.